International Symposium
for the Advancement of
Boundary Layer Remote Sensing

**Garmisch-Partenkirchen, Germany,
July 18 – July 20, 2006**

S. Emeis (Editor)

Institut für Meteorologie und Klimaforschung

Juli 2006

Forschungszentrum Karlsruhe

in der Helmholtz-Gemeinschaft

Wissenschaftliche Berichte
FZKA 7222

International Symposium for the Advancement of Boundary Layer Remote Sensing

Garmisch-Partenkirchen, Germany, July 18 – July 20, 2006

Extended Abstracts

Stefan Emeis (Editor)

Institut für Meteorologie und Klimaforschung

Forschungszentrum Karlsruhe GmbH, Karlsruhe
2006

This conference is organized by the
International Society of Acoustic Remote Sensing of the Atmosphere and Oceans (ISARS)
and the Forschungszentrum Karlsruhe GmbH.

The conference is sponsored by the German Meteorological Society (DMG)
and by METEK GmbH, Elmshorn (Germany).

ISARS 2006
Extended Abstracts

Table of Contents

Session 3 Applications of boundary layer remote sensing

Session 3a Environmental aspects, dispersion

Session 3b   Wind energy

Session 4   Comparison of remote sensing information with results of boundary layer models

Determination of turbulent fluxes in the ABL by different ground-based remote sensing methods

Kallistratova M.A.[1], Engelbart D.[2]

[1] Obukhov Institute of Atmospheric Physics Russian Academy of Sciences

margo@ifaran.ru

[2] Meteorological Observatory Lindenberg, DWD

New methods for determination of vertical profiles of turbulent fluxes in the ABL using ground based remote techniques are considered. Some results of recent experiments on estimates of momentum flux and/or heat flux with help of wind profiler radar, lidar, wind profiler radar/RASS, sodar/RASS, and sodar are presented. The main problems, achievements, advantages and disadvantages of different remote sensing methods used in the experiments are discussed.

Broadband Acoustic Backscatter Response of the Atmosphere

Frank Böttcher[1], Stuart Bradley[1], Andrew Martin[2]

[1] Physics Department, University of Auckland, Private Bag 92019, Auckland, New Zealand
f.bottcher@auckland.ac.nz & *s.bradley@auckland.ac.nz*

[2] StratoSonde Pty Ltd, Mulgrave, Victoria, Australia *andrew.martin@stratosonde.com*

Abstract

The frequency response of the atmosphere is well established both theoretically and in practice for narrow-band remote sensing devices such as conventional SODARs. Implementation of swept frequency acoustic profilers requires however an understanding of the frequency spectrum resulting from volume scattering of a broadband signal and it is not *a priori* evident that even the well known Bragg condition applies. In this paper we describe a number of approaches toward understanding this more complex atmospheric response. These include: theoretical analysis of idealized atmospheres; numerical modeling based on the relatively simple theory; and unconstrained numerical simulation of the broadband pulse interacting with various atmospheric reflectance profiles. Some of the results are very different from those expected for the narrow band case, but can be explained in simple physical terms. Happily the three modeling approaches show good agreement, lending support for using the theoretical model for insight into scaling relationships and parameter dependencies and use of the detailed simulation for evaluation of system performance against, for example, atmospheric profiles generated by mesoscale models.

1 Introduction

Conventional short pulse SODAR systems use the time information of the received signal to locate the reflectance source and the Doppler-shifted spectral response to derive the associated speed. This leads however to a rather limited range and resolution due to the required shortness of the pulse. Based on the ideas of (Bradley, 1999), in order to overcome these limitations, (Martin, 2004) introduced a new SODAR concept using a very long ($T \geq 30s$) but compressed (linear chirp) pulse. For this broadband signal the spectral response will be quite different compared to the short pulse. For instance, for two reflectance layers separated by Δz one would expect a modulated frequency due to Bragg scattering. It can be shown that this modulation will be periodic in the frequency domain with a spacing of

$$\Delta f = \frac{c}{2\Delta z} \tag{1}$$

where c is the speed of sound.

In the following we will consider the spectra of this long pulse system for idealized situations for which analytical results can be given and will also simulate an exemplary atmospheric response for a typical turbulent spectrum. Based on these results a simple numerical integration can then be used in order to simulate the atmosphere's response also for more complicated situations.

2 Received Signal for Idealized Reflectance Profiles

The signal from a reflector at height z_n is received after delay $t_n = 2z_n/c$. For a linear-chirp signal with bandwidth B and duration T the angular frequency is $\omega_0 + mt$ where $m := 2\pi B/T$. Then the received signal (amplitude is set to 1) is

$$s(t) = \int_0^\infty dz \, r(z) \cdot exp\big[i\big(\omega_0 + m(t - 2z/c)\big)(t - 2z/c)\big]. \tag{2}$$

For $m = 0$ Eq. (2) reduces to the conventional case of $s_{m=0}(t) = e^{i\omega_0 t} R(2k_0)$ where $R(2k_0)$ is the spatial Fourier transform of the normalized reflectance profile $r(z)$. We now assume three simple analytic forms of $r(z)$:

- (a) a peak at z_1, i.e. $r(z) = \delta(z - z_1)$,

- (b) a constant value between z_1 and z_2 (zero elsewhere) and

- (c) a Gaussian profile with standard deviation σ centered around z_1.

Then Eq. (2) can be integrated numerically and be compared to the analytic results. After some calculations the real parts of the latter are given by:

$$(a) \quad s_r(t) \quad \propto \quad cos\left[\omega_0(t - t_1) + m(t - t_1)^2\right] \tag{3}$$

$$(b) \quad s_r(t) \quad \propto \quad \sum_{k=1}^{2}(-1)^k \frac{sin\left[\omega_0(t - t_k) + m(t - t_k)^2\right]}{m(t_k - 2t) - \omega_0} \tag{4}$$

$$(c) \quad s_r(t) \quad \propto \quad a^{-3/4} \, exp\left[-\frac{2b^2}{a}\right] \left\{cos[\beta] - \sqrt{a - 1} \, sin[\beta]\right\}. \tag{5}$$

In Eq. (4) the asymptotic limit of the Fresnel integrals has been applied, in Eq. (5) the parameters are $a = 1 + 64m^2\sigma^4/c^4$, $b = (4m\sigma z_1 - 2cmt\sigma - c\omega_0\sigma)/c^2$ and $\beta = (4mz_1^2 - 4cmtz_1 - 2c\omega_0 z_1)/c^2 + \omega_0 t + mt^2 - b^2\sqrt{a - 1}/(2a)$. For multiple reflectors the received signal is just the sum of the individual solutions from Eqs. (3–5).

Fig. 1 shows the results for the cases (a) – (c) exemplary for $f_0 = \omega_0/2\pi = 1700 Hz$, $m/2\pi = 25 s^{-2}$ and $T = 15s$. Note, for a conventional signal every profile would yield the same single peak around f_0!
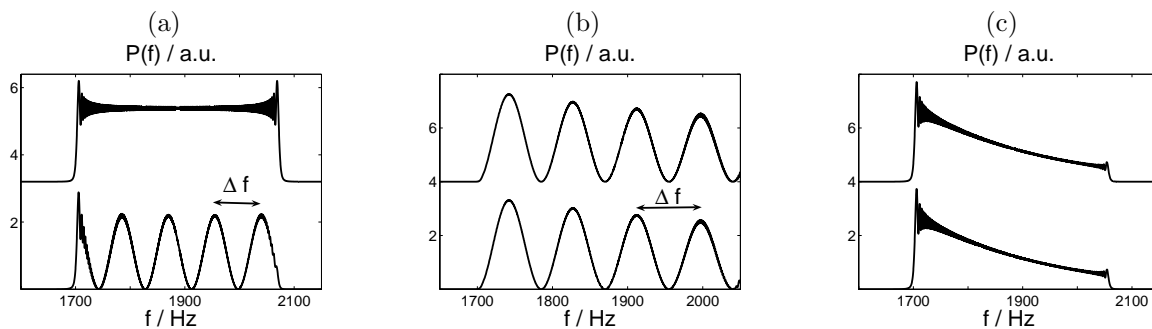
Figure 1: *Power spectra of the received signals. Plots are shifted for clarity of presentation.* **(a)** *One reflectance peak at $z_1 = 50m$ (top) and two peaks at $z_1 = 50m$ and $z_2 = 52m$ (bottom).* **(b)** *A constant reflectance between $z_1 = 50m$ and $z_2 = 52m$. In (a) and (b) the periodicity predicted by Eq. (1) is evident.* **(c)** *A Gaussian reflectance profile with variance $\sigma^2 = (0.03m)^2$ centered around $z_1 = 50m$. In (b) and (c) the top curves refer to the numerical integration of Eq. (2) the bottom ones to the analytic solutions given by Eq. (4) and (5) which agree well. Also there is an attenuation towards higher frequencies in contrast to case (a) which is in agreement with Eqs. (3-5).*

3 Doppler Shift and Random Profiles

To simulate a Doppler shift by means of numerical integration of Eq. (2) we can simply allow the profile to move upwards ($w > 0$) or downwards ($w < 0$) with speed w, e.g.

$z_1 \rightarrow z_{01} + w(t - t_1)$ with $t_1 = 2z_{01}/c$. Defining $\alpha = (1 - 2w/c)$ Eq. (3), for instance, becomes

$$s_r(t) \propto cos\left[\alpha\omega_0(t - t_1) + \alpha^2 m(t - t_1)^2\right] \quad (6)$$

which can again be used for comparison with the direct integration.

In a last step we introduce a random reflectance profile within some $[z_1, z_2]$. Following (Tatarski, 1967) we choose $r(z)$ such that its spectrum behaves like $R(k) \propto k^{-5/3}$ for large k and is finite for $k = 0$. To this end we used a *Kaimal spectrum* to generate $r(z)$. Results are presented in Fig. 2.
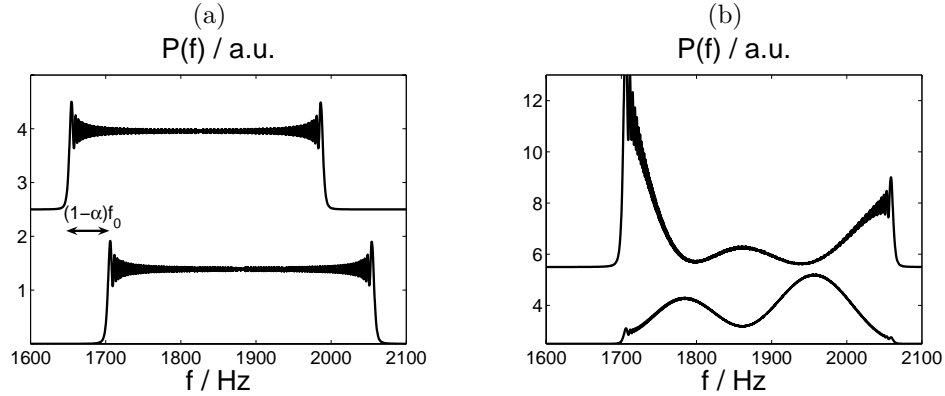
Figure 2: *Power spectra of the received signals. Parameters are the same as before. Plots are shifted for clarity of presentation.* **(a)** *A single peak at height $z_1 = 50m$ and $\alpha = 1$ (bottom) and $\alpha = 0.97$ (top).* **(b)** *Top and bottom plots refer to two different realizations of $r(z)$ between $50m$ and $51m$ (zero elsewhere). Clearly the spectrum looks significantly different.*

4 Conclusions

The spectral response of a chirped signal scattered at idealized reflectance profiles has been calculated and agree with the direct integration of Eq. (2). This allows implementation of more complicated profiles (random, Doppler-shifted) for numerical simulations. Also, various signal processing algorithms can be tested using idealized simulated received signals.

Literature

A. Martin, 2004: A new technology for SODAR providing very high resolution Boundary Layer profiling with small dead zone for measurements to 2000m, ISARS 2004.

S. G. Bradley, 1999: Use of Coded Waveforms for SODAR Systems, Meteorol. Atmos. Phys. 71, 15-23.

V. I. Tatarski, 1967: Wave Propagation in a Turbulent Medium, Dover Publication, INC., New York.

Estimating Momentum Flux in the ABL with Conventional Sodar Configuration

Rostislav D. Kouznetsov

Obukhov Institute of Atmospheric Physics, Moscow, Russia, e-mail: roux@ifaran.ru

Abstract

A new method for estimation of the vertical structure of momentum flux in the atmospheric boundary layer (ABL) from sodar measurements of wind speed and vertical velocity component was proposed by author on the previous ISARS. The field tests of the method performed in Summer 2005 with LATAN-3 sodar have confirmed the applicability of the method to real sodar measurements.

1 Introduction

The information on vertical structure of turbulent momentum flux is of importance for understanding the dynamics of air flows in the ABL. The vertical profiles of momentum flux and mean wind speed can be used to derive eddy exchange parameters, that would in principle allow to exclude the meteorological block from dispersion models.

The traditional *in situ* measurements of turbulence parameters are not suitable for most practical applications. The use of model turbulence profiles is not much helpful since they do not describe real profiles well under non-ideal conditions (Fischer et al., 1998). The windprofiler radars, Doppler lidars and RASS systems in principle can be used to measure momentum flux profiles in the ABL (see e.g. Engelbart et al., 2002; Perers and Kirtzel, 1994; Eberhard, 1992), however no comprehensive evaluation of accuracy of these measurements is known to the author. Moreover these remote methods require relatively expensive state-of-the-art equipment. The use of sodars and the method described below may provide inexpensive means that is suitable for routine monitoring of momentum flux profiles at least in the lower part of the ABL.

2 The method

It was shown empirically (Kouznetsov et al., 2004) that a simple relation between the momentum flux $\langle uw \rangle$ and the variance of vertical wind component σ_w^2 holds in the lower part of neutrally stratified ABL (but above the surface layer):

$$\langle uw \rangle = -0.77 \sigma_w^2. \tag{1}$$

This relation holds at least in the lower 100 meters. Using this relationship one can estimate the vertical structure of momentum flux in neutrally stratified ABL by means of a sodar (or any other remote sensing tool) that is able to measure σ_w^2 accurately enough. To adopt this relationship to arbitrary stratification conditions, Kouznetsov and Beyrich (2004) suggested to replace the coefficient in (1) by an empirical function of some stratification parameter.

The flux Richardson number is usually defined as:

$$\mathrm{Rf} = \frac{g}{\Theta} \frac{\langle w\theta \rangle}{\langle uw \rangle \, \partial V / \partial z}, \tag{2}$$

where g – gravity, Θ – potential temperature, and $\langle w\theta \rangle$ is the temperature flux. Rf is the ratio of buoyancy and mechanical production of turbulent kinetic energy.

The flux Richardson number can be used as a parameter of universal functions in a similar way as z/L is used in Monin-Obukhov theory. Let us introduce the empirical function $\mathrm{F}_{mf}(\mathrm{Rf})$ such as:

$$\langle uw \rangle = \mathrm{Sign}\left(\frac{\partial V}{\partial z}\right) \cdot \mathrm{F}_{mf}(\mathrm{Rf}) \cdot \sigma_w^2. \tag{3}$$

(The signum function is included to provide the generation of turbulence for any sign of the wind shear.) If the function $F_{mf}(Rf)$ is known, wind profile $V(z)$, σ_w^2 and temperature flux can be used to estimate the momentum flux.

Sodar is unable to measure the temperature flux. For this application the temperature flux can be parameterized as a linear function of altitude. It is equal to the surface value at the ground and zero at the top of the mixing layer. The height if a mixing layer can be derived from sodar echogramme. The surface value of the heat flux should be obtained from supplementary measurements.

The universal function $F_{mf}(Rf)$ was estimated from a data of LINEX-2000 experiment by Kouznetsov and Beyrich (2004) at altitudes 50 and 90 meters above flat homogeneous terrain. In a similar manner it was calculated from Zvenigorod-2005 data (see below). These estimates are summarized in Fig. 1. Each data point on the plot is the result of averaging of about 50 half-hour-long time series. It is seen that different estimates of $F_{mf}(Rf)$ agree well.

The shape of the empirical function $F_{mf}(Rf)$ indicates that the error in Rf estimate leads to much smaller relative error in $\langle uw \rangle$. The comparison of values of momentum flux estimated using this method with *in situ* measured those (Fig. 2) indicates nearly the same scattering as similar comparison for σ_w^2. This means that the error of the result is determined mostly by an error in σ_w^2 values measured by the sodar.

Figure 1. The empirical function $F_{mf}(Rf)$
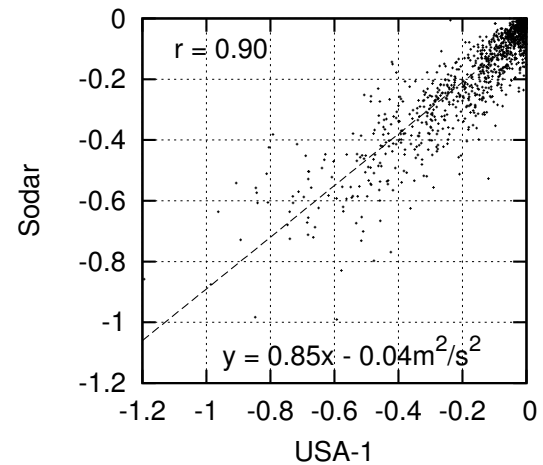
Figure 2. Comparison of remotely and *in situ* measured momentum flux. h=56m Half-hourly averaging. Zvenigorod, July 2005

3 Application

The measurements were performed in during July 2005 at Zvenigorod Scientific Station (ZSS) of Obukhov Institute of atmospheric physics. ZSS is located in a rural area with slightly inhomogeneous terrain 45 km to the west from Moscow. The measurements were performed by a PC-based LATAN-3 sodar system developed at IAPh (Kouznetsov, 2006). Two USA-1 sonic anemometers (METEK, Germany) installed at altitudes of 6 and 56 meters were used for surface and reference measurements correspondingly.

To illustrate the application of the method, a single day – July 10 2005 was selected from the whole data set. The sodar echogrammes and temperature and heat flux time series measured in Zvenigorod are shown in Fig. 3. Below the echogramme the profiles of wind speed, σ_w^2, $\langle uw \rangle$ and eddy viscosity coefficient K_m (derived from K-approach) were calculated. The profiles measured at 02:00 LT (nocturnal inversion), 07:00 (transitional, neutral stratification at the bottom) and 15:00 (convection) are shown. The wind shear $\partial V / \partial z$ was calculated using analytical approximation of $V(z)$.

The derived momentum flux profiles look reasonable and agree well with local measurements. The profiles of K_m are also reasonable, except the zone of near-zero wind shear. This is due to inapplicability of K-approach in these cases, when more adequate models should be used.

Figure 3. Sodar echogramme and the typical profiles of the wind speed V, the variance of vertical wind component σ_w^2, the momentum flux $\langle uw \rangle$ and the eddy viscosity coefficient K_m derived from sodar measurements for different stratifications of the ABL. Circles denote the data of *in situ* measurements at 56-m mast. Zvenigorod, 10 July 2005.

4 Conclusions and outlook

The acoustic remote sensing is promising method to measure turbulence profiles in the bottom part of the ABL. The outlined method gives reasonable results, however, it needs to be generalized to the case of zero wind shear. The method can be used with any sodar that is able to measure wind speed and σ_w^2 accurately enough.

The measured profiles of turbulent mixing parameters can be used in the dispersion models for urban areas instead of modeled those to improve the quality of air pollution forecasts.

Literature

Eberhard, W. L., 1992. Estimations of atmospheric boundary layer fluxes and other turbulence parameters from Doppler lidar data. Journal of Geophysical Research 97, 18409–18423.

Engelbart, D. A. M., Steinhagen, H., Kallistratova, M. A., 2002. LINEX-2000: Assessment of different methods for determination of reference flux profiles. In: Proc. 12-th Int. Symp. Acoust. Rem. Sens. Rome, Italy, pp. 339–342.

Fischer, B. E. A., Erbrink, J. J., Finardi, S., Jeannet, P., Joffre, S., Morselli, M. G., Pechinger, U., Siebert, P., Thomson, D. J. (Eds.), 1998. COST Action 710 – Final report. Harmonization of the pre-processing of meteorological data for atmospheric dispersion models. Directorate-General Science, Research and Development.

Kouznetsov, R. D., 2006. The new PC-based sodar LATAN-3. In: Proc. 13-th Int. Symp. Acoust. Rem. Sens. Garmisch-Partenkirchen, Germany, pp. ***–***.

Kouznetsov, R. D., Beyrich, F., 2004. Richardson flux number and estimation of momentum flux in the lower ABL. In: Proc. 12-th Int. Symp. Acoust. Rem. Sens. Cambridge, UK, pp. 49–53.

Kouznetsov, R. D., Kramar, V. F., Beyrich, F., Engelbart, D., 2004. Sodar-based estimation of TKE and momentum flux profiles in the atmospheric boundary layer: Test of a parameterization model. Meteorology and Atmospheric Physics 85, 93–99.

Perers, G., Kirtzel, H.-J., 1994. Measurements of momentum flux in the boundary layer by RASS. Journal of Atmospheric and Oceanic Technology 11, 63–75.

Advances in Acoustic Remote Sensing of the Atmosphere in Tomsk

Krasnenko Nikolay
Institute of Monitoring of Climatic and Ecological Systems
of the Siberian Branch of the Russian Academy of Sciences
10/3, Akademicheskii Pr., Tomsk 634055, Russia
E-mail: krasnenko@imces.ru

Abstract

Advances in acoustic remote sensing of the atmosphere made in Tomsk (Russia) for a 30-year period are considered. Sodars and ultrasonic meteorological systems developed in Tomsk are described. Results of theoretical analysis of methods for acoustic sensing of the atmosphere are presented including the interaction of the acoustic radiation with the atmosphere, optimization of the sodar parameters, and accuracy of sodar measurements of the atmospheric parameters. Results of investigations of the parameters of the atmospheric boundary layer above the ground surface and ocean with the sodars developed in Tomsk are given. Sodar-derived data are compared with the results of lidar sensing and ballon and radiozonde measurements of the atmospheric parameters.

1 Introduction

In Tomsk, work in the direction of atmospheric acoustics was started in 1974 when the problem of mastering **acoustic sounding of the atmosphere** was formulated and a group of specialists in atmospheric acoustics was organized at the Institute of Atmospheric Optics of the SB RAS. At that time, I took up work at the IAO SB RAS and had been engaged in the formulation and development of the theoretical principles of acoustic sounding of the atmosphere since 1974. In the next 20 years since 1979, I was engaged in all investigations on atmospheric acoustics as a head of the corresponding Laboratory of the Institute. In 1999, I took up for work at the Institute of Optical Monitoring of the SB RAS (former Special Gesign Bureau of Scientific Instrumentation "Optika" and Design and Technology Institute "Optika"; at present Institute of Monitoring of Climatic and Ecological Systems of the SB RAS) and organized again a scientific group, created an experimental base, and carried out scientific research in the given direction at the IMCES SB RAS. It is impossible to describe briefly all the results obtained by the staff over the 30-year period, but the main advances are described in monographs and reviews [1-5].

2 Results of the acoustic sounding of the atmosphere

To develop **acoustic sounding of the atmosphere**, as always at the beginning of work from nothing, in addition to the study of the formulated problem and interaction of acoustic radiation with the atmosphere as a propagation medium, an experimental base must be created for scientific research, including acoustic radars. Life experience demonstrated that creation of acoustic radars for atmospheric sounding is not only a science but also to a certain degree an art. During more than 30-year period, a number of prototypes and working acoustic radars have been created, including MAL-1, MAL-2, Zvuk-1, Zvuk-2 (renamed Volna-3), mS-1, and Zvuk-3 acoustic radars for sounding of the atmospheric boundary layer and measuring the characteristics of temperature stratification, wind velocity profile, structure constant of temperature fluctuations, etc. The Zvuk-1 acoustic radar was delivered to the Kemerovo Regional Center on Hydrometeorology (1990) and to the Russian Federal Nuclear Center (Chelyabinsk-70) together with an ultrasonic meteorological station (1996).
In theoretical investigatios, much attention was given to a study of mechanisms of acoustic radiation interaction with the atmosphere, theoretical calculations and optimal choice of the sounding system parameters, elaboration of new methods of sounding, study of the influence

of refraction on acoustic radar performance, search for new information opportunities of acoustic sounding, etc. [1, 2].

The foregoing provided the basis for a design of shielded parabolic reflector antennas used in the above-listed acoustic radars [5]. These antennas are one of the main part of an acoustic radar and determin its capabilities. The equipment was developed and a small-lot production of antennas for Zvuk-1 (Zvuk-2), mS-1, and Zvuk-3 acoustic radar modifications was organized.

The developed acoustic radars were used in numerous experiments and expeditions in our country and in Atlantic onboard the *Mstislav Keldysh* research vessel, where they demonstrated their high efficiency and importance for the study of the atmospheric boundary layer. Thus, for example, interdepartmental tests on measuring the wind shear conducted in the Alma-Ata airport in 1987 demonstrated that in such categorized airport as this, the MAL-2 monostatic acoustic radar could stably operate near a runway to measure the meteorological parameters during time intervals between takeoffs and landings of airplanes.

In connection with the severe problem of pollution of the atmosphere of industrial centers, acoustic radars can be very useful for systems of air basin monitoring; they provide information on the meteorological state of the atmospheric boundary layer in real time. The work performed for some years in critical (from the ecological viewpoint) regions of the country allowed us to collect initial data to estimate the ecological state of the atmosphere in these regions. Some experiments were carried out using a sodar, an aerosol lidar, base laser and *in situ* gas analyzers, and ground-based ultrasonic meteorological stations.

The characteristics of temperature stratification (especially of temperature inversions) obtained with acoustic radars are important for climatic prediction of situation hazardous from the viewpoint of atmospheric pollution. It was demonstrated that the statistics of characteristics of temperature stratification is different for different regions and depends on local features (orography of the locality), which results in different conditions for pollutant accumulation. In particular, the general analysis of the conditions of atmospheric stability for Kemerovo allowed us to conclude that the percentage of temperature inversions for this city is high, heights of their boundaries are low, and their spatial localization is relatively stable. All this alongside with low heights of stack mouths (50–120 m) explains unfavorable ecological conditions in industrial regions of the city when smoke plumes are cupped by temperature inversions, thereby increasing the pollutant concentration in the surface layer of the atmosphere. This was also confirmed by the result of laser sensing of aerosol fields of industrial origin.

It was demonstrated that laser and acoustic means of remote sensing of the atmosphere are rather efficient for air pollution monitoring in the city. In this case, a laser radar was used to monitor directly the distribution of aerosol impurities in the atmosphere of large territories, and an acoustic radar, used to monitor the atmospheric state, allowed the atmospheric stability to be monitored in real time and boundaries of temperature inversions to be determined, thereby facilitating the prediction of meteorological conditions hazardous from the viewpoint of air pollution.

Experimental works devoted to simultaneous sensing of the atmospheric boundary layer with acoustic radars and aerosol lidars demonstrated that the main obstacles for vertical aerosol propagation in the atmosphere are barrier layers of temperature inversions where aerosols are accumulated. Moreover, the height of the upper boundary of an aerosol cloud virtually coincided with the barrier layer height. Investigations also revealed a correlation between the atmospheric stratification parameters and concentrations of some gases, in particular, ozone and carbon dioxide.

Now two acoustic radars – Volna-3 at the IAO SB RAS and Zvuk-3 at the IMCEC SB RAS that has been operating continuously in the monitoring mode since December, 2004 – are in use.

3   Ultrasonic systems

The final result of two R&D performed under my supervision was the development of the onboard system, portable system, and various modifications of stationary automated meteorological complexes (AMC) for *in situ* measurements of the meteorological parameters (pressure, humidity, three wind velocity components, and temperature) and turbulent characteristics of the atmosphere. These systems have successfully passed the State tests, certification, and can be used to measure the friction velocity, turbulent heat flux, Monin–Obukhov length, structure constants of the temperature (C_T^2) and wind velocity fields (C_v^2), and many other characteristics with reconstruction of vertical profiles of meteorological characteristics in the atmospheric surface layer.

4   Conclusions

As a result of purposeful 30-year work of two Tomsk institutes of the Russian Academy of Sciences, the scientific community in the field of atmospheric acoustics obtained significant results on the State level. Five Candidate's Dissertations were defended by Shamanaeva L. G. (1984), Bochkarev N. N. (1986), Odintsov S. L. (1987), Bogushevich A. Ya. (2000), Mananko E. E. (2004) and two Doctoral Theses were defended by Krasnenko N. P. (entitled "Acoustic sounding of the atmospheric boundary layer") in 1998 and Bochkarev N. N. (entitled "Atmospheric optoacoustics of high-power laser beams") in 2005. A Lenin Komsomol Premium was awarded to Bochkarev N. N. in 1987, Premiums of the Siberian Branch of the USSR Academy of Sciences were awarded to Krasnenko N. P., Galkin V. I., Molchanov B. N., Fedorov V. A., and Fursov M. G. in 1985 and to Krasnenko N. P., Bochkarev N. N., Root A. G., and Fursov M. G. in 1989; Premium of the Tomsk Region was awarded to Krasnenko N. P. in 2005; a Stipend of the President of the Russian Federation for 2006–2008 was awarded to Krasnenko N. P, etc.

Literature

Krasnenko N. , 1986: Acoustic sounding of the atmosphere. Novosibirsk: Nauka. Sibirian Branch. 167 p. (in Russian).

Krasnenko N., 2001: Acoustic sounding of the atmospheric boundary layer. Tomsk. 2001. 278 P. (in Russian).

Krasnenko N., 1997: Development of atmospheric acoustic research at the IAO SB RAS / Opt. Atm. Okeana. 1997. V. 10. Nos. 4–5. P. 542-552.

Krasnenko N., A. Tikhomirov, 2002: Technical means and technologies of remote sounding of the atmosphere and underlying surface / Opt. Atm. Okeana. 2002. V. 15. No. 1. P. 51-61.

Krasnenko N., E. Mananko, 2004: Parabolic reflector acoustic antennas for atmospheric sounding / Methods and means for information transfer and processing: Intercollege collection of scientific works. No. 5. Romashev V. V., Bulkin V. V., eds. Saint Petersburg: Gidrometeoizdat. 2004. P. 83-98. (in Russian)

On the effects of atmospheric fine structure on the azimuths and grazing angles of acoustic signals at long distances from a pulse source.

Sergey Kulichkov , Igor Chunchuzov , Oleg Popov , Vitali Perepelkin , Alexander Svertilov
A.M. Oboukhov Institute of Atmospharic Physics Russian academy of sciences, Moscow, Russia,
e-mail: snk@ifaran.ru

The effect of atmospheric fine structure on the azimuth and grazing angle of infrasonic signals recorded at long distances from a pulse source is studied both theoretically and experimentally. The parameters of acoustic pulses propagated through the atmospheric boundary layer from a detonator source are analyzed. The pulse repetition period was 1 min and the signals were recorded at distances from 2 km to 6.5 km from a source. Variations in the azimuths and grazing angles of acoustic signals have been observed in all experiments. It is shown that these variations are mostly due to a presence of atmospheric fine-layered inhomogeneities that cause the fluctuations of the phase front direction of infrasonic waves and lead to the errors in determining of the azimuths and grazing angles of infrasonic signals.

1 Introduction

It was suggested in many experimental and theoretical works that the observed layers of turbulence may appear in stably stratified atmosphere as a result of different types of instabilities induced by internal gravity waves (IGWs) from various tropospheric sources of IGWs [1]. The observed vertical wavenumber spectrum of the wind and temperature inhomogeneities in stably stratified atmosphere has a K_Z^{-3} –form at high vertical wavenumbers K_Z. The upward propagating IGWs play an important role in establishing of the large-scale wind flows in the atmosphere due to their capability to transport momentum through atmosphere and deposit it to the large-scale flows via wave breaking processes. The latter arise only within the local space regions, such as the wave "crests" and "troughs", within which the local Richardson number Ri becomes less than ¼ , or local decrease of potential temperature exceeds its adiabatic value. As a result the horizontal layers of turbulence may appear in between the atmospheric layers of high stability causing the jumps in sound speed (or in their vertical gradients) across the boundaries between the stable and unstable layers. We assume that such a fine layered structure of the stable atmospheric boundary layer (ABL) and its temporal variability may sufficiently affect the phase characteristics of acoustic waves propagating through ABL. The errors in determining of the azimuths and grazing angles of infrasonic signals associated with the fine vertical structure of the stable ABL will be estimated here.

2 Instrumentation

The experiments were carried out at the base of the Oboukhov Institute of Atmospheric Physics during morning, day and night time hours to provide the occurrence of different types of the ABL stratification conditions. The vertical temperature and wind velocity profiles in the ABL up to a height of 600 m were continuously measured by a sodar and a temperature profiler. The radio-sounding wind and temperature data up to a height of 20 km were also available. A detonation-type generator [2-3] was used as an acoustic pulse source. The acoustic pulses of stable form with a peak acoustic pressure of 30-60 Pa at a distance of 50-100 m from source were generated due to a detonation of an oxygen-propane mixture with a 1-min repetition period. The broad spectral maximum of these pulses was in the frequency range 40-60 Hz.

3   Results

One example of the temporal fluctuations of the azimuths of the acoustic signals recorded by a 30-m triangle array of receivers at a distance of about 2.1 km from a source is shown in Fig. 1. The corresponding frequency spectrum of these fluctuations is shown in Fig.2. It should be noted that this spectrum was obtained during the night hours, when a temperature inversion was formed in the ABL and its stratification was stable. The spectrum clearly shows a presence of the fluctuations with dominant periods of 2-4 min and 8 min. (Fig. 2).
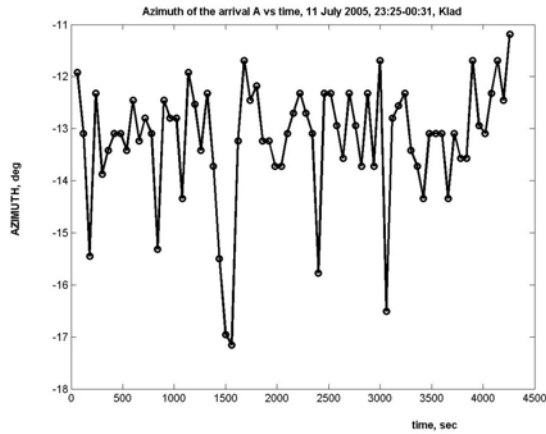
Figure 1. Fluctuations in the azimuths (vertical axis) of the acoustic signal arrivals received under stable conditions of the ABL, when an acoustic wave guide was formed near ground surface.
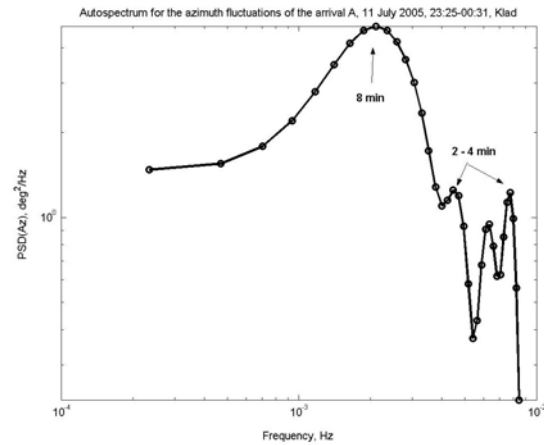
Figure 2. Autospectrum of the azimuth fluctuations shown in Fig.1.

4 Theory

The relationship between the observed values of the fluctuations in the parameters of acoustic signals(such as a signal duration τ, azimuth φ, and grazing angle θ) and the characteristics of the anisotropic wind velocity and temperature inhomogeneities in the troposphere was found with the use of their theoretical spectra obtained in [1]. The theory predicts a certain form for the frequency-wavenumber spectrum of the anisotropic inhomogeneities formed due to strong nonlinear interactions between IGWs of different scales. The errors in measuring of the azimuth φ and grazing angle θ occur mainly due to the fluctuations ($\delta\Delta t$) in the time delay Δt between the arrivals of a wave front at different microphones of a triangle array (fig.1). By using theoretical forms for the three-dimensional spectra of the horizontal (x- projection) wind velocity and temperature fluctuations at high vertical wavenumbers the following expressions for the variance of acoustic pulse travel time fluctuations $<\delta\tau^2(\mathbf{x}_I)>$ may be obtained:

$$<\delta\tau^2> = 2\pi\ R_0\ [(2\beta<\mu_T^2>+\alpha<\mu_\sigma^2>)/m^*]_0/3c_0^2 \qquad (\theta\neq 0), \qquad (1)$$
$$<\delta\tau^2> = 4\pi^{1/2}\ r\ (2\beta<\mu_T^2>+\alpha<\mu_\sigma^2>)/(3\ k_0c_0^2) \qquad (\theta\approx 0), \qquad (2)$$
$$(<\mu_T^2> = <\delta c^2(\mathbf{x},t)/c_0^2> \text{ and } <\mu_\sigma^2> = <v_x^2/c_0^2>)$$

where $R_0 = |z''(x_0)|^{-1} = |d(tg\theta)/dx)^{-1}|_{x=x0}$. is the curvature radius of a ray trajectory taken at a turning point with the coordinates $(x_0, z(x_0))$; the constants α and β are the coefficients of proportionality in the k_z^{-3}-power law decay of the vertical wavenumber spectra for the horizontal wind velocity and temperature inhomogeneities. The numerical values of α and β are in the range (0.1-0.3). The theoretically predicted range of vertical scales, within which the vertical spectra of anisotropic wind and temperature inhomogeneities follow the k_z^{-3} power law decay, is $m^* << k_z < m_M$, where m^* is the characteristic vertical wavenumber, above which

the nonlinearity forms a k_z^{-3}-spectral tail, and $m_M = m^* \cdot \exp(\beta^{-1})$ is the critical wavenumber, above which the spectral tail becomes unstable. Note that in the internal wave field the variances, $<v_x^2>$, of the fluctuations of the wind velocity projection v_x and of the vertical displacements, v_v^2, are related by: $2<v_x^2> = N_1^2 v_v^2$., where N_1 is the average value of the Brunt-Vaisala frequency in the lower tropospheric layer of 1km-depth. Therefore, the contributions of these variances into the variance of the refractive index μ can be expressed through $<v_x^2>$:

$$<\mu_T^2> = (N_1^2 v_v/g)^2/4 \approx (N_1^2 <v_x^2>/2g^2, \qquad <\mu_\sigma^2> = N_1^2 v_v^2/c_0^2 = <v_x^2>/c_0^2. \qquad (3)$$

The value of the variance $<\delta\tau^2>$ of the pulse travel time through a stably stratified ABL at a distance of 2.5 km from a source was estimated to be

$$(<\delta\tau^2>)^{1/2} = 4.5 \times 10^{-3} c = 4.5 \text{ мс} \qquad (4)$$

The following parameters were chosen to obtain (4): $R_0 \approx 35$ km; $<\mu_\sigma^2> = <v_x^2>/c_0^2 \approx (0.6/340)^2 = 3.1 \cdot 10^{-6}$; $(<v_x^2>)^{1/2} \sim 0.6$ м/c; $N_1 = 0.025$ rad/s; $<\mu_T^2> = 0.025^2 \cdot 0.6^2/19.6^2 = 5.9 \cdot 10^{-7}$; $m^* = N_1/(2<v_x^2>)^{1/2} \approx 0.03$ rad/m (which corresponds to the vertical scale $2\pi/m^* \approx 210$ m), and $\beta \approx 0.22$.

For the variances of the azimuth (φ) and grazing angle (θ) fluctuations of the pulse arrival we obtained the following expressions:

$$[<(\delta\varphi)^2>]^{1/2}/|<\varphi>| \approx 2 \, [<(\delta\Delta t)^2>]^{1/2}/|<\Delta t>|, \qquad (5)$$

$$(<\delta\theta^2>)^{1/2} \approx (c_0/x)(<\delta\Delta t^2>)^{1/2}/|<\sin(\theta)>| \qquad (6)$$

where $<\Delta t>$ is the mean value of the time delay of the arrival between two microphones.

A theoretical estimate of the rms error in measuring of the time delay between receivers yields $[<(\delta\Delta t)^2>]^{1/2} \approx 0.6 \cdot 10^{-3}$s. It does not exceed the accuracy ($\sim$1ms) of our measurements of the time delays Δt. The mean value of the azimuth $<\varphi>$ at a distance of 2.5 km was (-15) grad, and the mean delay between signal arrivals $|<\Delta t>| = 0.0228$ s. In this case, the relative error is $[<(\delta\Delta t)^2>]^{1/2}/|<\Delta t_2>| = 0.026$, therefore, the rms value of the azimuth fluctuations is $[<(\delta\varphi)^2>]^{1/2} \approx 1$ deg, which is in a good agreement with the experimental estimates of $[<(\delta\varphi)^2>]^{1/2}$ from the time series of φ in Fig.1.

It follows from (6) that the error $(<\delta\theta^2>)^{1/2}$ increases with a decrease of the angle θ, therefore, a correct determination of the very small values of θ, comparable to their measurement error, becomes practically impossible. For the conditions of the experiment carried out on August 9, 2004, we obtained $(<\delta\theta^2>)^{1/2} \approx 0.11$ rad ($\approx$6.5 deg), which is consistent with experimental estimates of $(<\delta\theta^2>)^{1/2}$.

Acknowledgements

Literature

1.Chunchuzov, I.P. On the high-wavenumber form of the Eulerian internal wave spectrum in the atmosphere // J. Atm. Sci., 2002, V.59, №14, P.1753-1772.

2. Kulichkov S.N., Chunchuzov I.P., Otrezov A.I., Perepelkin V.G., Tovchigrechko V.N. On the Coherent Reflection of Acoustic Pulses from Anisotropic Structures in the Atmospheric Boundary Layer // Acustica- Acta Acustica. 2001. V.87, 670-676.

3.Chunchuzov I.P., Kulichkov S.N., Otrezov A.I., Perepelkin V.G., Kallistratova M.A., Tovchigrechko V.N., Kadygrov E.N., and Kuznetsov R.D. An acoustic investigation of the statistical characteristics of mesoscale fluctuations in wind velocity in the stable atmospheric boundary layer // Izv., Atmos. Ocean. Phys., 2005, V. 41, No. 6, 761-782 (in English).

Statistical estimates of multiple scattering contributions to the transmitted acoustic radiation intensity

Shamanaeva Lyudmila, Burkatovskaya Yuliya
Institute of Atmospheric Optics of the SB RAS, 1, Akademicheskii Ave., 634055 Tomsk, Russia
Tomsk Polytechic University, 30, Lenin St., 634034 Tomsk, Russia, e-mail sima@iao.ru

Abstract

The contribution of multiply scattered radiation to the intensity of acoustic radiation transmitted through the lower 500-m plane-stratified turbulent atmosphere is estimated by the Monte Carlo method for a point-sized omnidirectional source. The dependence of the multiple scattering contribution on the source altitude above the absorbing Earth's surface and the seasonal variability of the multiple scattering contribution are discussed.

1 Introduction

 The problem of acoustic radiation propagation through the lower 500-m plain-stratified layer of the turbulent atmosphere has already been solved by us in (Shamanaeva, Burkatovskaya 2004) and (Shamanaeva, Burkatovskaya 2004a) using the Monte Carlo method. Distribution of the intensity of transmitted radiation as a function of the distance H from the vertical axis joining the source and the detector were obtained. In (Shamanaeva and Burkatovskaya 2004a), calculations were performed for a point-sized omnidirectional source placed at an altitude of 35 m above the absorbing Earth's surface for acoustic radiation frequencies $F = 1.7$ and 4.5 kHz and outer scale of atmospheric turbulence $L_0 = 10, 15, 20, 40, 60,$ and 80 m. In (Shamanaeva, Burkatovskaya 2004), results of calculations were presented for acoustic frequencies $F = 500–4000$ kHz (with a step of 500 kHz), and the frequency dependence of the multiply scattered radiation was discussed. In the present report, we investigate the dependence of multiple scattering contribution on the source altitude and seasonal variability of the multiple scattering contribution.

2 Dependence of the multiple scattering contribution on the source altitude

Calculations were performed for a point-sized omnidirectional source of acoustic radiation located at altitude $H_s = 5–35$ m (in a 5-m step) above the absorbing Earth's surface. The structure of the computational algorithm and the atmospheric model were described in detail in (Shamanaeva, Burkatovskaya 2004). The acoustic source power was 1 W. Acoustic radiation of the source was propagated through plane-parallel atmospheric layers with piecewise constant coefficients of acoustic radiation extinction (equal to the sum of the coefficients of classical and molecular absorption and scattering by temperature and wind velocity fluctuations) and normalized scattering phase functions. In the calculation of their altitude dependence, the vertical profiles of the air temperature, pressure, and sound velocity were set according to the standard mid-latitude summer atmospheric model (Glagolev 1970). The detector was placed at an altitude of 500 m. The distribution of the transmitted radiation intensity as a function of the distance H from the vertical axis passing through the source was calculated with estimation of multiple scattering contribution. Calculations were performed on a PC for 10^8 phonon histories, which ensured calculation errors in the range 2-32%.

Figure 1a and b shows the calculated dependence of the relative contribution of multiply scattered radiation to the transmitted radiation intensity, in %, on the source altitude H_s for the first zone of the hypothetical detector with radius $H = 10$ m and outer scale of turbulence

$L_0 = 10$ and 20 m. The acoustic frequencies are indicated on the *y*-axis. From the figure it can be seen that when the source altitude increases from 5 to 20 m, the multiple scattering contribution decreases noticeably. With further increase in the source altitude, it remains essentially unchanged. Therefore, a source altitude of 20 m can be recommended as optimal for acoustic sounding considering that multiple scattering is a noise signal component in the interpretation of acoustic sounding data.

a

b
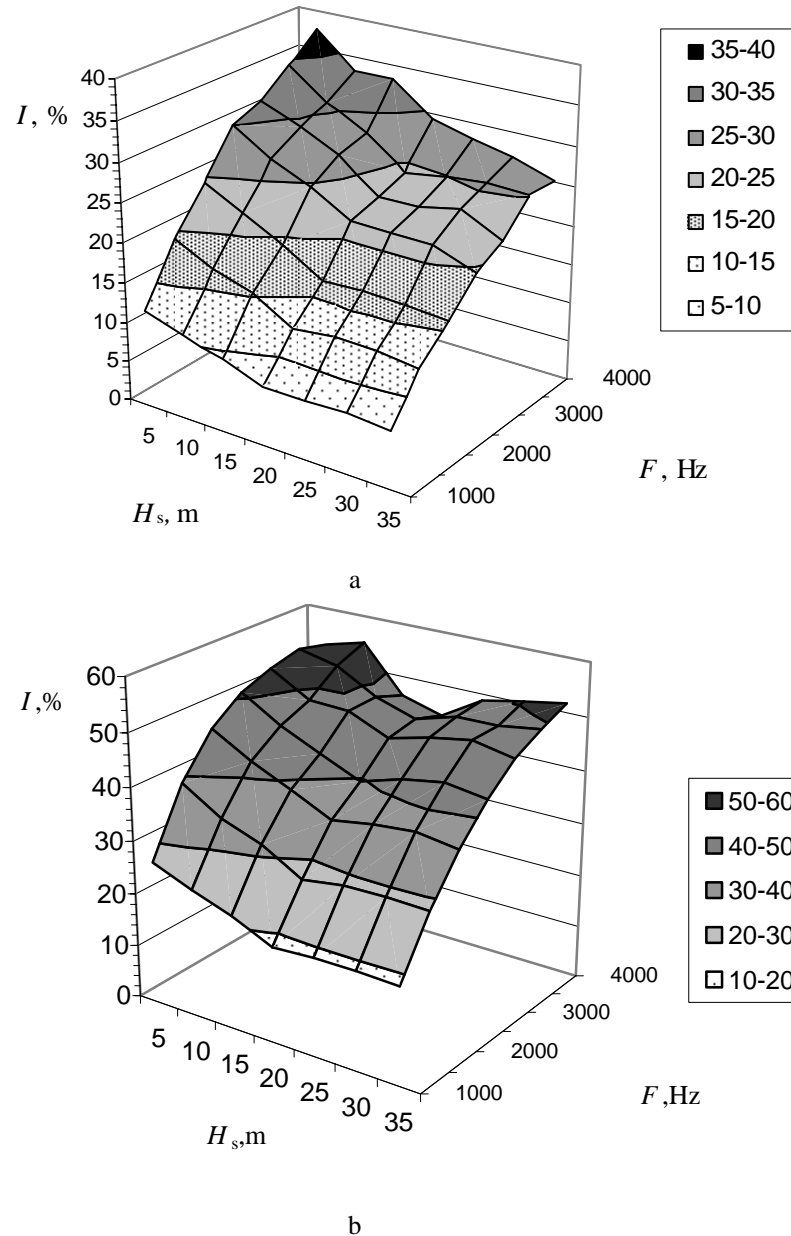
Figure 1. Dependence of the multiple scattering contribution to the transmitted radiation intensity on the source altitude for $L_0 = 10$ (a) and 20 m (b).

3   Seasonal variability of the multiple scattering contribution

To study the seasonal variability of the multiple scattering contribution to the transmitted radiation intensity, we performed calculations for the standard mid-latitude summer (Glagolev 1970) and winter atmospheric models (Matveev 1984; Komarov *et al*. 1996). Results of calculations of relative multiple scattering contributions, in %, for the first detector zone and summer and winter atmospheric models at $F = 500$–3500 Hz and $L_0 = 5$, 10, and 20 m are shown in Figure 2a-c. From the figure it can be seen that the multiple scattering contribution changes from summer to winter by 4–17%. Moreover, the multiple scattering contribution is

higher in summer and lower in winter. The difference depends on the acoustic radiation frequency and the outer scale of atmospheric turbulence. At $L_0 = 5$ m, it does not exceed 4%; at $L_0 = 10$ m, it is about 10% for $F = 2500$ Hz; and at $L_0 = 20$ m, it reaches 15–17%. The seasonal variability is more pronounced for frequencies from 1500 to 3000 Hz. The results of our calculations demonstrated that in summer the multiple scattering contribution to the transmitted radiation intensity is by 4–17% greater than in winter for the examined values of the outer scale of atmospheric turbulence. For larger L_0 values, the seasonal variability is even more pronounced.
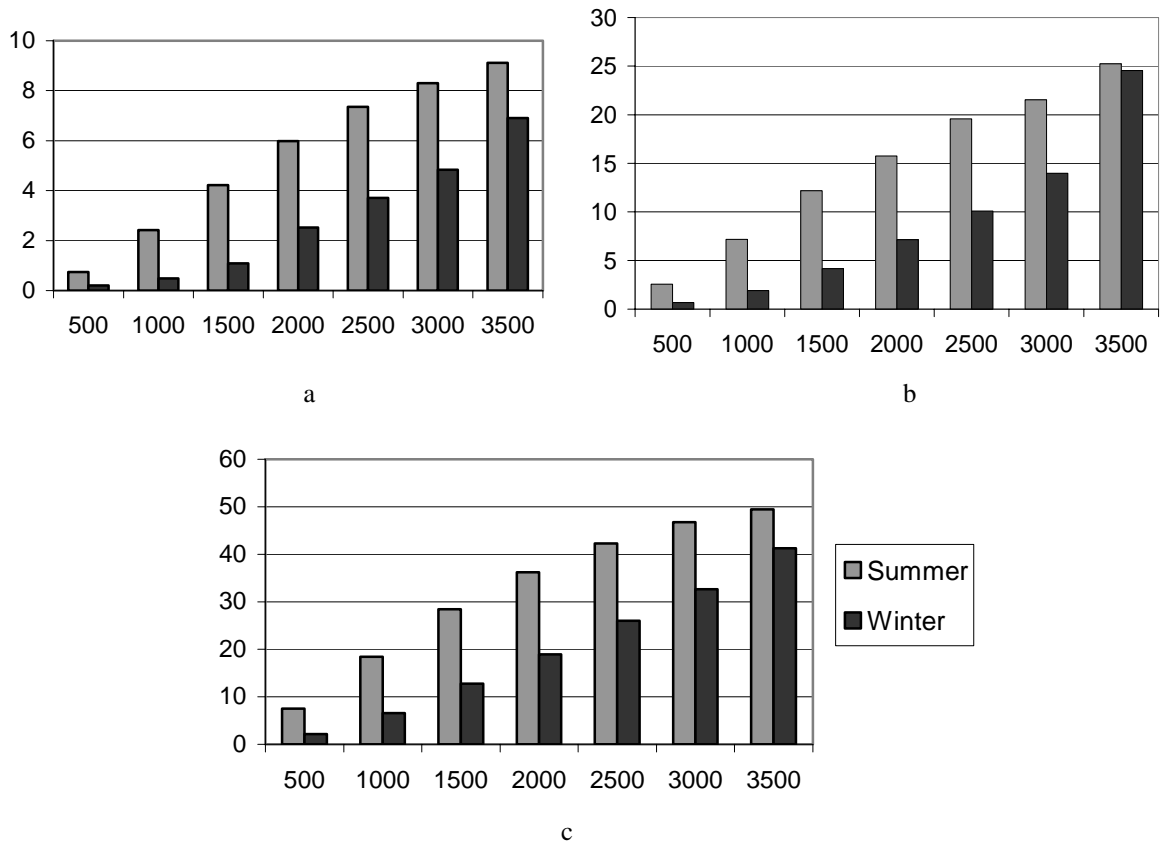
Figure 2. Seasonal variations of multiple scattering contribution to the transmitted radiation intensity for $L_0 = 5$ (a), 10 (b), and 20 m (c).

4   Conclusions

Statistical estimates of multiple scattering contribution to the intensity of acoustic radiation transmitted through the lower 500-m atmospheric layer demonstrated that at mid latitudes, its seasonal variations are 4-17%. A source altitude of 20 m is optimal for acoustic sounding. These quantitative estimates of multiple scattering contribution can be used in the interpretation of data of acoustic sounding.

Literature
Glagolev, Yu. A. , 1970: Handbook of the Physical Parameters of the Atmosphere, Gidrometeoizdat, Leningrad.
Matveev, L. T., 1984: Course in General Meteorology, Gidromrteoizdat, Leningrad.
Komarov, V. S., A. V. Kreminskii, K. Ya. Sineva, 1996: Computer data base of regional climatologic models of the temperature and wind velocity in the atmospheric boundary layer. Opt. Atm. Okeana, 9, No. 4, 484-488.
Shamanaeva, L. G., Yu. B. Burkatovskaya, 2004: Statistical estimates of multiple scattering contribution to the intensity of acoustic radiation transmitted through a lower 500-m layer of the atmosphere. Russian Physics Journal, 72-79.
Shamanaeva, L. G., Yu. B. Burkatovskaya, 2004(a): Study of multiple scattering effects on the acoustic wave propagation through a turbulent atmosphere. Proc. 12th Int. Symp. Acoust. Rem. Sens., Cambridge, 87-90.

Experience in application of acoustic sounding and radiometric data for supershort-term temperature and wind velocity forecast in the atmospheric boundary layer

Komarov Valerii and Lavrinenko Andrei
Institute of Atmospheric Optics of the SB RAS, e-mail:popov@iao.ru

Abstract

Results of application of the acoustic sounding and radiometric data for supershort-term temperature and wind velocity forecast in the atmospheric boundary layer based on the Kalman filter algorithm and a two-dimensional regression dynamical-stochastic model are discussed.

1   Introduction

It is well known that the problem of supershort-term (for a 3-h period) temperature and wind velocity forecast in the atmospheric boundary layer (ABL) has not yet been solved. This is because of the lack of data on the vertical temperature and wind velocity profiles in the ABL recorded with high time resolution and reliable methods of their short-term forecast. Only recently an actual opportunity of solving the above-indicated problem has appeared due to new systems of radiometric and acoustic sounding introduced in practice of atmospheric monitoring and new unconventional dynamical-stochastic approach to the forecast of meteorological fields under conditions of minimum initial information [Komarov V., et al, 2004]. The present report studies one of the possible methods of solving this problem within the framework of the dynamical-stochastic approach.

2   Method of solving the problem of supershort-term forecast

The problem of supershort-term forecast of a meteorological parameter involves estimation of its value at altitude h at the moment of time $t_0 + 1$ from measurements at the moment of time t_0 and at the preceding moments of time for a preset mathematical model. In our case, we used the model

$$\xi_h(k) = \sum_{m=h-i}^{h+i} \sum_{j=1}^{K} d_{m,j} \cdot \xi_m(k-j) + \varepsilon(k), \tag{1}$$

where $\xi_h(k)$ is the value of the meteorological parameter ξ at altitude h at the kth moment of time, $\xi_m(k-j)$ are values of the meteorological parameter measured at altitudes from $h-i$ to $h+i$ at moments of time from $k-1$ to $k-K$ (here m is the serial number of the current altitude within the limits of the examined atmospheric layer, $i = 1, 2, \ldots$ specifies the number of altitude layers in the examined atmospheric layer, j specifies the current time interval changing from 1 to $(k-K)$, $d_{m,j}$ are unknown model parameters, and $\varepsilon(k)$ is the model discrepancy caused by stochasticity of the atmospheric processes.

A parametrical dependence between ξ values at the kth moment of time and at the preceding $(k-j)$th moments of time does not allow us to take advantage of Eq. (1) for the forecast, since the parameters $d_{m,j}$ are unknown. Therefore, the forecast problem was solved in two steps: first the parameters $d_{m,j}$ were estimated with the help of the classical Kalman filter [Sage A., J. Melsa, 1971] from values of the meteorological parameter ξ measured at the kth and $(k-j)$th moments of time at altitude h and at altitudes adjacent to it, and then, proceeding from the assumption that the examined process is stationary, the forecast itself is made based on the estimated parameters $d_{m,j}$ and prognostic model (1) for the $(k + 1)$th moment of time.

3 Results of investigations into the quality of the developed method

The efficiency of application of the suggested method based on the Kalman filter algorithm and two-dimensional dynamical-stochastic model (1) for the supershort-term temperature and wind velocity forecast in the ABL was investigated. To this end, we took the data of remote measurements of the temperature and wind velocity with an MTR-5 radiometer and the Volna-3 three-channel Doppler sodar developed at the Institute of Atmospheric Optics, SB RAS, in the region of Tomsk (56.5N, 85E) in January, July, and October, 2004. The data of radiometric temperature measurements were obtained for the layer 0–600 m with a step of 50 m, and the data of sodar measurements of the wind velocity components were obtained at altitudes of 100, 150, 200, and 250 m. For the supershort-term forecast (with the term of forecast τ increasing from 0.5 to 3 h), the initial data were averaged over time periods of 30 min. The table below presents rms errors of supershort-term forecast of the temperature and zonal and meridional wind velocity components for the indicated terms of forecast τ and altitudes h from radiometric and sodar measurements.

Altitude h, m	Term of forecast τ, h					
	0.5	1.0	1.5	2.0	2.5	3.0
Temperature, °C						
50	0.2	0.3	0.4	0.5	0.6	0.8
200	0.2	0.3	0.4	0.5	0.7	0.8
600	0.3	0.5	0.6	0.7	0.8	0.9
Zonal wind velocity component, m/s						
100	0.6	0.6	0.7	0.7	0.9	1.0
200	0.8	0.9	1.0	1.1	1.2	1.4
250	1.0	1.1	1.2	1.3	1.4	1.5
Meridional wind velocity component, m/s						
100	0.5	0.5	0.6	0.6	0.7	0.7
200	0.6	0.7	0.8	0.9	1.0	1.1
250	0.7	0.8	1.0	1.1	1.2	1.3

From an analysis of the results presented in the table it follows that the suggested method provides high quality of the supershort-term forecast for all examined terms of forecast τ. Even for $\tau = 3$ h, the rms error varies within the limits of 0.8–0.9°C (for the temperature) and 0.8–1.5 m/s (for the zonal and meridional wind velocity components).

4 Conclusions

Thus, the method of supershort-term forecast of the temperature and wind velocity in the ABL based on the dynamical-stochastic approach gives reliable results not only for the term of forecast $\tau < 3$ h but also for $\tau = 3$ h. Hence it can be recommended for practical application given that the acoustic sounding and radiometric data are available.

Literature

Komarov V., S. Il'in, A. Kreminskii, N. Lomakina, Yu. Popov, A. Popova, S. Suvorov, 2004: Estimation and Extrapolation of the Atmospheric State Parameters on the Mesoscale Level Using a Kalman Filter Algorithm/ Jour. of Atmospheric and Ocean Technology., Vol.21, №3, pp.488–494.

Sage A., J. Melsa, 1971: Estimation Theory with Application to Communication and Control. McGraw-Hill, 496 pp.

On Physical Simulations of Long-Range Infrasonic Propagation in the Atmosphere

Sergey Kulichkov, Igor Chunchuzov, Oleg Popov, Vitalii Perepelkin, Alexander Svertilov, Anatolii Baryshnikov
A.M. Oboukhov Institute of Atmospheric Physics, Russian Academy of Sciences, Moscow, Russia,
e-mail: snk@ifaran.ru

Abstract

The results of a physical simulation of long-range sound propagation in the atmosphere are given. The property of similarity between the profiles of effective sound speed stratification for the atmospheric boundary layer (ABL) and for the land—the lower thermosphere thickness was used in the modeling of long – range infrasound propagation in the atmosphere. A detonation generator was used as a source of acoustic pulses. The experimental results show a structure similarity between the signals recorded in the atmospheric boundary layer and in the land-the lower thermosphere thickness.

1   Introduction

Infrasonic waves propagate throughout the atmosphere at distances of hundreds and thousands of kilometers from their sources, which is widely used in developing the methods of nuclear test monitoring (CTBT), in solving the problems of atmospheric sounding, etc. [1-2]. In this connection, the following problems arise: (1) the problem of developing correct theoretical models of long-range infrasonic propagation; (2) the problem of determining the effect of a fine inhomogeneous structure of the atmosphere on the characteristics of infrasonic signals; (3) the problem of developing the reliable methods of recording infrasonic signals and their isolating against the background of natural noise; and a number of other problems. One of the methods of solving the above-mentioned problems is to carry out experiments on a physical simulation of long-range infrasonic propagation in the atmosphere.

2   Instrumentation

In this work, for this purpose, we use the property of similarity of the paths of sound propagation in the atmospheric boundary layer (ABL) and in the atmosphere, as a whole, from the land surface up to the lower thermosphere. The corresponding sound velocity profile and ray trajectories are shown in Fig. 1. It follows from Fig. 1 that the form of the vertical profile of effective sound speed in the ABL is mainly similar to the corresponding profile up to heights of the lower thermosphere. In the form of this profile, one can conditionally isolate the regions corresponding to the "troposphere" (Tr), "stratosphere" (S), "mesosphere" (M), and "thermosphere" (T). The main advantage of the experiments on a physical simulation of long-range sound propagation in the atmosphere is that the vertical profiles of temperature and wind stratifications can directly be measured during these experiments. This allows one to make more correct comparisons between experimental data and the results of calculations according to different theoretical models, to find the most effective methods of signal recording, etc.
As a sound source, one can use different pulsed sources. In [3], a pulse acoustic oscillator was used as a sound source.

3   Results

Some experimental results are shown in Figs.2-3. The results of the parabolic equation code as applied to sound propagation in an inhomogeneous moving atmosphere yield a satisfactory agreement with experimental data even for calculation of the form of recorded signals. A satisfactory agreement between theoretical models and experimental data on the effect of anisotropic turbulence on fluctuations of acoustic signals propagating at long distances from their source is obtained in [4].
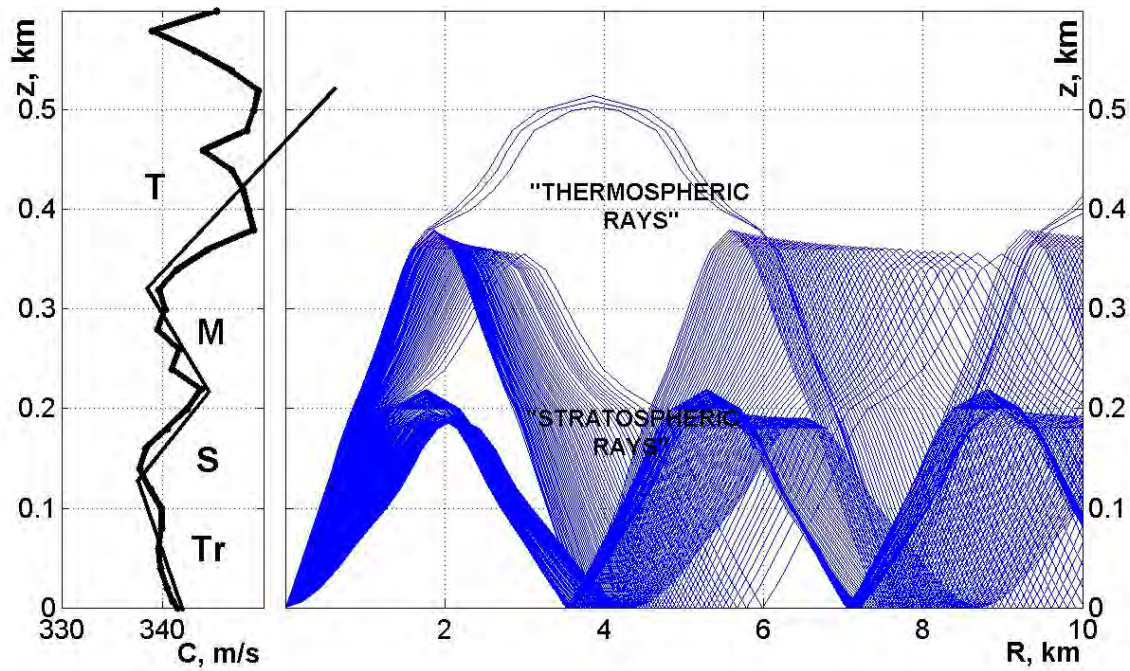
Fig.1. Profile of stratification of effective sound speed in the atmospheric boundary layer (**Tr** – "troposphere", **S** – "stratosphere", **M**- "mesosphere", **T** – "thermosphere") – on the left. Calculation of ray paths – on the right.
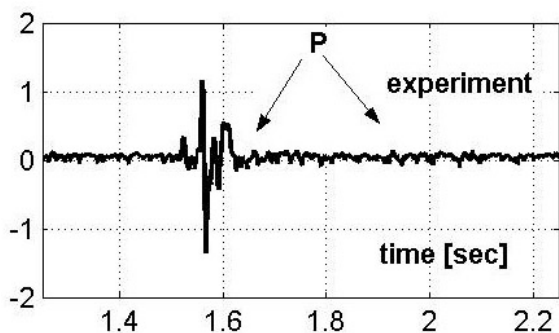
Fig.2. Acoustic signal at a distance of 2.5 km from its source.
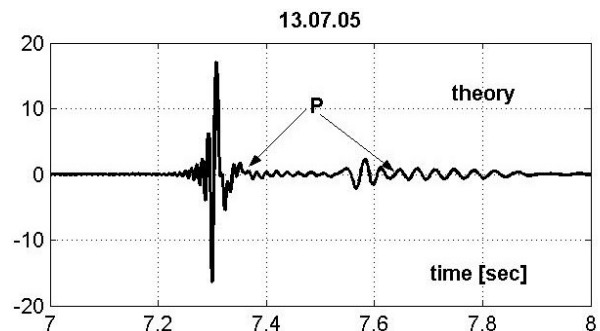
Fig.3. Acoustic signal (calculated according to the parabolic equation code) at a distance of 2.5 km from its source for the stratification profile in Fig. 1.

Acknowledgements

Literature

1. Research required to support comprehensive nuclear test ban treaty monitoring // National Research Council, Washigton, D.C.: National Academy Press, 1997, p.65.

2.Alexis Le Pichon, Milton Garce´s, Elisabeth Blanc, Maud Barthe´le´my, and Doug P. Drob. Acoustic propagation and atmosphere characteristics derived from infrasonic waves generated by the Concorde // Journal Acoust.Soc. Am. 2002. Vol. 111 (1). pp.629-641.

3.Chunchuzov, I., Kulichkov, S., Otrezov, A., Perepelkin, V. Acoustic pulse propagation through a fluctuating stably stratified atmospheric boundary layer // J. Acoust. Soc. Am. 2005. V.117, 1868-1879.

4. Sergey Kulichkov , Igor Chunchuzov , Oleg Popov , Vitali Perepelkin On the effect of atmospheric fine structure on the azimuths and grazing angles of acoustic signals at long distances from a pulse source // this Proceedings ISARS 2006.

On the Consistency between "Plume-like" Echograms and Temperature Pulsation Fields in a Convective Atmosphere

Rusakov Yuri

State Institution "Research and Production Association "Typhoon"; e-mail rusakov@typhoon.obninsk.ru

Abstract

Quantitative data are presented on the consistency between acoustic echo-signals and temperature pulsation field in the atmosphere. It can been concluded that there is a need to make some corrections to the sound backscattering model.

1   Introduction

The theory supposes (Tatarskii, 1967) that the lower atmosphere acoustic echogram shows unambiguously the temperature structure parameter (C_T^2) evolution in height and time. This concept is common for studying the fine atmospheric structure through acoustic sounding (e.g. Petenko et al., 1999). There are only few comparative studies of turbulence using synchronously the sodars and in-situ measurements. Our contribution closes partly this gap.

2   Instrumentation

With a one-component vertically oriented sodar calibrated absolutely against the Rayleigh target the sound backscattering has been investigated in summer, 2005 at a 200 m distance from the high tower (Obninsk, Russia). The sodar has specifications: frequency – 1600 Hz, pulse – 0,1 s, antenna diameter – 1,2 m. A set of meteorological parameters have been simultaneously recorded on the tower with a 1 Hz frequency.

3   Results

A demonstrative example is presented in Fig.1 of the correspondence between 3 min-averaged C_T^2 from in-situ (1) and sodar (2) data.
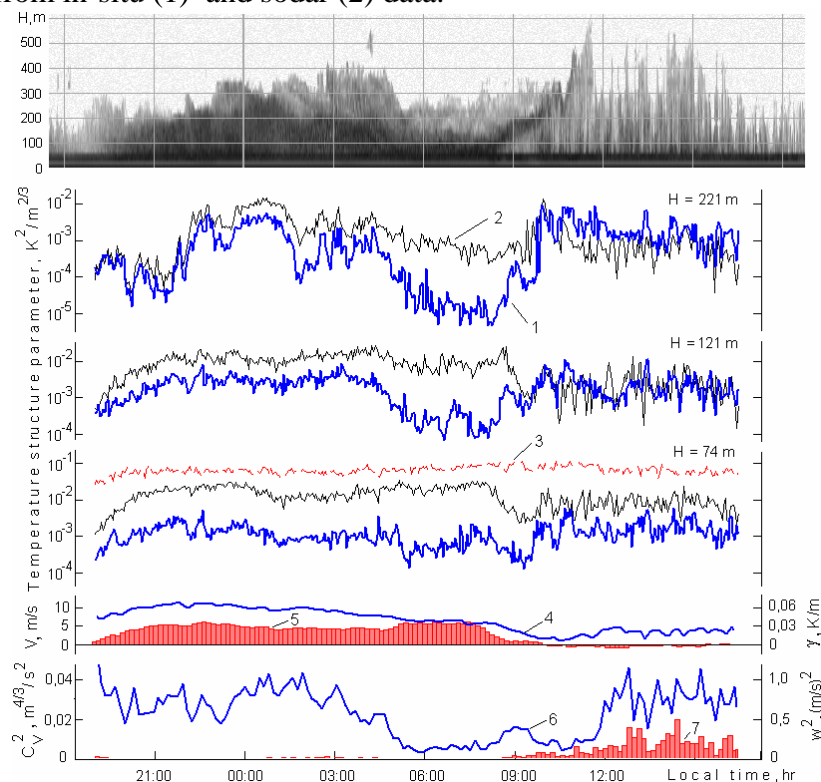
Figure 1. Consistency between C_T^2 from tower (1) and sodar (2) data at three heights H. 3 – echo-signal from 30 mm ball-calibrator above sodar antenna; 4 and 5 – wind velocity **V** and potential temperature gradient **γ** averaged within (2-221) m layer; 6 and 7 – wind structure parameter C_V^2 and energy of mesoscale (1-30 min) pulsations of wind vertical velocity $\mathbf{w}^2$ averaged within (74-221) m layer.

Fig.2 gives a typical example of the consistency between wind vertical velocity mesoscale pulsations w and C_T^2 (smoothed over 48 s and normalized to moving average over 30 min) according to sodar and tower data under convection.
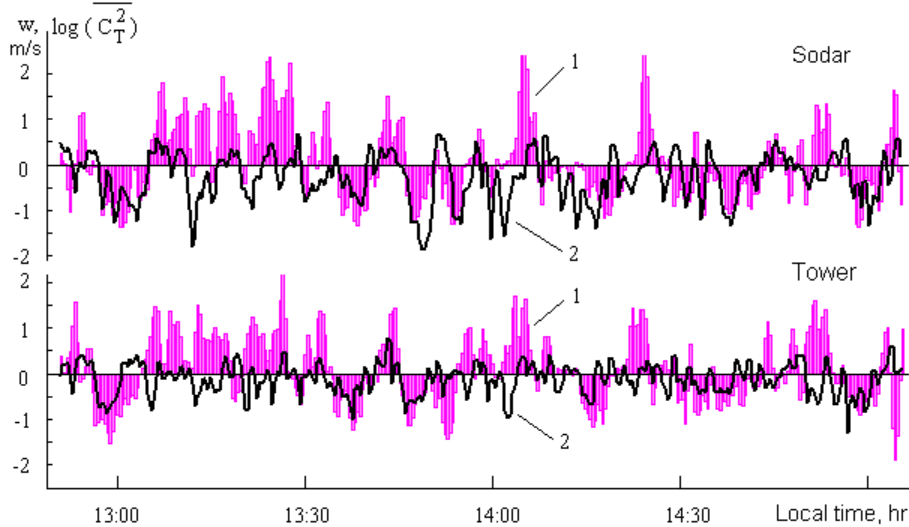
Figure 2. Mutual correspondence between wind vertical velocity (1) and logarithm of normalized temperature structure parameter (2) from sodar and tower data under convection. August 28, 2005. 221 m.

The data on modulation of the acoustic echo-signal intensity and turbulence characteristics by convective flows in the atmosphere are presented in Table.

Table. Ratio ($<C_{T+}^2>/<C_{T-}^2>$) of mean geometric and normalized C_T^2 in ascending ("+", w > 0.5 m/s) and descending ("-", w < -0.5 m/s) currents under convection according to tower and sodar data.

No	Date	Local time	Heights in the atmosphere, H						C_{V+}^2/C_{V-}^2
			74 m		121 m		221 m		(74m - 221m)
			Sodar	Tower	Sodar	Tower	Sodar	Tower	
1	Aug. 16	14^{06} - 17^{54}	4.1	3.1	5.8	1.3	4.1	1.2	2.1
2	Aug. 20	12^{03} - 17^{36}	2.9	2.6	3.7	2.5	4.0	2.0	1.6
3	Aug. 21	14^{10} - 17^{01}	4.3	2.6	5.4	1.4	3,4	1,6	2.1
7	Aug. 26	12^{06} - 17^{54}	1.5	3.1	2.8	1.9	2.5	5.5	1.2
9	Aug. 28	12^{36}- 17^{42}	2.5	2.4	5.1	2.2	4.2	1.7	1.8
12	Sept. 10	12^{01} - 16^{57}	2.1	2.1	2.3	1.8	2.8	1.2	2.0
Median			**2.7**	**2.6**	**4.4**	**1.9**	**3.7**	**1.7**	**1.9**
Sodar/Tower			**1.04**		**2.3**		**2.2**		

4   Discussion, Conclusions, and Outlook

The data and plots are quite typical for the majority of series realized under radiation inversion - to - convection development over a continental region. It follows from their analysis that such known concepts as a close association of the atmospheric reflectivity with C_T^2 and modulation of mesoscale turbulence by convective flows are still valid but there is also a need for some essential corrections to the theory of scattering and attenuation of acoustic waves in the atmosphere. The Bragg classic model of sound scattering is limited by those assumptions (primarily, allowing for smoothness of a medium) not corresponding to recent data on the structure of intermittent turbulence. *The work was supported by the Russian Foundation for Basic Research trough Grants 05-05-64399 and 04-05-65064.*

Literature

Tatarskii V.I., 1967: Wave propagation in a Turbulent Medium. Moscow, Nauka, 548 p. (In Russian).

Petenko I.V. and Shurygin E.A., 1999: A two-regime model for the probability density function of the temperature structure parameter in the convective boundary layer. – Bound. Layer Meteorol., v.93, pp. 381-394.

A Case Study of Anomalous Scattering of Acoustic Waves in the Atmosphere

Rusakov Maksim and Rusakov Yuri

State Institution "Research and Production Association "Typhoon"; e-mail rusakov@typhoon.obninsk.ru

Abstract

Cases of anomalous scattering of acoustic waves are considered when we observed most likely their "mirror" reflection from the boundaries of atmospheric inhomogeneities.

1   Introduction

A diversity of acoustic echograms result from the variety of mesoscale thermodynamic structures occurring in the atmospheric boundary layer. But there are such situations when the scattering process of acoustic waves is believed to be qualitatively extraordinary by itself. These situations, when analyzed, may advance greatly our views of possible mechanisms of wave scattering in the atmosphere.

2   Instrumentation

Vertical acoustic sounding of the atmosphere has been made continuously over last 2 years at the high meteorological tower site (Obninsk, Russia). An absolutely calibrated computerized sodar with its transmitted frequency of 1600 Hz, pulse duration of 0.1 s, averaging intervals of (6-48) s was used. Simultaneously, we measured the temperature, wind velocity (and their pulsations in some cases) at several tower levels.

3   Results

Not unusual for summer echogram is presented in Fig. 1a when there is severe nocturnal cooling of the earth's surface under conditions of strong wind and mixing. The anomaly is in a relatively high intensity of echo-signals with rather low temperature pulsations t' (c) in the atmosphere as well as in some orderliness of echogram patterns in the form of alternating dark and light inclined layers from the ground to inversion top. Normally (b), much higher t' (d) correspond to almost the same echo-signal intensity.
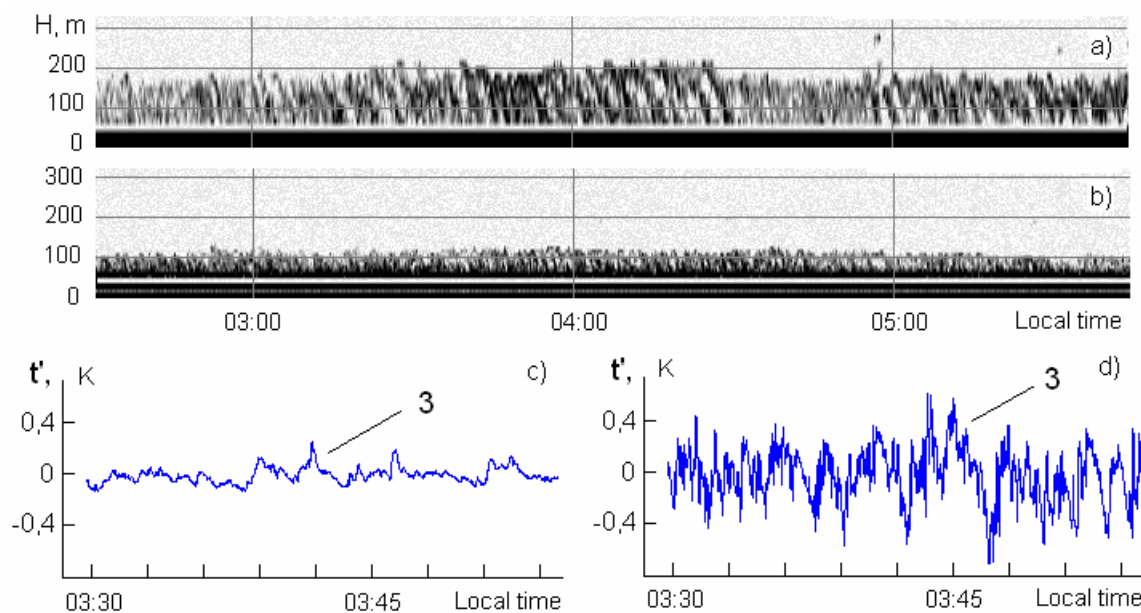
Figure 1. Anomalous (a) and typical (b) echograms of radiation inversion and realizations of temperature pulsations (3) at 74 m. August 24 (a, c) and August 26 (b, d), 2005.

But of more unique and physically significant was that situation which we had observed only 6 times. In two cases we succeeded in detecting not only an echogram, but the evolution of a sound echo-signal also. The echograms and oscillograms for this situation are shown in Fig.2. As is seen, during 3 hours there were strongly reflecting layers rising from the ground to 600 m or higher under normal meteorological conditions. In the first case there occurred surface inversion with a nearly 10°C intensity and light subsidence inversion was observed in the second case. No synoptic fronts were observed. The high-reflectivity zone was crossing the acoustic anemometer at 221 m for 1-5 s, the wind velocity being 8-10 m s^{-1}. The air temperature changed by $0,6^{\circ}$C in a matter of 1s and horizontal wind velocity decreased but the vertical one increased by 2 m s^{-1} within 5 s. The temperature and wind velocity returned to their original values 5-10 s later. This suggests that the phenomenon is local in character.
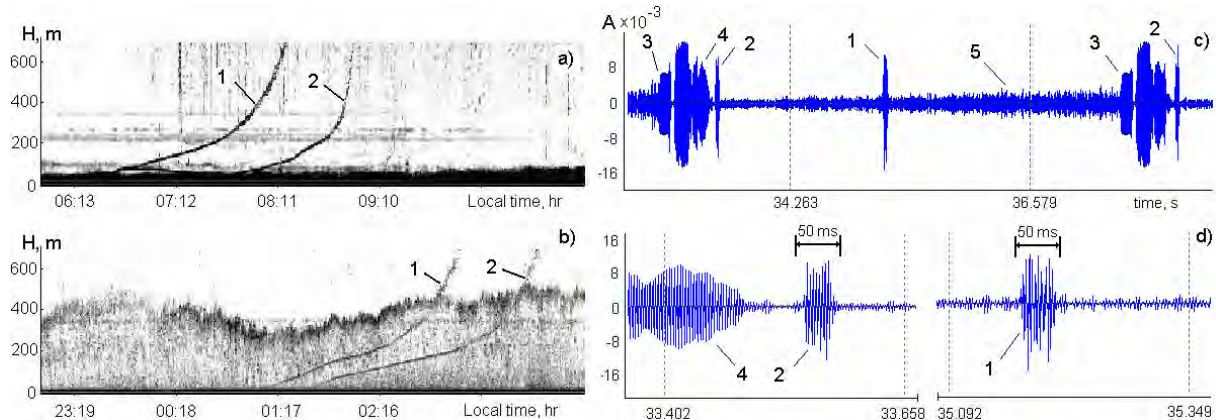
Figure 2. Echograms of atmospheric reflectivity (a, b) and typical oscillograms of echo-signal with low (c) and high (d) time resolutions during long observations of echo-signals with anomalous duration. November 3, 2005 (a, c, d) and February 24, 2006 (b).
1 and 2 – upper and lower anomalous echo-signals from narrow layers in the atmosphere; 3 – transmitting pulses with duration of 100 ms; 4 – signal from surface inversion; 5- acoustic noise; A – 16-binary sound card readings.

The most surprising thing was that the echo duration from the narrow layers (1, 2) was 35-40 ms, i.e. 2-3 times shorter than that of the sounding pulse, 100 ms. This fact was repeated over and over in each 6-second sounding cycles throughout the observational period of the anomalous phenomenon.

4   Discussion, Conclusions, and Outlook

The first anomalies considered suppose that there is a possibility of sound reflection on the boundaries of large vortices. With the anomalies of second type we can exclude from consideration not only the classic (Tatarskii, 1967) volume scattering of sound on the turbulence but diffuse scattering on the boundaries of inhomogeneities as possible underlying mechanisms. The only explanation of this phenomenon appears to be the mirror reflection of waves from some vibrating (rotating) inhomogeneity having a narrow scattering diagram. This is consistent with those depths of reflecting layers of about 5-10 cm at instant of crossing over an acoustic anemometer and their inclination of about $0,5^{\circ}$ with respect to the ground which were estimated from the above data.

The signal duration constancy with its change no more than 20% within two-hour observations and Doppler shift which corresponds to a 2-3 m s^{-1} velocity of descending currents are those persistent features remaining to be explained.

Literature

Tatarskii V.I., 1967: Wave propagation in a Turbulent Medium. Moscow, Nauka, 548 p. (In Russian).

Investigation of Complex and Horizontally Homogeneous Stable Boundary Layers using Doppler Lidar

Banta, Robert M., Darby, Lisa S., Pichugina, Y.L., Post, M.J., Brewer, W.A., and Hardesty, R.M.
Optical Remote Sensing Group, Chemical Sciences Division, Earth System Research Laboratory,
NOAA, Boulder, Colorado, USA and Cooperative Institute for Research in the Environmental
Sciences, Boulder Colorado (corresponding author: robert.banta@noaa.gov)

Abstract

Scanning Doppler lidar systems have been used at NOAA to study stable nighttime flows for two decades. A larger, CO_2-based Doppler lidar with a range of 15-20 km has shown that nocturnal downvalley flows in mountain valleys and basins have the structure of a low-level jet (LLJ). When these valleys exit onto a plain, the outflow also has the structure of a jet for many kilometers. The LLJ structure is important for horizontal transport, but it also generates shear in the subjet layer, which can produce significant vertical mixing through this layer. Quantitative relationships between LLJ and turbulence properties from data taken with a high-resolution Doppler lidar over the Great Plains of the United States are presented.

1   Introduction

Doppler lidar has been used as a tool for investigating nocturnal stable boundary layers (SBLs) at NOAA for two decades. In mountainous terrain, nighttime studies in valleys indicate a low-level jet (LLJ) structure to the downvalley flow, with a core of high wind speeds along the valley axis and the speeds diminishing above and below the jet maximum. In a wide basin in the western United States, LLJ structure is similarly noted in the downbasin flow at night. We investigate the cross-valley structure of these flows as revealed by Doppler lidar and what happens when valleys empty onto an adjacent plain or basin to form a valley outflow jet. The existence of a valley jet dominates horizontal transport processes in the valley, but it also generates a region of shear below the jet, which in turn generates turbulence and vertical turbulent diffusion. Examples of quantitative relationships between LLJ properties and turbulent mixing over flat terrain are described.

2   Instrumentation

Scan data from two Doppler lidars are presented in this paper. The bigger Doppler lidar, TEACO2, has a range resolution of 300 m, velocity precision of 60 cm s^{-1}, and a maximum range of often 15-20 km (Post and Cupp 1990). The smaller system, NOAA's High-Resolution Doppler Lidar (HRDL), has a range resolution of 30 m, velocity precision of ~10 cm s^{-1}, and a maximum range of ~ 2 km (Grund et al.2001). Both systems scan in azimuth and elevation, having greater-than-hemispheric scan coverage (i.e., able to scan to negative elevation angles).

3   Results

Cross sections taken from three-dimensional volume scans in Brush Creek, Colorado (Post and Neff 1986) and the Grand Canyon (Banta et al. 1999) indicate a core of downvalley flow near the bottom of the valley in each case. In Brush Creek (Fig. 1a) the jet core reaches ~5 m s^{-1} at a height of 100 m above the valley bottom, whereas for the much deeper Grand Canyon (not shown), the jet reaches 4 m s^{-1} at 400 m above the bottom. In the wider basin of the Great Salt Lake (GSL) in Utah of the western United States, LLJ structure has also been found (Fig. 1b), with speeds of 7 m s^{-1} at
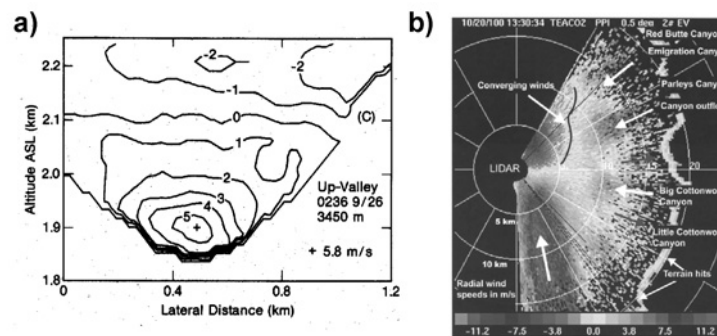
Figure 1. a) Cross-valley cross section of lidar radial velocity from Brush Creek, showing the core of high-velocity flow just above the floor of the valley. b) Horizontal plot (north up, east to left) of a conical Doppler lidar scan of the Great Salt Lake valley. 360° azimuth scan is at a fixed elevation of 0.5°.

300 m above ground level (AGL). In the GSL basin, however, the LLJ enters the southern end of the basin fully formed, indicating that the jet is a feature of the chain of basins, of which the GSL basin is one member (Banta et al. 2004, Darby et al. 2006).

When valleys having such jets empty onto a plain (or into a basin), the jet can persist for many kilometers as a valley outflow jet. Fig. 2a shows the structure of such an outflow jet emanating from a canyon in the Rocky Mountains near Boulder, Colorado, USA. Figure 2b shows that the outflow jet can penetrate at least 20 km out onto the plains to the east of the valley mouth (Banta et al. 1995a, 1996, 1997). Repeated Doppler-lidar scans showed that the jet is nonstationary, changing significantly in intensity and direction over periods of 20-30 min (Banta et al. 1995a, 1996; Darby et al. 1999; Levinson and Banta 1995). Vertical cross sections both along and across the flow indicate the presence of multiple speed maxima, which could be at different heights (Banta et al. 1996, 195b). Such outflow jets were also evident emanating from side canyons along the eastern wall of the GSL basin, persisting even after the formation of the down-basin jet (Fig. 1b). The presence or absence of these smaller-than-basin-scale flows had a significant effect on the transport and diffusion of tracer material in the basin (Darby et al. 2006).
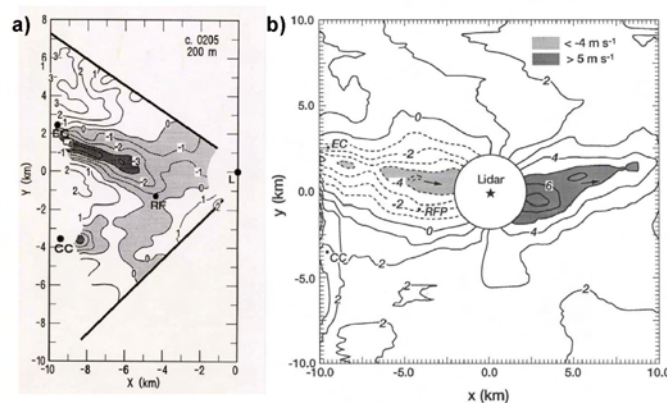
Figure 2. a) Horizontal cross section of 4 m s^{-1} flow emerging from Eldorado Canyon to the west of the lidar at (0,0), and b) extended scan in horizontal plane, showing outflow jet extending 20 km downstream.
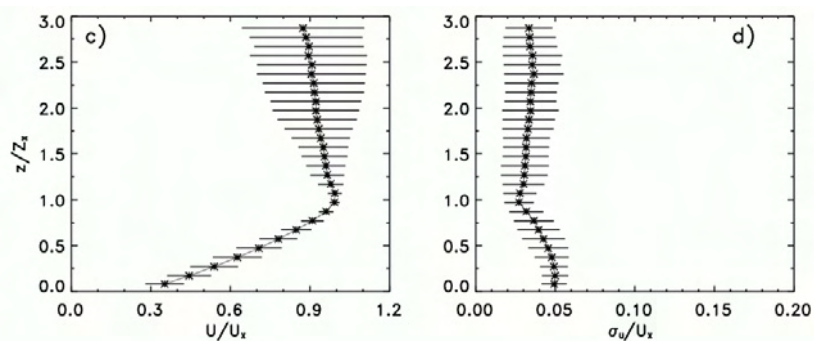
Figure 3. Composite vertical profiles of the normalized mean wind speed U/U$_X$ and standard deviation σ$_u$ /U$_X$ for streamwise component of the flow. Mean value indicated by asterisk (*) and standard deviation of the sample at each level indicated by horizontal error bars, with one standard deviation plotted in each direction. Profiles are for entire 6-night sample.

Downvalley or downbasin jets obviously have an important role in horizontal transport of airborne quantities in mountainous terrain, but they also generate significant shear, which in turn generates turbulence and vertical mixing in the layer below the LLJ nose. These processes have recently been studied over flatter terrain during two field programs over the Great Plains of the United States, the Cooperative Atmosphere-Surface Exchange Study of 1999 (CASES-99), and the Lamar Low-Level Jet Program of 2003 (LLLJP-03) using the High-Resolution Doppler Lidar (HRDL)(Banta et al. 2002, 2003, 2006). Vertical-slice scans oriented parallel to the mean wind direction were analyzed by using vertical bins and calculating the mean wind U and variance σ$_u^2$ for each bin, to form vertical profiles of each variable. The variance σ$_u^2$ is quantitatively equivalent to TKE for stable conditions (Banta et al. 2006). Velocities and heights were normalized by the speed and height of the LLJ (U$_X$ and Z$_X$, respectively), and composite profiles were formed using data from six nights when U$_X$ reached speeds of greater than 15 m s^{-1}. U$_X$ was found to be a more appropriate scaling velocity than the friction velocity u$_*$, which has traditionally been used for the SBL. Moreover, the near-surface peak value of the normalized streamwise standard deviation σ$_u$ /U$_X$ was found to have a value of 0.05 for the entire composited dataset (Fig. 3), as well as all stratifications of the dataset attempted (Banta et al. 2006). These studies show that the dominant control on turbulence magnitudes in the weakly stable BL are properties of the LLJ, rather than the details of turbulence interactions near the surface. LLJ properties are determined by large-scale processes, suggesting that parameterization of mixing in mesoscale and larger-scale models should be feasible, provided U$_X$ is properly predicted by the model.

4   Discussion, Conclusions, and Outlook

The role of scanning remote sensing instruments, such as lidars, in future boundary layer studies is to provide important interpretive data using the high spatial and temporal resolution of the datasets. The importance of measurements aloft in understanding transport processes cannot be too heavily emphasized, especially in stable atmospheric conditions. Features above the surface, such as low-level jets, are not adequately characterized by, and in fact are often invisible to, networks of surface measurement sites. Such elevated features often evolve over periods of 20-30 min, and this evolution may be missed by periodic sounding systems, such as balloons.

The features are often limited in spatial extent, which means they may be missed by fixed-location profiling systems. For example, sodar profiling systems in the dry climate of the Western U.S. (e.g., in Lamar, Colorado) have been found to lose signal during evening and morning transition periods, when temperature fluctuations diminish significantly, and at the nose of the LLJ, at which level turbulence levels also are significantly diminished (Dr. Neil Kelley, personal communication, 2003). Scanning Doppler lidar and other such systems should be an inportant component of future mesoscale and boundary-layer field campaigns.

Literature

Banta, R.M., Y.L. Pichugina, and W.A. Brewer, 2006: Turbulent velocity-variance profiles in the stable boundary layer generated by a nocturnal low-level jet. *J. Atmos. Sci.*, in press.

Banta, R.M., L.S. Darby, J.D. Fast, J.O. Pinto, C.D. Whiteman, W.J. Shaw, and B.D. Orr, 2004: Nocturnal low-level jet in a mountain basin complex. Part I: Evolution and implications to other flow features. *J. Appl. Meteor.*, **43**, 1348-1365.

Banta, R.M., Y.L. Pichugina, and R.K. Newsom, 2003: Relationship between low-level jet properties and turbulence kinetic energy in the nocturnal stable boundary layer. *J. Atmos. Sci.*, **60**, 2549-2555.

Banta, R.M., R.K. Newsom, J.K. Lundquist, Y.L. Pichugina, R.L. Coulter, and L. Mahrt, 2002: Nocturnal low-level jet characteristics over Kansas during CASES-99. *Boundary-Layer Meteor.*, **105**, 221-252.

Banta, R.M., L.S. Darby, P. Kaufmann, D.H. Levinson, and C.-J. Zhu, 1999: Wind flow patterns in the Grand Canyon as revealed by Doppler lidar. *J. Appl. Meteor.*, **38**, 1069-1083.

Banta, R.M., P.B. Shepson, J.W. Bottenheim, K.G. Anlauf, H.A. Wiebe, A.J. Gallant, T. Biesenthal, L.D. Olivier, C.-J. Zhu, I.G. McKendry, and D.G. Steyn, 1997: Nocturnal cleansing flows in a tributary valley. *Atmos. Environ.*, **31**, 2147-2162.

Banta, R.M., L.D. Olivier, P.H. Gudiksen, and R. Lange, 1996: Implications of small-scale flow features to modeling dispersion over complex terrain. *J. Appl. Meteor.*, **35**, 330-342.

Banta, R.M., L.D. Olivier, W.D. Neff, D.H. Levinson, and D. Ruffieux, 1995a: Influence of canyon-induced flows on flow and dispersion over adjacent plains. *Theoretical and Appl. Climatology*, **52**, 27-42.

Banta, R.M., D. Ruffieux, L.D. Olivier, and W.D. Neff, 1995b: Multiple structure of the Eldorado Canyon exit jet. *Proc., 7th Conf. on Mountain Meteor*, Breckenridge, CO, 17-21 July, pp. 322-325. Amer. Meteor. Soc, Boston, MA.

Darby, L.S., W.D. Neff, and R.M. Banta, 1999: Multiscale analysis of a meso-β frontal passage in the complex terrain of the Colorado Front Range. *Mon Wea. Rev.*, **127**, 2062-2081.

Darby, L.S., K.J. Allwine, and R.M. Banta, 2006: Nocturnal low-level jet in a mountain basin complex. Part II: Transport and Diffusion of tracer under stable conditions. *J. Appl. Meteor.*, **45**, in press.

Grund, C.J., R.M. Banta, J.L. George, J.N. Howell, M.J. Post, R.A. Richter, and A.M. Weickmann, 2001: High-resolution Doppler lidar for boundary-layer and cloud research. *J. Atmos. Ocean. Technol.*, **18**, 376-393.

Levinson, D.H., and R.M. Banta, 1995: Observations of a terrain-forced mesoscale vortex and canyon drainage flows along the Front Range of the Colorado Rockies. *Mon. Wea. Rev.*, **123**, 2029-2050.

Post, M.J., and W.D. Neff, 1986: Doppler lidar measurements of winds in a narrow mountain valley. *Bull. Amer. Meteor. Soc.*, **67**, 274-281.

Post, M.J., and R.E. Cupp, 1990: Optimizing a pulsed Doppler lidar. *Appl. Opt.*, **29**, 4145-4158.

Doppler Lidar Measurements Using a Fibre Optic System

Bennett, Michael and Christie, Simon
School of Chemical Engineering and Analytical Science, University of Manchester,
PO Box 88, Manchester, M 60 1QD, UK
Mike.bennett@manchester.ac.uk

Abstract

Doppler Lidar is conventionally implemented by heterodyning a reference signal of moderate power with the return signal from the atmosphere. For beats to occur, however, both signals must be in the same polarization state; this can be expensive to arrange within a fibre-optic system. We show that, by mixing the return signal into a fibre loop, the polarization of the resultant signal can be scrambled by the drift in frequency of the master oscillator. An intermittent beats signal can thus be obtained whatever the polarization of the reference signal.

1 Introduction

We have been working for some years developing a fibre-optic based Doppler Lidar which uses the principle of optical coherence to obtain range resolution (Bennett *et al.* 2004, Bennett *et al.* 2006). Infra-red radiation at $\lambda = 1.55$ μm from a DFB laser diode is split between a reference path and a signal path along single-mode fibres (SMF). Radiation following the signal path is amplified and transmitted towards a scattering target, whence some tiny proportion is returned to the instrument. This is then mixed (in a 50:50 fibre-optic coupler) with radiation that has followed the reference path. The beats signals on the two outputs from the coupler are in anti-phase; they are detected and their difference amplified to obtain an optimally sensitive detection.

A narrow-band beats signal is obtained when the delay engendered by fibre-optic loops along the reference path matches the path-length to the desired target. If the difference in path lengths exceeds the coherence length of the source, then the beats signal will be spread out over twice the source linewidth.

2 Polarization and Beats

The reference and signal fields must be in the same polarization state for efficient mixing to occur. Conventionally, the polarization of a monochromatic electro-magnetic wave is characterized as a point on the surface of the 'Poincaré sphere'. Thus, if we consider (for example) our reference power, p_r, it is proportional to the modulus squared of an electrical field vector, $\boldsymbol{E}_r$. As time progresses, the field vector describes an ellipse in E_x-E_y space with angular frequency ω_r, starting at phase φ_r. This ellipse may be described in terms of two angles: $\chi_r = \mathrm{Tan}^{-1}(\textit{(semi-minor axis)/(semi-major axis)})$ and ψ_r, which is the angle between the semi-major axis of the ellipse and the E_x axis. The polarization is then characterized on the surface of the Poincaré sphere as the point at latitude $2\chi_r$ and longitude $2\psi_r$. Points on the Equator thus have linear polarization, being horizontal at the Greenwich Meridian and vertical on the International Date Line. At the North (South) Pole we have right- (left-) handed circular polarization.

Mixing signal and reference fields, we then find that the intensity of the combined fields oscillates at angular frequency $|\omega_r - \omega_s|$ with amplitude $\boldsymbol{E}_r.\boldsymbol{E}_s^* + \boldsymbol{E}_r^*.\boldsymbol{E}_s$. The beats power, p_B (in an information sense) may be taken as half the square of the beats amplitude. We find that

$$p_B / p_{\mathrm{Max}} = \mathrm{Cos}^2(\psi_s - \psi_r)\,\mathrm{Cos}^2(\chi_s - \chi_r) + \mathrm{Sin}^2(\psi_s - \psi_r)\,\mathrm{Sin}^2(\chi_s + \chi_r).$$

Let now the angular distance along the great-circle route between $(2\chi_r, 2\psi_r)$ and $(2\chi_s, 2\psi_s)$ be c. The power of the Poincaré representation may be appreciated when it is seen that p_B / p_{Max} is

equal to $Cos^2(c/2)$. Thus, although the two polarizations can be described in terms of four parameters, the beats power depends upon c alone, p_B/p_{Max} varying from unity when $c=0$ to zero when $c=\pi$. And if the two polarizations are distributed uniformly over the sphere then the ensemble average $<p_B/p_{Max}> = \frac{1}{2}$.

3   Loop Scrambler

Within a fibre system, the optimal way to ensure polarization matching would be to use polarization-maintaining fibre and components throughout, aligning these with the linear polarization of the source. For economy's sake however, standard SMF was used. Any bending of the fibre then induces birefringence; at the output of a complicated system, the initial polarization has been entirely lost. This was compensated for manually by adjusting the orientation of a pair of tightly-wound loops ('Lefèvre's loops') along the path so as to optimize the signal. Re-optimization was required every time the reference delay loops were switched: clearly this was tedious.

Consider now the fibre arrangement shown in Figure 1. Ignore for the moment the secondary loop. Let the input (output) electric field vector to the coupler on the signal line be E_I (E_O). Similarly, let the field vector in the loop emerging from (returning to) the coupler be E_L (E_L'). We have $E_L' = e^{i\varphi}RE_L$, where $\varphi = nLv/c$ is the phase delay around the loop, R is a rotation tensor determined by the birefringence in the loop, L is the length of the loop, n the refractive index of the fibre, c the speed of light, and v the frequency of the source. As v drifts, φ will change quite rapidly.

Figure 1
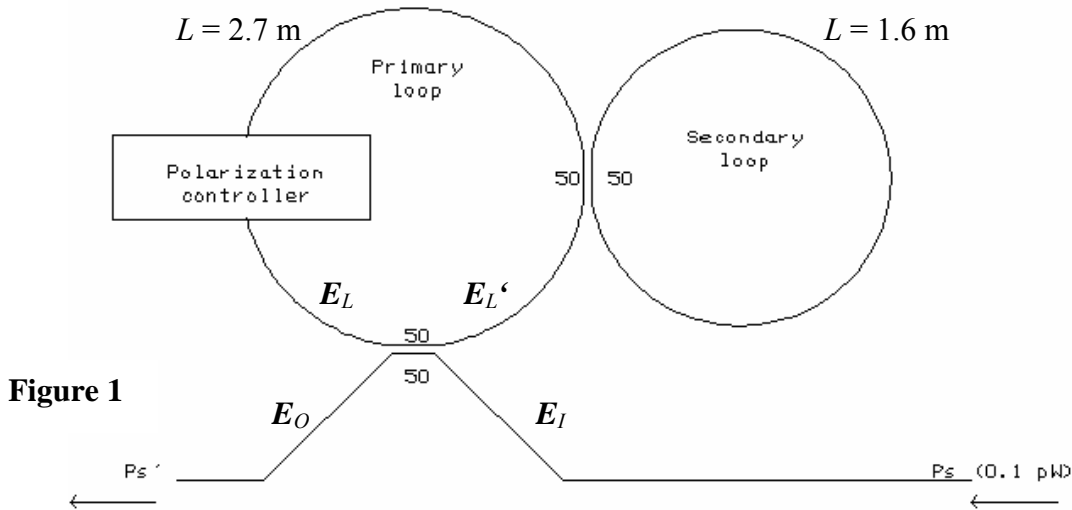
The mixing between (E_I, E_L') and (E_O, E_L) may similarly be described by a rotation tensor, with rotation angle θ. For a 50:50 coupler, $\theta = 45°$. Eliminating E_L, we then find that

$$\mathbf{E}_O = (I - Cos\theta\, e^{i\varphi}R)^{-1} . \left[(Cos\theta\, I - e^{i\varphi}R)\, \mathbf{E}_I \right].$$

We thus have a closed expression for E_O, which may readily be programmed to calculate its polarization trajectory on the Poincaré sphere as a function of φ for any desired parameters of E_I and R. It is more profitable, however, to write the inverse tensor as a binomial expansion, so that

$$\mathbf{E}_O \cdot \mathbf{E}_I^* + \mathbf{E}_O^* \cdot \mathbf{E}_I = Cos\theta\, |\mathbf{E}_I|^2 + \left[\sum_{n=1}^{\infty} Cos^{n-1}\theta\, (Cos\theta - 1)\, (e^{i\varphi}R)^n\, \mathbf{E}_I \right] \cdot \mathbf{E}_I^* + \text{Complex Conjugate}.$$

Since, as with the calculation of the beats power, the angle between E_O and E_I on the Poincaré sphere depends on $|E_O.E_I|$ alone, the leading term thus implies a constant angle between E_O and E_I, i.e. that the output polarization follows a circle on the Poincaré sphere as φ varies. The

first term in the series expansion, $e^{i\varphi}(RE_I).E_I$ adds an elliptical component. Subsequent terms, $e^{2i\varphi}(R(RE_I)).E_I$ give higher order harmonics. (The terms in $Cos^n\theta$ ensure convergence).

There are various degenerate cases: that when $RE_I = E_I$, i.e. E_I lies along the axis of the rotation tensor. In this case, the loop cannot change the polarization of the signal. Or that when (for example) $(RE_I).E_I = 0$, i.e. the input polarization has been rotated to be orthogonal to its original state. In this case, a term is missing from the harmonic expansion. (Subsequent terms may still be non-zero). The secondary loop shown in Figure 3 has been added because of the existence of such degenerate cases: the rotation tensors of the two loops can be arranged to have different axes so that the output polarization will still be scrambled regardless of the input polarization.

4   Experimental Implementation

The fibre-optic arrangements shown in Figure 3 were implemented on our Doppler Lidar system, with and without a secondary loop. A typical output without a secondary loop is shown in Figure 2. It may be seen that the beats power oscillates, seven broad maxima being identifiable over the 2 min shown. With the length of the primary loop being 2.7 m, this implies that the master oscillator has drifted at a rate of ~3 MHz s^{-1}. If a secondary loop (L=1.6 m) is added, the behaviour becomes even more chaotic.

Figure 2
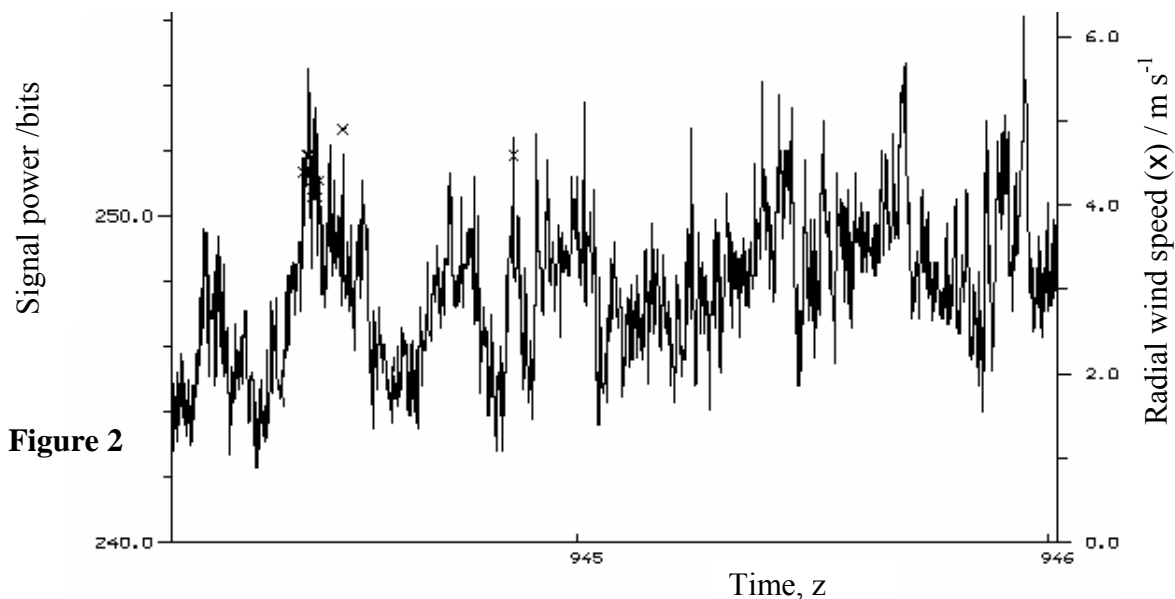
5   Conclusions

The addition of these loops permits a beats signal to be observed regularly irrespective of polarization changes induced by switching delay loops in the reference path. The system thus serves as a cheap and effective polarization scrambler. Note, however, that it will only work so long as the coherence length of the source is very much greater than L: changes in the phase of the input signal over short timescales lead to the optical power in the loop being alternately stored and flushed out, and hence to a very noisy output signal.

Literature

Bennett, M., S.G. Bradley, S. von Hünerbein, J. Pease, 2004: Comparison of wind profiles measured with Sodar and Doppler Lidar. ISARS 2004 (Cambridge, 12-16 July 2004), 141-144.

Bennett, M., H. Edner, R. Grönlund, M. Sjöholm, S. Svanberg, R. Ferrara, 2006: Joint application of Doppler Lidar and differential absorption lidar to estimate the atomic mercury flux from a chlor-alkali plant. Atmospheric Environment, **40,** 664-673.

Mixing height determination with lidar ceilometers - results from Helsinki Testbed

Münkel, Christoph

Vaisala GmbH, Schnackenburgallee 41d, 22525 Hamburg, Germany, christoph.muenkel@vaisala.com

Abstract

Helsinki Testbed is a research project of mesoscale meteorology. Six ceilometers situated in and around Helsinki are involved in this measuring campaign, reporting attenuated backscatter profiles. The mixing height derived from these profiles has been compared to values obtained from radiosoundings and a wind profiler with RASS option. During a quite long fair weather period in April and May 2006 daytime mixing height values of all instruments involved are in good accordance. The enhanced single lens optical concept of the ceilometers improves their ability to detect also nocturnal stable layers.

1   Introduction

Lidar ("light detection and ranging") is an active range-resolving optical remote measurement technique. Eye-safe commercial lidar ceilometers have as yet been mainly installed at airfields and meteorological stations to report cloud layers, vertical visibility, and cloud cover. Additionally, ceilometers are in use to estimate meteorological or slant optical range and dust concentration values.

While all these methods have been described in the standard literature (Weitkamp, 2005, pp. 175-181), the determination of mixing height with lidar ceilometers is up to now a matter of symposium presentations and papers describing measuring campaigns usually involving just one ceilometer and a few comparison sensors (Emeis et al., 2004; Eresmaa et al., 2006; Schäfer et al., 2004; Münkel and Räsänen, 2004).

The Helsinki Testbed research project is overcoming these shortcomings by providing data from six ceilometers placed in and around Helsinki, Finland, together with data from a wide range of other meteorological sensors including a wind profiler with RASS option and regular radiosoundings. Ceilometer data logging has started in November 2005 and will continue around the clock till September 2007. Helsinki testbed data can be accessed via http://testbed.fmi.fi.

2   Instrumentation

The ceilometer used within the Helsinki Testbed project is the Vaisala Ceilometer CL31 (Figure 1, left). It has a novel single lens design. The main innovation is the way the common lens is used for transmitting and receiving light. The centre of the lens is used for collimating the outgoing laser beam, whereas the outer part of the lens is used for focusing the backscattered light onto the receiver. The division between transmitting and receiving areas is provided by an inclined mirror with a hole in the centre as shown in the right part of Figure 1. This arrangement significantly reduces the optical cross-talk between transmitter and receiver, and increases the signal quality in the first 200 m of the measuring range, the part most crucial for mixing height determination.

The simplified lidar equation

$$P(x,\lambda) = \frac{c}{2x^2} \underbrace{P_0 A \eta O(x) \Delta t}_{\text{instrument specific}} \underbrace{\beta(x,\lambda)\tau^2(x,\lambda)}_{\text{attenuated backscatter}}$$

can be solved for the attenuated backscatter part. Since mixing height is determined mainly in clear sky situations, the attenuated backscatter is a good measure for the backscatter coefficient β being an indicator for the range resolved aerosol density.
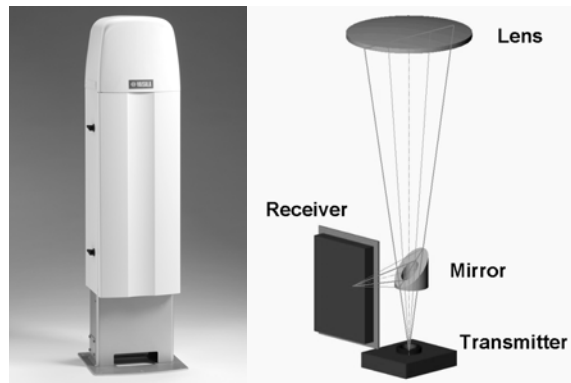
Figure 1. Ceilometer CL31, overall height = 1190 mm, and a schematic view of its optical concept.

A number of methods for retrieving mixing layer height from attenuated backscatter profiles have been introduced (Sicard et al., 2004; Martucci et al., 2004; Eresmaa et al., 2006). Helsinki Testbed data are being evaluated with a gradient method that selects the maximum of the negative gradient *(-dβ/dx)* of the backscatter coefficient to be the top of the mixed layer. Additionally, the idealized backscatter method that fits an idealized profile to a measured profile, and a variance method picking the altitude with maximum backscatter coefficient time-variance as the mixing height, have been tested.

For Helsinki Testbed the measuring parameters of the CL31 ceilometer are set to

Attenuated backscatter profile range	7700 m
Profile range resolution	10 m
Profile report interval	16 s

Its laser diode wavelength is 905 nm; it is operated at a mean pulse repetition rate of 8192 Hz. The pulse width is 110 ns; the pulse energy is monitored and adjusted to the eye-safe value of 1.2 μJ.

The distances between the different ceilometer sites vary between 8 km and 60 km.

At the airport Helsinki Malmi the ceilometer is situated close to a Vaisala Wind Profiler LAP-3000 with RASS option, the ceilometer site Vantaanlaakso provides regular radiosounding data.

3   Results

In winter and spring 2005/2006 there were very few periods without precipitation worthwhile studying, because most of the time the Helsinki area was covered by low clouds.
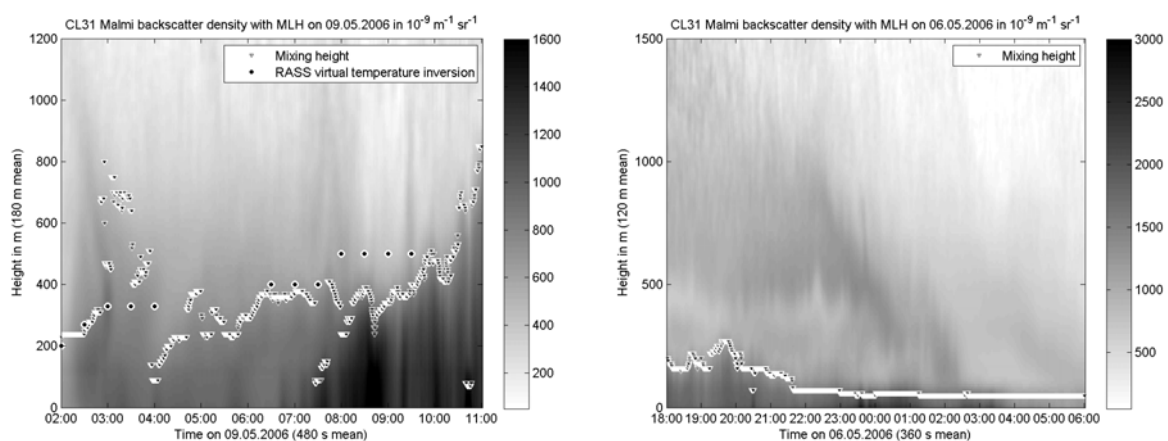
Figure 2. CL31 backscatter profiles with gradient method mixing heights and RASS virtual temperature inversions (left). Between 04:00 and 06:30 RASS reports an inversion layer above its measuring range of 400 m. Right: The enhanced optical concept improves nocturnal stable layer detection capability.

That is why data evaluation is mainly concentrating on the long fair weather period starting on 22.04.2006. This process is still ongoing, more examples and a detailed statistical data analysis will be presented at the ISARS 13 symposium.

Figure 2 (left) gives a comparison of mixing height calculated with the gradient method and virtual temperature inversions reported by the Malmi airport RASS. The development of a convective boundary layer after 09:00 local time is visible in the ceilometer backscatter profiles. The top of this layer is exceeding the measuring range of the RASS for that time.

Figure 2 (right) and Figure 3 show the ability of the CL31 ceilometer to monitor the aerosol structure of the atmosphere from 0 m to more than 2000 m altitude.
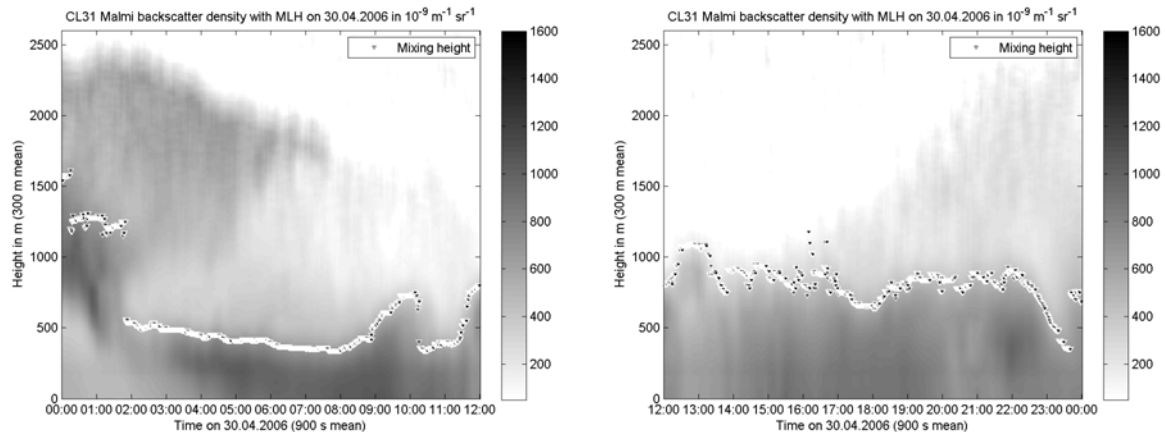
Figure 3. A one day backscatter density plot showing residual layers reaching altitudes exceeding 2000 m.

4 Discussion, Conclusions, and Outlook

The ceilometer data of the Helsinki Testbed project that have been evaluated so far confirm the potential of lidars to investigate the boundary layer and to report mixing height. Mixing height assessment was mainly based on a gradient method; future research will concentrate on the more sophisticated approaches idealized backscatter and variance method. The symposium presentation will also include comparison statistics, using data from comparison sensors and all ceilometers involved in the campaign.

Literature

Emeis, S., C. Münkel, S. Vogt, W. J. Müller, K. Schäfer, 2004: Atmospheric boundary-layer structure from simultaneous SODAR, RASS, and ceilometer measurements. Atmos. Environm. 38, 273-286.

Eresmaa, N., A. Karppinen, S. M. Joffre, J. Räsänen, H. Talvitie, 2006: Mixing height determination by ceilometer. Atmos. Chem. Phys. 6, 1485-1493.

Martucci, G., M. J. Srivastava, V. Mitev, R. Matthey, M. Frioud, H. Richner, 2004: Comparison of lidar methods to determine the Aerosol Mixed Layer top. Proceedings of SPIE, Vol. 5235, 447-456.

Münkel, C., J. Räsänen, 2004: New optical concept for commercial lidar ceilometers scanning the boundary layer. Proceedings of SPIE, Vol. 5571, 364-374.

Schäfer K., S. Emeis, A. Rauch, C. Münkel, S. Vogt, 2004: Determination of mixing layer heights from ceilometer data. Proceedings of SPIE, Vol. 5571, 248-259.

Sicard, M., C. Pérez, A. Comerón, J. M. Baldasano, F. Rocadenbosch, 2004: Determination of the mixing layer height from regular lidar measurements in the Barcelona Area. Proceedings of SPIE, Vol. 5235, 505-516.

Weitkamp, C. (Ed.), 2005: Lidar: Range-resolved optical remote sensing of the atmosphere. Springer, New York, 460 pp.

Influence of convective clouds on the turbulence structure of the boundary layer measured by Doppler Lidar

Roger Huckle, Andreas Wieser, Norbert Kalthoff, Ulrich Corsmeier
Institut für Meteorologie und Klimaforschung, Forschungszentrum Karlsruhe
andreas.wieser@imk.fzk.de

Abstract

The Doppler Lidar of the Forschungszentrum Karlsruhe was operated with a fixed beam pointing vertically upward to measure thermals generating the development of the convective boundary layer. Cumulus clouds passing over the Lidar showed different influence on the turbulent state of the middle and upper boundary layer depending on the state within their life cycle. Active and forced cumulus clouds were connected to strong upwinds underneath and in their base reaching up to 3 ms^{-1}, on the other hand passive clouds at are disconnected from the underlying boundary layer and have no influence on vertical wind speed and turbulence.

1   Doppler Lidar

The Doppler Lidar of the Institut für Meteorologie und Klimaforschung, Forschungszentrum Karlsruhe, a CLR Photonics WindTracer, is mounted on a swap body (Fig. 1) which makes transportation to different measurement sites easy. The complete system is installed in a shelter, with a two-axis scanner on its top which directs the laser beam into the atmosphere by two planar mirrors. The system is designed to run continuous and unattended. System control and measurement setup can be done from a remote site if the system is connected to Internet. Infrared light pluses of 2.0225 µm wavelength with 2 mJ energy are produced by a Tm:LuAG laser with a repetition rate of 500 Hz. They are transmitted and received by a 0.1 m telescope. The received signal is sampled every 10^{-8} s which corresponds to 1.5 m distance along the light path starting at a distance of 390 m, no measurement is possible closer to the Lidar.
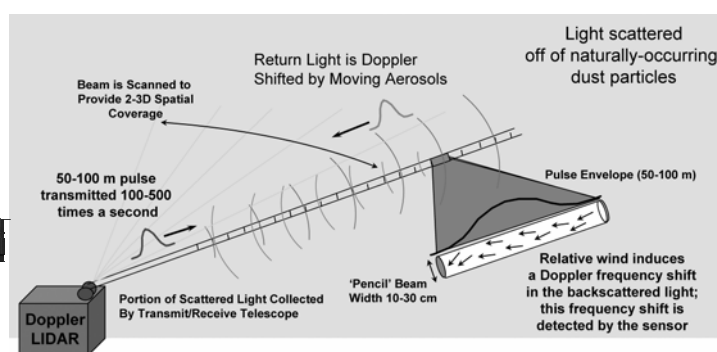
Figure 1: WindTracer 2 µm Doppler Lidar   Figure 2: Doppler Lidar measurement principle

The radial wind velocity is calculated for 100 range gates of 48 to 64 samples (72 – 96 m), which can be configured to be overlapping, connected or with spatial gaps, in real time for every laser pulse by FFT. To get a sufficient SNR at least 50 laser pulses have to be averaged. Typically the WindTracer is able to measure 6 to 9 km in horizontal direction. In vertical direction the range is limited by the aerosol concentration in the free troposphere, but within the boundary layer measurements are always possible. Increasing the averaging from 50 pulses which correspond to a 10 Hz data rate to 500 or even 5000 pluses can extend the range drastically. Depending on the type of clouds they can either extend the vertical range if they are optically thin, or block the measurement within a few 100 meters especially when they contain large quantities of liquid water.

2   Boundary layer height and cloud detection

The WindTracer Doppler Lidar was operated during several days on August 2004 at the site of the Forschungszentrum Karlsruhe in southwest Germany and during the CSIP Measurement campaign in June and July 2005 with the laser beam pointing vertically to measure the vertical structure of w in a convective boundary layer and the influence of convective clouds. The system was configured to use 48 samples per range gate to have maximum range resolution. Averaging was set to 50 or 500 pulses depending on the aerosol concentration, which is still fast enough to resolve turbulent structures.

A simple way to detect the boundary layer height is just using the SNR. For the example given in figure 3 the nocturnal boundary layer and mixing layer is characterized by a SNR >3, at the top of the boundary layer the SNR drops to -10, which is the lowest value at which reliable data can be obtained. The absolute numerical values depend on the aerosol and humidity concentration of the air mass and have to be adjusted to the actual situation. For case studies in situations without bigger changes of the air mass, the method is well suited.
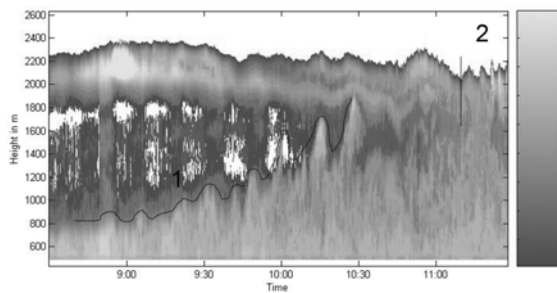
Figure 3: SNR for vertical Lidar measurements. Area 1 shows the pulsation of the growing mixing layer. At point 2 the mixing layer reaches the top of the residual layer.
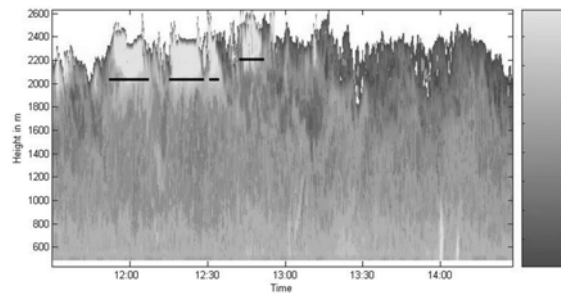
Figure 4: SNR for vertical Lidar measurements with convective clouds. Black lines are indicating cloud bases and temporal extent.

The laser light is not only reflected on aerosols > 0.5 µm but also on water drops and ice crystals. Clouds can therefore be easily detected by high values of SNR. For the example given in figure 4 the threshold value for cloud detection was set to a SNR >8. For adjusting this value additional data from a shortwave radiation sensor and cloud camera images are extremely helpful as well as the calculation of the cumulus condensation level if a radio sounding is available or the lifting condensation level from temperature and dewpoint measurements.

3   Vertical wind velocity and σ_w Profiles

Vertical wind velocity in the fully developed boundary layer exceeds ±3 m s^{-1} frequently and up- and downdrafts are alternating rapidly (Fig. 5). During periods with active clouds the vertical wind velocity increases even further and reaches its maximum near the cloud base and inside its lower part. The last of the four clouds at 12:45 – 12:53 has reached the end of its live cycle. The feeding winds have died down and no more energy from the boundary layer is transferred into this cloud. The cloud is probably in its last stage before dissolving.

Averaged vertical wind velocity and standard deviation profiles are calculated for the period with highest wind velocities (Fig. 6 + 7). The averaging time was set to 8 minutes because the temporal extends of the first two clouds which passed over the Lidar as well as the gaps between the clouds extended to approx. 8 minutes.
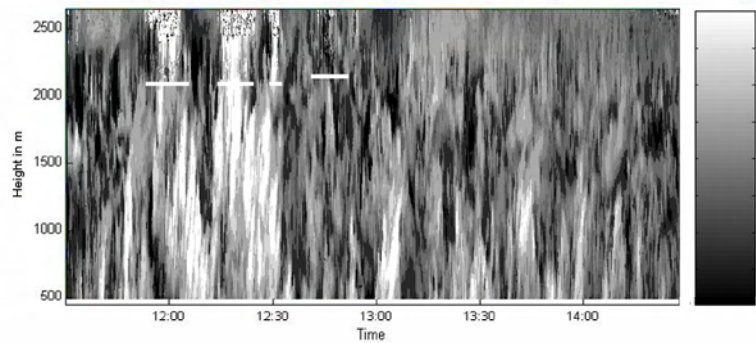
Figure 5: Vertical wind velocity in m s⁻¹ under convective conditions
with clouds. White lines indicate cloud bases and temporal extent.

Because of the limit to vertical movement of air at the earth surface and the inversion at the top of the boundary layer a typical vertical wind speed profile has its maximum in the middle of the boundary layer. When convective clouds are developing the upper lid for the rising air is broken up. Strong vertical winds prevail through the upper half of the boundary layer (Fig. 6) and the vertical wind is nearly constant with height above 1000 m whereas during cloud free periods the vertical wind speed is negative at the top of the boundary layer. The highly turbulent character of the transport of mass and humidity into convective clouds is visible in figure 7. The maximum of σ_w occurs at the top of the boundary layer, or even within the cloud. Under cloud free conditions the maximum of σ_w can be found as expected in the middle of the boundary layer.
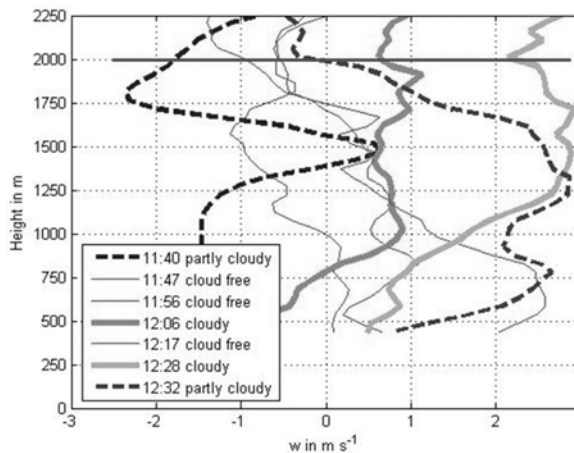
Figure 6: Profiles of vertical wind velocity for the 11:30 – 12:30 period . Cloud base is indicated as horizontal line as detected from SNR (Fig. 4).
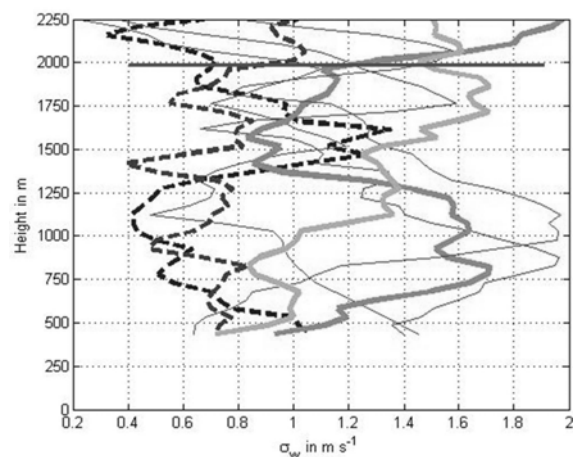
Figure 7: Profiles of σ_w for the 11:30 – 12:30 period. Linestyles and cloud base indication as used in figure 6.

4   Outlook

In the presentation these results from measurements at the site of Forschungszentrum Karlsruhe will be compared to measurements taken during the CSIP campaign in June/July 2005 in Chilbolton/England. During 17 days with convection the WindTracer Doppler Lidar was operated there just pointing vertically upward. Measurements during long cloud free periods as well as periods with cumulus clouds and even thunderstorm situations with heavy rainfall and hail are available. In situ measurements from the Dornier 128-6 D-IBUF research aircraft are available for five of the 17 days as well and will be used for intercomparison.

Two-dimensional Wind Retrieval Using a Doppler LIDAR

P.W. Chan (a) and A.M. Shao (b)

(a) Hong Kong Observatory, Hong Kong, China, email: pwchan@hko.gov.hk

(b) College of Atmosphere Science, Lanzhou University, Lanzhou, China

Abstract

The Doppler LIDAR at the Hong Kong International Airport (HKIA) gives the radial component of the wind. To better visualize the airflow at the airport area, two-dimensional wind field is analyzed using a variational method based on LIDAR data. This paper presents the retrieved wind fields in some cases of terrain-disrupted airflow. Because of limited data availability of the LIDAR in rain, a gust front case is studied using dual Doppler analysis of LIDAR and radar measurements.

1   Introduction

A Doppler LIDAR (location in Figure 1) is used at HKIA to monitor the airflow in the airport area in clear air. Terrain-induced airflow disturbances and gust front are two weather phenomena that could bring significant windshear to the aircraft. To better visualize the wind flow in such weather, 2-D wind fields are retrieved from the LIDAR data in 1-degree PPI scans, together with the radar data in case LIDAR has limited data availability in rain.

2   Retrieval method and comparison with anemometer data

The 2-D wind retrieval algorithm for LIDAR is modified from a two-step variational method for radar (Qiu et al. 2006). The cost function J to be minimized is given by:

$$J(u,v) = J_1 + J_2 + J_3 + J_4 + J_5 + J_6$$

$$= \sum_{i,j}\{W_1[(u-u_B)^2 + (v-v_B)^2] + W_2(v_r - v_r^{obs})^2 + W_3(\frac{\partial u}{\partial x} + \frac{\partial v}{\partial y})^2 + W_4(\frac{\partial v}{\partial x} - \frac{\partial u}{\partial y})^2$$

$$+ W_5(\nabla^2 u + \nabla^2 v)^2 + \sum_n [W_6(\frac{\partial v_r^{obs}}{\partial t} + u\frac{\partial v_r^{obs}}{\partial x} + v\frac{\partial v_r^{obs}}{\partial y})^2]\}. \qquad (1)$$

where u and v are the components of the retrieved wind field, subscript B the background field (generated from LIDAR radial velocity in the way described in Qiu et al. 2006), v_r the retrieved radial velocity, superscript obs the observed values, i and j the horizontal grid point and n the time index (three consecutive scans are used in each analysis). The weights are: W_1 = 0.1 (after the first step retrieval), $W_2 = 1$, $W_3 = W_4 = W_5 = 0.1$ and $W_6 = 10^4$. They are chosen empirically in this paper to ensure that the constraints have proper orders of magnitude.

	slope a	correlation coefficient
Wind speed	0.88	0.86
Wind direction	0.95	0.93
u component	0.86	0.91
v component	0.83	0.90

equation: y = a*x
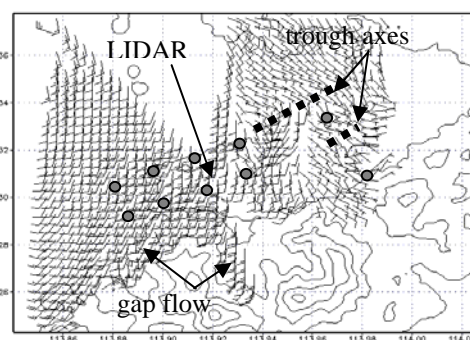
Table 1. Comparison results between the 2-D retrieved wind field based on the LIDAR (x) and the anemometer measurements (y).

Figure 1. 2-D retrieved wind field based on the LIDAR at 9:52 a.m., 30 August 2004. Anemometer stations for wind comparison (Table 1) are indicated by grey dots.

The retrieved wind fields are compared with the surface anemometer measurements inside the airport and at the neighbouring stations (Figure 1) in four cases of terrain-disrupted airflow in different wind regimes (10 September 2002, 20 January 2003, 30 August 2004 and 30 October 2005). Results are summarized in Table 1. The correlation coefficients are high (around 0.9). The wind speed from the LIDAR is generally higher because of greater altitude.

3   Analysis of terrain-disrupted airflow

Two examples of 2-D wind fields retrieved from the 1-degree PPI scans of the LIDAR are presented here. In the summer case (30 August 2004, Figure 1), south to southwesterly flow prevailed over the airport area. Gap flow occurred to the west of HKIA. On the other hand, the winds to the east of the airport were generally weaker and showed some wave features, possibly arising from terrain disruption.

In the spring case (20 January 2003, Figure 2), moderate easterly wind prevailed over the airport area in a stable boundary layer. The 2-D retrieved wind field based on the LIDAR clearly shows two salient features of the terrain-disrupted airflow, namely, occurrence of a microscale vortex east of HKIA and the convergence of southeasterly wind with the prevailing easterly to the west of the airport.
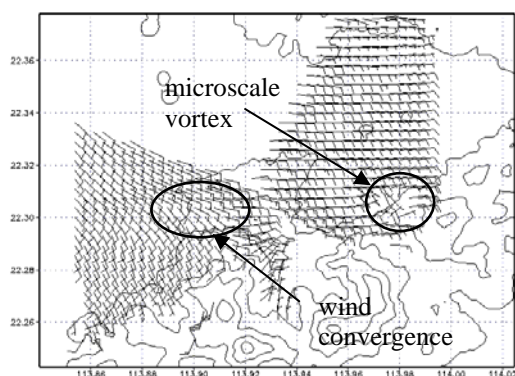
Figure 2. 2-D retrieved wind field based on the LIDAR at 9:56 a.m., 20 January 2003.
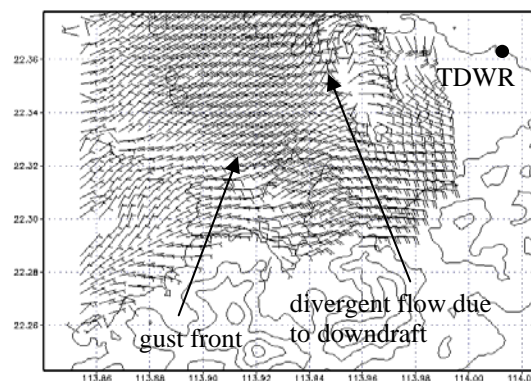
Figure 3. 2-D retrieved wind field based on LIDAR and radar at 4:22 p.m., 10 September 2002.

4   Analysis of a gust front

A gust front occurred to the northeast of HKIA on 10 September 2002 and moved southwestwards, bringing strong northeasterly wind to the airport. Due to sector blanking and rain, limited data were available for 2-D wind retrieval using the LIDAR alone. Wind data from 0.6-degree PPI scans of Terminal Doppler Weather Radar (TDWR, Figure 3) are also considered and Eq. (1) is modified by including another J_6 term for radar. The dual Doppler retrieval result is given in Figure 3, showing the strong northeasterly behind the gust front.

5   Conclusions

The modified two-step variational method works well in retrieving 2-D winds using LIDAR and radar data. The case studies revealed the detailed 2-D wind fields in terrain-induced disturbance and gust front.

Literature

Qiu, C.-J., A.-M. Shao, S. Liu, and Q. Xu, 2006: A two-step variational method for three-dimensional wind retrieval from single Doppler radar. *Meteorol. Atmos. Phys.*, 91, p.1-8.

Performance of a Doppler LIDAR in an Operational Environment

K.C. Wu, P.W. Chan and C.M. Shun

Hong Kong Observatory, Hong Kong, China, email: pwchan@hko.gov.hk

Abstract

A Doppler LIDAR has been operated by the Hong Kong Observatory at the Hong Kong International Airport (HKIA) since 2002. To the best of the authors' knowledge, it has the longest record of continuous operation for weather warning services in the world. This paper documents the data availability statistics of the LIDAR in different seasons and presents the accuracy of the radial velocity data by comparing with wind measurements from a ground-based anemometer and a remote sensing instrument (SODAR).

1 Introduction

A Doppler LIDAR was introduced to HKIA in 2002 to measure the wind in non-rainy weather conditions for low-level windshear detection at the airport. The LIDAR is required to measure at least up to about 8 km away in order to provide sufficient coverage for alerting windshear over the runway corridors (Shun and Lau 2002). The accuracy of radial velocity was specified to be 1 m/s. Using the large volume of data collected at HKIA over the years, this paper is the first attempt to document the availability statistics and the accuracy of the velocity data from the LIDAR in an operational environment.

2 Data availability statistics

Data availability of the LIDAR over four seasons in a year (February 2004 to January 2005) is studied. In each season, it is more or less isotropic with respect to the azimuth angle. As a result, the azimuthally averaged data availability curves are prepared (Figure 1). Two commonly used Plan Position Indicator (PPI) scans of the LIDAR are considered, namely, elevation angles of 1 degree and 4.5 degrees (for monitoring respectively the wind near the arrival and departure corridors).

For 1-degree PPI scans, the curves for different seasons appear to be quite similar. Data are available for at least 50% of the time up to about 8 km, providing sufficient coverage for the arrival corridors. For 4.5-degree PPI scans, the spring time (February to April) sees less amount of LIDAR velocity between 1.5 and 8 km compared to the other three seasons, possibly as a result of the lower cloud-base height. To improve the data coverage, combination of the LIDAR with a Doppler cloud radar may be a viable option.
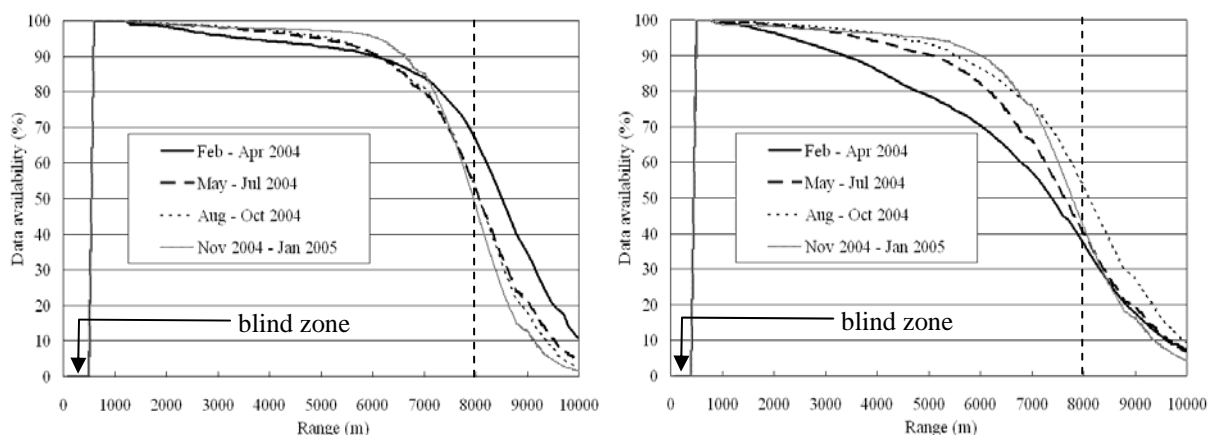
Figure 1. Data availability statistics for 1-degree PPI scan (left) and 4.5-degree PPI scan (right) in the period February 2004 to January 2005. The LIDAR has a blind zone of 400 m, over which no data are available.

In contrary to the seasonal average, the data availability pattern on an individual day may not be azimuthally isotropic, and could be related to cloud distribution in terrain-disrupted airflow. An example is shown in Figure 2. On that day, moderate to fresh easterly wind prevailed over Hong Kong with a temperature inversion of about 2 degrees at 500 m or so. The data availability diagram shows a wave-like feature downstream of a hill called Lo Fu Tau (height: 465 m AMSL) with a wavelength of 4 km. This is possibly due to wave clouds formed in cross-mountain airflow. On the other hand, no wave features are discernible west of LIDAR (where the mountains are taller) and data availability is generally higher over there.
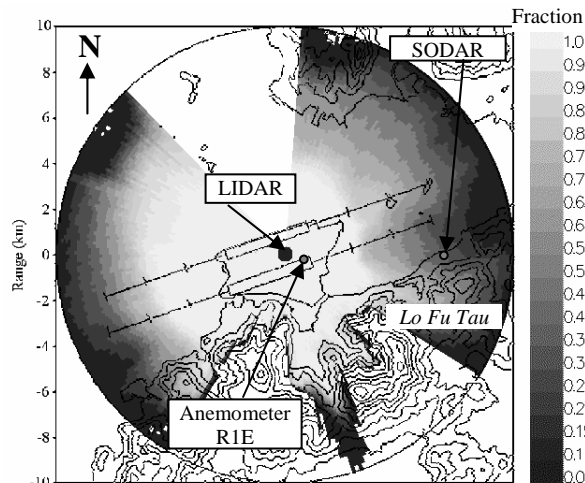
Figure 2. Data availability statistics for 4.5-degree PPI scan on 16 March 2004. Locations of meteorological equipment are also indicated on the map.
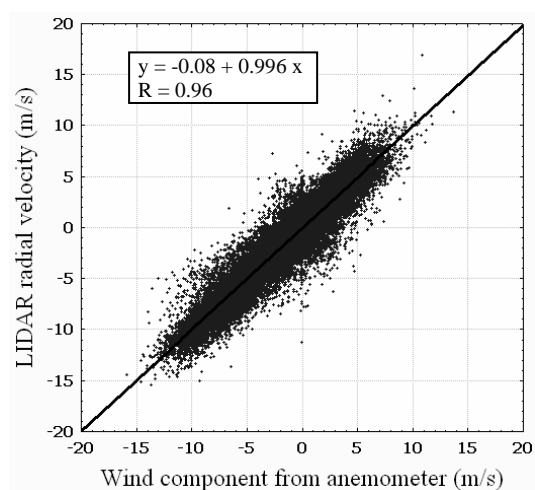
Figure 3. Comparison between LIDAR and anemometer data in the period March – November 2004.

3 Comparison with other instruments

The 1-second average wind data (of 4 Hz raw measurements) from the cup-vane anemometer R1E (Figure 2, about 18 m AMSL and 880 m from the LIDAR) are compared with the LIDAR's instantaneous measurements at that location from the 0-degree PPI scans (50 m AMSL). They are found to be well correlated (Figure 3). The bias and r.m.s. difference (LIDAR minus anemometer) are very small: -0.07 and 1.05 m/s respectively. The latter value is within the accuracy specifications of the LIDAR (1 m/s) and the anemometer (0.5 m/s). The LIDAR's instantaneous wind measurements from the 1-degree PPI scans are also compared with the 5-minute average wind at 170 m AMSL obtained by a 4.5-kHz SODAR (Figure 2, 7085 m away from the LIDAR). The study period is October 2005 to March 2006. The bias is again very small, less than 0.01 m/s. The r.m.s. difference is 1.97 m/s, slightly exceeding the accuracy specifications of LIDAR and SODAR (< 0.5 m/s). This may be attributable to the difference in sampling period.

4 Conclusions

The LIDAR at HKIA is found to provide the required coverage for the arrival runway corridors. The coverage for departure corridors in spring-time is affected by low cloud-base, sometimes related to terrain-disrupted airflow. The velocity data generally compare well with the anemometer and SODAR measurements.

Literature

Shun, C.M., and S.Y. Lau, 2002: Implementation of a Doppler Light Detection And Ranging (LIDAR) System for the Hong Kong International Airport. *10th Conference on Aviation, Range and Aerospace Meteorology,* American Meteorological Society, Portland, Oregon, USA.

Looking At Thermals during CSIP Using Doppler Lidar and Radiometer Data

Fay Davies[*], Karen E. Bozier and Chris G. Collier
School of Environment and Life Sciences, University of Salford, Salford, UK
[*]F.Davies@salford.ac.uk

Abstract

A large field program was carried out in Southern England in the summer of 2005 entitled Convective Storm Initiation Project, CSIP. As part of the field trial a pulsed Doppler lidar and a radiometer were set up by the University of Salford. Data from these two instruments have been used to investigate the behaviour of thermals in a convective boundary layer.

1   Introduction

The CSIP project involved a large number of UK universities through the UK Universities Facility for Atmospheric Measurements, UFAM, along with the Met Office and the Institute for Meteorology and Climate Research in Karlsruhe. The aim of CSIP was to investigate the mechanisms that affect convective precipitation through extensive measurements, over a series of intensive operation periods (IOPs) during the summer of 2005. The instruments were located around the Chilbolton Doppler radar facility and included two aircraft (see www.env.leeds.ac.uk/csip/). The University of Salford had a measurement site in Berkshire within a range of hills called the North Downs.

2.   Instrumentation

This work uses data taken with a pulsed Doppler lidar system and a ground based radiometer. The lidar has a wavelength of 10.6 um, a range resolution of 112 m, a minimum range of 700 m and a maximum range of 9 km. It measures aerosol backscatter and Doppler radial velocity and has a pulse repetition rate of 10 Hz (Pearson and Collier, 1999). The pulses are averaged to output data at a rate of 0.2 Hz. The system characteristics and accuracy are discussed in Davies *et al*. (2004) and comparisons with *in situ* balloon borne instruments have shown good comparison (Bozier *et al*., 2004). The lidar is housed in a mobile laboratory and has a scanning mechanism that enables the system to scan 295 degrees in azimuth and 45 degrees in elevation. The lidar was built by QinetiQ, Malvern. The lidar is eye-safe and was designed for use in urban situations (Collier *et al.* , 2005).

The radiometer is a temperature and humidity profiler with two frequency bands: 22-31 GHz for humidity profiling and liquid water path, and 51-58 GHz for temperature profiling. It was set to carry out boundary layer and full tropospheric profiling of temperature and humidity every 15 minutes and measured integrated water vapour and liquid water path at 1Hz at all other times. It was built by Radiometer Physics GmbH, Germany.

3.   Results

During the summer of 2005 the instruments were deployed over a period of 3 months. A series of 19 IOPs were conducted. The aim of the University of Salford measurements was to investigate, through examination of wind, turbulence and temperature profiling, low level forcing and its roll in the initiation of convective cells. This work will discuss the set up of the field trial and highlight some of the initial data analysis.

On July 28th 2005 a large storm event, being monitored by the CSIP instruments, led to a tornado over the city of Birmingham that caused extensive damage. During the early morning, strong boundary layer winds led to roll convection which was aligned with the wind flow. The turbulence structure within the roll convection was measured with the lidar and is shown in figure 1.
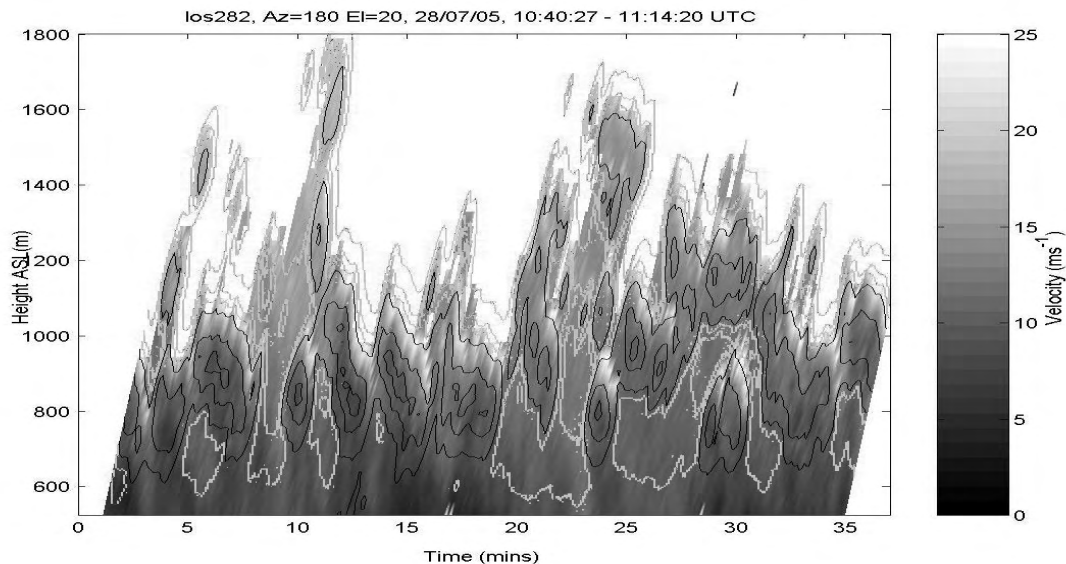
Figure 1. Velocity (shading) and aerosol backscatter (contoured) measured with the lidar using a fixed beam at an elevation of 20 degrees between 10:40 and 11:14 UTC on 28th July 2005.

4 Discussion

In this poster turbulence behaviour within the convective boundary layer will be shown. Analysis of the data is still in process but it is hoped that the radiometer data will be used in conjunction with the lidar data to examine the turbulence with the aim of gaining a better understanding of the vertical structure of the boundary layer thermals.

Literature

Bozier, K. E., Pearson, G. N., Davies, F. and Collier, C. G., 2004: 'Evaluating the precision of a transverse excitation atmospheric based CO2 Doppler lidar system with *in situ* sensors', *J. Opt. A: Pure Appl. Opt*. **6**, 608 – 616

Collier C.G., Davies F., Bozier K.E., Holt A.R., Middleton D.R., Pearson G.N., Siemen S., Willetts D.V., Upton G.J. and Young R.I., 2005: 'Dual Doppler lidar Measurements for improving dispersion models'. *Bull. A.M.S.*, **86**, 825-837

Davies, F., Collier, C. G., Pearson, G. N. and Bozier, K. E., 2004: 'Doppler Lidar Measurements of Turbulent Structure Function over an Urban Area'*, J. Oceanic Atmos. Tech.* **21**, 753 - 761

Pearson, G. N. and Collier, C. G., 1999: 'A pulsed coherent CO_2 lidar for boundary layer meteorology', *Quart. J. Roy. Meteorol. Soc.* **125,** 2703-2721.

Presentation of a network of MW-radiometers and sodars in the Italian region Veneto

Pernigotti Denise, Ferrario Massimo, Benassi Alessandro, Rossa Andrea, Sansone Maria
ARPAV-Meteorological Centro of Teolo, Teolo (PD) Italy, dpernigotti@arpa.veneto.it

Abstract

The Centro Meteorologico di Teolo (CMT) of the Regional Agency for Environmental Protection and Prevention of the Veneto Region (ARPAV) has recently installed a network of boundary layer profilers on its territory. The network consists of four passive microwave radiometers and four sodars, largely funded in the framework of the DOCUP[1] 2000-2006 Project. This paper presents the network and illustrates potential applications in air-quality forecasting, in particular the use of the thermal profile for in understanding PM_{10} concentration evolution.

1 Introduction

On the European scale the Po Valley certainly is a hot spot when it comes to air pollution issues, especially in the cold season because of the frequent occurrences of very stable meteorological conditions with marked thermal inversions, at times even below 100m above ground. Therefore, monitoring and predicting air quality conditions is an important service to the local authorities and the public at large, for heath prevention and protection.

In order to respond to these requirements, ARPAV CMT has recently installed a boundary layer profiler network (Fig. 1), which consists of one HATPRO radiometer, three MTP5-HE radiometers and four PCS-2000 sodars. Two instruments were funded by Padua Municipality, whilst the others were co-funded by the European Commission, Italian Government and Veneto Region within the DOCUP 2000-2006 Project. As such the network is the first of its kind in Italy and their principal applications are in the field of environmental emergency management and regional air-quality short time forecasting.
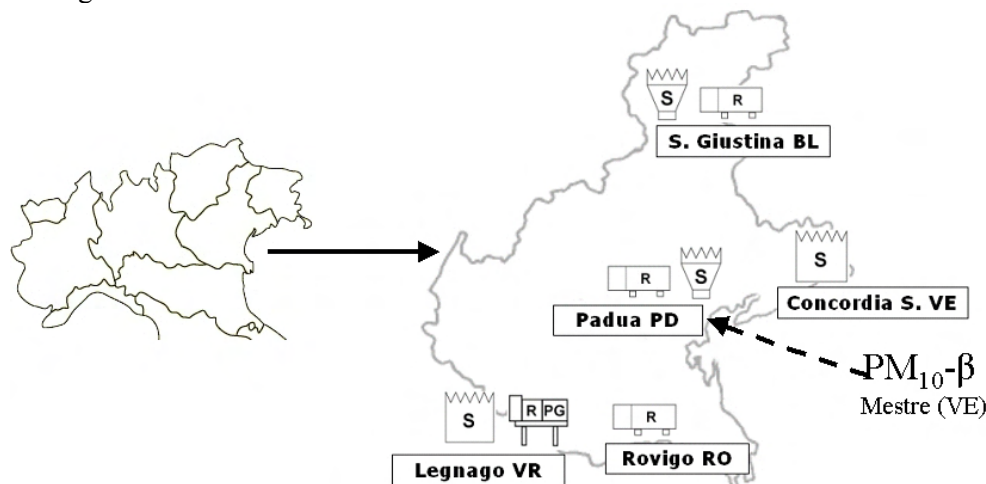
Figure 1. Northern Italy plus location of the PBL network (S=PCS2000 Sodar, R=MTP5-HE Radiometer, RPG=HATPRO RPG Radiometer). The location of the PM_{10} 2-h instrument is highlighted by the broken arrow.

2 Instrumentation and data set

The radiometer MTP5-HE, manufactured by Attex (Russia) and distributed by Kipp & Zonen (NL), is a well proven and robust instrument that measures temperature up to 1000m with a vertical resolution of 50m and a time resolution of 5'. Nominal accuracy is 0.3-0.4K for adiabatic and 0.8-1.2K for inversion conditions, while a good agreement within 1K was found for the CMT radiometers at Padua and Rovigo with the closest soundings in homogeneous conditions (Ferrario et al. 2006). Data

---

[1] DOCUP stands for DOCumento Unico di Programmazione, Obiettivo 2, Misura 4.3, co-funded by the national and regional governments of Italy and Veneto, and the European Commission.

availability in the first year of deployment is quite high for the Padua site with 97%, while the lower values for the other two sites, about 75%, are due to prolonged periods of malfunctioning.

The HATPRO, manufactured by Radiometer Physics GmbH (D), is a robust and easy to calibrate instrument that measures temperature and humidity up to 10000m with a vertical resolution of 200m (in PBL mode temperature is scanned every 50m up to 2000m), integrated water vapour, and liquid water content. Nominal accuracy here is 0.6-1K up to 10000m and 1K in PBL mode. Data of this radiometer have been used for 'eyeball' monitoring purposes so far, but are not included in the preliminary analysis presented here. Data availability in the first year of deployment is about 70% (the instrument doesn't measure in case of rain).

The SODAR is an established technology for measuring the vertical wind profile with a high temporal resolution. The instruments installed here are two PCS2000-24 (Padua and S. Giustina) and two PCS2000-64 (Legnago and Concordia S.), manufactured by Metek (D). For these instruments the declared measurement accuracy range from 0.1 to 0.3 m/s for horizontal wind intensity and from 1° to 5° for horizontal wind direction. The data availability of the first year of deployment is around 70% for the first level (40m), decreasing rapidly with height.

The PM_{10} concentrations are available every two hours in real time for four sites in Veneto. For the purposes of this study we only consider the station of Mestre, a site close to Venice and about 25 Km northeast of the Padua profilers. For the present analysis an episode of high PM_{10} concentrations (19-26 December 2005), and a full year of data starting 1 April 2005 were used.

3 Results

The main aim of this analysis is to investigate the ability of the radiometer and sodar sited in Padua to explain the evolution of the PM_{10} concentrations in the area, as represented by the Mestre station. Figure 2 shows PM_{10} concentrations and temperature profiles for a typical situation of high pressure and low winds on the Po Valley. The dependence of the diurnal cycle of PM_{10} on the presence and strength of the thermal inversion, as measured by the MTP5, is quite evident with concentration peaks coinciding with the marked nocturnal inversions. On the other hand, the effect of the inversions on the day-to-day accumulation is less obvious, i.e. there is an increase of the concentrations from 20/21 December to the 23rd, while thereafter the concentrations settle on a relatively high level, before decreasing substantially due to a meteorological disturbance with rain associated.
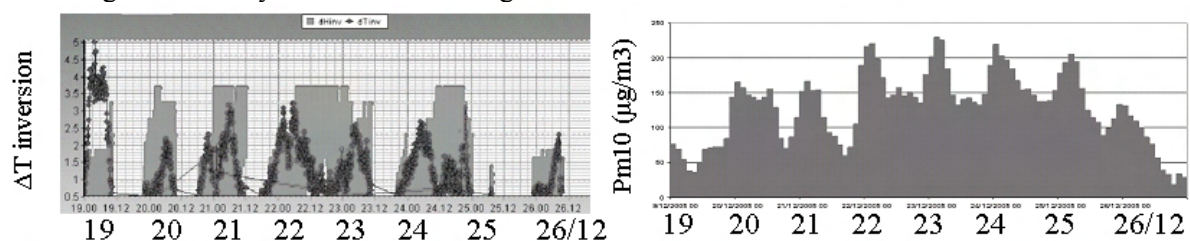
Figure 2: High-concentration episode 19-26 December 2005, inversions strength and height (left panel, dots and bars, respectively) and PM_{10} concentrations (right panel).

In addition, an attempt was made to find such dependence in the entire data set. Table 1 reports the correlation coefficients between PM_{10} concentrations and vertical profile information for temperature and wind. The frequency spectrum of the 2-hly PM_{10} concentration (not shown) exhibits a clear 24h peak, so that we look at the filtered data, i.e. 2-hly PM_{10} minus daily average which retains frequencies below 24 hours only. We calculate correlation coefficients between various profile variables and the following series: 2-hly PM_{10}, daily averaged PM_{10}, 2-hly PM_{10} minus daily average, and daily PM_{10} variance. It emerges that the most closely related meteorological variable is the difference in potential temperature between the 700m above ground level and the surface, then other parameters characterizing the thermal inversion, and then the wind velocity. Also, wind direction shows a correlation with the PM_{10} concentration. In fact, strongest episodes of pollution can be associated with north-westerly wind, blowing from the Po Valley, rather than north-easterly winds which bring clean air from the Adriatic sea.

It is interesting to note that the coefficients change sign when correlated with the normalized variance of PM_{10}. This is plausible as large diurnal variances, normalized by the daily average, are likely to be associated with substantial turbulence which, in turn, is acting to modulate and diminish PM_{10}.

Table 1: 1 year correlations values	ΔT 700m-surface	ΔT 200m-surface	ΔT inversion	Δh inversion	inversion base	wind dir 200m	wind dir 400m	wind vel 100m	wind vel 200m
2h PM_{10} vs 2h	0.50	0.44	0.40	0.33	-0.37	0.39	0.19	-0.25	-0.17
24h PM_{10} average vs 24 average	0.58	0.55	0.46	0.28	-0.51	0.41	0.16	-0.26	-0.16
2h PM_{10} filtered vs 2h filtered	0.33	0.35	0.23	0.24	-0.23	-0.11	-0.10	-0.13	-0.08
24h PM_{10} variance vs 24h average	-0.35	-0.30	-0.21	-0.15	0.30	-0.21	-0.16	0.17	0.17

Figure 3 reports the time series for the high-concentration episode of 19-26 December 2005 (see Fig. 2) of the first three rows of Table 1, i.e. of $\Delta\theta$ with 2-hly PM_{10}, daily averaged PM_{10}, and 2-hly PM_{10} filtered. Indeed, the correlation coefficients are significant with values of 0.65, 0.83, and 0.61, respectively. The highest correlation is found for the daily averages (Fig. 3, middle panel), when the thermal inversion is anti-correlated with the daily averaged wind 100m above ground featuring a coefficient of –0.89. The correlation between the 2-hly values of the latter two variables, on the other hand, is way lower (-0.29). The high-frequency part of the concentration (right panel) follows the thermal inversion signal nicely at times, but not always, pointing to another, independent factor that governs the pollutant. The first peak at about 24 hours, for instance, is coincident with very low winds.
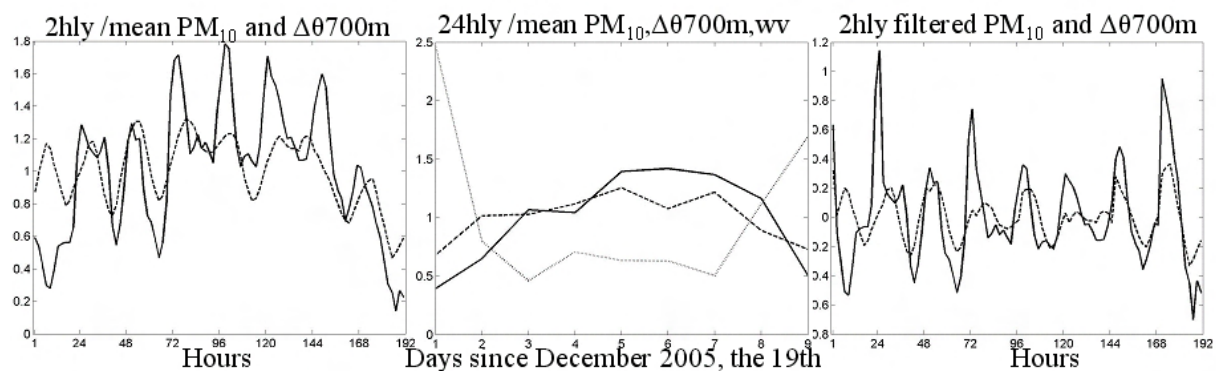
Figure 3. PM_{10} (solid), $\Delta\theta$ 700 (dashed) and wind velocity at 100m (dotted, only middle panel): 2-hly data (left panel) and 24hly average (middle panel), both scaled by the period mean, and 2-hly filtered data (right panel).

4 Discussion

As probably expected for a region like the Po Valley, the thermal profile of the atmosphere is the meteorological parameter most closely related to the evolution of PM_{10} concentrations, and this is true both for the high PM_{10} concentration episode and the entire year. This is indeed consistent with the high frequency of occurrence of high pressure situations featuring low winds in the Po Valley, especially during the cold season. The dependence of the day-to-day accumulation of PM_{10} on atmospheric stability (PM_{10} daily average) allowing a prediction of PM_{10} concentrations in the absence of synoptic forcing. The significant anti-correlation of thermal inversion properties with the low-level winds fits well in this line of reasoning. The intra-diurnal variability, as given by the 2-hly values, however, delivers a less coherent picture, probably highlighting that the details of the dynamics that govern both the balance between wind and thermal inversions, and the dispersion of the pollutant is beyond of what a simple linear correlation approach can reach.

References

Ferrario, M.E., A. M. Rossa, D. Pernigotti, M. Sansone. and A. Benassi, 2006. Presentation and first assessment of a radiometer network in the Italian region Veneto. Proc. of the Int. Conf. on Urban Climate, Goteborg, 10-16 June 2006.

Sansone, M., M. Bressan, D. Pernigotti, A. M. Rossa, M. E. Ferrario. and A. Benassi, 2006. A multiple regression approach to forecasting PM_{10} concentraion oin the city of Padua, Italy. Proc. of the Int. Conf. on Urban Climate, Goteborg, 10-16 June 2006.

Boundary layer temperature profile observations using ground-based microwave radiometers

Pospichal Bernhard[1], Susanne Crewell[2], Ulrich Löhnert[1], Thomas Rose[3]

[1] Meteorological Institute, University of Munich, Germany
[2] Institute of Geophysics and Meteorology, University of Cologne, Germany
[3] Radiometer Physics GmbH, Meckenheim, Germany

Abstract

The use of ground-based microwave profilers is an accurate and relatively inexpensive and way to continuously observe the temperature profile of the boundary layer with a high temporal resolution. Here we present observations of a 14-channel microwave radiometer (HATPRO) which has been used under various climatic conditions. To obtain the temperature profile with a high vertical resolution (down to 50 m close to the surface), observations are taken at seven frequencies (51 to 59 GHz) and under several elevation angles from 90 to 5 degrees. The error for the retrieved temperature profiles for the lowest 1000 m is less than 0.5 K.

1   Introduction

Microwave profilers which measure several frequencies along the 60 GHz oxygen absorption complex are a well established technique for observing the atmospheric temperature profile from the ground as well as from space. From the ground observations are typically taken in zenith direction at about 5 to 10 frequency channels from 50 to 60 GHz (Westwater et al., 2005). The vertical resolution decreases from about is about 500 m in 300 m height and rapidly decreases to 1 km in 5000 m height (Güldner und Spänkuch, 2001). The performance in the boundary layer can be improved significantly by scanning the atmosphere under different elevation angles. This paper presents a new instrument optimized for this purpose as well as some measurement examples.

2   Instrumentation

The HATPRO (Humidity And Temperature PROfiler) microwave radiometer (Rose et al., 2005) continuously measures thermal emission by atmospheric components (water vapor, oxygen, cloud water) at 14 channels located in 2 frequency bands. Seven frequencies are located along the high-frequency wing of the water vapor absorption line at 22.235 GHz, and 7 channels are located along the low-frequency wing of the oxygen absorption complex around 60 GHz.

Figure 1. Photograph of a HATPRO microwave profiler.

For boundary layer retrievals observations are taken at 6 elevation angles from 90 to 5 degrees. For the highest frequency (59 GHz) which is nearly opaque this results in a variation of about 1-2 K. This makes clear that a high receiver stability and low noise level of HATPRO is absolutely necessary for a successful observation. Profiles of water vapor and temperature are derived from the observed brightness temperatures via multi-variate regression algorithms based on a large (at least 10 years) of atmospheric profiles from radiosoundings. Retrieval algorithms were developed for the traditional zenith pointing geometry as well as a so called boundary layer retrieval which involves the angular information of the highest four frequencies. The theoretical accuracy of the latter algorithm outperforms the zenith algorithm strongly within the boundary layer (Fig. 2): For the lowest 1500 m of the troposphere the accuracy is below <0.5 K). It should be noted that in this approach a horizontally homogenous atmosphere is assumed.
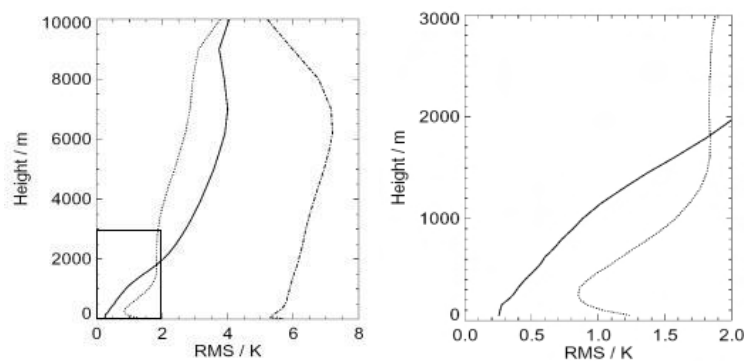
Figure 2. Theoretical RMS for zenith temperature profile retrievals (dotted) and improved profiles below 1500 by performing elevation scans. The standard deviation of the data set is shown by the dashed line.

3   Results

During the last year, HATPRO microwave radiometers have been operated under very different climatological conditions. The data set includes observations from the high mountain station Schneefernerhaus in the German Alps in winter, results from the LAUNCH campaign in summer 2005 at Lindenberg (Germany) which show mid-latitude summer conditions. Furthermore, tropical measurements in Darwin as part of the Tropical Warm Pool International Cloud Experiment (TWP-ICE) as well as in Djougou, Benin as part of the African Monsoon Multidisciplinary Analysis (AMMA) have been performed.

During the two month campaign at Lindenberg HATPRO observations could be compared to radiosoundings by the German Weather Service. The comparisons (Fig.3) revealed a good agreement in different meteorological conditions with an RMS below 0.6 K below 1 km. Taking into account the differences caused by the observation of different air volumes, e.g. the radiosonde drifts away, this excellent comparion confirms the theoretical results.

The capability of the radiometer to detect shallow night-time inversions very well was investigates by comparing the observation with the ones by a 100 m mast located directly next to HATPRO. The statistical comparison over the whole period showed an RMS of ~0.5 K for 40 and 100 m height which is better than the one between the radiosonde and the mast. Looking at the temperature gradient (Fig. 4) the possibility of detecting inversions (up to 6 K/100m) with a good accuracy of 0.7 K. Largest discrepancies occur when the temperature gradient is positive, e.g. the surface is heating and spatial differences occur which do not allow the assumption of horizontal homogeneity.
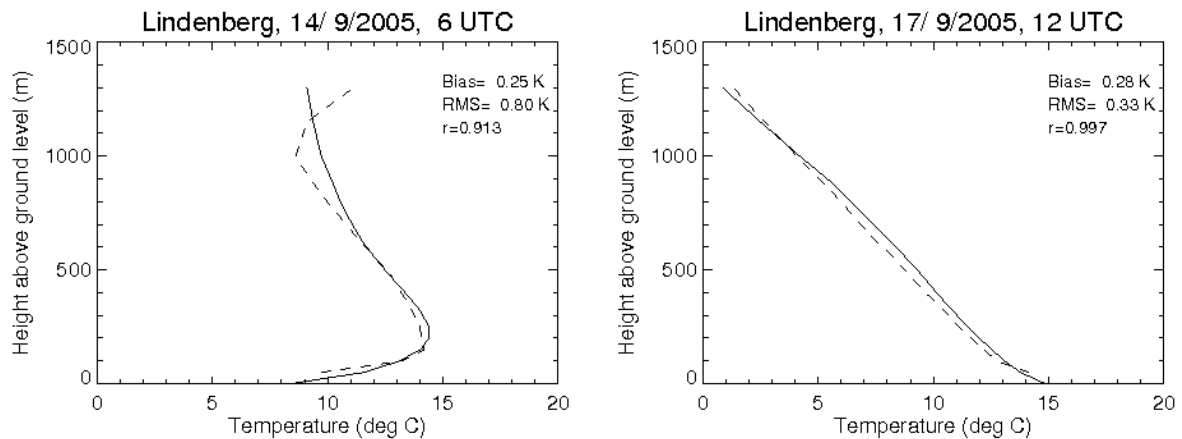
Figure 3. Two examples of boundary layer temperature profiles from Lindenberg, Germany. Dashed lines are radiosonde measurements, solid lines represent retrieved temperature profile from HATPRO boundary layer scans. Left: Shallow morning inversion. Right: Well-mixed daytime profile.
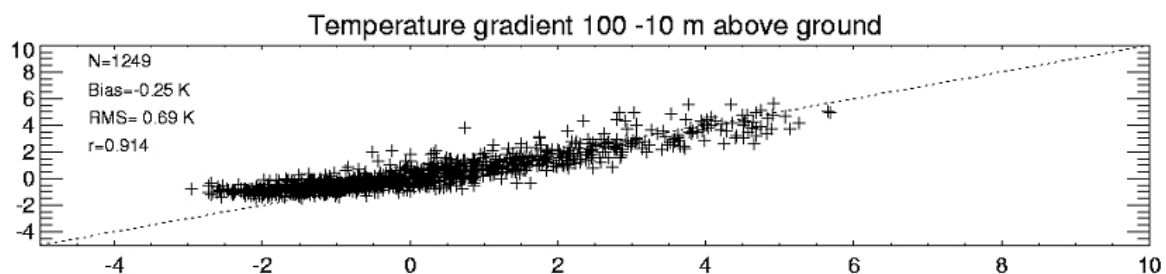
Figure 4. Comparison of HATPRO temperature gradient (x-axis, Kelvin) with corresponding values by a 100 m mast (y-axis) in Lindenberg.

4   Discussion, Conclusions, and Outlook

The possibilities for continuous observations of boundary layer temperature profiles by a highly stable ground-based microwave radiometer have been shown. The use of several observation angles compared to zenith observations improves the accuracy of temperature profiles for the lowest parts of the troposphere significantly by about a factor of 2 down to 0.5 K. Further work with these data include climatological studies on the diurnal cycle of the boundary layer temperature profiles in different climate zones as well as their use for the evaluation of numerical weather prediction models.

Literature

Güldner. J. and D. Spänkuch, 2001: Remote Sensing of the Thermodynamic State of the Atmospheric Boundary Layer by Ground-Based Microwave Radiometry, *J. Atmos. Oceanic Technol.*, 18, 925-933.
Rose T., S. Crewell, U. Löhnert, C. Simmer, 2005: A network suitable microwave radiometer for operational monitoring of the cloudy atmosphere, *Atmospheric Research* **75**, 183-200
Westwater, E. R., S. Crewell, and C. Mätzler, 2005: Surface-based Microwave and Millimeter wave Radiometric Remote Sensing of the Troposphere: a Tutorial, *IEEE Geoscience and Remote Sensing Newsletter*, pp. 16-33. ISSN 0161-7869.

Characterization of the Daytime Convective Boundary Layer Using an Advanced Radar Simulator

Danny Scipión, Phillip Chilson, Evgeni Fedorovich and Robert Palmer

School of Meteorology, University of Oklahoma, Norman, OK

e-mail: dscipion@ou.edu

Abstract

The daytime atmospheric convective boundary layer (CBL) is characterized by strong turbulence that is primarily caused by buoyancy forcing at the heated underlying surface. The present study considers a combination of radar and large eddy simulation (LES) techniques to characterize the CBL. Data representative of a daytime CBL with wind shear have been generated by LES, and used in the virtual boundary layer radar (BLR) with multiple vertical and off-vertical beams and frequencies.

1   Introduction

Strong turbulence caused by buoyancy forcing at the heated underlying surface is one of the main features of the daytime atmospheric convective boundary layer (CBL). Ensuing convective motions transport heat upward in the form of convective plumes or thermals, which together with associated downward motions effectively mix momentum and potential temperature fields so that vertical gradients of their averaged profiles are usually rather small. The CBL is topped by the entrainment zone where stable stratification inhibits vertical mixing, and vertical gradients of averaged meteorological fields exhibit their maxima. The present study focuses on quantifying the CBL depth, entrainment zone thickness and turbulence parameters, using a combination of radar and large eddy simulation (LES) approaches. The LES provides the input fields for an advanced boundary layer radar (BLR) simulator capable of flexibly probing the virtual atmosphere using multiple vertical and off-vertical beams and frequencies. The BLR output data are then employed to estimate CBL characteristics, which are compared to the ground-truth LES data.

2   Estimation the structure function parameter of refractivity (C_n^2) from the LES

The LES code to be employed in our study is described in Fedorovich et al. [2004] and Conzemius and Fedorovich [2006]. It was extensively tested in comparison with several other representative LES codes and against experimental data for clear CBLs with and without wind shear, and was found to confidently reproduce turbulence structure for a broad variety of flow regimes observed in the clear CBL. The simulation runs have been performed in a rectangular $(X \times Y \times Z) = 2000 \times 2000 \times 2000$ m^3 domain on a $200 \times 200 \times 200$-cell grid with a uniform spacing of 10 m.

The following external simulation parameters have been prescribed for the run. Free-atmosphere wind: 5 m s^{-1} in the x direction, 0 in the y direction. Free-atmosphere potential temperature gradient: 0.004 K m^{-1}. Surface kinematic heat flux: 0.2 K m s^{-1}. Surface kinematic moisture flux: 10^{-4} s^{-1}. Surface roughness length: 0.01 m. The LES output for the radar simulator was generated with 1 s time discretization in a sub-domain of 750 m$\leq x \leq$1250 m, 750 m$\leq y \leq$1250 m, 200 m$\leq z \leq$1200 m. The output included resolved (in the LES sense) three-dimensional fields of potential temperature (θ), specific humidity (q), flow velocity components(u, v and w), and subgrid turbulence kinetic energy (E).

Estimation of the structure function parameter of refractivity (C_n^2), is based on the gradient of the refractive index ($n = 1 + N \times 10^{-6}$), where N is the refractivity, and is calculated using [Bean and

Dutton, 1966]:

$$N = \frac{77.6}{T}\left(P + 4811\frac{P_w}{T}\right), \tag{1}$$

where P is pressure (hPa), assuming standard atmosphere, $P_w(q, T)$ is water vapor pressure (hPa), and $T(P, \theta)$ is temperature (K).

The structure function parameter of refractivity (C_n^2), is estimated from the n field as

$$C_n^2(x, y, z, t) = \frac{[n(x, y, z + \Delta z, t) - n(x, y, z, t)]^2}{\Delta z^{2/3}}, \tag{2}$$

where Δz is the vertical resolution.

3   Radar Simulation

Following the work of Muschinski et al. [1999], the parameters of the virtual BLR include: frequency (915MHz), full half-power beam width (9°), resolution (50 m) and beam inclination (variable).

The signal amplitude is proportional to the C_n^2 and inversely proportional to r_0, which is the range of the center of the scattered volume. The phase difference is proportional to the velocity vector, according to [Muschinski et al., 1999]:

$$V(t_0 + \tau) = A' \sum_{p=1}^{N} \sqrt{C_n^2(t_0 + \tau)^{(p)} W_r^{(p)} W_b^{(p)}} \cdot \exp[-j(\varphi_0^{(p)} + \mathbf{k}_B^{(p)} \cdot \mathbf{v}_p(t_0 + \tau)\tau)], \tag{3}$$

$$A' = \frac{G}{\lambda r_0^2}\sqrt{0.0330}k_B^{-11/6}, \tag{4}$$

where G is a contant proportional to the power transmitted and gain of the transmitter and receiver, k_B is the Bragg wavenumber ($k_B = \frac{4\pi}{\lambda}$), $\mathbf{k}_B^{(p)}$ is the Bragg wave vector that is directed from the center of the antenna to the center of the pth LES grid cell and has the lenght k_B, $\mathbf{v}_p$ is the instantaneous radial velocity, and W_r and W_b describes the range weighting function [Holdsworth and Reid, 1995; Yu, 2000; Cheong et al., 2004] and beam-pattern weighting function, respectively [Yu, 2000; Cheong et al., 2004]:

$$W_r(x, y, z) = \exp\left[\frac{(r - r_0)^2}{2\sigma_r^2}\right], \tag{5}$$

$$W_b(x, y, z) = \exp\left[-\frac{(\theta_x - \bar{\theta}_x)^2}{2\sigma_x^2} - \frac{(\theta_y - \bar{\theta}_y)^2}{2\sigma_y^2}\right], \tag{6}$$

$$\theta_x = \tan^{-1}\left(\frac{x}{z}\right),$$

$$\theta_y = \tan^{-1}\left(\frac{y}{z}\right),$$

where $r = \sqrt{x^2 + y^2 + z^2}$ is the range, and the variance $\sigma_r = 0.35c\tau_p/2$, where c is the speed of light and τ_p is the pulse width [Doviak and Zrnić, 1993], $\bar{\theta}_x$ and $\bar{\theta}_x$ describe the antenna beam pointing in degrees and $\sigma_x = \sigma_y = \theta_1/2.36$ are proportional to the beamwidth (θ_1) in degrees.

An estimation of any variable X at $t_0 + \tau$ was achieved using the linear interpolation scheme of [Cheong et al., 2004]:

$$X(t_0 + \tau) = (1 - \tau)X(t_0) + \tau X(t_1). \tag{7}$$

The spectrum is estimated from the time series data, and then white noise is added to the spectrum. From this noisy spectrum, the three central moments are calculated (power, mean radial velocity and spectrum width). The noise is estimated using Hildebrand and Sekhon [1974] algorithm. Figure 1 shows an example of a particular flow estimated by the virtual BLR.
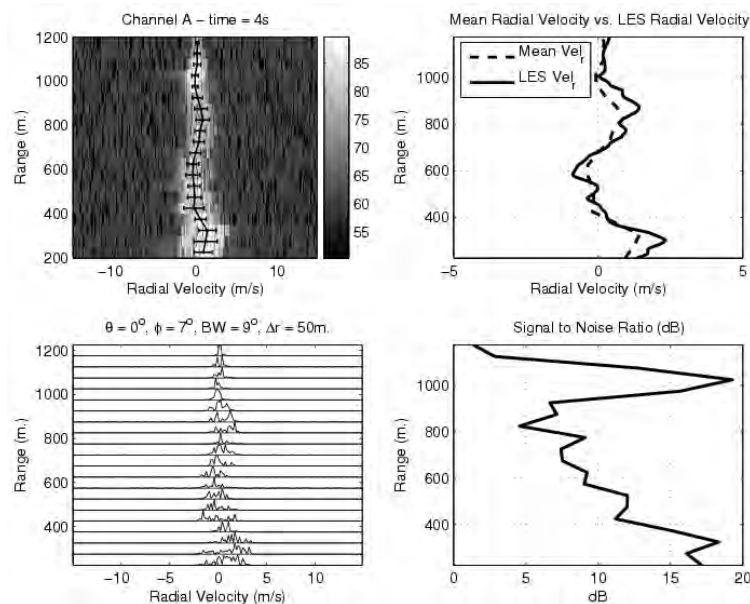
Figure 1: Spectral analysis of the time series data. Top-left: intensity spectrum with additive white noise. The continuous line represents the mean radial velocity and the error bars the spectrum width. Top-right: comparison between the mean radial velocity estimated from the time series data and the true radial velocity from the LES. Bottom-left: normalized stacked spectra. Bottom-right: signal to noise ratio. The peak of the SNR corresponds to the CBL top (inversion layer).

4   Conclusions

The virtual boundary layer radar provides a useful tool to study and characterize the CBL. Capabilities include off-vertical beam positions and different frequencies. BLR mean radial velocity estimated from the time series shows good agreement with velocity fields retrieved from the LES. Future work will include implementation of the range imaging technique [Palmer et al., 1999; Luce et al., 2001; Chilson et al., 2003] to obtain C_n^2 with higher resolution.

References

Bean, B. R., and E. J. Dutton, 1966: *Radio Meteorology*. Natl. Bur. Stand., Monogr. 92, Supt. Doc. U.S. Govt. Printing Office, Washington, D.C.

Cheong, B. L., M. W. Hoffman, and R. D. Palmer, 2004: Efficient atmospheric simulation for high-resolution radar imaging application. *J. Atmos. Oceanic Technol.*, **21**, 374–378.

Chilson, P. B., T.-Y. Yu, R. G. Strauch, A. P. Muschinski, and R. D. Palmer, 2003: Implementation and validation of range imaging on a UHF radar wind profiler. *J. Atmos. Oceanic Technol.*, **20**, 987–996.

Conzemius, R. J., and E. Fedorovich, 2006: Dynamics of sheared convective boundary layer entrainment. Part I: Meteorological background and large-eddy simulations. *J. Atmos. Sci.*, **63**, 1151–1178.

Doviak, R. J., and D. S. Zrnić, 1993: *Doppler Radar and Weather Observations*. Accademic Press, San Diego, CA, second edition.

Fedorovich, E., R. Conzemius, and D. Mironov, 2004: Convective entrainment into a shear-free linearly stratified atmosphere: bulk models re-evaluated through large-eddy simulations. *J. Atmos. Sci.*, **61**, 281–295.

Hildebrand, P. H., and R. S. Sekhon, 1974: Objective determination of the noise level in doppler spectra. *J. Appl. Meteorol.*, **13**, 808–811.

Holdsworth, D. A., and I. M. Reid, 1995: A simple model of atmospheric radar backscatter: Description and application to the full correlation analysis of spaced antenna data. *Radio Sci.*, **30**, 1263–1280.

Luce, H., M. Yamamoto, S. Fukao, D. Helal, and M. Crochet, 2001: A frequency domain radar interferometric imaging (FII) technique based on high resolution methods. *J. Atmos. Sol.-Terr. Phys.*, **63**, 221–234.

Muschinski, A. P., P. P. Sullivan, R. J. Hill, S. A. Cohn, D. H. Lenschow, and R. J. Doviak, 1999: First synthesis of wind-profiler signal on the basis of large-eddy simulation data. *Radio Sci.*, **34**, 1437–1459.

Palmer, R. D., T.-Y. Yu, and P. B. Chilson, 1999: Range imaging using frequency diversity. *Radio Sci.*, **34**(6), 1485–1496.

Yu, T.-Y., 2000: *Radar studies of the atmosphere using spatial and frequency diversity*. Ph.D. thesis, University of Nebraska-Lincoln.

Doppler Wind Lidar and Radar Wind Profiler – Comparison of Instruments and Discussion of Various Measurement Methods

Siegfried Vogt, Andreas Wieser

Institut für Meteorologie und Klimaforschung, Forschungszentrum Karlsruhe

Siegfried.Vogt@imk.fzk.de

Abstract

A novel coherent Doppler Wind Lidar (CLR Wind Tracer Doppler Lidar) shall be presented. The second part will cover various scan and operation modes: PPI and RHI scan modes for the Lidar; clear air and RASS modes for the wind profiler RASS. Both systems were operated side by side in July 2004. Selected wind profiles and plots of the wind vector as a function of time and altitude generally are in good agreement.

1   Doppler Wind Lidar

The Doppler Wind Lidar (CLR Photonics Wind Tracer Doppler Lidar) comes in its own shelter which is accommodated separately together with all necessary equipment necessary to operate the Lidar system, such as the transceiver, control units, real-time processor, and the data storage system. On top of the container a two-axis scanner is fixed, which directs the laser beam into the atmosphere by two planar mirrors. The Wind Lidar uses a pulsed laser with a pulse repetition frequency of 500 Hz. This means that every 2 milliseconds, a laser pulse of 425 ns is transmitted into the atmosphere. The pulse is 50 – 100 m long and 10 – 30 cm wide, depending on the distance from the Lidar. The system has a sampling rate of 10 nanoseconds; this corresponds to a sampling distance of 1.5 m.
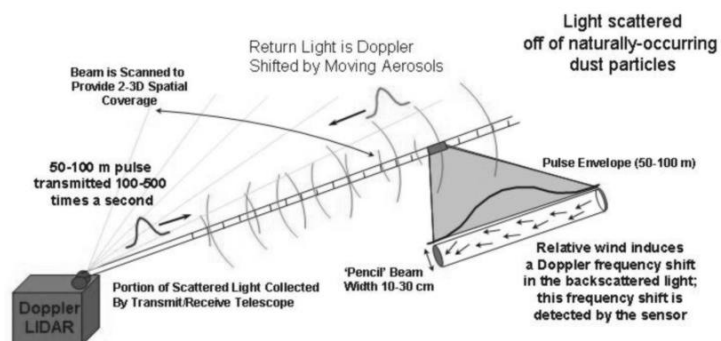
Figure 1 Side view of the Doppler Wind Lidar   **Figure 2** Principle of the Doppler Wind Lidar

The wavelength of the laser used is 2 µm, which means that the laser is eye-safe for human beings. A small part of the laser light is backscattered by aerosol particles of 0.5 µm in diameter at least. Such particles are nearly always present in the atmosphere. The aerosols move with the air movement, as a result of which the backscattered light that hits the sensor again experiences a frequency shift according to the Doppler effect. At the frequency applied, this shift amounts to 1 MHz per 1 ms^{-1} radial wind.

By means of a two-axes scanner, the laser beam can be moved in any direction of the half space above the measurement container, such that wind values can be collected from any direction or height up to a maximum distance of 10 km. This distance depends on the current aerosol distribution. In the absence of clouds, the upper edge of the atmospheric boundary layer is reached at least. By clouds, fog, and precipitation, the distance is reduced significantly.

2   Different scan modes

To determine the three-dimensional wind field, the laser beam of the Lidar has to be adequately moved in various directions by the two-axes scanner. Basically, there are two types of scanning mode: plane-position indicator (PPI) and range-height indicator (RHI). During a PPI scan, the scanner remains at a constant elevation angle while moving in azimuth. These scans are preferably used to assess the horizontal variability of the wind and directional shear. During an RHI scan, the scanner remains at a constant azimuth angle, while moving in elevation. RHI scans layers of wind shear, either directional shear or speed shear.

By way of example, Fig. 3 presents the positions of the Lidar measurement values (blue) of the RHI scan mode at 495 – 525 m height and a horizontal distance of 700 – 2000 m from the Lidar. In addition, the corresponding mean position is displayed (open star). To calculate a wind profile for every height interval, a sine fit has to be carried out to determine the horizontal wind speed (amplitude), direction (phase), and vertical wind velocity (offset) in a VAD manner (Fig. 4).
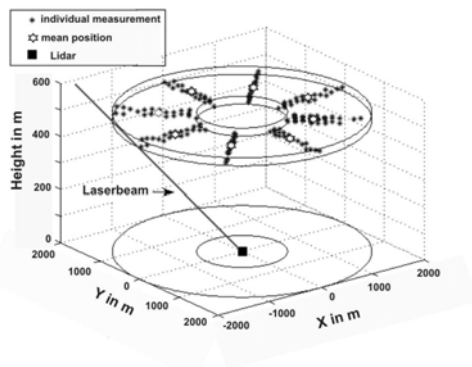
Figure 3 Position of the Lidar measurements   **Figure 4** Sine fit for this height interval
            at the height interval of 495-525 m   left: convective daytime   right: stable nighttime
            and horizontal distance of 700-2000 m

The RHI scan mode with eight azimuth positions selected allows to determine within the shortest period of time (120 sec) the wind vector at all measurement heights from volume elements of the same size starting from low heights and at constant horizontal distance from the Lidar. Due to the relatively large scanned volume, from which the wind vector is determined, a too homogeneous wind field may be obtained in case of strong convective turbulence.

PPI scans with fixed, but small elevation angles and variable azimuth are favourable to study the horizontal variability of the wind field. The scanning geometry at large elevation angles (> 75 deg) is similar to the measurement geometry of a wind profiler. This scanning method, however, has the drawback of measurement values being available from heights above 500 m only due to the intrinsic dazzling of the Lidar or taking much longer than the RHI mode if several PPI scans at different elevation angles are carried out to get measurements near ground as well. An accurate wind profile can only be estimated if the wind field remains unchanged during around 5 minutes - the time for a suitable stack of PPI scans.

3   Operation modes of the Radar Wind Profiler

The dominant scattering objects of the Radar Wind Profiler with wavelengths in the decimetres to metres are turbulent inhomogeneities of the atmospheric refractive index caused

by variations of moisture and temperature. Near the ground, this measurement scheme often suffers from severe interference of ground clutter resulting from buildings or natural obstacles. Also in cases of weak natural turbulence echoes, no wind estimation is possible in this so-called clear air mode. If a wind profiler is equipped with a radio-acoustic sounding system (RASS), the scattering structures are produced artificially by sound waves. The velocity with which these structures are moving results from adding the velocity of sound to the wind velocity. Based on this scattering mechanism, a second method of wind vector estimation results. The advantage of the RASS mode is its immunity to the above-mentioned interferences. Another advantage of an RASS is that there are no restrictions due to fog and clouds, contrary to optical methods. The maximum vertical range of an RASS, however, is significantly shorter than that of a Wind Profiler.
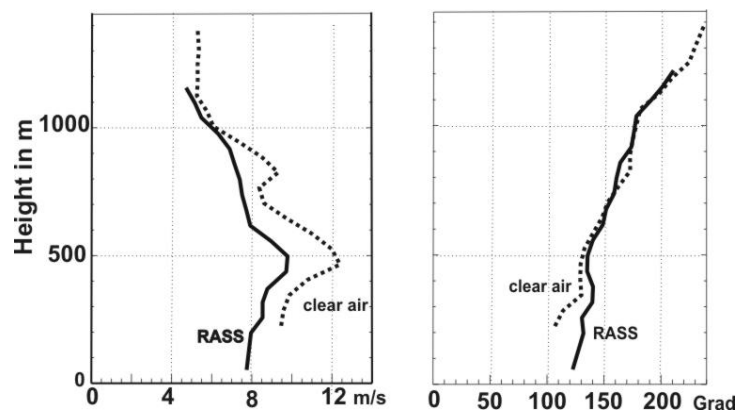
Figure 4 Profiles of wind speed (left) and direction (right) estimated by the clear mode (blue) and RASS mode (red) for 7/7/04 18:39UTC

4   Comparison of instruments

In July 2004, the Doppler Wind Lidar was run side by side with a wind temperature profiler (WTR) over a time period of two days. For the comparison of the wind values, data from a 200 m high measurement tower and radiosonde data were used in addition. In case of weak thermal turbulence as it was the case on 07/07/2004, the wind profiles of all instruments agree reasonably well, see Fig. 5. In case of strong convection, the wind speeds and wind directions measured by the Doppler Wind Lidar and Radar Wind Profiler differ considerably. These differences are attributed largely to the varying measurement volumes.
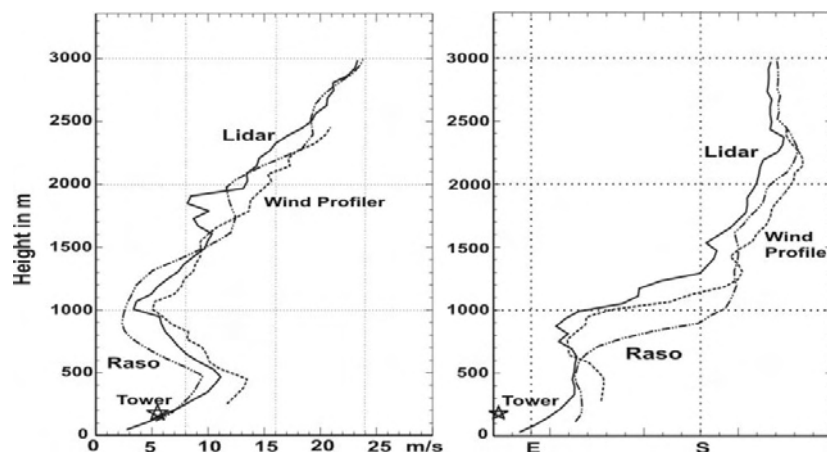
Figure 5 Profiles of wind speed (left) and direction (right) estimated by the Wind Lidar, Wind Profiler Rass, radiosonde, and tower anemometer for 7/7/04 14:00UTC

Total Precipitable Water Estimation Derived From Radio Acoustic Sounding System (RASS) During Coupling Processes Equatorial Atmosphere (CPEA) Campaign 2004

Eddy Hermawan[1] and Fikri Muhammad Abdul Wahab[2]

1) National Institute of Aeronautics and Space (LAPAN) Bandung, Indonesia
2) Meteorology and Geophysics Department of Bogor Agriculture University (IPB) Bogor, Indonesia

E-mail : eddy@bdg.lapan.go.id

Extended Abstract

Estimation of Total Precipitable Water (TPW) in the lower troposphere at Bukittinggi in West Sumatera, Indonesia (0.2^0 S; 100.3^0 E) with good time and spatial height resolution has been done. We used the Radio Acoustic Sounding System (RASS) data when we estimated the TPW parameter during the Coupling Processes Equatorial Atmosphere (CPEA) Campaign started from April 10 to May 9, 2004 by applying the Weisner et.al (1970) method. We also analyzed the *Boundary Layer Radar* (BLR) data when we investigated the updraft and downdraft air mass activities from surface up to 5 km as shown in **Fig. 1** below.
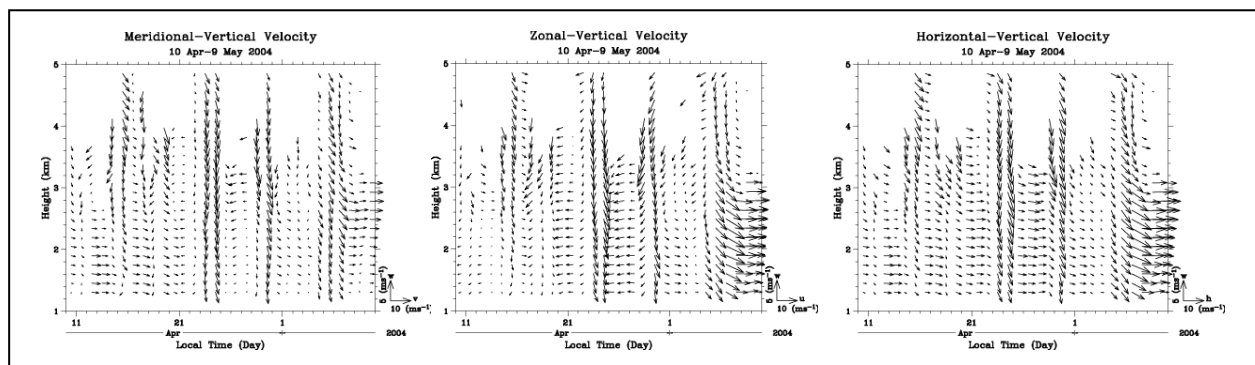
Fig. 1. The time-height section of meridional-vertical, zonal-vertical and horizontal-vertical wind velocity observed by BLR during the CPEA campaign from 10 April to 9 May, 2004 at Kototabang

From **Fig.1** above, we can see that the downward of wind velocity were occurred in two times on 24 April and 5 May, 2004, respectively as show in **Fig. 2 a** and **b** below.
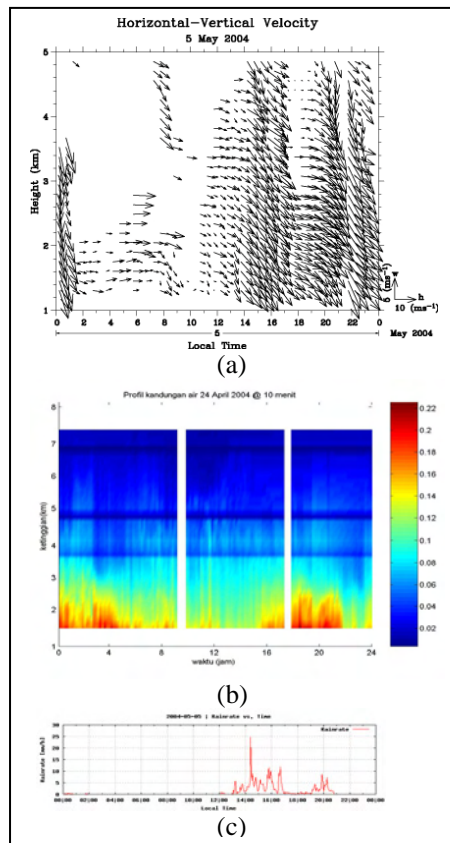
Fig. 2.a. As the same as Fig 1, but for the horizontal-vertical wind velocity on 24 April 2004
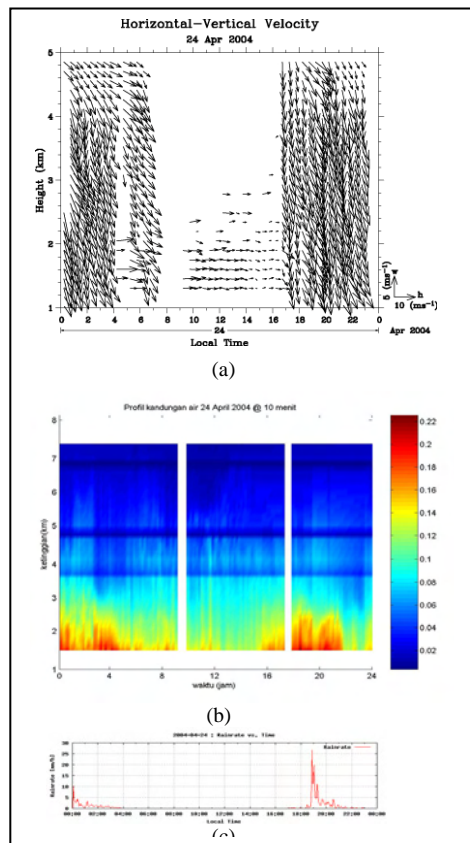
Fig. 2.b. As the same as Fig. 2.a, but for 5 May 2004

Concerning a single column observation by applying the Cross Correlation Function (CCF) method, we found an a good agreement between BLR, RASS and radiometer data when we investigated the vertical profile of TPW parameter, especially on April 24 and May 5, 2004 are about 0.43 and 0.35, respectively. Although both values are small relatively, but they are significant statistically as shown in **Table 1** and **Figs. 3a** and **3b** below.

Tabel 1. The correlation results between rainfall and TPW on 24 April and 5 May, 2004, respectively

		Rainfall	TPW			Rainfall	TPW
Rainfall	Pearson Correlation	1	0.427(**)	Rainfall	Pearson Correlation	1	0.349(**)
	Sig. (2-tailed)	.	0.000		Sig. (2-tailed)	.	0.000
	N	144	144		N	144	144
TPW	Pearson Correlation	0.427(**)	1	TPW	Pearson Correlation	0.349(**)	1
	Sig. (2-tailed)	.000	.		Sig. (2-tailed)	.000	.
	N	144	144		N	144	144

** Correlation is significant at the 0.01 level (2-tailed).
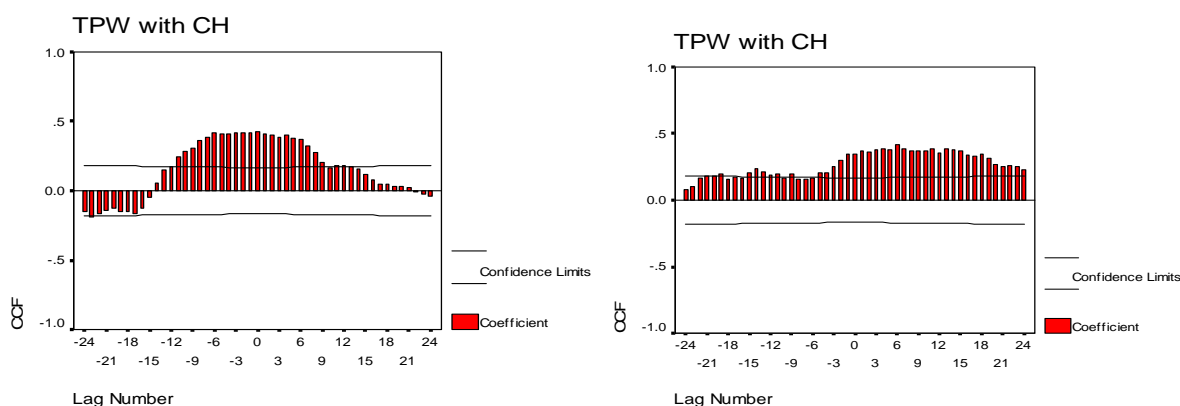
Fig. 3. The CCF value between rainfall and TPW on 24 April 2004 (a) and (b) for 5 May, 2004

From this study we can see that we need more stations for detailed statistical analysis with longer data time observations. We suspect that rainfall over this station is mostly effected by the local effect such as the Bukit Barisan mountains which covers this area.

Keywords : RASS, TPW, radiometer and BLR

Are Doppler sodar systems ready for prime time?

Ken Underwood

Atmospheric Systems Cooperation, 24900 Anza Dr., Santa Clarita CA 91355

Why is it that Doppler sodar technology is not yet fully accepted as operational instruments by national weather services, airports, etc.? Why is it that the first step in many research programs reviewing sodar technology often begins with tower-based inter-comparisons? Is there a basic distrust of sodar technology? Are there applications for which sodar technology is uniquely positioned?

The author examines these questions (and many more) by considering sodar technology, boundary layer applications and user expectations.

Robust estimation of spectral peak position for Doppler systems

Bradley, Stuart

Physics Department, University of Auckland, New Zealand (s.bradley@auckland.ac.nz)

Abstract

We formally analyse the formation of a noisy spectrum in a remote sensing system having a shaped-envelope pulse where the echo return signal strength is height-dependent and in which each scattering volume comprises an ensemble of Doppler-shifting reflecting elements. This leads to a scheme in which the spectral peak position can be optimally estimated using a weighted quadratic least squares fit. Our analysis is performed in three separate ways: theoretically; via computer simulation; and via analysis of operational field data. In addition to providing error estimates, we are able to prove a method for significantly improving peak position estimation.

1   Introduction

Doppler remote sensing systems require estimation of the position of the spectral peak in the presence of noise (Gaffard et al., 2006).. The method described below is based on that used by Metek, although other methods were also evaluated in the course of this work. Unfortunately page limitations here preclude a detailed review, or full coverage.

2   Theory

A sinusoidal signal $s(t) = h(t)\cos(2\pi f_T t)$ is transmitted during $0 < t < \tau$, where f_T is the transmitted signal frequency and $h(t)$ is the pulse envelope. The Doppler echo signal received from an atmosphere of reflectivity profile $g(z)$ by an array of M microphones spaced d apart, is a voltage $v(t)$ containing noise voltage $e(t)$, whose spectral density can readily be shown to

be

$$\frac{dV}{df} = \int_{-\infty}^{\infty} v(t)e^{-2\pi j f t} dt \approx MS(f)G(\kappa) + \frac{dE}{df} \qquad (1)$$

where S, G and E are the Fourier transforms of s, g and e and κ is a spatial wavenumber equal to twice the acoustic wavenumber divided by cosine of the zenith angle. Using an FFT, a discrete spectrum is obtained at N_f frequencies f_i, spaced by Δf and we write V_i for $(dV/df)_i \Delta f$ etc. where, for Gaussian-distributed E_i, the probability of recording a spectral amplitude magnitude between $|V_i|$ and $|V_i| + d|V_i|$ is a Gaussian of width σ_E centred on $\overline{|V_i|}$. The power spectral estimate at f_i is $P_i = V_i^* V_i = |V_i|^2$ and the resulting probability distribution gives $\overline{P_i} = \overline{|V_i|}^2 + \sigma_E^2$. In other words, there is a systematic *overestimate* of the power spectral value by the noise power quantity $\overline{N} = \sigma_E^2$. Consequently, we subtract from the spectrum an estimate, $\hat{N}$, of the mean power level when no signal is present (i.e. from the highest range gates) giving a *reduced power spectrum* $P_i' = P_i - \hat{N}$. This results in moments $\overline{P_i'} = \overline{|V_i|}^2$ and $\sigma_{P_i'}^2 \approx 2\overline{N}(2\overline{P_i'} + \overline{N})$. Various pulse envelope shapes are used, but all allow $\overline{P_i'}$ to be represented as a Gaussian of amplitude P_{max} and width σ_f centered on frequency f_D. For example, $h(t) = h_0$ gives $\sigma_f \tau \approx 0.37$, and a Hanning envelope gives $\sigma_f \tau \approx 0.62$. If the nearest spectral frequency to the peak position is labelled f_0, and we write $i = (f_i - f_0)/\Delta f$ and $y_i = \ln(P_{ref}/\overline{P_i'})$ then $y_i = a + ri(2\varepsilon + i)$ is quadratic in index i and linear in parameters $a = (f_0 - f_D)^2/(2\sigma_f^2) - \ln P_{max}/P_{ref}$, $r = (\Delta f)^2/(2\sigma_f^2)$ and $\varepsilon = (f_0 - f_D)/\Delta f$. These parameters are readily rearranged to give peak power P_{max}, Doppler frequency f_D and spectral

width σ_f. Least-squares is used to estimate the three coefficients of the quadratic using $2Q+1$ points centred around f_0 (typically $Q = 2$ or $Q = 3$). We use an odd number of fitting points because explicit solutions for parameters and their variances can be written in terms of simple known sums over powers of integers and many terms are zero. The uncertainties in the estimated parameters all depend on

$$\sigma_{y_i}^2 = \sigma_{P_i'}^2 / \left(\overline{P_i'}\right)^2 = 2\hat{N}\left(2\overline{P_i'} + \hat{N}\right)/\left(\overline{P_i'}\right)^2 = 2\left[1 + 2\left(\overline{P_i'}/P_{max}\right)SNR\right]\left(\overline{P_i'}/P_{max}\right)^{-2} SNR^{-2} \quad (2)$$

where the signal-to-noise ration is $SNR \approx P_{max} / \hat{N}$. The *relative* uncertainties in P_{max}, f_D, σ_f and σ_{SNR} depend on the 4 quantities r, ε, Q and SNR. The length of the time series included in the Fourier transform is generally around one pulse length, and this means that typically $\Delta f^{-1} \approx \tau$ and r ranges from 1.3 for a Hanning window to 3.7 for an un-windowed time series. Generally $Q = 2$ or 3. The average value of ε is 0 and the rms value is 1/6.

3   Results

Fig. 1 shows relative uncertainties vs *SNR* for the unweighted least-squares case.
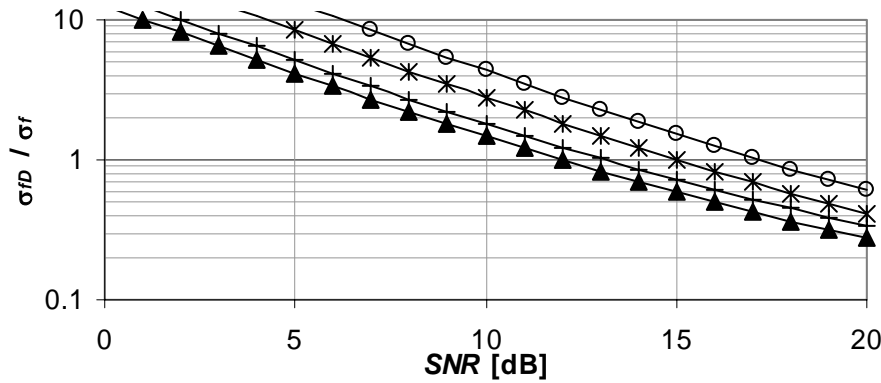
Figure 1. Relative error in signal spectrum peak value. Five-point fit with peak at a spectrum frequency, $\varepsilon = 0$, $r = 1$, $Q = 2$ (plus sign); five-point fit with peak 1/3 of the distance between spectrum frequencies, $\varepsilon = 1/6$, $r = 1$, $Q = 2$ (circles); seven-point fit with peak at a spectrum frequency, $\varepsilon = 0$, $r = 4/9$, $Q = 3$ (triangles); and seven-point fit with peak 1/3 of the distance between spectrum frequencies, $\varepsilon = 1/4$, $r = 4/9$, $Q = 3$ (crosses).

With the constraint that the width of the fitted points is the same for $Q = 3$ as for $Q = 2$, the uncertainties for these two cases are not very different, with a maximum factor of about 3/2 improvement when $Q = 3$. In all cases the dependence of uncertainty on *SNR* can be approximated from (2) as SNR^{-1}. Quite large *SNR* values of around 15 dB are required to obtain an estimate of spectral peak position to within the signal spectral width. For a system having a $\tau = 0.05$ s pulse at transmitted frequency $f_T = 4500$ Hz, this corresponds to a resolution in radial velocity component of 0.75 m s^{-1}. For this reason, it is generally necessary to perform such curve fitting over a large number, N_{av}, of spectra to obtain reduction in uncertainty by $N_{av}^{1/2}$. For example, and using the system parameters as above, if $N_{av} = 40$ then the uncertainty in radial velocity reduces to around 0.1 m s^{-1}.

After obtaining the N_f samples, a further N_+ zero-voltage values can be appended to the time series samples before performing the FFT. This changes the spectrum step to $\Delta f = f_s / (N_f + N_+)$ and, with Hanning windowing, $r = 1.3(1+N_+/N_f)^{-2}$. This process does not change the *SNR* since no extra signal power or noise power is introduced and signal and noise are reduced in equal amounts in the reduced spectral intervals. However, more points are provided around the spectral peak for the fitting process, giving improved peak position resolution. The choise of $N_+ \approx 2N_f$ gives a good distribution of data points across the quadratic signal peak. The measurement errors for the log-spectrum are greater in the wings of the

signal spectral peak. This suggests use of weighted least squares fitting using weights of $\sigma_{y_i}^{-2}$ (an iterative process is used to determine weights). It is found that weighting improves estimates even more than zero-padding. The above statistical moments theory was tested via a Monte Carlo code. The main conclusion is that padding the time series will give improved peak frequency estimates, but if padding is used, there is little advantage in using weighted fits. The methods were also applied to *raw* spectral data recorded from a Metek SODAR/RASS sampled at 44100 Hz. Fig. 2 shows a power spectrum (P_i values) from the range gate centered at 197 m. Estimation of *SNR* using the wings of the spectrum around the peak value gives *SNR* = 8 dB. Points for both the unpadded case and with padding to 3 times the original length are shown. It can be seen that padding simply interpolates, as expected.
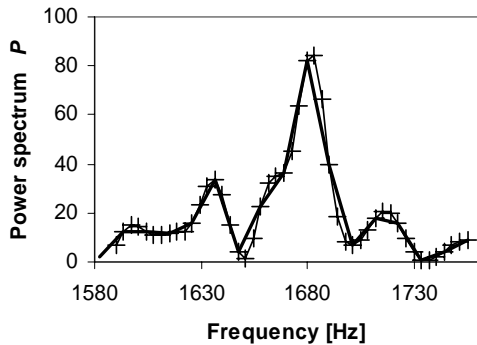
Figure 2. A local spectrum taken from range gate 13 (height 197 m) and for which the estimated *SNR* is 8 dB. No padding (dark line); and padding with $N_+ = 2N_s$.
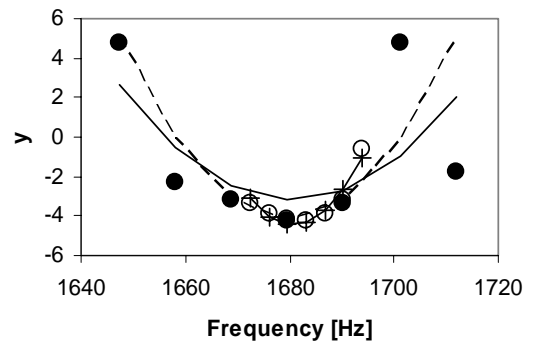
Figure 3. Plot of log corrected power spectrum from data in Fig. 2 and with Q =3. Data with no padding (dark dots); unweighted fit with no padding (solid line); weighted fit with 3 iterations and no padding (dashed line); data with $N_+ = 2 N_s$ (open circles); and unweighted fit to padded data (line with plus marks).

In Fig. 3 the data values y_i for the quadratic fit are shown with unweighted and weighted Q=3 fits for both unpadded and padded cases. There is not much difference between the 4 cases, except for some refinement in σ_f estimation. However, it is evident from Fig. 3 that the goodness of fit is improved for the padded case. These results are summarised as follows:

	unpadded		padded	
	unweighted	weighted	unweighted	weighted
f_D [Hz]	1681±2	1680±1	1681±2	1681±2
σ_f [Hz]	9.7±0.9	7.5±0.9	5.1±1	5.7±1

4   Discussion, Conclusions, and Outlook

A systematic method for estimating spectral moments is developed theoretically and then tested via simulated random data and against actual field data. One advantage of this approach is that it provides formula for obtaining *a priori* estimates of the effects of various design decisions. There is strong evidence that zero-padding the samples for a range gate will give better estimates of moments, not because of any improvement in SNR, but because of better numbers of sample points near the spectral peak.

Literature

Gaffard, C., Bianco, L., Klaus, V., Matabuena, M., 2006: Evaluation of moments caculated from wind profiler spectra: A comparison between five different processing techniques., Met. Zeitschrift, **15**, 73-85.

SODAR Measurements of Wing Vortex Strength and Position

Bradley, Stuart[1]; Mursch-Radlgruber, Erich[2]; von Hünerbein, Sabine[3]

[1]Physics Department, University of Auckland, New Zealand (s.bradley@auckland.ac.nz)
[2]Institute of Meteorology, University of Natural Resources and Applied Life Sciences, Vienna, Austria
[3]Institute of the Built and Human Environment, University of Salford, Salford, UK

Abstract

A method is described for real-time visualisation of aircraft wing-tip vortices based on measurement data from a line array of SODARs. A grid of velocity estimates is obtained every 2 s at 25 m horizontal spacing and 10 m vertical spacing. The data comprising each velocity field 'snap-shot' are then fit, using non-linear least-squares, with a simple vortex model. The best fit for each velocity field image gives estimates of vortex pair strength and position, together with estimates of the accuracy of these parameters. It is found that estimates of position and spacing can be obtained to around ± 4 m and of vortex circulation to ± 50 m^2 s^{-1}.

1   Introduction

The safe spacing between flight path aircraft is largely determined by the general downwash following each aircraft due to its wing tip vortices. Current methods for vortex detection and estimation of strength, such as various RADAR, LIDAR and massive microphone array configurations, are generally expensive and complex. Gerz et al. (2002) summarize the state of the art for LIDARs, commenting that LIDAR seems to be the only technology capable of operating reliably under most meteorological conditions but not in fog or heavy rain, and extensive post-processing may be required.

SODARs are inherently short-range instruments, operate in fog and clean air, and provide information relating to turbulent eddy dissipation rate (closely linked to vortex decay). Burnham and Rudis (1997), and Mursch-Radlgruber, et al. (2004) show that SODARs can usefully record wing vortex dynamics, and Bradley et al. (2006) has shown that data availability is likely to be higher for this application than for conventional SODAR applications.

The purpose of this current paper is to show how the wind field data collected from an array of SODARs can be integrated into a comprehensive vortex visualisation and quantitative assessment tool.

2   Methodology

Four centrally-controlled vertical-beam SODARs are spaced 25 m apart in a line perpendicular to, and on one side of, the flight path about 1.5 km from the touch-down point (Fig. 1).
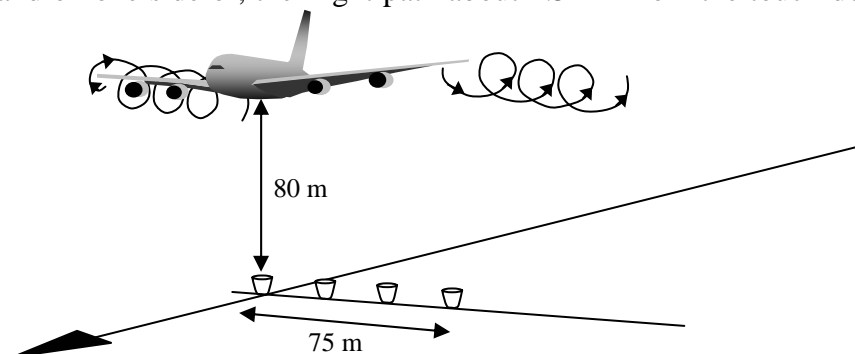
Figure 1. The configuration of the 4 SODARs in the array

The velocity field is dominated by pairs of vortices which are part of the bound vortex of circulation Γ providing lift on the wings. The tangential velocity v_θ at radius r around each vortex can be approximated by the potential flow form

$$v_\theta = \frac{\Gamma}{2\pi\, r}.$$

The pair of vortices interact, forcing each other downward. Similarly the zero vertical velocity condition at the ground can be thought of as due to a pair of image vortices below the ground, and these interact to force the vortex pairs apart. The vortex structure also interacts with the atmosphere, so measurements are required of the vortex pair spacing s, and centre position (x_c, z_c) over time.

Here we model the velocity field as comprising a 4-vortex structure, and fit the resulting model to the SODAR velocity field to obtain the parameters Γ, s, x_c, and z_c. The model velocity field is also smoothed by taking into account the SODAR scattering volume size. The model, which is non-linear in its parameters, is fit to the data using a non-linear least squares routine.

3   Results

A 45-minute time series of vertical velocities from the four SODARs was analysed. The record was visually searched for sequences of around one minute which appeared to contain vortices. In this way the start and end times for 20 such sequences were identified and initial guesses of $x_c = 20$ m, $z_c = 65$ m, $\Gamma = 150$ m^2 s^{-1}, and $s = 20$ m were used.

The mean event rms residual vertical velocity error was 0.83 m s^{-1}. For comparison, rms vertical velocities were calculated from non-event times, giving 0.48 m s^{-1}. This 'natural' variation is partly due to actual vertical velocity fluctuations, and partly due to statistical errors in velocity retrievals caused by background noise in the SODAR signal. SODAR Doppler spectra are usually averaged over typically 40 profiles, but in this application velocities are estimated from each separate spectrum, giving relatively large random errors in the vertical velocities. The least squares model is contributing about 0.34 m s^{-1} rms velocity error. Considering that volume-averaged vertical velocities due to vortices will often be greater than 3 m s^{-1}, the model is contributing of order 10% error to these peak values.

Fig. 2 shows a typical time series of estimated Γ values for an event. Parameter estimation uncertainties are shown as error bars. The low values of Γ at the start of the event may be due to incorrectly identifying the event start time. In this example there is little development of Γ with time.
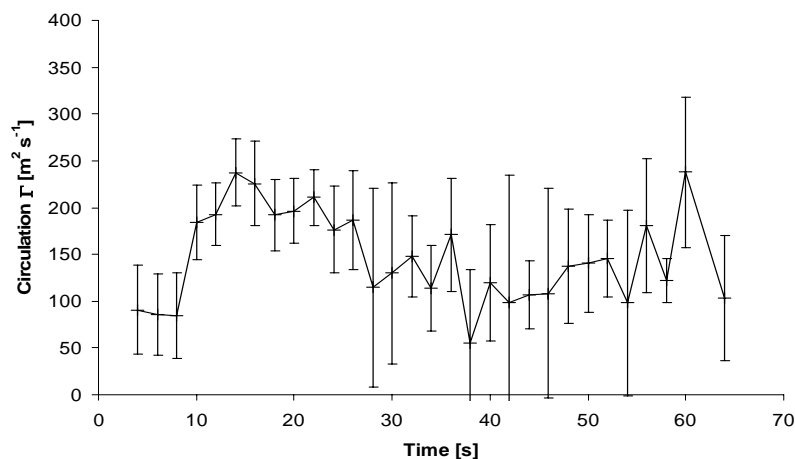
Figure 2. A typical development of vortex strength Γ during an event. Error bars show parameter uncertainties.

Fig. 3. shows estimated vortex spacing s and height z_c for an event. In this case z_c falls rapidly initially and then more slowly, whereas s increases slowly initially and then more rapidly, as expected. The overall rate of vortex descent is about -0.7 m s^{-1}, although we do not actually know the type of aircraft involved.
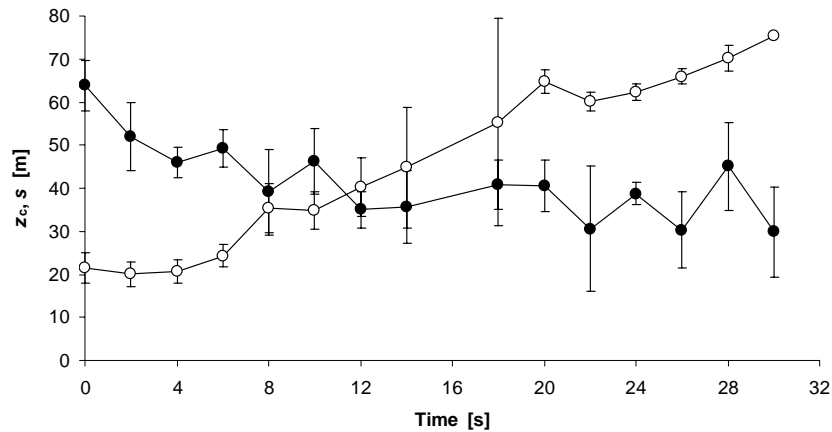
Figure 3. An example of the evolution of vortex height (filled circles) and half-spacing (open circles) in which the spacing increases substantially.

Over the 20 events, the mean parameter uncertainties were 50 m^2 s^{-1} for Γ, 5 m for s and 4 m for postion.

4 Discussion

The temporal resolution (2 s) of this configuration is very good in comparison with other vortex measurement approaches. However, the horizontal spatial sampling (25 m) of the vortex flow has been restricted by the number of available SODARs and is quite large compared to the characteristic scale of a typical aircraft wing vortex. Hahn (2002) finds that the core is about $\pm 0.07s$ or about ± 2.5 m wide, which agrees with LIDAR measurements (Coustols et al., 2004). Consequently, finer spatial resolution than, say, 2 m in the vertical, will probably not yield increased information about the vortex structure.

In this paper we have developed a simplistic potential flow four-vortex model which allows us to put in context these spatial and temporal sampling scales. The position and spacing of the vortex pair was determined to about 5 m, and vortex strength to around 25%: uncertainties which are adequate for air traffic purposes.

Literature

Bradley, S. G., S. von Hünerbein, S., and K. H. Underwood, 2006: Operational reliability and accuracy of SODARs in wing vortex characterization. *12th ARAMS*, Atlanta, Georgia, 5pp.

Burnham, D. C. and R. P.Rudis, 1997. JFK-1 Wake vortex sensor intercomparisons. *1st NASA Wake Vortex Dynamic Spacing Workshop,* NASA/CP-97-206235, L. Credeur and R. Perry, ed., NASA Langley Research Center, Hampton, VA, 333-341.

Coustols, E., L. Jacquin, F. Moens and P. Molton, 2004. Status of ONERA Research on Wake Vortex in the Framework of National Activities and European Collaboration. ECCOMAS 2004, Finland.

Gerz, T., F. Holzäpfel, and D. Darracq, 2002: Commercial aircraft wake vortices. *Progress in Aerospace Sciences*, 181-208.

Hahn, K. U., 2002. Coping with wake vortex. *ICAS* 2002.

Mursch-Radlgruber, E., S. G. Bradley, and S. v. Hünerbein, 2004: Vortex Detection And Ranging (VODAR). *Proc. 12th Int. Symp. Ac. Rem. Sens.*

A Modular PC-Based Multi-tone Sodar System

D. Contini [1], F. M. Grasso [1], G. Dargaud [2], G. Mastrantonio [2], A. Viola [2], U. Bonafè [3]
CNR-ISAC, Istituto di Scienze dell'Atmosfera e del Clima, [1] Lecce, [2] Roma, [3] Bologna, Italy
d.contini@isac.cnr.it

Abstract

In this work we describe a new modular multi-tone sodar system based on and entirely controlled by a PC. The system uses two synchronised I/O cards and a specifically developed software to handle all the function of the sodar including on-line processing of data. The system is sufficiently versatile that it can be used as sodar or minisodar with a minimum of external electronics. An example of the results with the system used as minisodar is reported.

1   Introduction

The system that is presented is a multi beam Doppler sodar, where all functions are handled by a PC in which two commercial I/O cards are used for the timing of all sodar functions, for the generation of tones, and for the echoes acquisition. All these functions are accomplished under the PC supervision with an appositely developed program that has the capabilities of on-line processing as well as post-processing and also data simulation. If appropriate antennas are available, the system may operate using high frequencies (as a minisodar) or low frequencies (as a standard sodar), by emitting tones of different frequencies in the suitable directions. Up to four antennas can operate simultaneously and the signal on each channel is acquired, digitally filtered and post-processed separately. The external electronics is minimized by using only a simple antenna preamplifier and a commercial power amplifier (for burst generation) at each antenna/beam. A decreasing of maintenance and of spurious electronic problems is expected with the reduction of the electronics.

2   Instrumentation

A scheme of the system developed is reported in Fig. 1(a) and it is based on a PC with 2 acquisition cards (NI-PCI4451). Each card controls two sodar channels and has two analog inputs, two analog output channels and several digital I/Os. For each channel a 16 bit I/O converter is used to record each echo, so that a dynamic range of about 96 dB is obtained. The 2 interconnection boxes do not contain electronics but they are simply electrical connections that reroute the different signals acting as interface between the PC, the commercial power amplifiers (Crest FA4) and the antenna pre-amplifiers, simultaneously providing electrical test points to monitor the operations of the different parts of the system. It also furnishes the electrical power to the pre-amplifier directly from the main board of the PC. For each channel/beam, echoes are independently over-sampled, digitally filtered, eventually decimated and analysed to retrieve the Doppler information. For each step a window that shows the details of the process is available on the screen, so that the digitised and filtered signal, the FFT, the facsimile intensity record, the vertical wind field and averaged quantities may be visualised in real time. The spectrum resulting from each FFT application is analyzed and for each antenna-channel the radial velocity is obtained, by using the two step procedure described by Mastrantonio and Fiocco (1982). Several subroutines have been included that allow wind velocity and direction calculations as well as time-averaging of results that could be saved on independent files and figures. The software allows the presence of periods of passive acquisitions in which the transfer function (TF) of each transducer is evaluated. The TF are successively used to take into account the variation of the transducer response as a function of the frequency during calculation of radial wind velocities. This procedure reduces random errors on velocity measurements (Contini et al, 2004). The system can perform a

decimation of the acquired signals, after digital filtering, in order to cope with two opposite needs: high frequency acquisition of the echoes and a reasonable amount of data to be post-processed on line and to be saved in the raw data files. The only piece of non-commercial electronics is the antenna pre-amplifier that has been developed at ISAC-CNR. It has a digital part that performs an electronic switch between reception and transmission state, based on a "burst" analog signal and a digital control coming from the PC. During transmission state the pre-amplifier is an open gate for the pulse going to the antenna transducers. After the switching on reception state, the echo signal coming from each antenna is processed by three stages of amplification. The first stage is composed by a transformer coupled with a low noise amplifier, while the second stage is an active pass-band filter (type Sallen-Key) planned to give a uniform answer in the range 1300-4000 Hz. Finally a third output stage, which also acts as a buffer, is able to furnish up to 100mA to the external load. In this last stage a logic net allows to select one of five total gains available, from 80 dB to 100 dB. The gain of the preamplifier is controlled by the PC through the digital lines of the acquisition card, therefore it is possible to use an automatic selection of the preamplifier gain in order to use, in each environmental condition, the maximum possible dynamic range during digitalisation of the signals. A photograph of the pre-amplifier card is reported in Fig. 1(b) and it shows that the electronics is placed in a metal box with rain-protected connectors.
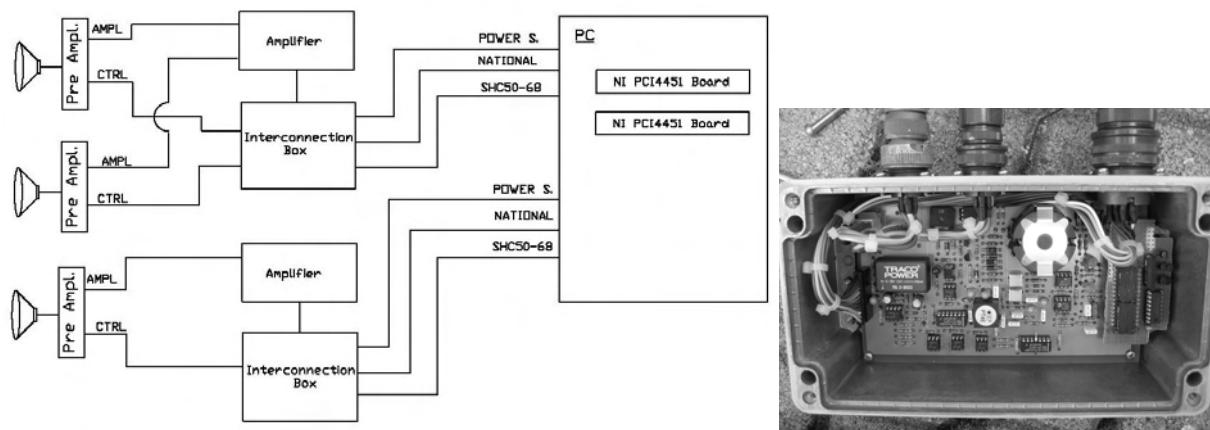
Figure 1. Schematic of the 3-channel sodar system (left). Photo of the preamplifier card (right).

TIME (LST) – 15/05/2005 - Lecce, Italy
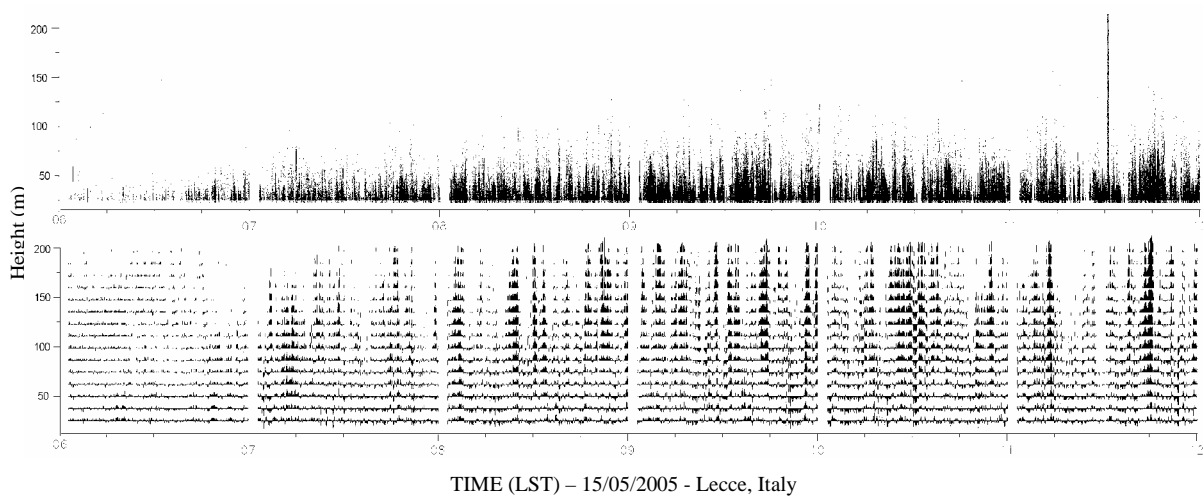
Figure 2. (a) Example of fax plot of the vertical antenna. (b) Corresponding plot of the vertical wind velocity.

3   Results

As a first application the system was equipped with a single vertical minisodar antenna. The antenna (77 cm in diameter and 140 cm tall) was placed, during April and May 2005, at the experimental field of the Lecce Section of ISAC-CNR and it was equipped with a transducer (Electro-Voice DH7). The system was emitting pulses at 4000 Hz (0.1 s long) with a 2 s repetition rate. The system was programmed to acquire 28000 points at 20000 Hz and a decimation factor of 6 was used after filtering with a Butterworth digital filter (30th order) with a pass-band between 3800 Hz and 4200 Hz. The evaluation of the Doppler shift was performed on 18 range gates with a vertical resolution of about 13.4 m. The search interval for the Doppler shift was 400 Hz and the computational interval was 130 Hz. An example of results, referring to the sunrise of 15th May 2005 is reported in Fig. 2, where the facsimile intensity record is shown together with the vertical wind velocity. Only data with a S/N greater than 0.75 have been included in the figure. The S/N was calculated according to the procedure reported in Mastrantonio & Fiocco, (1982). The three minutes of passive acquisition for the evaluation of the TF are visible at the beginning of each hour. In the figure the growth of thermal turbulence with the relative generation of convective structures is visible. Results indicate that the system is correctly working and several tests of the system used as a low frequency sodar (not shown) bring to the same conclusion. The ability to work in a wide range of frequencies and situations make the system versatile for boundary-layer research.

4   Discussion, Conclusions, and Outlook

In this work a multi-tone modular sodar system entirely based on a PC equipped with commercial acquisition cards is presented. The system works under the supervision of a software developed at ISAC-CNR using the LabWindows CVI platform. The PC controls all sodar functions including the antenna preamplifiers that have been appositely developed. A decrease of maintenance and of spurious electronic problems is expected with the reduction of the electronics as well as an increased capability to operate in adverse environments. The system could be further developed in the future and it is open to several possibilities. For example, the employment of acquisition cards with on-board capabilities of Digital Signal Processing (DSP) could reduce the time necessary for on-line processing, allowing an increase in the data rate. This could be useful in turbulence analysis. Another development could be based on network capabilities of the platform used to develop a complete remote control of the sodar system. It has also to be put in evidence that some of the system performances could actually be improved, at relatively low cost, with the evolution of the commercial PC without any significant change in the system.

Literature

Contini D., Mastrantonio G., Viola A., Argentini S. 2004: Mean Vertical Motions in the PBL Measured by Doppler Sodar: Accuracy, Ambiguities, Possible Improvements. *Journal of Atms. And Ocean. Techn.*, **21**, pp. 1532-1544.
Mastrantonio, G., G. Fiocco, 1982: Accuracy of wind velocity determinations with Doppler Sodar. *J.Appl.Met.*, 21, pp. 820-830.

Acoustic tomography for estimating temperature and wind flow

Ivana Jovanović[†], Luciano Sbaiz[†] and Martin Vetterli[†§]

[†] School of Computer and Communication Sciences, Ecole Polytechnique Fédérale de Lausanne (EPFL),
CH-1015 Lausanne, Switzerland

[§] Department of Electrical Engineering and Computer Sciences, University of California at Berkeley (UCB),
Berkeley, CA 94720, USA

email: {ivana.jovanovic, luciano.sbaiz, martin.vetterli}@epfl.ch

Abstract

We consider the problem of reconstructing superimposed temperature and wind flow fields from acoustic measurements. A new technique based solely on acoustic wave propagation is presented. In contrast to the usual straight ray assumption, a bent ray model is considered in order to achieve higher accuracy. We also develop a lab size experiment for temperature estimation.

1   Introduction

Tomography is generally defined as a method that recovers an unknown multi-dimensional field from the interaction between the considered medium and radiation emitted through it. The fact that the sound propagation is strongly influenced by wind and temperature enables the use of acoustic tomography methods in determining these meteorological quantities. The temperature field reconstruction is a scalar tomography problem. Under quite general conditions, acoustic time of flight data typically provide the information needed to solve this problem. The reconstruction of wind field, however, is a vector tomography problem where the time of flight measurements are not sufficient for unique recovery of the field. Braun and Hauck [1] pointed out that time of flight measurements only allow to reconstruct the source-free component of the vector field and they propose to estimate the remaining (curl-free) component using additional line-integral measurements. The two line integrals, referred to as *longitudinal* and *transversal* interactions, actually correspond to the integration of the tangential and normal component of the sound speed along the propagation path.

In [2] we showed that the transversal interaction can be inferred from the angle of arrival of the sound waves. Based on time of flight and angle of arrival measurements, we proposed an algorithm to entirely reconstruct temperature and wind field. The algorithm alternates between estimating the ray trajectories and the fields of interest. High reconstruction accuracy is achieved by replacing the commonly assumed straight-ray model with a bent-ray model [3].

We also developed a lab size experiment, where we focus only on estimating the temperature from the time of flight measurements. This small scale experiment aims at showing the feasibility of our acoustic tomography method, identifying the practical problems and providing the bounds on the achievable accuracy. The same setup can be extended to wind flow estimation in the case when a wind source is outside the region of interest (source-free vector field).

2   Problem statement

We consider a certain region of interest surrounded by emitters and receivers. Each emitter is sending an acoustic signal to all the receivers. We model the signal propagation using the sound ray theory. Instead of the commonly used straight ray model we take into account the ray refraction due to the wind flow and temperature gradient. In order to compute the ray trajectory we use the equations derived by Ostashev [4] for the ray path in inhomogeneous moving medium.

$$\dot{x}(s) = c\frac{b}{\|b\|} + v,$$

$$\dot{b}(s) = -\frac{c_0 \nabla c}{c} - J_v b + \frac{b \cdot v \nabla c}{c}$$

The sound speed c is as a sum of an average speed c_0 and a variation Δc, $c = c_0 + \Delta c$. In the above equations, s and x are respectively the arc length and the space coordinate measured along the ray path, J_v is the Jacobian matrix of the vector wind field v, and b is the vector with norm $\|b\| = c_0/(c + n \cdot v)$ and direction $n = b/\|b\|$ normal to the wave front. In order to compute the ray path, we use the initial conditions $x(0) = x_E$ and $b(0) = c_0/(c(0) + n(0) \cdot v(0))$. The starting point corresponds to the position of the emitter and the initial ray direction $n(0)$ is chosen such that the ray reaches the receiver. In dry air, the temperature T can be inferred from the speed of sound through the relation $c = 20.05\sqrt{T}$. More precise dependence takes into account humidity of the air and can be derived from the gas equation.

2   Iterative algorithm

We propose an iterative algorithm that can be briefly described as follows:
1. Measure the time-of-flights and the directions on the physical system.
2. Start from an initial estimate of the wind and the temperature, e.g. no wind and temperature of 20°C.
3. Compute the ray trajectories for the current estimates.
4. Compute the time-of-flights and the directions of arrival for every trajectory.
5. Compare the measurements with the simulation results and deduce the error fields.
6. Update the node variables of the estimated fields (linearizing the relations between the node variables and the measurements) and go to the step 3.

The effectiveness and convergence of the algorithm are tested on synthetic data. The true temperature distribution is shown on Fig. 1(c), while the wind speed is constant 7m/s. Around a circle with a radius of 1m we placed 8 emitters and 8 receivers. The region is divided into the tessellation cells [see Fig. 1(a)] and the temperature and wind fields are estimated at the nodal points. From the simulation results we found that the error in the amplitude of the wind speed is $\Delta v = 0.25$ m/s, or equivalently the relative error is 3.5%. In the case of temperature estimation the relative error is less than 1%. Since c and T are in one-to-one correspondence, in the simulations, we focus on estimating c. The algorithm converges after 5 iterations.

3   Experimental setup and results

In our experimental setup, 12 emitters and 12 receivers are placed around a 1m radius circle. We use piezoelectric transducers to send and receive the acoustic signal. Every emitter/receiver is equipped with one amplifier/preamplifier. The transmitted and acquired signals are interfaced with a PC by the Motu 24I/O audio card. This card provides 24, 24-bit/96kHz analog inputs and outputs. The possibility to connect 4 of them together allows extending the number of input and outputting channels to 96. Here, we remark that the spatial resolution of the reconstruction is mainly due to the number of measuring devices that we use.

We use the measurements of the time of flight between every emitter and every receiver and hence, the time delay estimation is crucial to our experiment. We choose to send a signal composed of two parts, a pure sinusoidal part at 40 kHz followed by a pseudo-random sequence modulated at 40 kHz. The peak of the correlation function between the sent and received signal corresponds to the time delay up to the sampling period. The remaining fractional delay is then computed using the phase delay of the sinusoidal part. The precision of the fractional delay depends on the length of the sinusoidal part we use and the
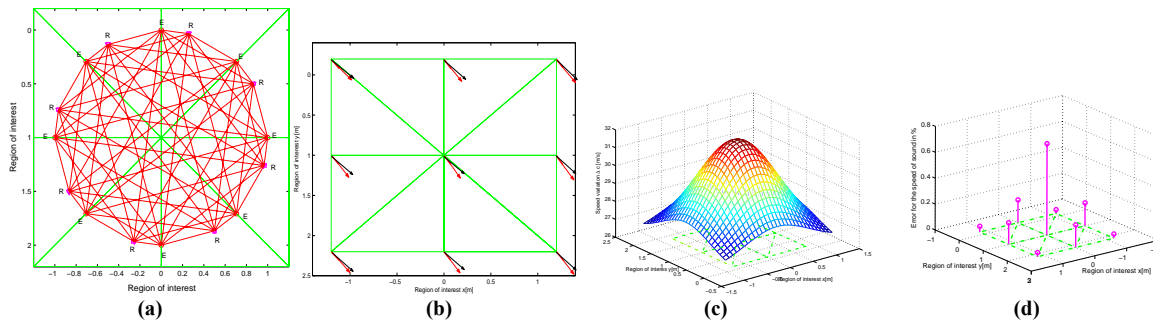
Figure 1. (a) The setup of 8 emitters and 8 receivers. **(b)** The true (ful-line) and the reconstructed (dashed) wind field. **(c)** The true Δc field. **(d)** The relative error with respect to the average speed of $c_0 = 344$ m/s.
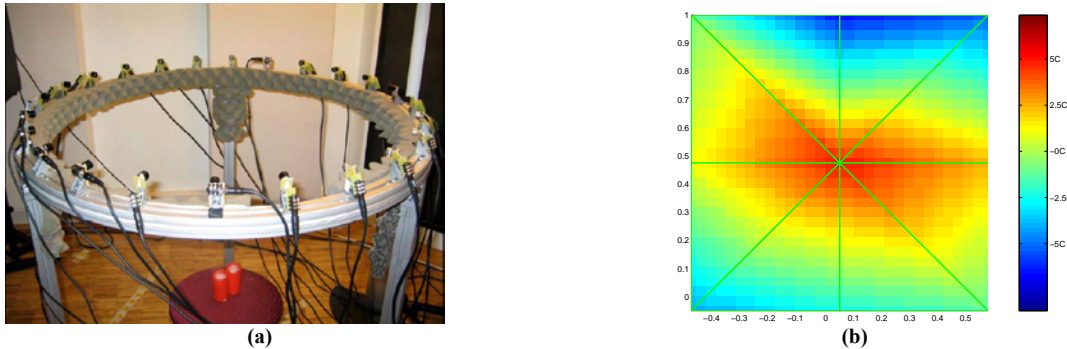
Figure 1. **(a)** The experimental setup with 12 emitters and 12 receivers. **(b)** The temperature reconstruction around the candle.

later is limited by the arrival of the first reflection. In this case, the accuracy of the time delay estimate is of the order of 1e-07s and is found as the maximum delay deviation computed from 10 consecutive measurements assuming no temperature changes meanwhile. The most difficult part is the positions and the transducers' delay calibration. To avoid complicate distance calibration we exploit the very good precision of the time delay estimates and use these measurements to compute the positions and the delays of the transducers. In this way the positions are determined up to the precision of 5mm, for the distances of 1m, and the transducers' delay within the accuracy of 1.5e-05s. Obviously, this is not enough for high precision estimation since all these uncertainties result in an absolute error of $\Delta T = 3$°C. However, the error is mainly systematic and its influence can be cancelled if we aim at estimating only the temperature variation from a fixed known temperature value. In Fig. 2 we show the experimental setup and the first experimental result. We computed the temperature distribution around a candle placed in the middle of the ring. The coarse tessellation and the strong convection from the candle limit additionally the precision and leave a considerable room for improvements.

4   Conclusions

We demonstrate the feasibility of the tomography method for estimating wind and temperature distribution and identified the practical problems. In the future work we intend to increase the precision of the temperature estimates and to add the estimation of the wind flow.

Literature

[1] Braun, H., Hauck, A., 1991: 'Tomographic reconstruction of vector fields', IEEE Transaction on Signal Processing, vol. 39, no. 2

[2] Jovanović, I., Sbaiz, L., Vetterli, M., 2006: 'Acoustic tomography method for measuring temperature and wind velocity', IEEE International Conf. on Acous. Speech and Signal Proces. Toulouse, France.

[3] Sbaiz, L., Vetterli, M., 2003: 'Acoustic flow tomography', Technical Report, LCAV-EPFL

[4] Ostashev, V. E., 1997: 'Acoustic in moving inhomogeneous media, E&FN, SPON, London

Validation of a Chirp SODAR Against a 430m Tower

Martin, Andrew,
StratoSonde Pty Ltd, Melbourne, Australia.
andrew.martin@stratosonde.com

Abstract

A 430m tower located about 200km from Melbourne is instrumented initially with 2 sonic anemometers, one at 52m and one at 429m. A newly developed chirp SODAR is co-located with the tower for the purpose of validation, calibration and assessment of data availability. The various aspects of this SODAR validation and associated error sources and error mitigation strategies will be discussed.

1   Introduction

The biggest issue facing any new SODAR measuring technology is validation of the measurements against an independent reference. There have been other concerns raised in the literature about variation of calibration with height and data availability. Because of the remote measurement capability of SODARs, obtaining a suitable reference system thus is very difficult. This paper describes the use of a 430m instrumented tower that is being used to validate a new SODAR technology using long chirp signals [1]. The new system is known as a Remote Acoustic Microstructure Profiler (RAMP).

2   Instrumentation

An acoustic linear chirp profiler that uses matched filters on four receivers operating simultaneously enables very high spatial resolution wind and turbulence profiles to be obtained to 500m. The system is showing potential to work to a minimum of 1000m in most weather conditions without loss of data. In heavy rain the EDR is not available.

Figure 1. This new RAMP instrument, recently developed in Australia, enables very high spatial and temporal resolution profiles of the boundary layer. The system consists of four receive antennas and one centre transmit antenna shown here being assembled. The centre transmit has since been replaced by four transmit antennas placed outside the receive antennas to overcome issues identified in the first testing.

The transmitted linear frequency chirp signal waveform frequency, f is simply described as; $f = f_0 + (df/dt)t$ (1) where $df/dt = B/T$ (2), T is the chirp time (typically 37 seconds), B is the chirp bandwidth (typically 1000Hz) described by; $B = f_F - f_0$ (3), f_0 is the start frequency of the chirp (typically 3000Hz) and f_F is the final frequency of the chirp. The BT product is thus 37,000 for these signal properties providing a very high system gain. The chirp is transmitted via parabolic antennas set at between 12 and 17 degrees from the vertical. The system is implemented with a co-located transmit and receive antenna in a bi-static mode

using listen-while-send techniques. This arrangement allows the dead zone to be held to around 10m even when using a 37s transmit pulse. The received signal is processed in a matched filter using cross-correlation to obtain the output phase and amplitude as a function of height $g(\tau)$ so that $g(\tau) = \int_{-\infty}^{\infty} f(t)f^*(t-\tau)dt$ (5) where $f(t)$ is the time sampled complex input data and $f^*(t-\tau)$ is the complex conjugate of the transmitted chirp signal. To measure the wind profile, the four receiver antennas simultaneously obtain Doppler vectors from North, South, East and West. These vectors are then subtracted to provide North-South and East-West phase information from which wind speed and direction vs height are easily obtained. The subtraction has the advantage of removing any common system dependent phase shifts as well as removing any common noise and interference.The tower instrumentation consists of 2 u-v sonic anemometers, one at 50m and one at 429m.

3 Errors

There are many sources of error that can compromise the performance of a SODAR. These errors are well set out in [2]. This new SODAR seeks to overcome many of the errors of conventional SODARs by using a completely different signal processing scheme as well as using long transmit pulses to increase system gain. The results of the design of this new SODAR and the associated error mitigation are set out in Table 1 (errors are set out in [2]).

Sources of calibration error	Effect of error on the new system
Geometrical	
Height estimation errors.	Corrected using ground temperature measurement.
Errors in Tilt angle.	Error cancellation by subtracting opposite beams.
Errors in scattering angle.	Error cancellation by subtracting opposite beams.
Bias in wind estimation	
Uncertainties in calibration standard.	Sitting error minimised to the West, shielding may be an issue in other directions, means and std dev used for initial analysis.
Incomplete beam data	System maintains high signal-to-noise ratio.
Variances in SODAR averages from varying number of samples.	There is no averaging of data between wind profiles.
Separation of sampling volumes.	The test sites are separated by 500m. The flat terrain of the site minimises this effect.
Different averaging schemes between SODAR and standard.	The system pulse length is 37 sec that provides a 37 second averaging of the measurement. The sonic data is also averaged for 37 sec to minimise this effect.
Noise problems	
Spectral peak position errors.	The Doppler is recovered in each range gate by accumulating the phase shift between samples and substantially removes this issue.
Loss of signal to noise ratio.	The high system gain (see 2 above) is able to maintain a high signal-to-noise ratio to the maximum range of the system.

Table 1. Table of error sources [2] and the mitigation of these errors on the new system.

4 Results

In initial testing against the tower the results were encouraging. The first measurement of speed and direction shown in Figure 2 indicates some agreement between the sonic anemometer and the profiler. Analysis of the mean and standard deviation shows that there are some problems with this system arrangement. It turns out that the greatest source of error is in the arrangement of the antennas and associated baffles. This sensitivity is due mostly to

the simultaneous N, S E, and W measurements and not to any of the errors set out in Table 1. In an attempt to isolate the errors a wind shear analysis was carried out to eliminate any effects of the ground wind that could mask system errors and is shown in Figure 3.
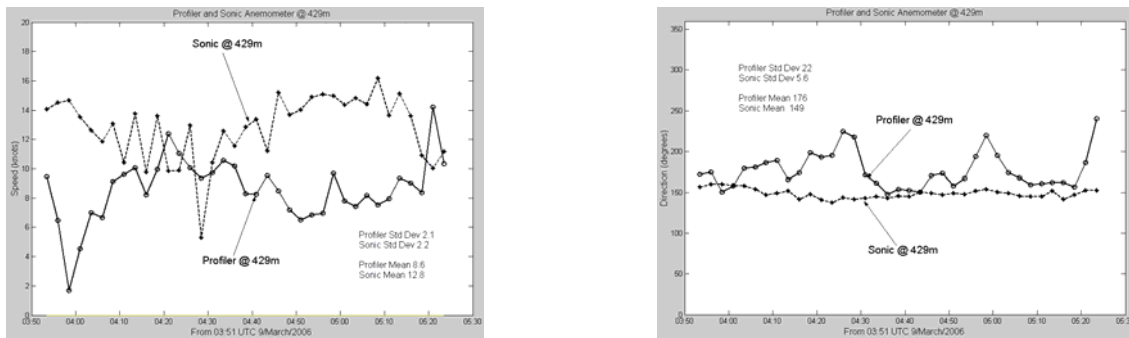
Figure 2. Wind speed and direction measurements at 429m from a sonic anemometer and the wind profiler. The profiler shows a lower speed than the sonic but with similar standard deviations. The profiler direction error is around 17 degrees and its standard deviation is about 4 times higher that the sonic anemometer.
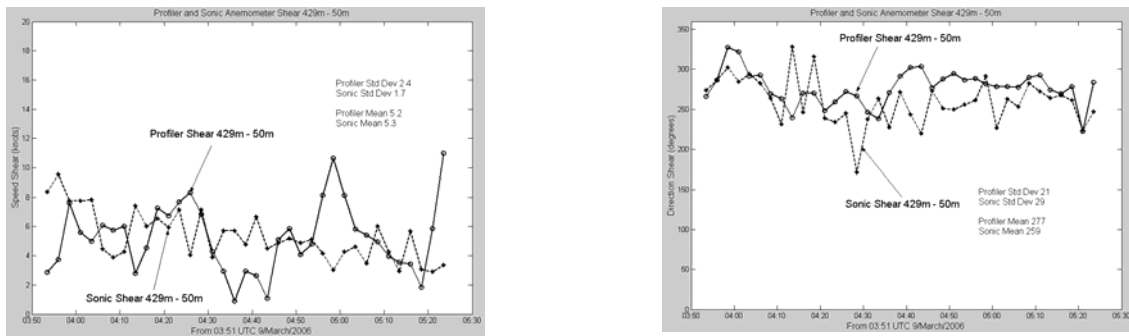
Figure 3. Wind speed and direction shear between 50m and 429m for the sonic anemometer and profiler. The speed error has now gone indicating a problem with the ground speed estimation from the local anemometer. The mean direction error of 17 degrees is still evident, the standard deviations of the direction are now similar.

From Figure 3 there appears to be a problem with the ground speed measurement as the profiler on its own shows better agreement with the anemometer. The direction error at 429m persists. In later testing in 30knot winds, this direction error was much worse and the speed error increased to 4 knots in 11 knots of shear. The system was modified to use four transmit antennas operating simultaneously. The initial results from the modified system show very good agreement of the mean wind direction and speed at 50m but there are still some differences in the standard deviations that need to be resolved.

5   Discussion, Conclusions, and Outlook

A new type of SODAR called a RAMP is showing promise for a high spatial and temporal resolution profiler to a height of 429m with potential for reliable measurements to 1000m. Many of the errors associated with conventional short pulse SODARs have been reduced by the design of the RAMP system. Significant sources of error associated with the antenna arrangement at high wind speeds are being identified and reduced.

Literature

[1]   **Martin, A., 2004,** "A new technology for SODAR providing very high resolution boundary layer profiling with small dead zone for measurements to 2000m", ISARS 2004, Cambridge, UK.
[2]   **Bradley, S.G., Antoniou, I., von Hunerbein, S., Kindler, D., de Noord, M., and Jorgensen, H., March 2005,** "SODAR calibration for wind energy applications", final reporting on WP3, EU WISE project NNE5-2001-297, The University of Salford, Greater Manchester, UK ISBN 0-9541649-1-1

Radioacoustic Sounding of the Horizontal Wind in the PBL
Does it have the Future?

Yuriy N. Ulyanov[1], Valery I. Vetrov[2] and Nina G. Maksimova[3]

1 National Technical University "KhPI", Kharkov, Ukraine (ulyanov@kpi.kharkov.ua)
2 Company Res.-and-Production Ass. "Lantan", Moscow, Russia (vetrov@lantan-npf.ru)
3 Kharkov National University of Radio Electronics, Kharkov, Ukraine (shifrin@kture.kharkov.ua)

Abstract

The paper is devoted to the potentialities of the radioacoustic sounding method when monitoring the vertical wind structure in the PBL. For RASS, it is not characteristic neither a high level of electromagnetic pollution inherent in radar wind profilers nor the fallability peculiar to the sodar ones due to the ambient sound noise. In the paper, methods of horizontal wind measurements with RASS are reviewed basing on our developments and radioacoustic wind sounding experience, as well as on the developments of other authors.

1   Introduction

Nowadays, for wind profile measurements, radar and sodar wind profilers are used almost everywhere, although two main shortages always are to be taken into consideration: significant levels of electromagnetic pollution of the environment due to radar operation, and the noise dependence of the sodar efficiency. History of the RAS method development shows that from the very beginning it was intended for remote determination of the wind field characteristics in the PBL (Smith, 1961). As compared with the radar wind profiler, RASS is capable to operate with much less power budget (as less as 40 dB), whereas, as compared with the sodar one, it is unreceptive to the ambient acoustic noise. Thus, restrictions for using such an engineering at aerodromes, populated areas and industrial zones can be removed. Thereupon we would like to share our experience in the use of the method of radioacoustic sounding of the PBL lower layer for measurements of the horizontal wind velocity and direction. The emphasis is placed on the practical realizability of different wind RAS methods.

2   Radioacoustic Wind Sounding Methods and Instrumentation
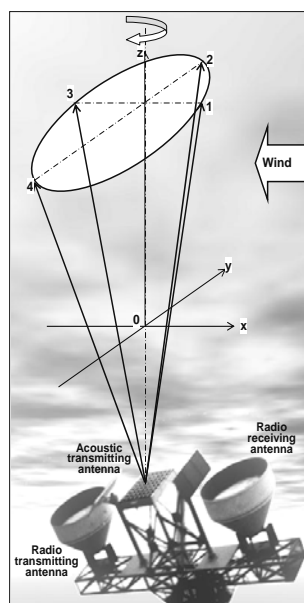
Figure1. Multiple four-direction RAS wind measuring method.

First RAS methods developed for measurements of wind profiles, in principle, did not differ from each other and were implemented with multiple radioacoustic sounding in different directions (Fig.1). *Per se,* they were like the radar elevation-distance-measuring multi-beam methods of target characterization. In spite of their theoretical high accuracy, the RAS methods did not become customary in meteorology. This is caused mainly by limitation in the RASS efficiency stipulated by wind velocity v. Already at $v > 3..5\text{ms}^{1}$, almost the complete loss of echo-signal had been observed due to the wind blowing the sounding parcel beyond the Doppler radar radiation pattern and, as a consequence, due to the drop in signal-to-noise ratio (Babkin et al, 1980). The situation was essentially improved, i.e. the range of wind velocities to be measured was widened owing to the RASS designed with the sound source moving along the wind horizontal projection (Babkin et al, 1987). This provided a basis for a new RAS method (Fig. 2), wherein a rate of change of the echo-signal envelope was used as the source of information (Maksimova

et al, 1988).

 The method efficiency was restricted by conditions of the weak dynamic turbulence typical for the nocturnal PBL. In addition, an error of the wind measurements was increasing and exceeding ±0.5 ms^{-1} with the increase of the vertical wind shear (Vetrov et al, 1997). This techinque did not become widespread due to its low efficiency and limitation in the maximum measured horizontal wind velocity (of 8..10 ms^{-1}).

In order to remove the constraints and to heighten the RASS efficiency, the method of inclined RAS (IRAS) has been developed. It unites the wind adaptation and wind measurements (Ulyanov et al, 2000). The adaptation method by means of inclined sounding is grounded on the peculiar deformation (stipulated by the wind influence) of initially spherical equiphase surfaces: as a result of the wind action, the wave front takes the form of the ellipsoid surface flattened out and elongated in the wind direction (Fig.3). On the surface, there are two regions capable reflect and focus radio waves into the point of initial radiation of acoustic and electromagnetic oscillations. Both regions are crossed with the azimuthal plane

Figure 2. Wind RAS method with a movable acoustic source.

whereon the local horizontal wind vector lies. When radiating and receiving radio pulses from the same point in the plane of the local horizontal wind, that is down wind and against it, the difference in Doppler shifts ($\Delta\Omega_D$) of the reflected radio signals appears to be as much as possible ($\Delta\Omega_D = \Omega_{D1} - \Omega_{D2} = \max$), as compared with sounding in other azimuthal planes.
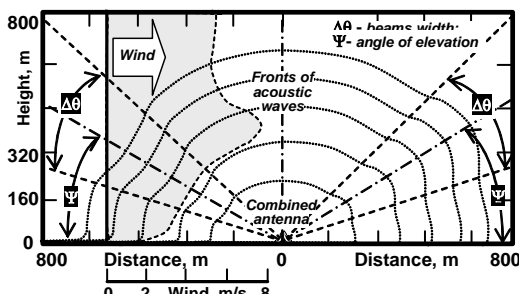
Figure 3. IRAS method concept.

Under conditions of the real PBL, this appears to be possible, when realizing inclined sounding with the system having matched phase centres for acoustic and electromagnetic radiation in the interval of elevation angles $\Theta = (40° \div 45°) \pm 15°$. In the given method, at circular sounding, at EM wavelength λ_e, a value of azimuth, for which the difference in Doppler shifts reaches maximum ($\Delta\Omega_{Dmax} = \Omega_{Dmax} - \Omega_{Dmin}$), is being selected, and the local wind is being calculated by the formula: $V_H = \lambda_e \Delta\Omega_{Dmax}/(8\pi\sin\alpha)$.

For implementation of the method described above, it was necessary to have developed a special combined acoustic-electromagnetic antenna (Fig. 4) with the increased noise-immunity for operation at small elevation angles (Ulyanov et al, 2001).

5. Construction of the combined static antenna.

The RASS efficiency being low in such a variant of the
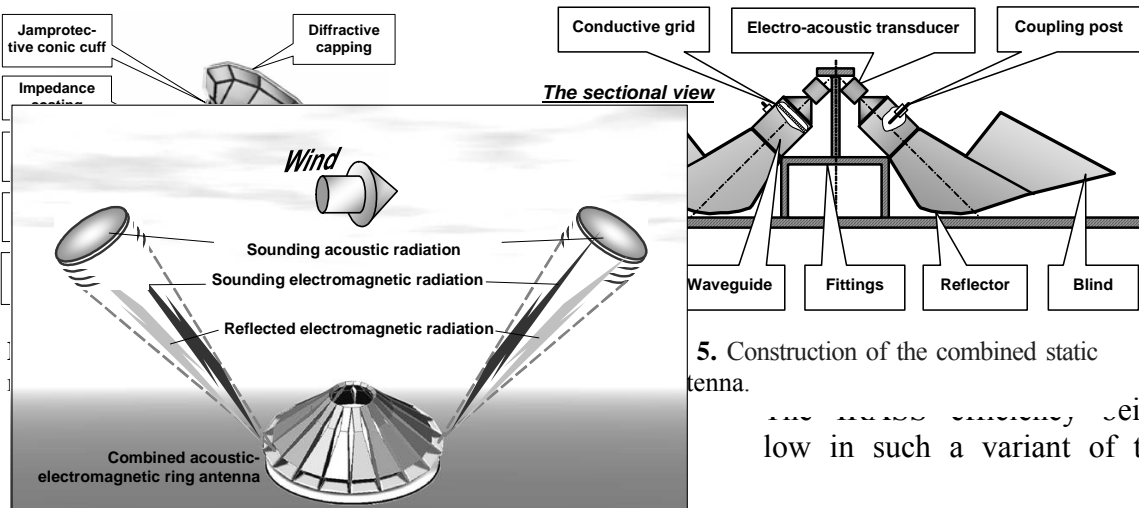
Figure 6. Wind IRAS method with static combined ring antenna.

IRAS method implementation can be heightened, when using the static circular combined antenna shown in detail in Fig. 5 (Ulyanov et al, 2002). The entire hardware (Fig. 6) incorporates 18 such separate partial acoustic-electromagnetic horn-parabolic antennas whose main optical axes are directed at elevation angle of about 45^0.

Superposition of phase centres of acoustic and electromagnetic oscillations in the antennas is achieved owing to the common horn radiators whose feeding rectangular waveguides serve also as the soundguides. When using the given combined circular antenna, it is possible not only to fulfil the adaptation of such a RAS technique to the wind in the sounded volume, but also automatically determine the characteristics of the wind flow in addition to the air temperature profiles.

The fact, that only the frequency characteristics of the echo-signal are needed to be measured in such a variant of RASS, predetermines rather high accuracy of the measurements. Numerical estimations show that errors of wind parameters and the temperature obtained in the lower 500 m with IRAS are comparable with those obtained with modern radiosondes.

3 Conclusion and Outlook

Our investigations show that the inclined radioacoustic sounding system by itself can be successfully applied for measurements of the wind profiles in the lower PBL because of its good electromagnetic compatibility and capability to be used in populated areas and industrial zones with a high level of acoustic noise. On our opinion, its outlook is rather optimistic.

Literature

Smith P. L. : Remote measurements of wind velocity by the electromagnetic-acoustic probe. /Conf. proc. 5th Ann. convention on military electronics, Wash. (O.C.), 1961, rep. N 419, pp 43-53.

Babkin S. I., Miloserdova G. N., Orlov M. Y., Ulyanov Y. N. et al: Determination of temperature, velocity and direction of the wind in low atmospheric layer by the radioacoustic sounding method. / Meteorology and Hydrology, 1980, №8, p. 36-45, in Russian.

Babkin S. I., Panchenko A. Y., Proshkin E. G., Ulyanov Y. N.: Measurements of the horizontal wind velocity vector with the vertical radioacoustic sounding. / Proc. of XI All-union Conf. on Laser and Acoustic Atm. Sounding, USSR, Tomsk, 1987, P.2., p. 153-157., in Russian.

Maksimova N. G., Panchenko A. Y., Proshkin E. G., Ulyanov Y. N. : Inventor's certificate #4046462, 1988. A method of radioacoustic wind shear measurements, in Russian.

Vetrov V. I., Skvortsov V. S., Ulyanov Y. N. : Some aspects of sodar-RASS application for wind measurements / Ext. Abstracts of COST-76 Profiler Workshop, 1997, Engelberg, Switzerland, vol. II, p. 217-220.

Ulyanov Y. N., Butakova S. V., Vetrov V. I., Skvortsov V. S. : Patent of the Russian Federation #2152055, 27.06.2000. A method of inclined radioacoustic atmospheric sounding., in Russian.

Ulyanov Y. N., Butakova S. V., Vetrov V. I., Skvortsov V. S. : Patent of the Russian Federation #2168818, 10.06.2001. Combined radio- and acoustic antenna, in Russian.

Ulyanov Y. N., Butakova S. V., Bedin V. S., Buslovsky S. F. : Patent of Ukraine #46150, 15.05.2002. Hardware for radioacoustic atmospheric sounding., in Ukranian.

Sodar Measurements of Wind Velocity Profiles in Urban Areas

Vladislav Yushkov[1], Stefan Emeis[2], Margarita Kallistratova[3], Rostislav Kouznetsov[3]

[1]Physical Faculty of Moscow State University <yushkov@fryazino.net>; [2]Institut für Meteorologie und Klimaforschung (IMK-IFU), Garmisch-Partenkirchen; [3]Obukhov Institute of Atmospheric Physics, Moscow

Abstract

Data on vertical profiles of wind speed and its variance over Moscow obtained by yearly uninterrupted sodar measurements are presented. Their comparison with the data obtained earlier over Hannover show common features of urban wind field.

1   Introduction

Sodar is the most simple and inexpensive device among ground-based remote sensing systems for wind field studies in the urban boundary layer, UBL (see, e.g., [1, 2]). However, in large cities the conditions for sodar operation are not favorable, because traffic noise restricts the height range of sounding. For instance, sodar AeroVironment-3000 in Hoboken downtown reached only about 100 m of height, and sodar Sintec MFAS could not operate in the downtown at all [3]. To reduce the traffic noise interference the sodars are usually situated at city periphery, where wind field is not representative for the centre of urban heat island. Sodars have been used in many complex experiments (e.g., *KONGEX and VISAS-1987* in the Vienna area; *ECLAP* in Paris and its rural suburbs; *URBAN2000* in Salt Lake City; *ESCOMPTE-* 2001 in Marseille, *BUBBLE* 2001-2004 in Basel). Nevertheless, the sodar measurements were performed mostly during short-term IOPs of those experiments, and not much reliable statistical information on the UBL wind field was published. The few exceptions are studies [4, 5], where long-term data on wind field over a few German cities were collected. Below the results of sodar soundings in the center of Moscow, and their comparison with sodar soundings at Hannover are presented.

2   Instrumentation and results

Two permanent sodar measuring sites are arranged in Moscow: one in the centre, another at Moscow State University (MSU), closer to the city periphery. The sites are situated in the middle of urban quarters close to noisy traffic ways (see Fig. 1). Research sodars LATAN-3 designed in the Institute of Atmospheric Physics (IAPh) are used for the measurements [6]. The carrying frequency is 1700 Hz; vertical resolution is 20 m; maximal sounding range is 520m. Measurements in Hannover were carried out by commercial sodar METEK DSD3X7 (1500 Hz, resolution 12.5 m) placed on the periphery of the town away from housing area [5].

Figure 1. The antenna systems of the sodar Latan-3 at two measuring sites: on the roof of the IAPh building in the center of Moscow (left) and on the roof of Physical Faculty of MSU (right).

Sodar Latan-3 has an enhanced interference immunity. Besides, special measures were undertaken to reduce the influence of the ambient noise, and field testing was carried out to find an optimum criterion for noisy data screening. In Fig. 2 (left) the percent of successful

soundings on week days and holydays and its diurnal courses are shown. In rush hours about 80% of data were rejected. However, even 20% of observation time gives reliable estimation of the averaged horizontal speed, because it is uncorrelated with the traffic noise. In Fig. 2 (right) the time series of vertical velocity component, w, and its STD, σ_w, in both sites are presented. Vertical velocity oscillates near zero on average. However, on week days a small positive value of w was observed. This artefact is caused by the screening procedure, which discards descending air motions that are correlated with weak echo-signal. So, the measurements of w in the UBL should be treated carefully. The data on w STD, on contrary, are reliable enough, since the screening procedure discards only the weak motions, which do not contribute much to variance. The STD had a large diurnal variation, increasing in 4-5 times under convection. On the average, its magnitude in the town centre was 1.5 times larger than at the periphery.
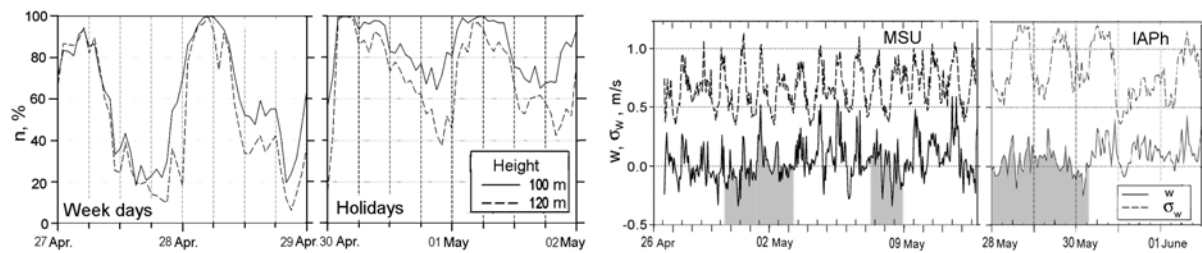
Figure 2. Left: Fraction of valid samples of wind velocity measurements at the MSU site. Right: Time series of w and σ_w at height 100 m. Gray color corresponds to holidays, when the traffic noise was much weaker.

The sounding height range also depends (apart from the traffic noise) on the height distribution of the intensity of turbulent inhomogeneities that scatter sound waves. An instance of a distribution of the maximum heights at the Moscow measuring sites are shown in Fig. 3 (left). An example of sodar echogram and wind speed and turbulence profiles in winter over the Moscow downtown by sodar LATAN-3 is shown in Fig. 3 (right).
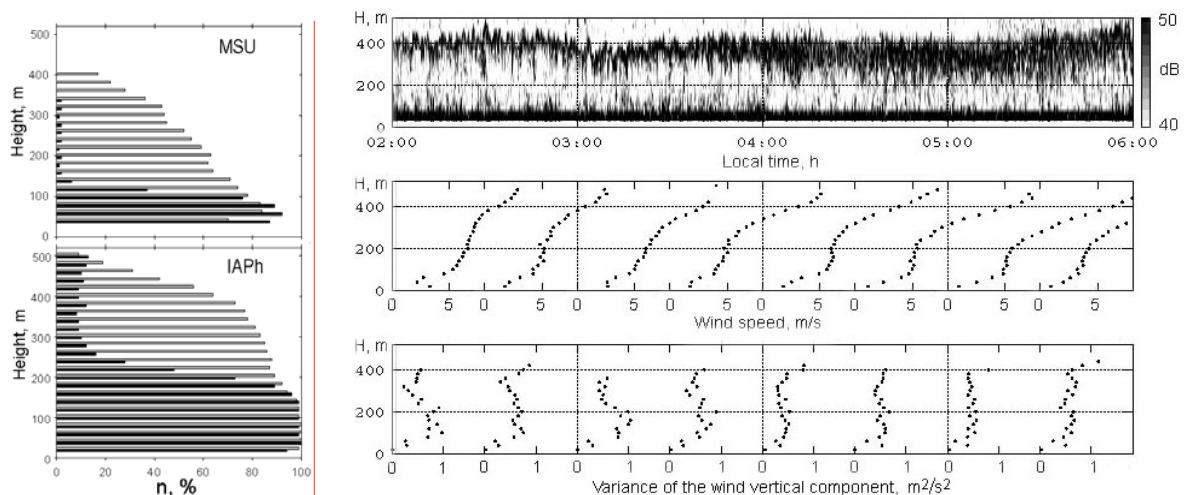
Figure 3. Left: Distribution of the maximum sounding range at nights. Black bars – under low-level surface inversions; gray bars– under slightly stable stratification. Right: A night fragment of echogram, and V and σ_w^2 profiles, IAPh, 20 Jan 2006 under strong frost: temperature near ground was -29° C.

In Figs. 4 and 5 a comparison of vertical profiles of wind speed and time series of turbulence obtained during long-term sodar measurements in the centre of Moscow and in Hannover is presented. The season patterns of the profiles have a common character in both cities. The magnitude of w variance in Moscow in summer is larger that it is in Hannover. The likely cause is the more intensive influence of the urban heat island in the centre of a city than in a city periphery.
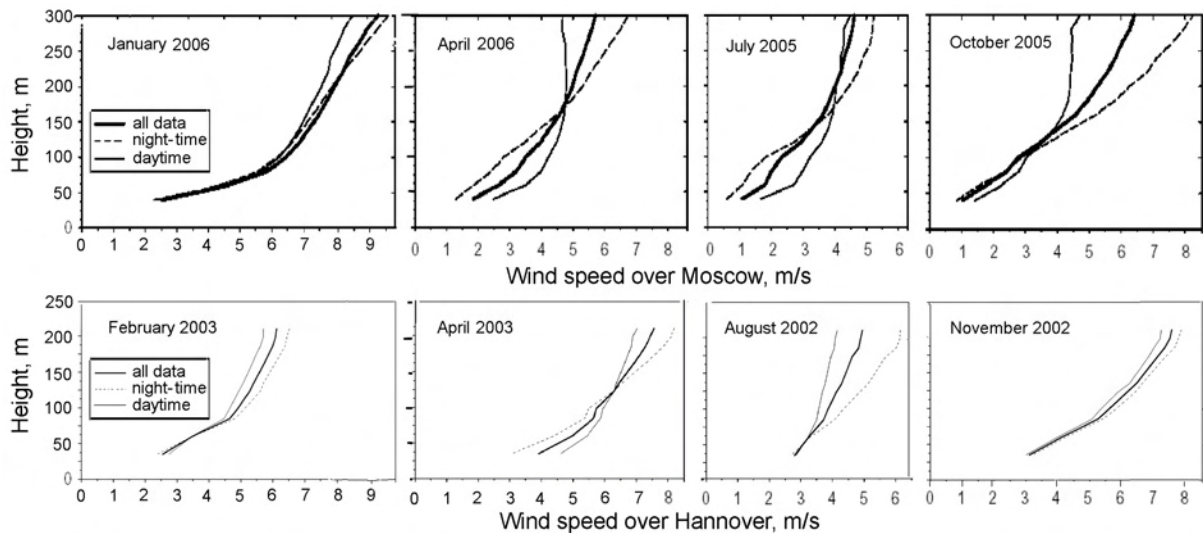
Figure 4. Monthly mean wind speed profiles for four seasons at Moscow (top) and Hannover (bottom)
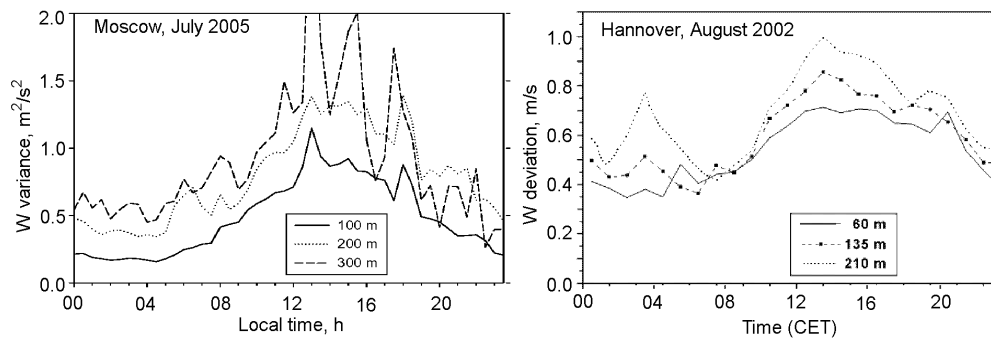
Figure 5. Monthly mean time series of σ_W^2 at the centre of Moscow and σ_W at Hannover in summer.

3 Conclusions

A positive experience of continual sodar measurements was gained in 2002-2004 at Hannover, and in 2005-2006 at Moscow, where two sodar measuring sites are located close to main streets with intensive traffic. Results of the acoustic sounding over both cities confirm the known basic particularities of a town canopy: mixing layer thickness and variance of vertical wind component are enlarged, and horizontal speed is reduced in downtown areas in comparison with the periphery. The vertical speed variance had a large daily course, increasing in 4-5 times under convection. On average, its magnitude in the downtown was 1.5 times higher than in the periphery. The statistical data on wind fields obtained in large cities can be used to estimate the influence of the urban wind field on the dispersion of air pollution.

Literature

[1] **Troude, E.D., B. Carissimo, A.I. Flossmann, 2002:** Relative influence of urban and orographic effects for low wind conditions in the Paris area. Boundary-Layer Met.*,* **103**, 493-505.

[2] **Kallistratova, M. A., 2003**: The use of sodar in studying urban climate: a review. Proceed. 5th Intern. Conf. on Urban Climate*,* 1-5 Sept. 2003, Lodz, Poland, Part 2, 335-340.

[3] **Berg, L.K., R.M. Reynolds, K.J. Allwine, A. Blumberg, 2006:** Comparisons of measurements made using two sodars in an urban environment. Proceed. 6th Symp. Urban Environ., Jan 2006, Atlanta, USA, paper JP2.9.

[4] **Peters, G., B. Fischer, 2002**: Parameterization of wind and turbulence profiles in the atmospheric boundary layer based on sodar and sonic measurements. Meteorol. Zeitschrift, **11**, 255-266.

[5] **Emeis, S., 2004**: Vertical wind profiles over an urban area. Meteorol. Zeitschrift, 1**3**, 353-359.

[6] **Kouznetsov, R.D., 2006**: New PC-based sodar LATAN-3. This collection.

Flow field detection using acoustic travel time tomography

Barth, Manuela, Arnold, Klaus, Raabe, Armin

Universitaet Leipzig, Institut fuer Meteorologie, Stephanstr. 3, 04103 Leipzig, Germany, mbarth@uni-leipzig.de

Abstract

Acoustic travel time tomography uses the dependency of sound speed from temperature and flow properties along the propagation path to measure these parameters. An algorithm is introduced which is capable of resolving the two-dimensional flow field within a certain measuring area comparable to the resolution of the temperature field. Different flow fields have been simulated in order to show the reconstruction properties of the algorithm. Furthermore an experiment has been carried out, which demonstrates the applicability of the acoustic tomographic method to detect temperature and flow fields in a closed convection chamber.

1   Introduction

Acoustic tomography in meteorology is used as a method for determining distributions of temperature and wind within a certain measuring field (Arnold et al., 2004; Ziemann et al., 2002). These experiments have shown the difficulties of reconstructing the scalar and vector field in a concurrent resolution.

Since the speed of sound in air depends mainly on the acoustic virtual temperature and flow properties along the propagation path (positive in direction of sound propagation, negative otherwise), measurements of the travel time provide information on those quantities whereas the positions of the source and receiver (length of sound rays) have to be known exactly. The separation of the scalar influence of temperature and the directional influence of the flow vector on the speed of sound is done using reciprocal sound ray paths (reverse direction: forward, backward). To achieve information from the whole measuring site, sound sources and receivers have to be positioned around the field in a way, which different sound ray paths cover the area of interest nearly homogeneously.

In order to easily investigate different experimental set-ups and to test new algorithms, a small scale tomographic system has been developed (Holstein et al., 2004; Barth et al., 2004). The accuracy for the sound speed estimation depends on the accuracy of travel time measurements (3 μs with current hard- and software) and on the accuracy of the determination of the source and receiver positions. Considering measurements relative to an initial measurement, the time error has to be treated, which leads to a sound speed estimation error from 0.4 m/s (distance between source and receiver: 1 m) down to 0.04 m/s (distance: 10 m).

2   Tomographic reconstruction of flow fields

Present work concentrates on the implementation of an algorithm to reconstruct the vectorial flow field with the same spatial resolution as the temperature field can be reconstructed.

The reconstruction of two-dimensional distributions of temperature and flow is done using tomographic techniques. First of all, the measuring site has to be divided into separated grid cells where in the line integrated acoustic travel time information is backprojected. For the scalar temperature, only the portion of each sound ray path within one grid cell is crucial. For the flow field, components (x-, y-direction) are analysed separately and depending on the direction of the sound propagation. Figure 1 shows an experimental set-up with 8 sources and 8 receivers, which are distributed around a measuring site of 1.2 m × 1.2 m (left). To test the algorithm, a spatially highly resolved flow field has been simulated. Corresponding to the set-up, travel times and flow information along the sound ray paths have been calculated. These values serve as input data for the tomographic reconstruction. The result is shown on the right side of figure 1.
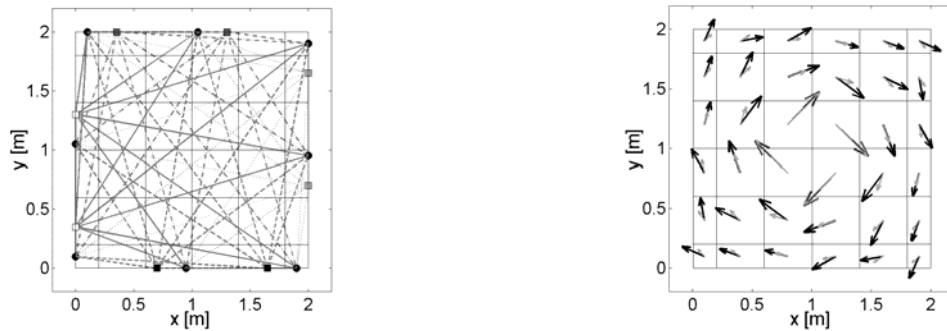
Figure 1. Left: Predetermined set-up for the test of the tomographic reconstruction of flow fields consisting of 8 sources (squares) and 8 receivers (circles) around the measuring site. Grey lines indicate the sound ray paths, horizontal and vertical black lines the tomographic grid. Right: Simulated eddy averaged on the tomographic grid cell size (grey arrows) and reconstructed flow field (black arrows).

3   Experimental results

The described algorithm was applied in the barrel of Ilmenau/Germany (Ilmenauer Fass online). This cylindrical convection cell is characterised by two plates (ground/ceiling), which can be heated/cooled. In consequence of heating and cooling, a nearly constant flow develops within the cell, which could be detected using the system of acoustic travel time tomography (Fig. 2).
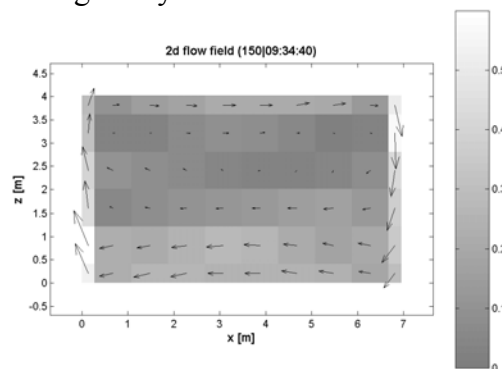
Figure 2: Tomographically reconstructed flow field within the barrel of Ilmenau using acoustic tomography. Grey scale indicates flow velocities, arrows denote the direction of the flow (arrow length proportional to flow velocity).

4   Outlook

Simulations and measurements showed the capabilities of the new algorithm to reconstruct flow fields from acoustic travel time measurements. Although first measurements were done indoors, there are no general restrictions using the system outdoors to detect the flow field within the boundary layer or to investigate vertical structures, e.g. Furthermore an extension of the system to investigate three-dimensional distributions is planned.

Literature

Arnold, K., Ziemann, A., Raabe, A., Spindler, G., 2004: Acoustic tomography and conventional meteorological measurements over heterogeneous surfaces, Meteorol. Atmos. Phys., 85, 175-186.

Barth, M., A. Raabe, P. Holstein, R. Müller, A. Ziemann, K. Arnold, D. Mackenzie, E. Starke, M. Seliger, 2004: Acoustic travel time tomography as a tool to investigate temperature distributions on different spatial scales. In: proceedings of the ISARS 2004.

Holstein, P., A. Raabe, R. Müller, M. Barth, D. Mackenzie, E. Starke, 2004: Acoustic tomography on the basis of travel-time measurements. Meas. Sci. Technol., 15, 1420-1428.

Ilmenauer Fass, online (May 2006): www.tu-ilmenau.de/ilmenauer-fass.

Ziemann, A., K. Arnold, A. Raabe, 2002: Acoustic tomography as a Remote Sensing Method to Investigate the Near-Surface Atmospheric Boundary Layer in Comparison with In Situ Measurements. J. Atmos. Ocean. Techn., 19, 1208-1215.

Linux Grid Sodar (LiGriS), a tool to integrate Sodar and Other Meteorological Sensors in a Grid Sensor Network (GSN)

Elefante, Cosimo, Conte, Dario, Marra, Gian Paolo, Mastrantonio, Giangiuseppe
Institute of Atmospheric Sciences and Climate of the Italian National Research Council
Via per Monteroni, 73100 Lecce – Italy
c.elefante@isac.cnr.it

Abstract

The Grid Sensor Network represents a prototype that allows the integration of the technology grid in the management of the sensor networks, supplying various facilities for the remote control of these instruments and of the access to these resources. The *LiGriS* is a case study realized to concretely verify the potential offered by this new infrastructure.

1   Introduction

The dynamics or in general the phenomena which take place in the atmospheric boundary layer (ABL) are very complex because of the great number of variables, such as the feedback processes, the highly non-linear interactions between different scale motions and, above all, the turbulence that characterizes the exchange processes in this part of the atmosphere.

The ABL plays a crucial role for several reasons: it is the layer in which energy (in the forms of water vapor, heat and momentum) is transferred from the surface to the atmosphere and vice versa; it is also a place in which a large amount of human activity residuals are released.

Knowledge of the ABL structure is therefore basic for studying the atmospheric dynamics and the transport of pollutants and its diffusion in the atmosphere.

To study these topics, many different measures are needed which are usually gathered by sensors that are based on different technologies and principles. It is often necessary to assimilate these measures into mathematical models in order to be able to describe the phenomenon and its evolution. Therefore numerical models may need to automatically access the sensors to get the data. In such a context, it is necessary to manage many various types of instruments, with different and non-standard operative procedures. Then the information obtained must be integrated together to be able to describe the present phenomena in the ABL. Furthermore, the necessity of remote control of the instrumentation and access to the information gathered on the part of the interested scientific community present itself more often.

A solution to this problem can be represented by the application of the technology grid through the development of Grid Sensor Networks, modern sensor networks created to facilitate the control and management of monitoring systems for meteorological and environmental parameters.

2   Grid Sensor Network

The application Grid Sensor Network (GSN) is born to facilitate the control and management of modern sensors of meteorological parameters developed utilizing the infrastructure grid.

The application has been developed according to the web applications, therefore allowing us to have a flexible system and also independent from the platform, but at the same time utilizable from any accessible point on the Internet network.

The GSN allows the individualization of all the grid sensors on the grid network, visualization of the characteristics, the carrying out of the acquisitions or the discharge of previously acquired data.

The non-homogeneity of the remote sensing systems is due to different technical hardware, software and the management of different instruments. This non-homogeneity becomes a critical and fundamental point in the implementation of a common infrastructure for the management of the sensor networks.

Therefore, the use of a common specific technology, which may be easily adapted to different applicative contexts, resulted necessary.

This objective has been achieved by integrating, at the interior of the system, the specific international standardization of sensors SensorML[1], developed by Open GIS Consortium(OGC), which supplies an XML outline for the definition of the geometric characteristics, dynamics and the measurements of different sensors.

The research module of the grid sensor permits the visualization of all the grid sensors available on the VO grid network, showing the instruments condition and the base characteristics. The use of the grid infrastructure has allowed us to integrate in GSN all the research systems of the resources supplied by Monitoring and Discovery Service (MDS) [2], which is a service of Globus Toolkit, that allows to obtain information on the resource grid, present in the Grid. In particular, a new Information Provider (IP) has been developed, a service capable of supplying information regarding a single resource [3][4].

Through these facilities, the GSN will be able to make inquiries on the computational grid and obtain a list of all the available grid sensors containing: the type of sensor, the location in which it is installed, the host address (in order to contact it). All information is found dynamically by specific file sensorml.xml associated with the instrument.

The GSN allows the user to carry out the acquisitions through the sensor that it has individualized. After having furnished all input parameters necessary to the instrument, one can directly visualize on the web the physical magnitude that is being controlled.

The LiGriS (Linux Grid Sodar) represents an innovative instrument for acquisition thought to completely integrate itself at the interior of Grid Sensor Network.

3   Conclusion and Future Works

The work completed up to this moment in the development of the Grid Sensor Network has permitted the realization of a software infrastructure, capable of managing any type of grid sensor that could be presented. The traditional sensor networks do not have the well developed potentials of the GSN. With the GSN, the user will not need external systems to identify a sensor or to individualize its geographical location, but will be able to directly use research systems set-up in a disposition for identifying and using the grid sensor.

In this project, the limits which we established to exceed as it relates to this infrastructure, were those of providing the scientific community with an identification, monitoring and control system of the data acquisition instruments. However, future objectives are those of directly automating the access systems to such instruments and therefore, allowing the integration with the models of environment simulation. In the initialization phase, the same model will make an inquiry on sensors in the area of interest and will ask them to carry out acquisitions needed as input for successive evaluations and processes.

Literature

[1] **Mike Botts, 2004,** "Sensor Model Language for In-situ and Remote Sensors", University of Alabama in Huntsville, pp. 1-4.

[2] **I. Foster, C. Kesselmann, W. Allcock, 2001,** "The Data Grid: Towards an Architecture for the Distributed Management and Analysis of LargeScientific Datasets", Journal of Network and Computer Applications.

[3] **Foster I., Kesselman C., Fitzgerald S., Czajkowski K.** "Grid Information Service for Distributed Resource Sharing".

[4] **Leon Kuntz,** "GRIS Specification Document: Creating New Information Providers", www.globus.org

Peculiarities of Signals Processing at Radio Acoustic Atmosphere Sounding

Kartashov V.M., Proshkin E.G., Babkin S.I., Kostyuk I.V.
Kharkov National University of Radio Electronics, 14, Lenin Av., 61166, Kharkov, Ukraine
E-mail: res@kture.kharkov.ua

Abstract

The algorithms of radio acoustic systems' signals processing, constructed with allowance for a radio wave transformation in the channel and making it possible to perform qualitative measurements of atmosphere parameters not only with the fulfilled Bragg condition but with $q \neq 0$ (q is a parameter of the Bragg condition disruption) and complex sonic pulses radiation, are synthesised in this work.

1   Introduction

Results of sonic speed and temperatures measurements performed with radio acoustic atmosphere sounding systems in most cases contain a systematic error, which does not decrease as a result of averaging, and only when using simple acoustic pulses and fulfilled Bragg condition the results of measurements are free of systematic errors.

The presence of the systematic error in the results of measurement performed with the RAS systems is attributed, on the one hand, to a change in the form (structure) of the radiated electromagnetic oscillations at dispersion on a sonic pulse, and, on the other hand, an application of the traditional signal processing algorithms.

2   Instrumentation

Hence, the signal processing algorithms used in rasdars are not adequate to the processes taking place in the detection channel. Let us consider derivation of the radio acoustic systems signals processing algorithms constructed with regard to a radio wave transformation in the channel and allowing to realize qualitative measurements of the atmosphere parameters not only with the fulfilled Bragg condition but with $q \neq 0$ and also with complex acoustic pulses radiation.

Let us present the observation equation or scattered field being received in the general form in the radio acoustic sounding problem

$$E_1(\vec{r},t) = \Re\left[E(\vec{r},t), S(\vec{r},t)\vec{\Theta}(\vec{r},t)\right] + n(\vec{r},t), \qquad (1)$$

where $E(\vec{r},t)$ - is an electromagnetic signal complex envelope; $S(\vec{r},t)$ - is an acoustic signal complex envelope; $\vec{\Theta}(\vec{r},t)$ - is the atmosphere parameters vector; $\Re$ - is an operator of signals transformation in the channel (a scattering operator); $n(\vec{r},t)$ - is the additive noise field; $\vec{r}$ - is a space point radius-vector. At the output of the receiving antenna the process being received is the function of time t

$$U_1(t) = U_{ES}(t,\vec{\Theta}) + n(t), \qquad (2)$$

where U_{ES} - is a useful signal at the antenna output with the given functions E and S.

When sounding the atmosphere with the aim to measure temperature (the majority of recognized rasdars precisely this problem) the medium parameters vector $\vec{\Theta}$ can be presented with a unified integral characteristics c_S i.e. acoustic velocity depending on temperature, wind velocity, pressure, humidity etc. On the other hand, c_S is a parameter of the target movement i.e. an acoustic wave packet.

Let us consider the problem of c_S value estimation. It is known from the radio systems theory (Petrov A.V., Yakovlev A.A., 1984; Shirman Ya.D., Manzhos V.N., 1981; Tikhonov V.I., 1983) that the synthesis of the optimal mathematical operator of the measuring system and formation of the optimal solution are based on the use of the likelihood function which, as applied to the given problem, can be written as $w(U_1/c_S)$.

The form of the scattered signal or reference oscillation for the processing device (its complex envelope) can be defined according to the following expression

$$U_{ES}(r,q) = \int_{-\infty}^{\infty} E(2r' - r)S^\bullet(r')e^{jqr'}dr' , \qquad (3)$$

where r' is the longitudinal space coordinate, r is the signals displacement along the coordinate r'. If we present r in (3) as $r = ct$ where c is the electromagnetic waves propagation velocity then (3) becomes a function of time t.

3   Results

Thus, the problem of rasdars processing devices should be reduced to formation of the ample statistics $X(U_1, c_S)$ in the interval of possible values of $C : c_S \in (c_{S\min} - c_{S\max})$ and finding of c_S corresponding to the maximum of the function $X(U_1, c_S)$. The optimal output effect can be the module value of the complex correlation integral $Q(c_S)$

$$Q(c_S) = \left| \int U_1(t) U_{ES}(t, c_S) dt \right|, \qquad (4)$$

where $U_{ES}(t, c_S)$ is the reference signal. The values of c_S are grouped together with the functional dependence with $k_S : k_S = 2\pi f_S/c_S$ and, consequently, with the parameter of the Bragg condition disruption $q = 2k_S - k_e$.

Thus, the considered procedure of estimation consists in calculation of the correlation integral (4) values totality in n points making it possible to reproduce the required curve $Q(c_S)$ with a sufficient precision finding of the maximum of the function $Q(c_S)$ in the interval being analyzed and the value of c_S corresponding to the found maximum.

4   Discussion, Conclusions and Outlook

The offered approach makes it possible to build processing algorithms with different forms of radiated radio and acoustic signals removing specific errors peculiar to RAS systems through "correct" extraction of useful information from the received oscillations.

An essential dissimilarity of the offered estimation algorithm from the parameters measurement devices widely spread in practice consists in the reference signal. In the given case the reference oscillations in different points of C range differ in type, form but not in the value of the parameter such, for example, as frequency, as is customary. Only in the point where the value of the parameter of disruption $q = 0$ the reference signal coincides in the form with the radiated signal.

Literature

Petrov A.V., Yakovlev A.A., 1984: Analysis and Synthesis of Radio Engineering Complexes. (In Russian) M.: Radio and Communication. 246 pp.

Shirman Ya,.D., Manzhos V.N., 1981: Theory and Technology for Radar Information Processing on the Noise Background. (In Russian) M.: Radio and Communication. 416 pp.

Tikhonov V.I., 1983: Optimal Reception of Signals. (In Russian) M.: Radio and Communication. 320 pp.

Acoustic Antennas for Atmospheric Research

Krasnenko Nikolay
Institute of Monitoring of Climatic and Ecological Systems
of the Siberian Branch of the Russian Academy of Sciences
10/3, Akademicheskii Pr., Tomsk 634055, Russia
E-mail: krasnenko@imces.ru

Abstract

Experience and special features of the development of acoustic antennas for remote sensing of the atmosphere is described. Problems of analysis and synthesis of shielded reflector parabolic acoustic antennas for atmospheric research are investigated. A generalized technique and recommendations on optimization of geometric parameters for shielded acoustic antennas of this type are presented. Results of experimental investigations of the developed antennas are given that support the theoretical premises and demonstrate the practical applicability of the developed technique.

1   Introduction

Antennas are the main parts of various acoustic systems [1]. To use the energy potential of an acoustic system in full degree, the antenna must be close to perfect and have narrow directional pattern and low level of side lobes (LSL). This is due to several reasons, including strong external acoustic noise, low level of received signals, and the need for environmental protection from high-power acoustic radiation.

Nowadays, reflector parabolic antennas are most widespread in atmospheric acoustics by virtue of relative simplicity of their design. In this case, a parabolic reflector, which provides a narrow directional pattern (DP) for sufficiently small overall antenna dimensions, is used to focus an acoustic beam. A protective shield is used to reduce the level of side lobes and to eliminate the influence of external noise as well as to protect the environment from high-power acoustic radiation. However, these acoustic shields increase significantly the overall antenna dimensions.

A common disadvantage of the previous methods for calculating and synthesizing shielded reflector parabolic antennas [2 - 4] is the preset antenna parameters (the reflector diameter and the protective shield height or aperture angle). This hinders significantly synthesis of acoustic antennas, because if the antenna has the parameters that differ from the preset ones, additional calculations of the amplitude and phase distributions of the acoustic pressure field across the aperture must be performed to obtain the sought-after DP. However, these methods provide the basis for the development of a generalized technique of synthesizing the geometric parameters of acoustic antenna shields. The development of such antennas was accompanied by their experimental testing.

2   Results

The methods of calculating the parameters of acoustic and electromagnetic antennas coincide in many respects, which essentially simplifies the problem under study. In particular, the Kirchhoff integral, used for calculations of acoustic and electromagnetic antennas [2-5], is used to calculate the acoustic pressure field distribution across the transmitting antenna aperture. The shield height and the upper aperture radius (or the aperture angle of the protective shield) are the geometric parameters that must be calculated to design such an antenna.

Using the above-described technique, we designed and developed two antennas: a transmitting acoustic antenna for the acoustic station with small height of the protective shield and a transceiving antenna for the Zvuk-3 acoustic radar [5, 6].

All antennas developed by us for our sodars were systematized. Their characteristics are tabulated and examined [5].

3   Conclusions

In this report, investigations of the characteristics of shielded acoustic reflector antennas are generalized. The developed generalized technique of calculating the geometric parameters of protective antenna shields has been described, and the parameters of the developed shielded reflector antennas used in actual atmospheric investigations are systematized. This data enable the design of antennas of this type to be significantly simplified and reduced either to a choice of the antenna with already preset characteristics or to rather simple calculations of the antenna parameters using.

Our investigations of shielded parabolic reflector antennas with horn loudspeakers demonstrated [5, 6] that acceptable amplitude and phase distributions of acoustic pressure field across the transmitting antenna aperture can be obtained at rather small shield heights (much smaller than those recommended in [2, 3]).

An interesting feature arising in calculations of phase distribution, which explains the discrepancy between the optimal geometric parameters of the protection shield recommended in [2] and [3] must also be pointed out. In [2] it was found that to obtain the optimal shielded antenna directional pattern, it is necessary that the shield height and the radius of its transmitting (upper) aperture were three times greater than the unshielded reflector radius. In [3] it was found the optimal shield sizes were determined by the aperture angle of the protective shield rather than by the shield radius; however, it was also recommended that the protective shield must be three times greater than the unshielded reflector radius.

However, as follows from our equatons, the protective shield height must be the greater, the greater the number of wavelength falling within the unshielded reflector aperture. This testifies to the correctness of conclusions made in [2] and [3], though their formulation was different. This is explained by the fact that these conclusions were made for acoustic radar antennas whose directional pattern widths must be of the order of 10 deg [1]. To realize such directional patterns, it is necessary that from 2 to 5 wavelengths fall within the unshielded reflector aperture radius; therefore, the authors of both papers were right in the specific considered cases.

Literature

Krasnenko N., 2001: Acoustic sounding of the atmospheric boundary layer. Tomsk. 2001. 278 P. (in Russian).

Adekola S., 1976: Toward a more general integral formulation of the pressure field of an echosonde aperture antenna / J. Acoust. Soc. Am. V. 60, No. 1, p. 230 – 239.

Krasnenko N., A. Root. 1989: Investigation of shielded parabolic antennas of acoustic radars / Deposited in VINITI 06.02.1989. Moscow, No. 766-V89 DEP, 26 p. (in Russian).

Strand O., 1971: Numerical study of the gain pattern of a shielded acoustic antenna / J. Acoust. Soc. Am. V. 49, No. 6, part 1, p. 1698 – 1703.

Krasnenko N., E. Mananko, 2004: Parabolic reflector acoustic antennas for atmospheric sounding / Methods and means for information transfer and processing: Intercollege collection of scientific works. No. 5. Romashev V. V., Bulkin V. V., eds. Saint Petersburg: Gidrometeoizdat. 2004. P. 83-98. (in Russian).

Krasnenko N., E. Mananko, 2004: Synthesis of shielded acoustic antennas for atmospheric researches / Proc. of the 12th Intern. Symp. On Acoust. Remote Sensing and Associated Techniques of the Atmosphere and Oceans. Cabridge, UK. (CD ROM). TuB16, p. 1-4.

Architecture, design and implementation of a scalable digital beamformer for switched beam acoustic sodars

Liaskas, T.J., Stephanou, G.J., Martakos, D.
Department of Informatics and Telecommunications, National and Kapodistrian University of Athens,
Panepistimioupolis, Ktiria TYPA, GR-15784, Athens, GREECE
E-mail: tliaskas@di.uoa.gr

Abstract

One of the most important units in phased array sodars is the beamformer. The architecture and the implemented device presented here offer flexibility, scalability, modularity and most of all independence on a variety of antenna relevant parameters (like the number and type of elements, topology, operating frequency, interfacing with a computer system etc). The main module is a programmable multi-channel pattern generator. The error in the produced phase differences is small, less than 0.6° for the digital units and 1.2° for the analog ones.

1   Introduction

Many systems of acoustic radars have been developed in their over 50 years history, varying from the pioneer efforts to the latest commercial products of phased array sodars. One of the most important units in phased array radars is the beamformer. Main operation of this unit is to produce the proper phase differences α_i (during transmission) and the time delays n_i (during reception) needed to steer the beam in the desired direction. For a planar array of MxN elements, each one placed at (x_i, y_i) coordinates and for beam placed on the (φ_0, θ_0) direction, α_i and n_i are computed according to the following equations [Martakos et al, 1990]:

$$\alpha_i = -2\pi(x_i \sin\theta_0 \cos\phi_0 + y_i \sin\theta_0 \sin\phi_0) \qquad n_i = \left\lceil \frac{Q \cdot a_i}{2\pi} \right\rceil, \quad Q = 2^{N_b}, \quad i = 1,2,...,MxN \qquad [1]$$

2   Architecture

The main module of the beamformer is a programmable multi-channel pattern generator. It's operation is based on the conversion of 8 bit static RAM circuits to 2^N-bit shift registers [Liaskas et al, 1995]. The shifting is done using the α_i values described in equation [1]. The principle of operation during transmission is presented in Figure 1. Patterns formed using this technique, are stored in RAM memory during programming. The RAM cells output their contents and form the square waveforms during operation stage (acting in two modes, transmit and receive). A bank of low pass filters and amplifiers is used in further stages to convert these square waveforms to sinusoidals, suitable for driving phased array antennas.
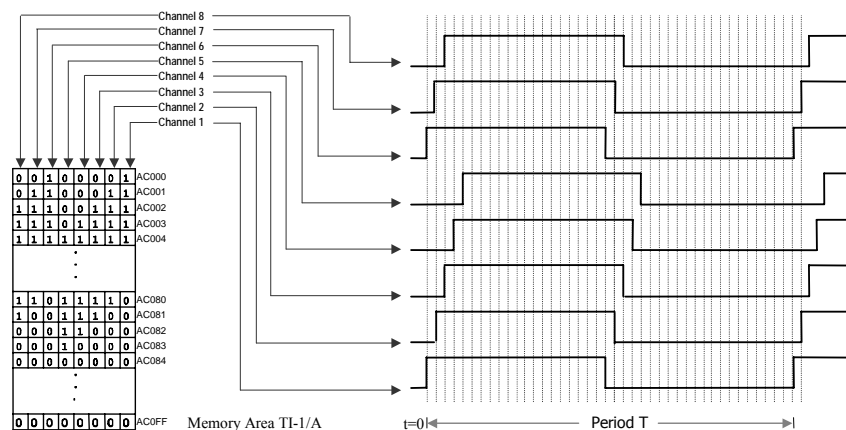
Figure 1: A sample of output signals (arbitrary shifted in time) for an 8-channel pattern generator module.

Properly formed patterns are also generated for controlling the sampling of the received signals (by DAPD units, one unit per each antenna's element). The fast adder uses these samples while the system operates as a partial sum beamformer. The pattern generator's output data, the bit rate and the word length are fully programmed.

The beamformer communicates with a personal computer through the standard parallel (centronics) port, using a dedicated interface module. Thus it is connectable to almost all modern computer systems. The architecture is presented in Figure 2(a) and permits independent control on every antenna's element, a novel feature in the systems of this type.

3   Implementation and measurements

An experimental prototype based on the proposed architecture was designed and has been developed in the Department of Informatics and Telecommunications and is used to a modular switched beam digital acoustic radar system (titled SBEDAR) [Liaskas et al, 1996].
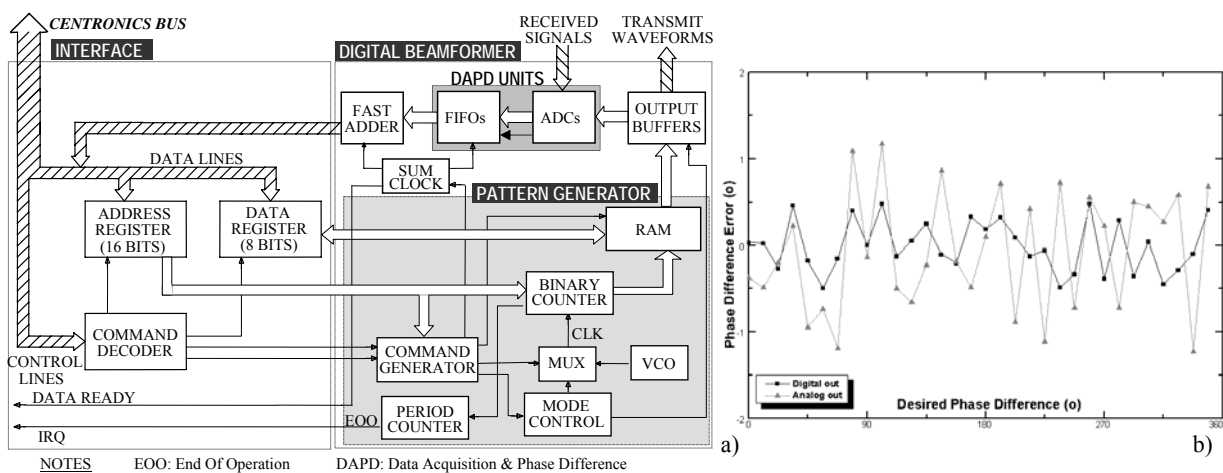
Figure 2: a)Block diagram of implemented beamformer's architecture b)measurement of phase difference errors

The implemented device is capable to drive array antennas of up to 31 elements, due to usage of 4 RAM banks of 8 bits each (one channel is always used for control). For larger arrays, more than one devices of this type may be used in parallel, forming a scalable system.

The programming of the beamformer is done through a special set of commands developed in hardware and software level. All system's software is developed as an external library, providing a mini extension of a high-level programming language.

Measurements on the accuracy of phase generation unit have been done and provide very good agreement in coordination with the values expected from the specifications set in the analysis stage. The errors among the desired phase differences and the measured ones are less than 0.6° for the outputs of the digital pattern generator, and less than 1.2° after transforming them to sinusoidal waveforms. These error measurements are presented in Figure 2(b).

References

Martakos, D., Liaskas, T.J., & Stephanou, **G.J., 1990**: A microprocessor based beam-forming system for digital switched beam acoustic radar, Proc. of 5th Int. Symp. Acoustic Rem. Sens. of Atm. & Oceans, New Delhi, India, Feb. 6-9 1990, Editor S.P.Singal, pp. 135-140

Liaskas, T.J., Martakos, D. & Kayafas, E., 1995: A novel design of a digitally controlled multichannel pattern generator, Proc. 7th Int. Symp. On Modern Electrical & Magnetic measurement, Prague, Sep 13-14, pp. 442-446

Liaskas, T.J., Martakos, D. & Stephanou, G.J., 1996: Development of modular switched beam digital acoustic radar, Proc. of 8th Int. Symp. Acoustic Rem. Sens. of Atm. & Oceans, Moscow, Russia, May 27-31 1996, pp. 3.43-3.48

High Resolution Measurement of EDR Using a chirped SODAR

Martin, Andrew,
StratoSonde Pty Ltd, Melbourne, Australia,
andrew.martin@stratosonde.com

Abstract

EDR measurements with a vertical resolution of 8m, a temporal resolution of 2minutes and a range of 500m are obtained from a chirped RAMP SODAR from the standard deviation of the Doppler spectra. These EDR profiles can be readily used to obtain an estimate of the virtual temperature profile as well as for estimating the lifetime of aircraft wake vortices.

1   Introduction

A Remote Acoustic Microstructure Profiler (RAMP) [1] or chirped SODAR is used to obtain high-resolution EDR measurements. The EDR is obtained from the standard deviation of the Doppler spectra of a vertical profile. For a typical profile to 520m, 3000 data points are used to obtain each spectrum for each of the 64 range gates providing a vertical resolution of 8m. The EDR data can be combined with the signal strength, ground temperature and lapse rate to gain an estimate of the vertical temperature profile. The EDR is also very useful for estimating aircraft wake vortex lifetimes.

2   Instrumentation

The EDR or σ_W profile is obtained from the standard deviation of the spectra from a vertical Doppler measurement and easily provides 64 profile values with a 2minute update rate. The magnitude of vertical incremental temperature changes ΔT in a range gate Δz can be estimated using

$$\Delta T = k(C_T^2)^{3/4}\Delta z/(\sigma_W T_0^{1/2}) \tag{1}$$

where C_T^2 is the turbulent signal strength and σ_W is the standard deviation of the vertical wind speed or turbulent decay and T_0 is the ground temperature [2]. This is provided that the signal-to-noise ratio is sufficient and the clutter is minimised to ensure high quality input data for the key parameters. Calibration is required to estimate the value of k. The virtual temperature profile can then be estimated by addition of the ground temperature and lapse rate.

3   Results

The results of EDR profiling and its use with the turbulent signal strength to obtain temperature and estimate wake vortex lifetime are shown in Figures 1 to 4.
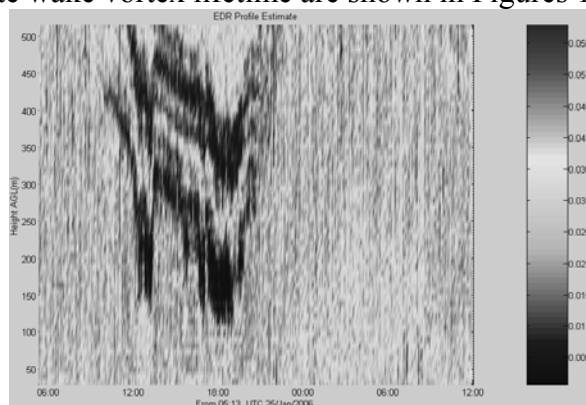
Figure 1. EDR for a 30 hour period, Melbourne, Australia. The record begins in the late afternoon. After sunset, stratification develops and the EDR reduces substantially in the stratification. The EDR is at a minimum just before sunrise. As heating develops after sunrise, the stratification breaks up and the EDR returns to higher values.
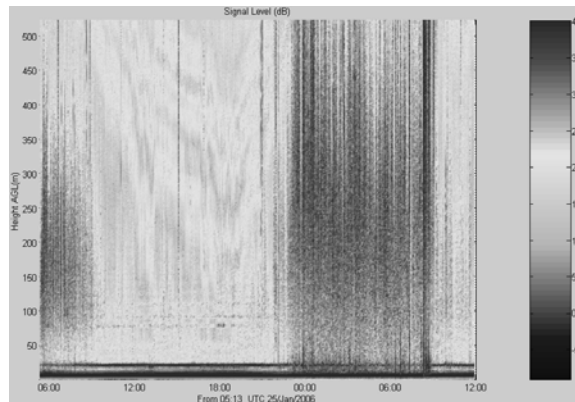
Figure 2. The vertical return signal level is obtained after removing the propagation dependent path loss. This enables a better estimate for the value of C_T^2 to be obtained. The stratification after sunset is readily evident. Reflections from local clutter are evident as horizontal lines. The strong clutter below 20m is removed before using this data to estimate the temperature profile.
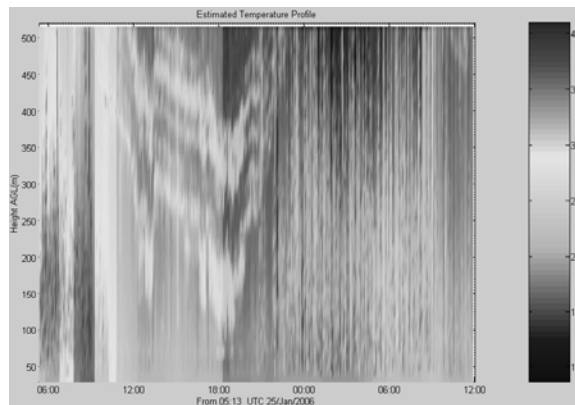
Figure 3. Estimated virtual temperature profile in degrees C. The increase in temperature of about 6 degrees C associated with the stratification is readily evident. The ground temperature was derived from a local weather station with half hour updates and this resulted in some step changes of the temperature.

The non dimensioned lifetime of aircraft wake vortices can be easily estimated from the EDR [3] using $Lifetime = -1.3 * \ln(EDR) + 1$ (2).

4   Discussion, Conclusions, and Outlook

The use of a high resolution RAMP system can readily be applied to obtain high resolution profiles of the EDR. The EDR measurement can be applied with the turbulent signal strength to obtain a high resolution temperature profile.

Literature

[1]   **Martin, A., 2006, "**Validation of a Chirp SODAR Against a 430m Tower", in Proc. ISARS 2006.

[2]   **Bradley, S.G., 2006, "**Private communication".

[3]   **Proctor, F., 2004,** "TASS Driven Algorithm for Wake Prediction (TDAWP)", WakeNet USA, Boca Ranton, Florida, 16-17 March 2004.

Automatic Detection of Mixing Layer Depths and their Meaning under Stable Conditions using Sodars

Neff W.D. (1), Helmig D. (2), and Grachev, A. (3)

[1]NOAA/Earth System Research Laboratory, Physical Sciences Division, Boulder, Colorado 80305,
william.neff@noaa.gov

[2]University of Colorado, Institute for Arctic and Alpine Research, Campus Box 450, Boulder, CO 80309

[3]University of Colorado, Cooperative Institute for Research in the Environmental Sciences c/o
NOAA/ESRL/PSD, 325 Broadway, Boulder, CO 80305

Abstract

This paper focuses on the use of an acoustic sounder, or sodar, to document the behavior of shallow (< 50 m) boundary layers thought to account for very high concentrations of nitrogen oxide (NO) found in past experiments at the South Pole. An automatic mixing layer detection method was developed and applied to half-hour average data for the period from 23 November through 30 December, 2003. The use of a tethered balloon profiling wind, temperature, nitrogen oxide, and ozone provided for interpretation of sodar boundary layer profiles for the period December 12-30.   For the same period, sonic anemometer 2-m turbulence measurements linked surface processes to the evolution of the boundary layer in response to changing radiative balance and synoptic weather processes.

1   Introduction

While sodars provide valuable pattern recognition capabilities for the study of the stable atmospheric boundary layer, automatic detection of key boundary layer properties, as with most remote sensors, present a number of challenges. Under stable conditions, In particular, sodars reveal a complex distribution of echo structures including simple ground-based echo layers, elevated scattering layers, internal wave phenomena, and intermittent turbulence. However, with recent interest in snow-atmospheric chemical exchange at both Summit Station Greenland and in Antarctica, a critical feature to quantify is the depth through which emissions from the surface can mix. In particular, photodenitrification of the snow at the South Pole in several past experiments has provided a surface source of a relatively short-lived species that tracks very closely the mixing layer depth. In this study we have used sodar and other supporting data from South Pole Station, Antarctica. Both sodar reflectivity and surface turbulent fluxes were obtained in half-hour averages. Because the South Pole lacks a diurnal cycle, transitions between stable and convective conditions typically occur in response to air mass changes and changes in the surface radiation balance due to cloud cover. This paper will address 1) profile classification using a decision-tree approach, 2) interpretation of sodar reflectivity using tethersonde profiles of nitrogen oxide, ozone, and meteorological profiles, 3) comparison with surface micrometeorology.

2   Instrumentation

A minisodar was deployed at the South Pole from November 18 to December 27, 2003. It was located about 140 m west of the Atmospheric Research Observatory (ARO). The sound source was a compression driver located at the focal point of a parabolic dish some 1.2 m in diameter. A separate receiving antenna system was located next to the transmitting antenna: this so-called bistatic arrangement reduced the effect of reverberations in the system and provided a lower minimum range. When the antennas were first deployed on the snow surface we found a minimum range of about 4 m. However, when the antennas were elevated to avoid drifting of snow, the minimum range increased to about 14 m because of reverberation between the antenna and the snow surface.

The operating frequency was 2100 Hz, the pulse repetition period was 1.18 s, and the pulse length was 0.020 s. The pulse length 0.020 s provided a resolution of about 3 m while the

period of the sounding gave a maximum range of about 180 m ± 2.5 m, depending on air temperature. In the course of one hour, for example, approximately 3000 scans are accumulated to provide a detailed time-height cross-section of the strength of the scattered signal, which describes in great detail the behavior of the ABL. Routine wind (1 level) and temperature (3 levels) were measured on the Station's 22-m tower. Twice-daily rawinsondes were also available.   For the last two and a half weeks of the program, tethered-balloon measurements provided a series of temperature and wind profiles together with profiles of ozone and nitrogen oxide along with sonic anemometers providing surface fluxes of sensible heat and momentum (Helmig et al., 2006b).

3   Results
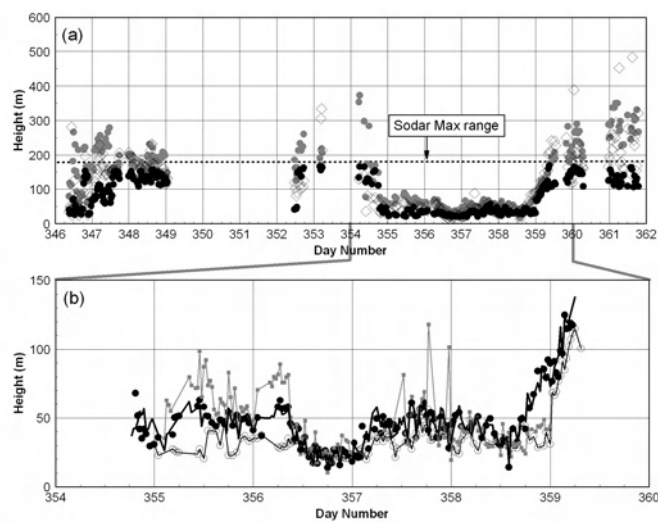
Figure. (a) Time series of sodar-observed mixing depth (solid dots) compared with various diagnostic boundary layer depth equations, and (b) time series for Days 355-359 for sodar-derived mixing depth (open circles) and those derived from two different estimators, and with echo half-amplitude height (solid dots).

4   Discussion, Conclusions, and Outlook

Analysis of surface turbulence data, obtained during the later part of the experimental period, using simple diagnostic expressions showed success with very shallow (<50 m) mixing layers and overestimation for greater depths in comparison with sodar data. The surface stress was found to be the most robust surface parameter controlling boundary layer mixing. Comparison with balloon profiling of NO suggested that the sodar-determined mixing height was only an upper bound on the mixing height with slow diffusion and/or increased conversion of NO with height possibility explaining the rapid falloff with height of NO within the mixing layer. Results from this study are described in greater detail in Neff et al. (2006)

Literature

Helmig, D., Johnson, B., Oltmans, S., Neff, W.,Eisele, F.,Davis, D., 2006: Elevated Ozone in the Boundary Layer at the South Pole. Atmos. Env. (Submitted)

Neff, W., Helmig, D., Grachev, A., Davis, D., 2006: A Study of Boundary Layer Behavior Associated with High NO Concentrations at the South Pole using a Minisodar, Tehtered Balloon and Sonic Anemometer. Atmos. Env. (Submitted)

The algorithm of evaluation of optimum directions and frequencies of air sounding by acoustic systems

Vasilchenko A., Kartashov V.
Kharkov National University of Radioelectronics (61166, Kharkov, pr. Lenina,14, the Chair of Radioelectronic Systems) E-mail: res@kture.kharkov.ua; andrey943@datasvit.net;

The issues of selection of optimum as regards minimum noise disturbances of directions and frequencies of sounding sodar are considered. The synthesis of corresponding algorithms for different criteria of optimality was carried out. The efficiency of algorithms was checked by the method of mathematical simulation.

1   Introduction

The external noise is the basic factor that limits effectiveness of operation of acoustic sounding systems.

The application of Adaptive Phased Antenna Arrays (APAA) as a receiving antenna of AASS allows implementing adaptive spatial or spatial-frequency selectivity and it is an effective mean to abate external noises and disturbances.

As opposed to the radiolocation tasks when the position of the target identifies strictly the direction of radiation, the target in the acoustic sounding is a sufficiently big distributed object and that allows to change the direction of sounding within the definite ranges.

If we select those directions and frequencies as the basic sounding parameters that ensure the lowest level of noise output of the system, we can improve the usable sensitivity of the acoustic air sounding systems and, thereby, to enhance effectiveness of acoustic radar operation.

2   Results

The analysis of jamming environment is in the direct creation of the dependence of the integral noise power N_o on the direction of the primary maximum of directional diagram θ_0, φ_0, and carrier frequency f_0.

One can apply such an approach for the AASS with APAA which operate according to the algorithms using priori information on the sounding direction and frequency (parametric algorithms).

Hereat, the dependence function of the AASS integral noise output is written in the shape of $N_0(\theta_0, \varphi_0, f_0) = \delta \cdot \vec{W}_{opt}(\theta_0, \varphi_0, f_0) \hat{R} \cdot \vec{W}^H{}_{opt}(\theta_0, \varphi_0, f_0)$, where $\vec{W}_{opt}$ is the vector of the optimum weighting factors, $\hat{R}$ is the valuation of the noise correlation matrix (in absence of the useful signal), δ is the arbitrary constant.

3   Discussion, Conclusions, and Outlook

Irrespectively from the criterion according to which the adjustment of weighting factor of APAA is made, the creation of output function allows to evaluate the jamming environment and spatial-frequency spectrum (SFS) of noises and to determine the best sounding direction and frequencies as regards to the noise level.

The adaptive methods of control of the weighting factor allow to achieve the satisfactory results in suppressing noises falling into the antenna beam or the pass band of the AASS. However, in this case the, as a rule, the shift of the primary maximum of the direction diagram or amplitude-frequency response channel takes place and this leads to the losses of the usable signal. Therefore,

when selecting sounding directions and frequencies it is necessary to organize sufficient spatial and frequency separation of noise and usable signal.

In order to evaluate necessary spatial and frequency separation it's expedient to apply division of the spatial-frequency spectrum into definite zones within which you can obtain a particular qualitative result that, in its turn, will define the priorities at selection of sounding directions and frequencies.

The general principle of such a sounding can be shown by the example of two-dimensional SFS obtained by the method of mathematical simulation of the array.

In Figure 1 the areas corresponding to the noise directions and frequencies are shown by black color. We shall call these areas *the interference zone*. The radiation and reception of signals in these frequencies and directions within the interference zone is unacceptable.

In some neighborhoods of the interference zone we can highlight the area of directions and frequencies at positioning on which the noise falls into the antenna beam of the direction diagram or pass band of the amplitude-frequency characteristic. We shall call this area *the conditionally safe zone* (shown by gray color).
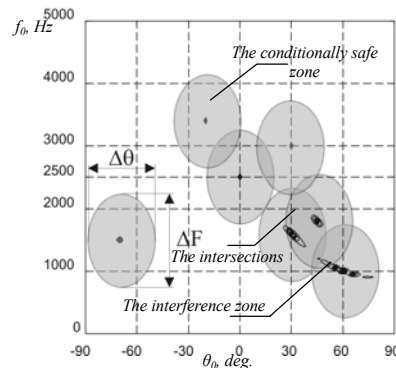
Figure 1.

The shape of the conditionally safe zone is determined by the section of array factor by the plane at the level of 3dB or 10dB. The size of the conditionally safe zone along the frequency axis is determined by the corresponding pass band ΔF, and along the angle axis by the width of the direction diagram $\Delta\theta$. *The intersections* of conditionally safe zones determine areas of frequencies and directions at positioning on which two or more interferences fall into the primary maximum. The sounding at frequencies and in directions within the intersection area (zone) is undesirable.

We shall call the rest of the frequencies and directions area *the safe zone*. The selection of frequencies and directions for sounding within the safe zone gives the best results as regards the provision of maximum signal-noise correlation and allows to enhance the possibility of satisfactory operation (as regards the interference) and to improve significantly the actual sensitivity of the system. In cases when the safe zone is absent or does not satisfy the sounding conditions, it is possible to select directions and frequencies within the conditionally safe zone or intersection zone. However, in this case the qualitative characteristics of the system may decline.

Literature

1 *Krasnenko N.P.* Acoustic Air Sounding. Novosibirsk: Nauka, 1986

2.*Kartashov V.M., Sytnik O.V., Vasilchenko A.A.* The Algorithm of Evaluation of Optimum Directions and Frequencies of Air Sounding By Acoustic Systems // Radiotekhnika: All-Ukrainain Interdepartmental Scientific and Engineering Reports Book 2001 Issue 121 pps. 42-46

3. *Titarenko L.A.* Adaptive Spatial Signal Processing in Conditions of a Priori Uncertainty – Kh. KhNUR; Collegium, 2004, p. - 216

The new PC-based sodar LATAN-3

Rostislav D. Kouznetsov

Obukhov Institute of Atmospheric Physics Moscow, Russia, e-mail: roux@ifaran.ru

Abstract

The new Doppler sodar system LATAN-3 was developed at Obukhov institute of Atmospheric physics. The system design is described. The results of field tests are presented.

1 Introduction

The sodar LATAN-3 was developed at Obukhov Institute of atmospheric physics. The primary motivation for the development was a need for a sounding system for turbulence measurements in the atmospheric boundary layer (ABL). Traditionally the sodars are used for measurements of wind profiles and qualitative analysis of vertical structure of the ABL. Nowadays many manufacturers offer systems that are able to reliably measure wind profiles without need of a qualified personnel. The drawback of that is a lack of flexibility which is required for non-standard applications like turbulence measurements.

2 System design

The hardware of LATAN-3 is shown in Fig. 1. The sodar contains minimum of electronic modules. The generation of sounding signal and digitizing of echo-signal is implemented on PC-soundcard. The only functional electronic modules are power amplifier (Amp1), switch (SW) and microphone amplifier (Amp2). The switch is controlled by the parallel port of the PC.

The LATAN-3 sodar is designed to be operated with parabolic dish antennae. It had been successfully operated with antennae of LATAN-1 (IAPh, Russia) and Echo1D (H.Hertz Institute, Germany) sodars as well as with LATAN-2 mini-sodar antennae without any modification in hardware.

The software of sodar is written in general-purpose languages and consists of several small programs that can be used independently. The operating parameters are controlled by configuration files. The sounding cycle is governed by a script that is responsible for timing and sequence of soundings, for processing of echo-signals and for storage of resulting data. This script calls external programs to get every echo-signal and to process it. The sodar algorithms were designed to process each particular echo-signal separately. The processing program extracts from each echo-signal three numbers for each range gate: signal intensity, noise intensity and radial velocity component. Afterwards, the mean wind speed components and their variances can be estimated. The radial wind components for each range gate are estimated from FFT-spectrum of corresponding part of echo-signal. The set of graphical tools were developed to average and preview the sodar data. They operate independently of other sodar programs. The performance of low-end Linux-based PC is enough for system operation with currently implemented data processing.

3 Field tests

The field testing of LATAN-3 sodar was performed in during July 2005 at Zvenigorod Scientific Station of IAPh (ZSS or Zvenigorod). ZSS is located in a rural area with slightly inhomogeneous terrain 45 km to the west from Moscow. The ultrasonic anemometer USA-1 (METEK, Germany) installed at the top of the 56-m meteorological mast was used as reference. For evaluation of accuracy of measurements the 30-minute averaging was used.
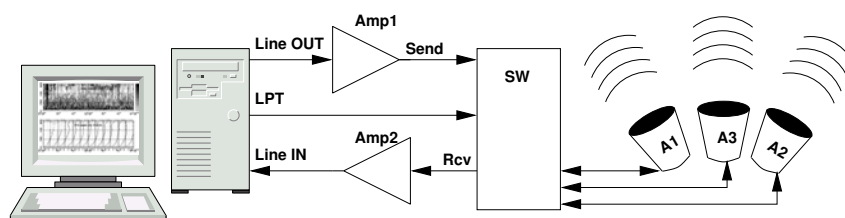
Figure 1. The LATAN-3 sodar hardware
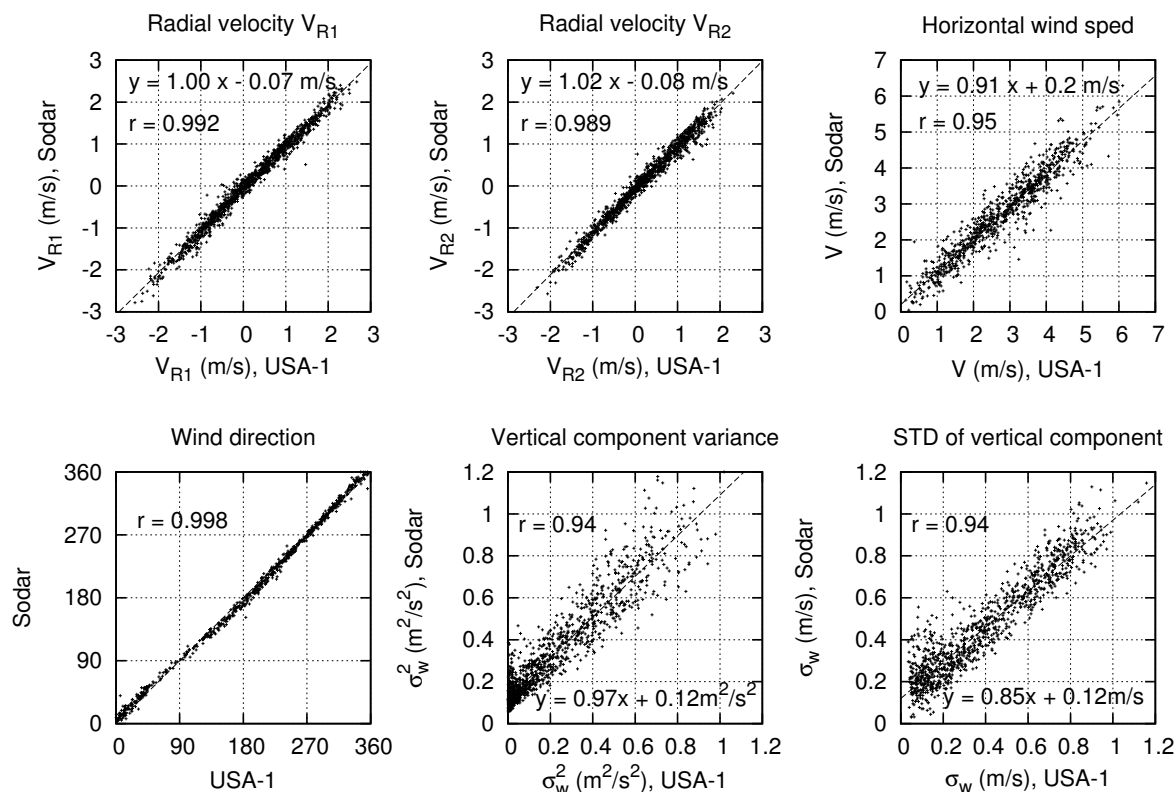
Figure 2. The results of comparison of LATAN-3 data with *in situ* those

The results of field test are shown in Figure 2. The variance of vertical wind component values measured from each single sounding was found to contain an additive noise that results from data processing algorithm and is almost constant in time. The variance of this noise $(0.07\text{m}^2/\text{s}^2)$ was subtracted from σ_w^2 values measured by sodar before calculating σ_w.

4 Conclusion

The simple, flexible and open-for-improvements sodar system LATAN-3 was developed.

The results of a field tests of LATAN-3 indicate a good agreement of sodar-measured wind components and their variances with those measured locally on the meteorological tower. Currently implemented algorithms perform separate processing of individual echo-signals. This makes it possible to study relatively fast processes in the atmospheric boundary layer.

Currently two systems of this type are in permanent operation in Moscow. One is located in the center of the city, another one is operated about 7 kilometers to south-west from the center, at the roof of physical faculty of Moscow University. The system has proven its ability to operate in a noisy urban environment.

An Overview and Highlights from a Special Session at the 2006 EGU on Boundary Layers in the High Latitudes

Neff, W. (1), Argentini, S. (2), and Anderson, P. (3)

[1]NOAA/Earth System Research Laboratory, Physical Sciences Division, Boulder, Colorado 80305,
william.neff@noaa.gov
[2] ISAC/CNR, Area di Ricerca di Roma Tor Vergata, Via del Fosso del Cavaliere, 100, 00133 Roma-Italy
[3] British Antarctic Survey, Natural Environment Research Council, High Cross, Cambridge, UK

Abstract

Boundary layers in high latitudes, including those over sea ice and the high terrain of Greenland and Antarctica, present major challenges for weather and climate models. This special session at the spring meeting of the European Geosciences Union focused on both observational studies and the application of weather and climate models.

Overview

Past sessions of the European Geosciences Union (EGU) have dealt with boundary layers in the context of air-sea and air-land interaction, from theoretical perspectives, and indirectly in applications such charcterizing snow-atmosphere exchange processes, particularly for gas exchange. In 2006, we introduced a special session to address progress in observing, understanding, and modeling boundary layers in high latitudes. A total of six oral talks and seventeen posters were presented based on observational and/or modeling programs in the Arctic and the Antarctic. In this presentation we will review contributions focused on the following areas:

- Studies on boundary layer phenomena at field sites such as
  - Concordia Station, Antarctica: multi-sensor studies of the evolving boundary layer, clouds and radiative processes
  - Drifting Arctic ice stations (SHEBA): Stable boundary layer regimes, flux-profile relationships.
  - Kohnen Station, Antarctica: Surface energy budget, modeling, low-level jets.
  - Halley Station, Antarctica: multi-sensor studies of the evolving boundary layer, snow-atmosphere gas exchange.
  - South Pole Station, Antarctica: snow-atmosphere gas exchange, the stable boundary layer in the absence of a diurnal cycle, synoptic/terrain control of low-level flows.
  - Summit Station Greenland: Radiative cooling/warming in the atmospheric surface layer, snow-atmosphere gas exchange, flux-profile relationships.
- Regional meteorology and modeling of Greenland and Antarctica
  - Testing of boundary layer schemes: Effect of surface roughness on scalar transfer, LES simulations of katabatic flows,
  - Regional models: ablation/accumulation of snow, optical turbulence, large-scale katabatic flows and barrier winds
  - Regional observations: extreme weather events, large-scale katabatic flows and barrier winds
- Future high-latitude observatories (SEARCH): Interpreting data from new Arctic observatory sites around the Arctic Ocean.

Literature

http://meetings.copernicus.org/egu2006/
AS2.04 Boundary Layers in High Latitudes: Observations and Modeling (co-listed in CR)
Abstracts: http://www.cosis.net/members/meetings/sessions/accepted_contributions.php?p_id=184&s_id=3436

Remote sensing method to investigate the diurnal variation of the vertical structure of the atmospheric boundary layer

Stefan Emeis and Klaus Schäfer
Institute for Meteorology and Climate Research – Atmospheric Environmental Research
Forschungszentrum Karlsruhe GmbH, Kreuzeckbahnstr. 19, 82467 Garmisch-Partenkirchen,
Germany, stefan.emeis@imk.fzk.de

Abstract

Simultaneous surface-based remote sensing with optical (ceilometer) and acoustic (sodar) methods allows inferring the diurnal variation of the structure of the atmospheric boundary layer with high temporal resolution. Primarily the convective boundary layer, the nocturnal stable surface layer, and the residual layer can be identified from the measured vertical profiles of optical and acoustic backscatter intensity and the acoustically measured variance of the vertical velocity component. The potentials of a combined operation of these two remote sensing techniques is shown in different examples from different places and seasons. The method is not limited with height because the ceilometer can detect aerosol concentration differences up to 3000 to 4000 m above ground.

1   Introduction

The thermal structure of the atmospheric boundary layer and the height of the mixing-layer (MLH) are essential quantities when assessing the air quality and the vertical dispersion of air pollutants because they determine and limit the speed and the range of vertical dispersion. As most of the aerosol particles are usually confined to atmospheric layers below MLH, the knowledge on the depth of the mixing layer can also be employed to convert optical depths measured from satellites into near-surface air quality information (Sifakis et al., 1998). Vertical dispersion and MLH depend heavily on the synoptic weather situation. An extremely pronounced diurnal variation of these phenomena can be observed in spring and summer under clear sunny skies over land.

In Central Europe, MLH can easily reach 2000 m and more in spring and summer. The use of modern ground-based remote sensing techniques in order to follow the diurnal variations of these layers seems promising. Beyrich (1997) has listed the possibilities which arise from the use of acoustic backscatter intensities from a sodar. An enhanced method which makes use of the backscatter intensity and the variance of the vertical velocity component simultaneously is described in Emeis and Türk (2004). Direct detection of MLH from acoustic backscatter intensities is limited to the order of about 1 km. Optical remote sensing offers higher height ranges of at least several kilometres. An estimation of MLH from optical backscatter intensities from ceilometer measurements is presented in Schäfer et al. (2004).

2   Methodology

From the acoustic and optical remote sensing data the following features will be analysed by an automated procedure: the height of a turbulent layer (H1) characterized by high acoustic backscatter intensities due to thermal fluctuations and a high variance of the vertical velocity component (σ_w), the height of a surface-based or lifted inversion (H2) characterized by high acoustic backscatter due to a sharp increase of temperature with height and simultaneously low σ_w, and the height of the surface-based aerosol layer (H3) characterized by the maximum of the vertical gradient of the optical backscatter intensity. Details for H1 and H2 are described in Emeis and Türk (2004), and for H3 in Schäfer et al. (2004). The combined analysis of optical and acoustic remote sensing information is presented in Emeis and Schäfer (2006).

Acoustic remote sensing by sodar also yields wind fields that in principle could be used for determination of the MLH, too. Because the wind information above the inversion was not regularly available, wind data have not been included into the scheme for the determination of the MLH. Radiosonde information at noon is available for most of the dates in the results presented. For some dates such information was at hand also for midnight. Inversions derived from steps in temperature (increasing potential temperature with height) and/or humidity (decreasing relative humidity with height) in the radiosonde profiles have not been used in the abovementioned determination for H1, H2, and H3 but have only been plotted for comparison with the results presented below.

3   Results
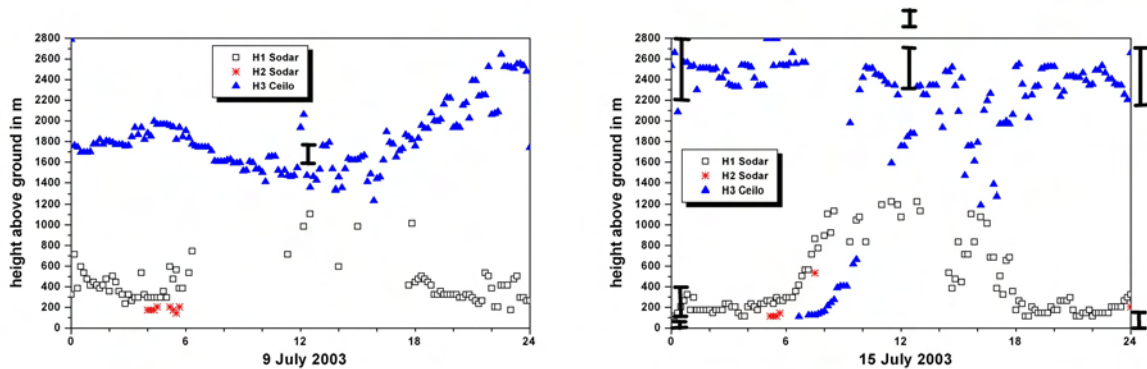
Figure 1. H1 (squares) and H2 (asterisks) from sodar and H3 (triangles) from ceilometer data taken in Budapest for 9 (left) and 15 (right) July 2003. Bars indicate temperature inversions from radiosonde data.

Fig. 1 shows examples for MLH determination for summer days with the formation of a convective boundary layer (CBL) during the day. During the night the stable surface layer (below H1) can be distinguished from the residual layer (between H1 and H3). On July 15, 2003 it can be observed that the layer with high aerosol content (H3) develops later than the thermal structure of the CBL (H1). Lifted inversions (H2) are nearly absent in this period. The height variation in H3 partly comes from large-scale vertical motions connected to synoptic weather systems.
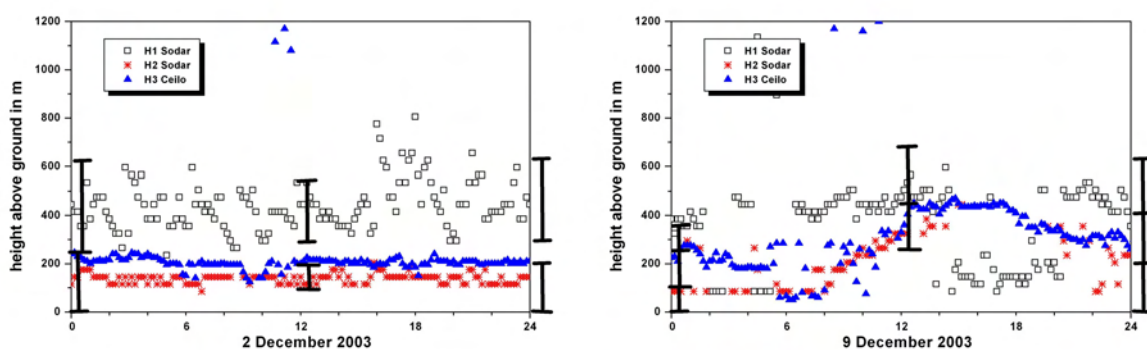
Figure 2. H1 (squares) and H2 (asterisks) from sodar and H3 (triangles) from ceilometer data taken near Munich for 2 (left) and 9 (right) December 2003. Bars indicate temperature inversions from radiosonde data.

Fig. 2 shows examples for MLH determination for two winter days dominated by a foehn flow north of the Alps. H2 signifies the foehn inversion in these evaluations. On December 2 the height of foehn inversion (H2) compares very well with the height of the aerosol-loaden layer H3. H1 is higher than H2 and H3 because there is considerable turbulence in the foehn flow above the inversion. On December 9 a weak cold front disturbed the stable layer below the foehn inversion in the late morning hours.
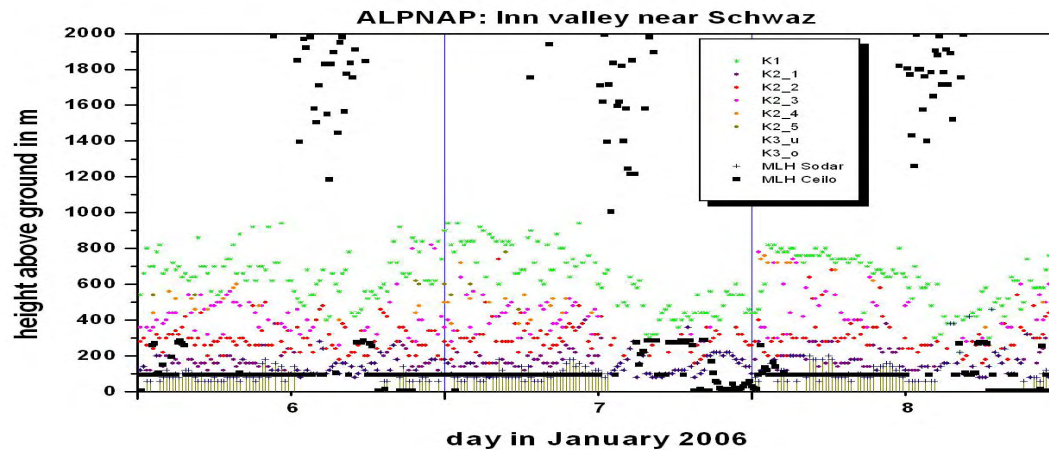
Figure 3. H1 (asterisks labelled 'K1'), several lifted inversions H2 (circles, labelled 'K2_1' to 'K2_5'), and surface-based inversions (vertical lines) from SODAR and H3 (squares labelled 'MLH Ceilo') from ceilometer data taken in the Inn valley east of Innsbruck for 3 days (January 6-8, 2006).

Fig. 3 shows a more detailed analysis of the stable stratification during clear and very cold winter days in an Alpine valley with snow cover. The analysis of H2 has been refined and splitted into the separate detection of the height of the surface-based inversion and up to five lifted inversions. The height of the surface-based inversion coincides well with the aerosol-loaden layer H3. Only for a few hours during the afternoon the surface-based inversion is broken up by the sunshine.

4   Conclusions

The combined operation of acoustic and optical remote sensing techniques offers the possibility to analyse the vertical structure of the atmospheric boundary layer. Because the acoustic technique observes thermal structures and the optical technique observes the aerosol distribution different layers like the stable surface layer, the convective boundary layer and the residual layer can be easily distinguished. The high temporal resolution of this data is a great advantage compared to radiosonde data twice or four times a day. Such boundary layer structure data bears a great potential in emission studies and air quality assessments.

Acknowledgements

Literature

Beyrich, F., 1997: Mixing height estimation from sodar data - a critical discussion. Atmos. Environ., **31**, 3941-3953.

Emeis, S. and K. Schäfer, 2006: Remote sensing methods to investigate boundary-layer structures relevant to air pollution in cities. Bound-Lay. Meteorol., DOI: 10.1007/s10546-006-9068-2.

Emeis, S., M. Türk, 2004: Frequency distributions of the mixing height over an urban area from SODAR data. Meteorol. Z., 13, 361-367.

Schäfer, K., S.M. Emeis, A. Rauch, C. Münkel, S. Vogt, 2004a: Determination of mixing-layer heights from ceilometer data. In: Klaus Schäfer, Adolfo Comeron, Michel Carleer, Richard H. Picard, Nicolas Sifakis (eds.): Remote Sensing of Clouds and the Atmosphere IX, Proc. SPIE, Bellingham, WA, USA, Vol. 5571, 248-259.

Sifakis, N., N. Soulakellis, D. Paronis, 1998: Quantitative mapping of air pollution density using Earth observations: a new processing method and application to an urban area. Intern. J. Rem. Sens., **19**, 3289-3300.

On the vertical structure of the Atmospheric Boundary Layer over the sea

Helmis G. Costas

Department of Applied Physics, Faculty of Physics, University of Athens, Greece

University Campus, Building Phys.-5, 15784, Athens, GREECE

e-mail:chelmis@phys.uoa.gr

Abstract

The main characteristics of the mean and turbulent vertical structure of the Marine Atmospheric Boundary Layer (MABL) were examined, using both remote and in situ sensing instrumentation. The observations indicated a very stable surface layer up to the height of 150-200m followed by slightly stable to neutral conditions at higher levels, while there was a frequent development of a Low-Level Jet (LLJ) on the top of the intense surface based inversion. The plausible mechanism for the development of the LLJ is the inertial oscillation due to the frictional decoupling over the sea which is associated with the strong stability of the MABL lower layer.

1. Introduction

In recent years the study of the MABL has been the main topic of interest for atmospheric physics, since uncertainties related to the parameterization of the mass, heat and moisture exchange between the air and sea existed and certain atmospheric phenomena such as the development of LLJ or intensified thermal stratifications are associated with the MABL (Smedman et al, 2004). This study was conducted in the frame of the CBLAST-Low project which was aimed at the understanding of the air-sea interaction and the coupled atmospheric and oceanic boundary layer dynamics at low wind speeds (Edson et al, 2004). The objectives of this work are the study of the characteristics and the vertical structure of the MABL and the understanding of the possible cause for the development and evolution of the marine LLJ, which is associated with the strong stability of the MABL lower layer.

2. Instrumentation

The experimental campaign was carried out during the summer of 2003 (31st of July to 27th of August) at Nantucket Island, MA, USA. The experimental site was on the south western side of the island, at a distance of 94m from the shoreline over relatively flat terrain. A commercial (Remtech PA2) SODAR system was in operation yielding, at 30 minute intervals, the mean values of the horizontal wind speed and direction and the vertical component of the wind w, the standard deviations of the three wind components, the momentum fluxes $\overline{u'w'}$ and $\overline{v'w'}$ and the atmospheric static stability. On a 20m mast there were two levels (10 and 20m) of high-rate sampling (20Hz) sonic anemometers and fast hygrometers for the estimation of the momentum, sensible and latent heat fluxes while there were also measurements of the mean wind, temperature, relative humidity at 5, 10, and 20m height from slow sensors. Information regarding temperature, RH, wind speed and direction, air pressure, precipitation, and downward solar radiation at 1 min intervals was provided by a 2m mast. Also a laser ceilometer was detected the cloud base height continuously while rawinsondes were launched at the experimental site every four to six hours each day.

3. Results and Discussion

During the experimental period, a LLJ was developed frequently at low heights, on the top of the surface based strong temperature inversion (the first 200-300m of the MABL). The 8th of August is a good example of the vertical structure of the upwind MABL and the characteristics of the developed LLJ. During this day the area of Nantucket was affected by a warm front passage, during the morning hours, accompanied by an increase of the wind speed and a shift of the wind direction to the south. According to the ceilometer data the cloud base height decreased from 5000m at 08:00 UTC to 250m by 12:00 UTC with scatter rainfall. Conversion from UTC to LST requires a subtraction of 4 hours (LST = UTC - 4hr). Fig.1a gives the vertical profiles of the horizontal wind, from three radiosonde launches at 00:04, 05:30 and 13:17 UTC. The wind direction is almost constant above 300m up to 1000m from

SW while at lower levels a small shift to the south is evident. During the first flight the development of a LLJ into a shallow layer at 220m height with 11.6m/s max value is observed while during the next flight the wind max (13.9m/s) was ascend at 380m height and at the third flight the LLJ into a deep layer (200m) with a maximum value of 15.4m/s.
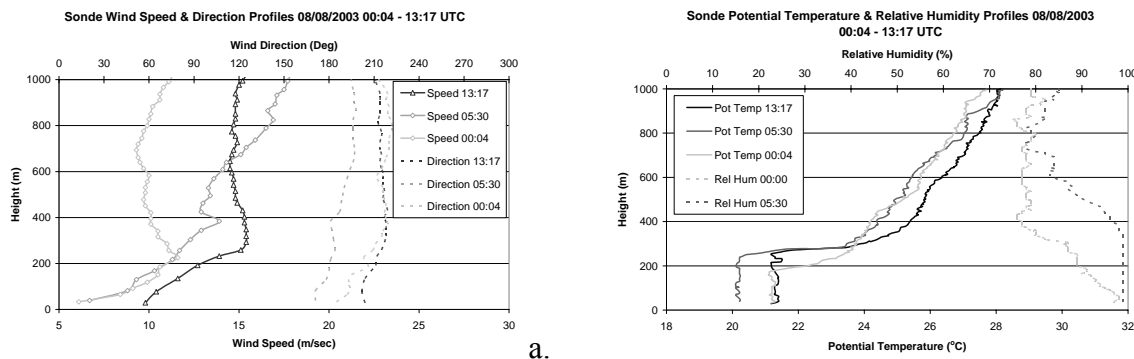
Figure 1: **a**. Vertical profiles of the horizontal wind speed and direction, estimated by three radiosonde launches at 00:04, 05:30 and 13:17 UTC during 08/08/2003
b. Vertical profiles of the potential temperature and the relative humidity, estimated by the radiosondes during 08/08/2003.

The potential temperature profiles (Fig. 1b) show a relatively neutral surface layer, which deepens with time (from 170 to 250m), followed by a very strong temperature inversion layer with gradient $\Delta\theta/\Delta z = 4^{o}K/100m$ and less stable layer ($\Delta\theta/\Delta z = 0.4^{o}K/100m$) higher up. The LLJ was developed on the top of the temperature inversion layer. The humidity profiles show high surface layer values (more than 95%) which rapidly decrease higher up. From the time-height cross sections of the wind speed vectors (Fig. 2), S-SW flow during the first four hours with moderate wind speed is evident. The frontal passage modify the wind flow giving
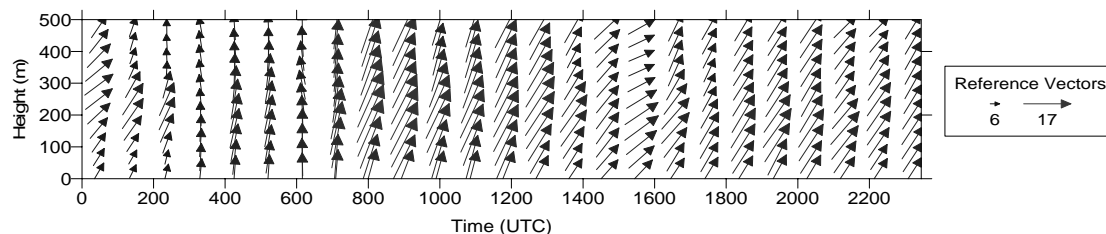
Figure 2: Time-height cross sections of the wind speed vectors estimated by the SODAR for 08/08/2003.

a directional shift to the south, an intense increase of the wind speed (16-17m/s) after 07:30 UTC and the development of a strong LLJ. After 13:00 UTC the wind flow was SW and the speed was decreased. The time-height cross section of the wind speed is given in Fig. 3. During the first hours wind maxima are observed at heights between 250 to 300m, in agreement with the radiosonde measurements, while after 06:00 UTC the development of a strong and persistent LLJ was evident. During the period from 07:00 to 11:00 UTC the LLJ covers a deep layer (more than 300m) with very strong wind speed (17m/s) at the core layer while after 11:00 UTC the LLJ layer was restrained and the wind speed decreased to 14m/s. During the afternoon and evening hours the LLJ gradually descended and remained at the height of 150-200m with lower values at the core layer. Very stable to slightly stable conditions with elevated inversion layers characterize the vertical structure of MABL during the first six hours while after the LLJ development, slightly stable to neutral conditions with elevated inversion layers were observed below its core and neutral conditions existed above (see Fig. 4). After 14:00 UTC, when the LLJ was restrained, stable to slightly stable and neutral conditions prevailed below and above the LLJ core respectively. The horizontal wind speed hodographs derived from the SODAR data for the time period from 00:00-18:00 UTC at the level of 250m height alongside with the radiosonde measurements from four flights
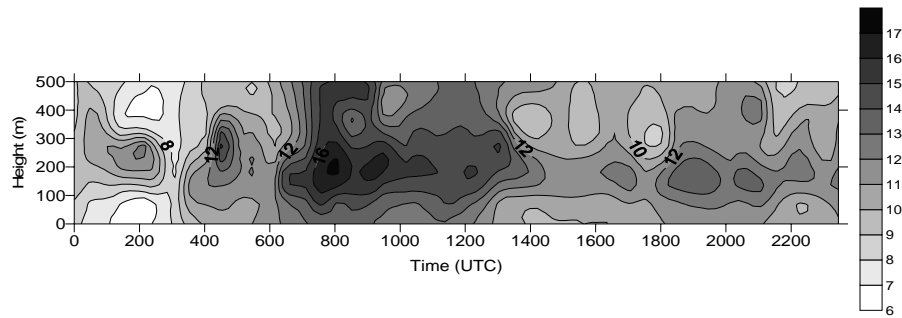
Figure 3: Time-height cross sections of the wind speed estimated by the SODAR for 08/08/2003.

during the day are given in Fig. 5. The wind vector oscillation and the clockwise veering are evident in both wind speed hodographs and this confirms the fact that the possible cause for the development of the LLJ is the inertial oscillation due to the frictional decoupling.
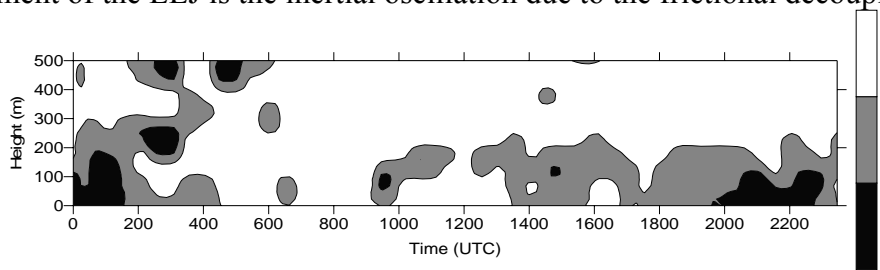
Figure 4: Time-height cross sections of the atmospheric stability classes estimated by SODAR for 8/08/2003. Stability classes 1, 2 and 3 correspond to stable, slightly stable and neutral stratification respectively.
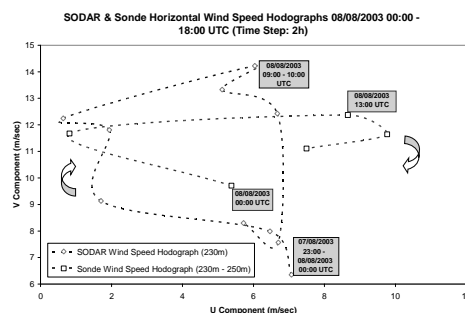
Figure 5: SODAR and Sonde horizontal wind speed hodographs at 230m height for 07/08/2003 13:00 – 08/08/2003 04:00 UTC.

4   Conclusions

Under moderate to high wind, very stable stratification characterizes the lower part of the MABL while under very strong wind neutral conditions are exhibited at the lower part associated with an intense temperature inversion layer above. On the top of the intense ground based inversion layer or above the elevated layer, a LLJ was frequently developed and persisted. A plausible mechanism for the development of the LLJ is the inertial oscillation due to the frictional decoupling associated with the strong stability at the lower part of the MABL.

Acknowledgements

References

Edson J., Crofoot R., McGillis W., Zappa C., 2004: Investigations of flux-profile relationships in the marine atmospheric surface layer during CBLAST, 16th Symposium on Boundary Layers and Turbulence, 9-14 August 2004, Portland, ME.

Smedman AS, Hogstrom U., Larsen G., Johanson C., Rutgersson A., Sjöblom A., Kahma K. K. and Pettersson H., 2004: Towards a fundamentally new understanding of the marine atmospheric boundary layer, 16th Symposium on Boundary Layers and Turbulence, 9-14 August 2004, Portland, ME.

Comparison of Wind Fields in the ABL over Big City and Nearby Rural Site by Simultaneous Sodar Measurements

Margarita Kallistratova*, Rostislav Kouznetsov*, Mikhail Pekour[†], Vladislav Yushkov[‡], Alexander Svertilov*
*Obukhov Institute of Atmospheric Physics, Moscow; [†]Pacific Northwest National Laboratory, Richland, USA;
[‡]Moscow State University, Russia; e-mail: margo@ifaran.ru

Abstract

Simultaneous measurements of wind profiles in the Moscow downtown and in a contiguous rural area were carried out in autonn and in summer time. The urban-rural wind speed difference strongly depended on thermal stratification, strength of wind, and altitude. On average, wind speed in the downtown was less than in the rural area, with 1-2 m/s difference below 100 m and 0.5 -1 m/s at levels above 200 m; wind direction difference was within 10-20 deg. Sometimes the differencies were many times higher than averaged values.

1   Introduction

To comprehensive experimental study of urban impact on wind field and its differentiation with climatic and orographic effects the simultaneous measurements in urban and nearby rural area are necessary. In the last decade several field champagnes were carried out with sodar networks, which provided such measurements. However, statistical data on urban-rural wind field difference in the ABL are not numerous. For instance, only three day data were published from the vast set of data obtained in Rome and the surrounding area [1]. The similar situation have turned out with data acquired in Paris and its rural suburbs [2], and in Moscow and its neighborhood [3]. Below some results of study of urban-rural wind speed difference are presented.

2   Instrumentation and Results

Two one-month-long measurement campaigns were carried out in October 1993 and in July 2005. Two identical sodar operated simultaneously in the center of Moscow megapolis, at the roof of the Obukhov Institute of Atmospheric Physics (IAPh), and at Zvenigorod Scientific Station (ZSS) of IAPh, which is located in a weakly inhomogeneous rural area 45 km to the west from Moscow. The sites separation was large enough to avoid urban wake impact on the rural site for all wind directions, although both sites were usually within the same synoptic system. The LATAN series of sodars developed in IAPh were used in both campaigns: LATAN-1 in 1993 [4], and LATAN-3 (that is more tolerant to ambient noise) in 2005 [5]. An example of a diurnal series of the synchronous sodar data is shown in Fig. 1.
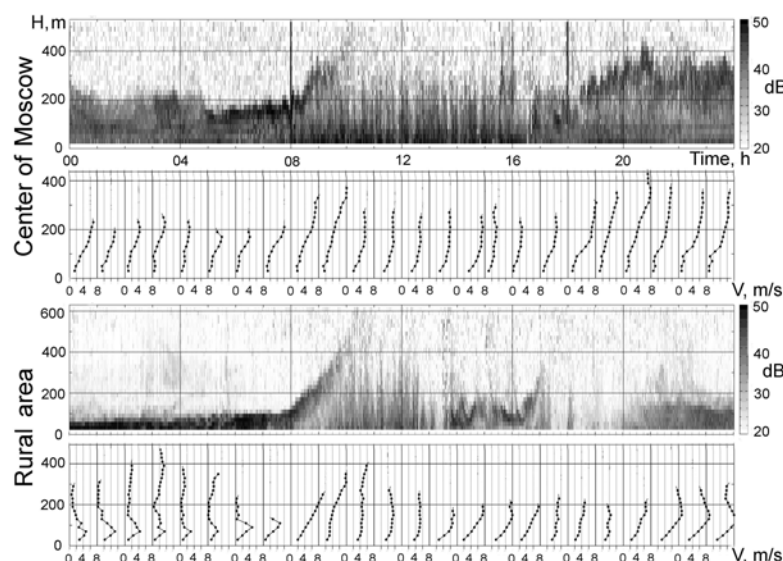
Figure 1. The echograms and 30-min averaged wind speed profiles at Moscow and ZSS, 23 July 2005.

The thermal stratification and mixing height at two sites differ significantly. The upper bound of nocturnal turbulized layer over the city is located much higher, and the morning convective activity below it starts earlier than in rural area. In the night-time the low level jet is usually developed in rural area. It is much less pronounced in the city. The difference in the wind speed between the two sites is strongly dependant on altitude, thermal stratification, and strength of wind. The monthly averaged diurnal cycles of wind speeds for three altitudes are shown in Fig. 2. In the summertime the diurnal cycle of the wind speed in the city is much more pronounced (especially at lower heights) than in rural area. In the fall the thermal stratification of the ABL did not vary much during the day, so the wind speed did not change much at both sites as well. The wind direction in Moscow does not differ much from that in the ZSS (Fig. 2, right). The wider histogram for July is caused by the strong variability of wind direction under weak winds, which prevail at that time.
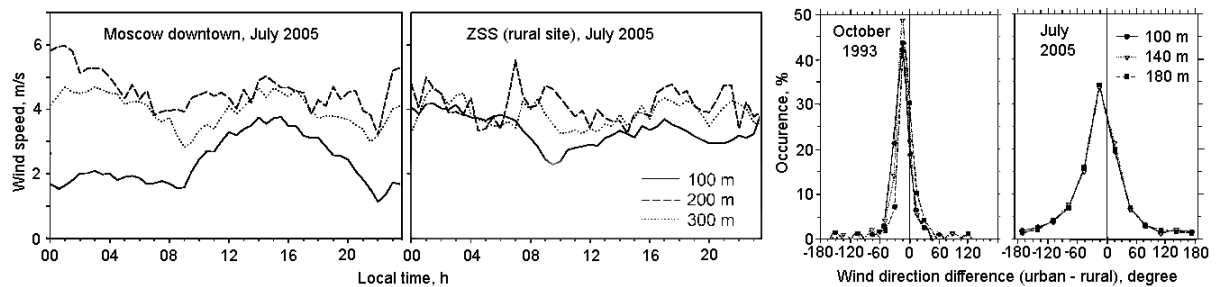
Fig. 2. Averaged diurnal course of wind speed over urban and rural areas (left); wind direction difference (right).

The corresponding scattering plots are shown in Fig. 3. In October, when both natural and antropogenic heating in the city are small, the height dependence of the wind speed difference is caused mostly by the difference in roughness between urban and rural areas. The urban-rural difference in the wind speed depends also on the wind speed itself (Fig. 3, right). Under windy conditions the influence of urban roughness is stronger and reaches larger altitudes than in a calm. Under weak wind the influence of convection on wind profile gets stronger.
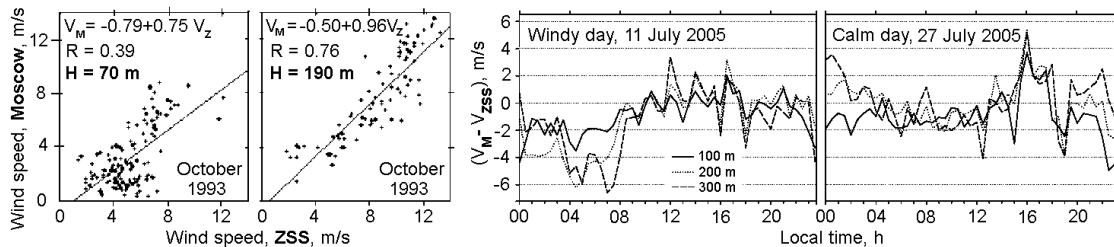
Fig. 3. Urban-rural wind speed scattering plots for two altitudes for the fall time. Wind velocity urban–rural difference under strong and weak wind for the summertime.

In Fig. 4 the urban-rural wind speed scattering plots are shown for the both seasons and for all data obtained. The histogram presented in the right part of the Fig. 4 shows almost symmetrical distribution of wind-speed difference with the median shifted to smaller speed over the city. The shape of wind profiles in urban and rural areas differs significantly (Fig. 5).
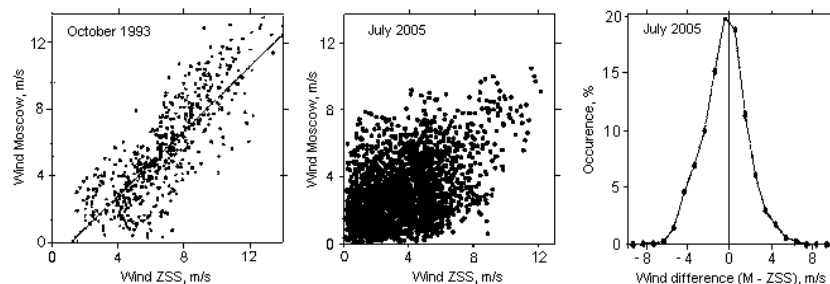
Figure 4. Urban-rural wind speed scattering plots and histogram of wind speed urban-rural difference.

In Fig. 5 the monthly averaged wind profiles measured in Moscow and at ZSS are shown. In October, the shapes of urban and rural profiles are almost similar, and in July the profiles differ much in shape and in magnitude.
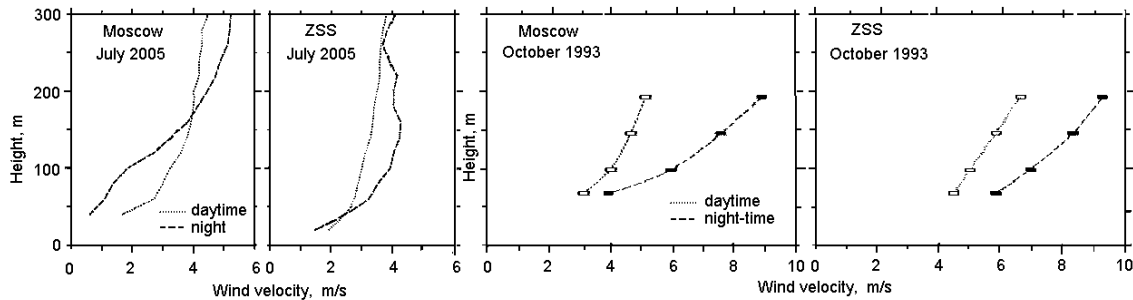
Figure 5. Monthly averaged wind speed profiles over the urban and rural areas for two seasons.

Urban-rural difference in height and temporal behavior of vertical velocity variance is clear seen in Fig. 6.
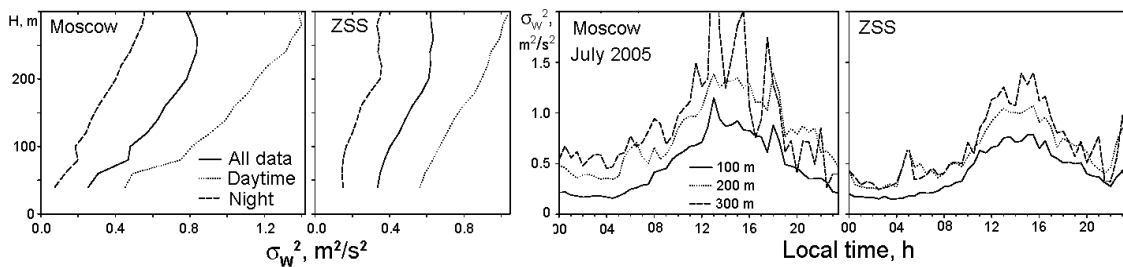
Figure 6. Vertical profiles and time series of vertical component variance in two sites

4   Conclusion

In the fall the influence of urban area on the wind field may be explained by enhanced roughness in the city rather than by heat island effects, because both, the radiation heating and anthropogenic heating of the city are small in that time of year. The shape of the averaged wind profiles is similar in both sites; profiles reveal almost linear increase of speed with height in daytime and in night-time as well.

Mixing height and wind speed differ significantly at the sites in summer season: in average urban mixing height is twice as large as rural one, with occasional difference up to the factor of 4. The nocturnal low level jet is a usual feature of rural area, and is rarely observed at the downtown site. In daytime the mean speed difference at 200 m level above the ground is in the order of 2 m/s (city winds slower) while at night the difference is up to 4-5 m/s. This diversity of wind field is obviously caused by effects of strong solar heating of the city area in daytime and slower cooling at night. On average, wind direction difference was within 10 deg. in fall as well as in summer season. No evidence of urban breese was found.

Literature

[1] **Mastrantonio, G., A.P. Viola, S. Argentini, et al., 1994**: Observations of sea breeze events in Rome and the surrounding area by a network of Doppler sodars. Bound.-Layer Met., 71, 67-80.
[2] **Dupont, E., L. Menut, B. Carissimo, J. Pelon, P. Flamant, 1999:** Comparison between the atmospheric boundary layer in Paris and its rural suburbs during the ECLAP experiment. Atmos. Envir. **33** 979–994.
[3] **Kallistratova, M.A., M.S. Pekour, 1994**: Sodar study of wind field and turbulence over a big city. Proceed. of ISARS'94, 3-7 October 1994, Boulder, USA, 7.13-7.18
[4] **Pekour, M.S., M.A. Kallistratova, 1993**: Sodar study of the boundary layer over Moscow for air pollution application. Appl. Phys. B, **57**, 49-55.
[5] **Kouznetsov, R.D., 2006**: New PC-based sodar LATAN-3. This collection.

Internal gravity waves in the lower atmosphere: spatial and temporal characteristics

Kniffka, Anke [1], Arnold, Klaus [1], Barth, Manuela [1], Ziemann, Astrid [1], Chunchuzov, Igor [2], Kulichkov, Sergey [2], Perepelkin, Vitaly [2]

[1] Leipzig Institute for Meteorology, University of Leipzig, Germany
[2] Oboukhov Institute of Atmospheric Physics, Russian Academy of Sciences, Moscow, Russia
e-mail: kniffka@uni-leipzig.de

Abstract

The effects of internal gravity waves (IGW) on the lower atmosphere were studied by using a combination of different acoustic remote sensing methods. Several measurement campaigns were carried out under stably stratified atmospheric conditions, to examine the influence of the IGW on the variation of acoustic signals.
The discrete temporal and spatial scales found in the measured fluctuations are typical for ducted IGW in the wave-guides formed by the temperature and wind stratification in the lower atmosphere.

1 Introduction

IGW can generate wind and temperature fluctuations with periods from several minutes to a few hours at horizontal scales from hundred metres up to a few kilometres. These fluctuations correspond with the variability of the acoustic signals propagating through the atmospheric boundary layer, such as the travel time, signal amplitude or the angles of arrival. The motivation of this study was the investigation of statistical characteristics of these acoustic parameters to obtain a better appreciation of the influence of IGW on turbulent regimes inside stable atmospheric boundary layers.

2 Instrumentation

To measure meso-scale wind speed and temperature fluctuations different acoustic methods were used. On the one hand, an acoustic pulse sounding method was developed previously for this purpose (Chunchuzov, 2002; Chunchuzov et al., 2005). Acoustic pulses of stable form were generated by means of a detonation of the air-propane mixture in the special tube. Spatially distributed microphones received the acoustic pulses at distances of some kilometres from the generator. This method is a special kind of acoustic tomography of stable ABL based on the existence of the acoustic wave guide near ground surface due to formation of the temperature inversion and vertical wind shear near ground surface.

On the other hand the acoustic travel time tomography was applied. This technique utilised the dependence of sound speed on temperature and wind vector to derive the distribution of these quantities within the measuring area (Arnold et al., 2004; Ziemann et al., 2002). The measuring system consists of several sound transmitters (loudspeaker) and receivers (microphones), which are distributed within a landscape, inside or around the area of interest.

The measuring systems were adapted during several measuring campaigns, separated at the Zvenigorod (Russia) and Melpitz (Germany) research stations in 2004, combined at the joint experiment in Zvenigorod 2005. During the 2005 experiment, the both measuring systems utilised the same sound source (detonation tube) and the travel time differences of this signal due to different propagations paths or reflection levels were recorded at several observation points.

The existence of wave-guides near ground surface was confirmed by the analysis of the vertical wind speed and temperature profiles (Brunt-Vaisala Frequency) in the atmospheric boundary layer, which were continuously controlled by a SODAR/RASS and a profile mast.

3   Results

One example of the signal generated by a pulse generator, and received far away from it, is shown in Figure 1. This Figure illustrates the dependence of the shape of the signal on a distance from the source and on an azimuth of propagation with respect to the mean wind direction. Depending on the distance between the sound source and the receiver, the azimuth and the atmospheric stratification, the microphones receive different arrivals of the transmitted signal. The signal shown in the middle panel "splits" on a set of arrivals A, B, C and D due to wave guiding propagation in the given azimuthal direction. The same signal received at the point forest 1 OIAP (fig. 1, lower panel) with another azimuth does not contain different arrivals, which is a result of anti-guiding character of propagation of the signal in the upwind direction (Chunchuzov et al., 2005).
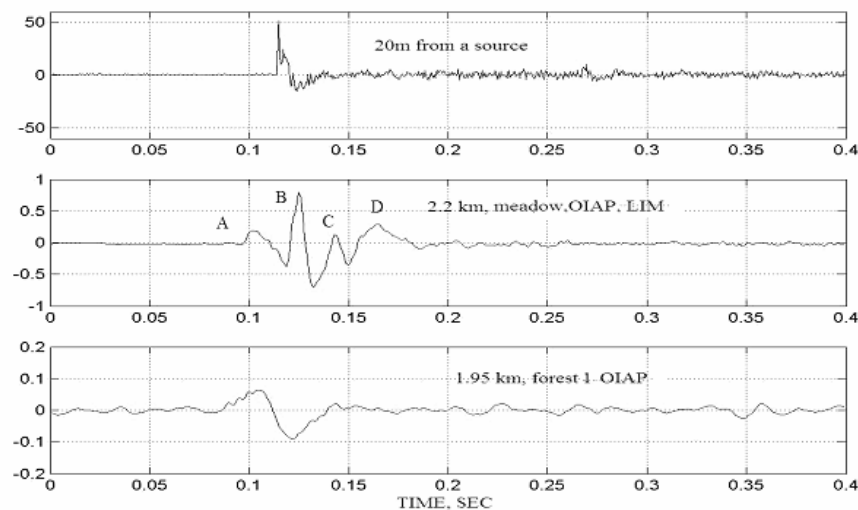
Figure 1. Example of the acoustic signal received on 12 July, 2005 (00:11:55 local time) close to the acoustic source (upper panel), and about 2 km away from the source (middle and lower panels) at the two points with different azimuths relative to the source. The vertical axis is an acoustic pressure in Pa.

For the one-hour time series the cross-coherences and multi-coherence function (K_0) as well as the corresponding phase spectra where calculated. An indication for the occurrence of organised wave structures inside the considered time interval is, that at the same time the multi-coherence function is one and the sum of the phase differences is zero.

The coherence and phase spectra for the travel time differences were calculated as an example for a small triangle (R1, R2, R3) with a side length of about 30 m and a bigger triangle (L1, R2, P5) with side length of 135 m to 400 m, which were located approximately 2.5 km in the same direction from the generator. In Figure 2 examples of the coherence and the corresponding phase spectra are shown for a one-hour time period for the selected triangles.

It is seen from phase spectra, that for the bigger triangle (L1, R2, P5) only low-frequency fluctuations 1 - 2 $\cdot 10^{-3}$ Hz (periods from 16 to 8 min) give a zero value for sum of phases and a multi-coherence close to one. The estimated horizontal wavelengths of such fluctuations are 2.5 to 2.9 km, which are comparable to the maximal sizes of the big triangle. Their horizontal speed is about 3.5 - 4 ms^{-1}.

For the small triangle (R1, R2, R3) with 30 m side lengths the dominant periods are within the following intervals, where the coherences take maxima with the zero sum of phases: 30 - 8 min, 5.5 - 3.5 min and 2.5 - 2 min. Due to small sizes of the triangle it is possible to estimate only fluctuations with short wavelengths about 150 to 200 m and low phase speeds (less than 1.5 ms^{-1}).
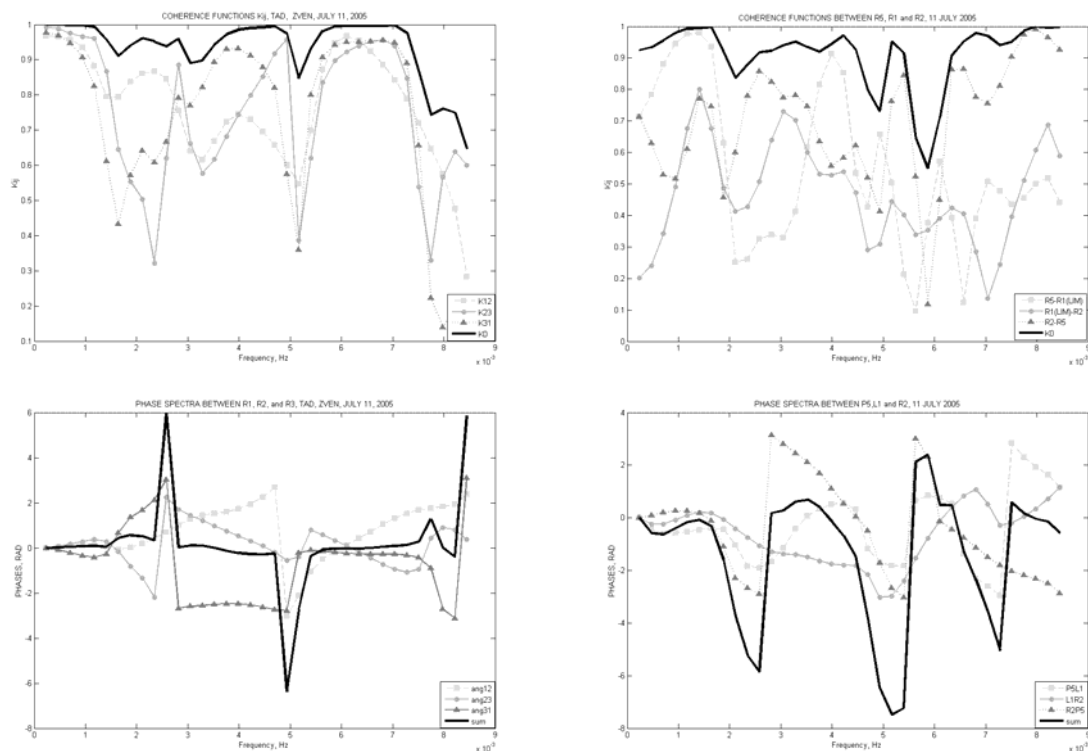
Figure 2. Coherence (upper panel) and spectra of the phase differences (lower panel) of the travel time on 12th July, 2005 for a one-hour night time period. On the left side a small triangle with 30 m sides (receiver: R1, R2, R3) was chosen, on the right side a bigger triangle with a side length of several hundreds meter (receiver L1, R2, P5). A maximum of the coherence together with a sum of the phase difference equal zero indicates the occurrence of internal gravity waves.

4 Discussion and Outlook

First estimates of the horizontal scales of travel time fluctuations revealed their discrete nature, which may be associated with the existence of the discrete spectrum of internal wave modes in the wave-guides formed in the lower atmosphere. The travel time measurements with an array of spatially distanced receivers allowed us to find the relationship between horizontal and temporal scales of the fluctuations by calculating their cross-coherences and corresponding phase spectra. Further investigation should concentrate on the generalisation of the received results to characterise the impact of the IGW on the lower atmosphere, and to incorporate this impact in numerical models.

Literature

Arnold, K., Ziemann, A., Raabe, A., Spindler, G., 2004: Acoustic tomography and conventional meteorological measurements over heterogeneous surfaces. Meteorol. Atmos. Phys., 85, 175-186.

Chunchuzov, I.P., 2002: On the high-wavenumber form of the Eulerian internal wave spectrum in the atmosphere. J. Atm. Sci., 59, 1753-1772.

Chunchuzov, I.P., S. Kulichkov, A. Otrezov, V. Perepelkin, 2005: Acoustic pulse propagation through a fluctuating stably stratified atmospheric boundary layer. J. Acoust. Soc. Am. 117, 1868-1879.

Ziemann, A., K. Arnold, A. Raabe, 2002: Acoustic tomography as a Remote Sensing Method to Investigate the Near-Surface Atmospheric Boundary Layer in Comparison with In Situ Measurements. J. Atmos. Ocean. Techn., 19, 1208-1215.

Characteristics of the Local Circulation in the Low Tiber Valley Inferred by the Statistical Analyses of Wind Measurements.

Mastrantonio[1], Giangiuseppe, Viola[1], Angelo, Petenko[1,2], Igor, Argentini[1], Stefania
[1] ISAC-CNR, Via Fosso del Cavaliere 100, 00133 Rome, Italy
[2] A. M. Obukhov IAP, RAS, 3 Pyzhevsky, Moscow, 109017, Russia
e-mail: g.mastrantonio@isac.cnr.it

Abstract

In this work, the local circulation in Rome and the surrounding area is studied using the statistical analysis of the wind field. The wind data were recorded by Doppler sodar systems and by meteorological stations. The meteorological information recorded at the Fiumicino Airport, was used to select data associated to different meteorological conditions. Profiles were used to obtain vertical structure and depth of air flows, while direction and speed were used to characterise the local circulation components. No significant change of the local circulation in the period 1994-2003 emerges from the analysis of surface wind data at the Fiumicino airport.

1   Introduction

The low level circulation is the result of a non linear interaction between large scale and local circulations. The latter often prevails in the Mediterranean regions, especially in the warmer periods, and has important effects on agriculture and other forms of human activity. The local circulation plays a major role in the processes of transport and diffusion of pollutants, in particular around and inside the urban areas where these may affect the air quality and the health of the population. In this work, the local circulation in Rome and the surrounding area is studied by using the statistical analysis of the wind field. The main objective is to see if any evidence of a local circulation modification in the period 1994-2003 emerges if the synoptic scale components are filtered out as much as possible. The area, within the lower Tiber valley and surrounded by hills, is adjacent to the Tyrrhenian sea located to the southwest. It is well known that in the area the sea breeze is the prevalent component of the local circulation. Colacino (1982) shows how, during the summer, sea breeze modifies the local structure of the boundary layer and affects the urban heat island. Mastrantonio et al. (1994) highlight the sea breeze vertical structure and its time-space evolution by using a net of sodars.

2   Instrumentation and data analysis

The time series of wind data were recorded by Doppler sodar systems operating in the area, and by meteorological stations. The meteorological information reported in the METAR (the

AMA: Ponte Malnome; 41°51' N; 12°19' E, 65 m a.s.l.
FCO: Fiumicino Airport; 41°46' N; 12°14' E, 4 m a.s.l.
IFU: University "La Sapienza"; 41°54' N; 12°31' E, 60 m a.s.l.
PDM: Pratica di Mare Military Airport; 41°40'N; 12°27' E , 12,2 m a.s.l.
UCEA: Ufficio Centrale Ecologia Agraria; 41°53'54"N; 12°28'46" E 66,4 m a.s.l.
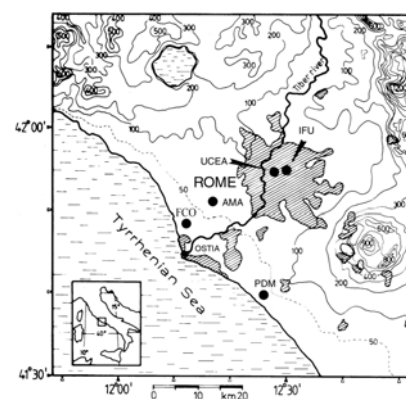
Figure 1. Map of the area around Rome with the location (full dots) of the measurement sites.
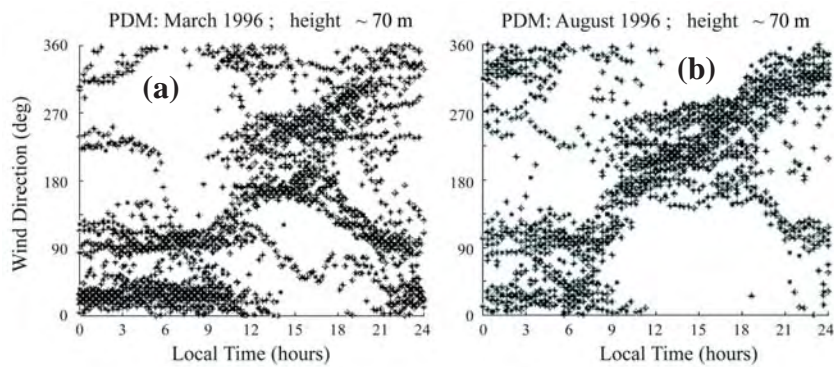
Figure 2. Daily wind direction statistics measured by sodar at PDM in March (**a**) and August (**b**).

international code to report routine, hourly weather conditions at air terminals), collected in the last ten years at the Fiumicino Airport, were used to select the different meteorological conditions and to reject data not associated to fair-weather conditions. Ten minutes averaged wind profiles recorded by 3 sodars simultaneously operating in the area were used to retrieve the vertical structure and depth of the air masses involved in the local circulation. The statistical analysis of the daily behaviour of the wind, on a monthly and seasonal basis, made the characteristics of the local wind (speed and direction) clearly emerging. In Figure 2 the scatter diagrams of the wind directions measured at 70 m at PDM are shown for March and April. The direction clusters associated with the diurnal and nocturnal circulation are evident. The duration appears different, according to the season. In Figure 3 the nocturnal wind direction profiles, associated with the direction cluster of the sector 0-40° in Figure 2, are shown. The decoupling between the lowest and higher atmospheric layers allows to estimate the depth of the nocturnal local circulation. The mean intensity profiles (not shown) reveal a jet-like shape typical of gravity currents. The information of the direction and starting time of the wind at some locations was used to determine the origin of the circulation. The wind speed statistical analysis evidenced the relative intensity of local circulation components and the effect of their interaction.

3   Results and discussion

At Pratica di Mare two different types of gravity currents are recorded, the first (a drainage flow: direction sector 0°-40°) originating in the low Tiber Valley and flowing over the city of Rome, the second (a katabatic flow: direction sector 80°-130°) from the hills East of PDM. It may be noticed (Figure 2b) how in summer the latter starts a couple of hours before the former. The recording of the one or of the other as well as the diurnal direction spread is likely due to the synoptic scale forcing. A similar analysis at AMA (not shown) evidences, during the night, the combined effect of several local circulation components: the drainage flow from the Tiber Valley,
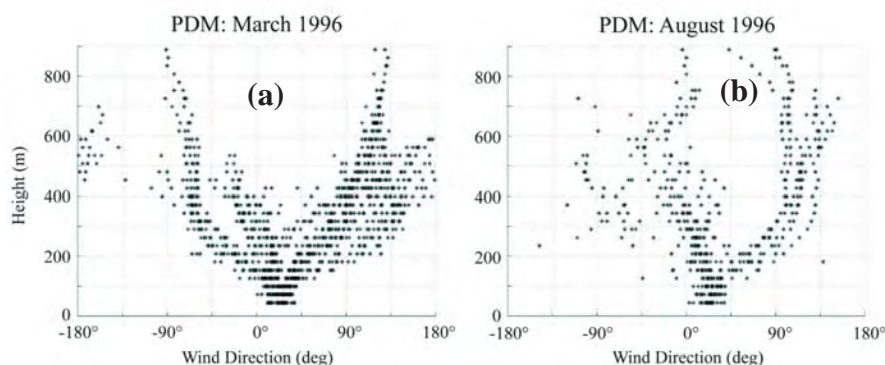
Figure 3. Nocturnal direction wind profiles associated with the cluster of the sector 0°-40° in Figure 2: (**a**) March (**b**) August .
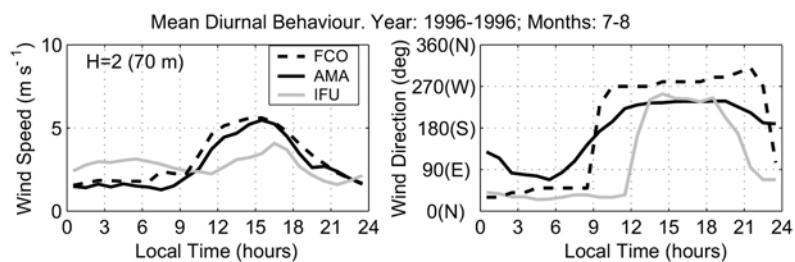
Figure 4. Mean diurnal behaviour of the local wind at FCO, AMA, IFU, during July-August 1996
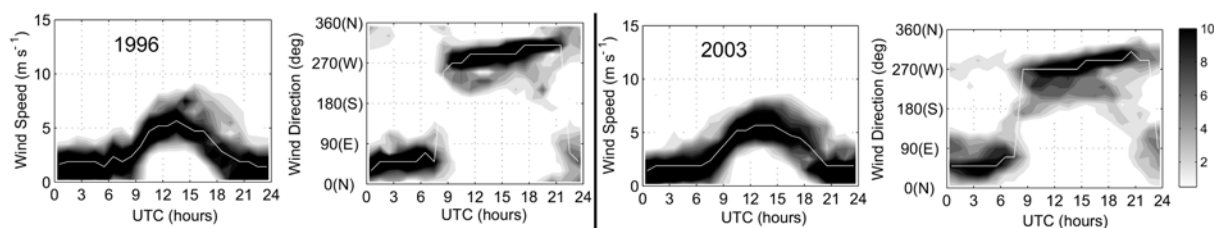
Figure 5. Mean diurnal behaviour of the local wind at FCO during July-August 1996 (left) and 2003 (right).

the katabatic flow from the hills SE of AMA and the land breeze. The relative forcing of the flows varies during the night so that their direction changes accordingly. The nocturnal wind speed in this location is low (0-2 ms^{-1}) compared with those recorded at the other sites (2-6 ms^{-1}). At IFU, a channelling effect due to the Tiber Valley is present in addition to the drainage flow and to the land breeze. The statistical analysis of the wind at different sites (not shown) reveals how sea breeze shows itself from March to October, generally more frequently close to the coast than inland at IFU. For July-August 1996 the mean diurnal behaviours of the wind at FCO, AMA, IFU (Figure 4) have been considered to estimate the inland mean propagation time of the sea breeze.

A similar analysis of the wind data recorded in July and August of each year from 1994 to 2003 during fair-weather conditions (examples for years 1996 and 2003 are shown in Figure 5) does not reveal any appreciable difference of the circulation at the site, from year to year.

4 Conclusions and Outlook

A statistical analysis of wind data recorded in Rome and surrounding area shows that it is possible to filter out most of the synoptic components and to obtain the diurnal time-space evolution of the local circulation. The analysis carried out for the period 1994-2003 (at FCO) suggests the possibility to use data collected at different sites even if in different years (but same months) to reconstruct the wind field in the area if most of the synoptic contribution is appropriately filtered.

Literature

Colacino, M., 1982: Observation of a Sea Breeze Event in Rome Area. Arch. Meteorol. Geoph. Biokl., Bd **30**, 127-139.

Mastrantonio G., A.P. Viola, S. Argentini, G. Fiocco, L. Giannini, L. Rossini, G. Abbate, R. Ocone, M. Casonato, 1994: Observations of sea breeze events in Rome and the surrounding area by a Network of Doppler sodars. Boundary Layer Meteorology , 71, 67-80.

Climatological Study of Fog Events on the Tyrrhenian Coast in the Proximity of Rome

Petenko[1,2], Igor, Mastrantonio[1], Giangiuseppe, Viola[1], Angelo
(1) ISAC-CNR, Via del Fosso del Cavaliere, 100, 00133 Roma, Italy
(2) IAPh RAS, Pyzhevskiy, 3, 109017 Moscow , Russia
E-mail: i.petenko@isac.cnr.it

Abstract

The annual and diurnal behaviours of the occurrence of different types of fog and visibility as well as the statistical distribution of wind during fog events on the Tyrrhenian coast at the airport of Fiumicino (Rome) for different seasons were determined for years from 1994 to 2004. The analysis of sodar observations made showed that the upper flow can be responsible for the transportation of moist air to the land.

1   Introduction

The fog creates safety problems to car traffic, to airplane landing and to airport operations. Moreover, it affects vegetation life since it facilitates the attack of phyto-pathogenous agents during the warmer periods and the vegetation freezing due to micro drop deposition during cold periods. Fog episodes may frequently occur on the coast where the airports of Fiumicino and Pratica di Mare report problems caused by the phenomenon. The previous studies showed that the fog at these sites manifests itself in several shapes, i.e. as continuous fog, shallow fog, mist, and fog patches.

The purpose of this study was to determine the main characteristics of the occurrence of the fog events and its correlation with the meteorological conditions.

2   Instrumentation

The data of observations obtained from the system MARA at the airport of Fiumicino during the years from 1994 to 2004 were used in this study. These data include every 5 minutes measured values of wind speed and direction from 4 sensors installed at 10-meter masts, as well as temperature, relative humidity and pressure values. Moreover, information on visibility, types of fogs and cloudiness, etc. contained in the so called METAR (METeorological Airport Report) recorded every 30 minutes, were analyzed. The data from radiosounding and sodar observations at the airport of Pratica di Mare at 20 km to SE from Fiumicino were also used.

3   Results

3.1. Statistical Distributions of Fogs and Accompanying Winds
Figure 1 shows the histograms of the number of fog events as a function of (a) hour of day and (b) month of year. The diurnal behaviour clearly indicates the increase of the occurrence in the first morning hours with a peak around 6 UTC. The peak in the diurnal behaviour for winter season seems to be later in time being compared with the same for the summer period. The annual behaviour shows a prevalence of fog events in the first three months of the year. In figure 1 the diurnal behaviours of the occurrence of different visibility classes in summer (c) and in winter (d) are given. All the considered visibility classes are characterized by the increase of their occurrence in the night time with the maximum before the sunrise. It can be hypothesised that this is due to the increase of the land breeze wind speed, which usually intensifies in hours before the sunrise decreasing, as a consequence, the fog concentration. For the class of visibility < 1 km, a relative maximum is observed in March when the

temperatures of the sea and the land during the night are probably more similar causing the decrease of the land breeze wind speed.
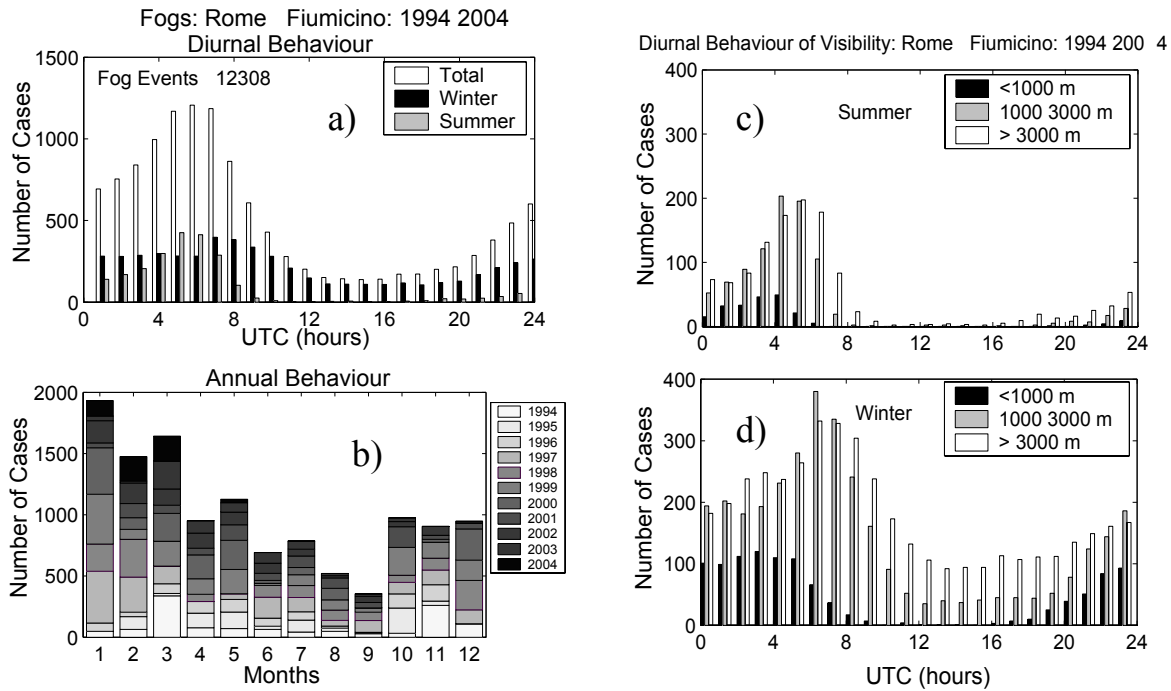
Figure 1. Histograms of number of fog episodes as function of hour of day (a) and month of year (b). Diurnal behaviour of different classes of visibility in summer(c) and in winter(d).

Figure 2 shows the distribution of winds observed during fogs separately for night and day time. The wind speed associated with fog episodes is low, and generally less than 3 m s^{-1}. The prevailing direction is E-NE that is quite similar to the wind behaviour during the land breeze and observed for situations with both clear and covered sky. The wind direction from West occurs only during the day time. However, as the area of Rome is not known for having frequent fog events, the advection of fog from East cannot be considered as a possible mechanism of its origin.
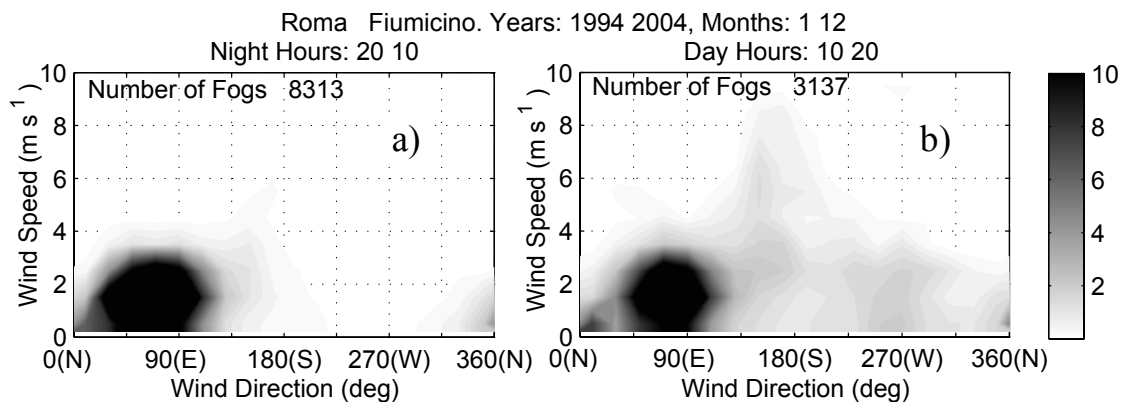
Figure 2. Statistical distribution of wind speed and direction observed during fog events.

3.2. Results of a Case Study

To clear up the origin of fogs we present the results of the case study of one fog episode observed at the airport of Pratica di Mare on 17 January, 1997 (Martano et al., 2005). The meteorological conditions and the phenomenology in the analysed particular case were quite similar at these two sites. The facsimile in Figure 3a shows a situation of atmospheric stability with three main layers. The highest one is at a variable height between 600-800 m and has the thickness of approximately 100 m. From this layer, air masses fall down toward the ground

occasionally, as testified from the vertical velocity diagram (figure 3b). The sodar wind profile (figure 3c, d) shows that at the layer between 0 and 150-200 m the wind comes from Nord-East, while at the middle one (between 200 and 600-800 m) it comes from the West. The upper layer is the interface band between the middle layer and the overhanging synoptic circulation. The latter begins from 1400 m where the wind speed is less than 1 m s^{-1} and comes from South as shown from radiosounding measurements. We can hypothesise that even if the fog episodes are associated with the low level flows coming from NE-E, the contribution from the marine air advection that slides above the land breeze layer has a main role. This breeze can contribute to the cooling of the marine air with probable consequent formation of fog banks. As the potential temperature of the air masses coming from NE-E is several degrees lower than that one of the overhanging air (see figure 3e), this circumstance, in presence of partial vertical mixing, favours the fog formation if the marine air has relative humidity close to the saturation.
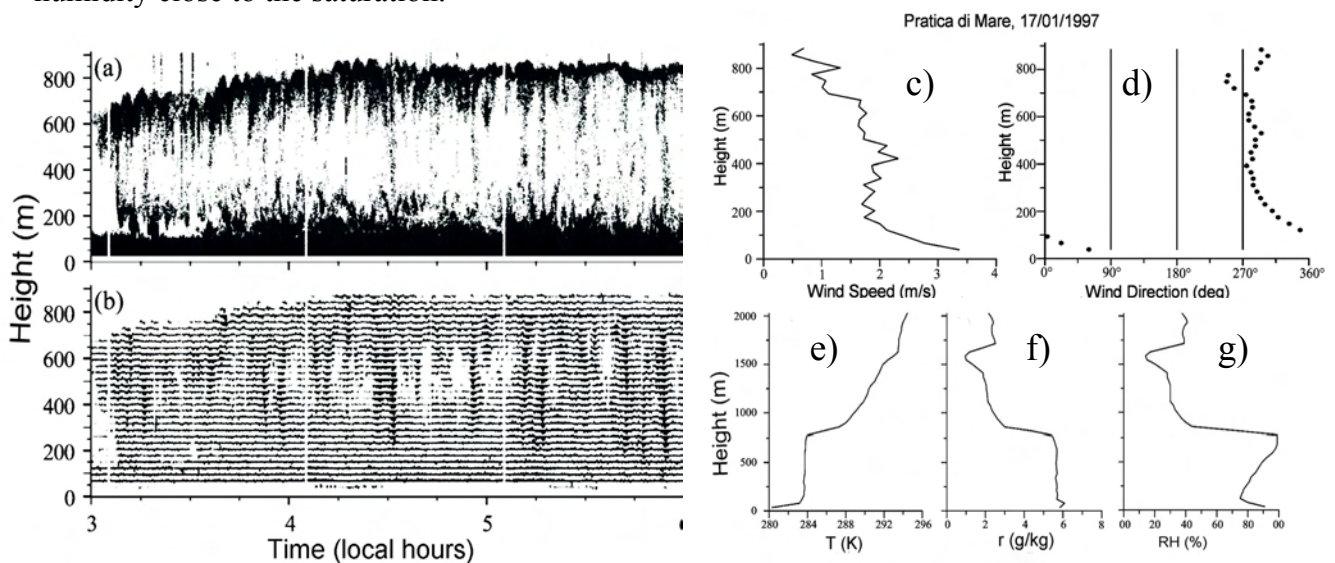
Figure 3. Sodar echograms (a) and the vertical velocity diagram (b). Profiles of wind speed (c) and direction (d) measured with sodar, temperature (e), mixing ratio (f) and relative humidity (g) measured with radiosonde. Pratica di Mare, 17 January 1997.

The annual and diurnal behaviours of the occurrence of fog events and the visibility show that the maximum of the probability of fog and the minimal values of visibility are observed in morning hours around 6 UTC during months January-March. The statistical distribution of wind during fog events was determined for different periods of the day and different seasons. The main feature is that the prevailing direction of surface wind during fog events is ENE that corresponds to land breeze wind. But this does not mean that the fog is advected from this direction. The sodar and radiosonde observations showed that the wind direction changes with height, and above 100 m the wind comes from the NW sector, i.e. from the sea. This upper flow can be responsible for the transportation of moist air to the land, which after descending produces fog.

Literature

Martano, P., D. Cava, G. Mastrantonio, S. Argentini and A. Viola. 2005: Sodar detected top-down convection in a nocturnal cloud-topped boundary layer: a case study. Boundary-Layer Meteorology, 115-1, 85-103.

The potential of additional vertical soundings to detect the flow and temperature structure in and around an urban area

Piringer, Martin and Baumann-Stanzer, Kathrin
Central Institute for Meteorology and Geodynamics, martin.piringer@zamg.ac.at

Abstract

In winter 2004/2005 and spring 2005, an extensive measurement campaign took place in Linz and surroundings, Austria, supplementing the already rather dense ground-based meteorological network of downtown, sub-urban and rural stations (the latter at different heights) by continuous vertical soundings with a Metek Sodar/RASS, a Remtech PA2 Sodar and, during episodes, with a Vaisala tethered balloon carrying a meteorological sonde. Results from two case studies, the highest PM10 episode during winter and an anti-cyclonic period in spring, will be presented. The main focus will be on the additional gain of information by the vertical sounders.

1   Introduction

Urban meteorological campaigns are of increasing importance as it is realized today that the urban boundary layer is more complex than the classical homogeneous atmospheric boundary layer mainly due to the buildings which introduce a large amount of vertical, artificial and impervious surfaces and increase the surface roughness. As a consequence, wind and temperature fields, the surface energy balance, the mixing height and other important parameters are altered, compared to the rural surroundings (Fisher et al., 2005; Piringer and Joffre, 2005). This work focuses on urban modifications of wind and temperature profiles observed by vertical sounders in Linz, Austria, and discusses the problems to be encountered when operating meteorological instrumentation in built-up areas.

2   Instrumentation

The dense local air pollution and meteorology monitoring network run by the federal government of Upper Austria delivers near-ground wind and temperature information. The wind measurements, although correctly measured in 10 m above ground, are often subject to local influences, mainly by buildings. This network was supplemented by vertical sounding devices and sonics at three sites: a Remtech PA2 sodar and one Metek ultrasonic anemometer were placed at the confluence of the river Traun into the Danube east of Linz, a site classified as rural and apt to detect the undisturbed approaching flow to the city; a Metek sodar with 1290 MHz RASS extension together with a Metek ultrasonic anemometer were operated at a power plant site ("urban"; see Baumann-Stanzer and Piringer, this volume, for a picture of the site) near the city centre of Linz; to the west of the city centre, where a narrow section of the Danube valley opens into the basin of Linz, a Vaisala tethersonde system was operated temporarily during PM_{10} episodes. As the operation of the instruments at the power plant site was negatively influenced by construction noise and a moving crane, the sodar/RASS system was moved to the former sodar site. At this undisturbed site, the height of 50 % data availability could be doubled, from about 270 m to 540 m, compared to the industrial site.

3   Results

The goal of the measurement program was to give insight into the vertical wind and temperature structure in the area of Linz during PM_{10} episodes. Such episodes in winter are known to occur frequently during periods of stagnations when inversions and vertical wind shear are important. Both can only be detected by vertical soundings.

The strongest episode in the winter 2004/05 occurred between 8 – 10 February, 2005, when the daily spatial average of PM_{10} culminated at 140 µg/m^3, well above the threshold of 50 µg/m^3. The meteorological situation was tipically anti-cyclonic with upper-level warm air advection. An elevated temperature inversion detected by the hourly tethersonde launches was present throughout the episode, its base first in about 600 m above ground on 8 February, but decreasing to about 300 m towards the end of the measurements in the morning of 10 February. Within the inversion, south-westerly airflow prevailed, thus creating strong wind shear at the elevated inversion base below which easterly winds were observed. Another level of enhanced wind shear was found at 100 m height at night at the tethersonde site, separating the easterly flow aloft from the westerly down-valley flow. The low-base elevated inversion together with the low wind speeds and a longer precipitation-free spell are seen as the meteorological causes for the peak PM_{10} levels on 10 February.

The vertical range of the sodar/RASS at the urban site was restricted to 300 m above ground to assure a data retrieval rate as high as possible with respect to the poor operating quality of the site. Thus it detected the upper-level inversion only very late during this episode. The PA2 sodar at the rural site east of the city gave wind information up to about 500 m above ground. Easterly to south-easterly winds prevailed within this range; on 10 February, south-westerlies were observed above about 300 m, well in accordance with the last tethersonde profiles.

The combination of all these measurements revealed a complex pattern of the night-time near-ground wind field: there is inflow to the city centre from all directions at night, probably stimulated by the urban heat island effect. This effect creates strong near-ground wind shear in parts of the city, especially to the west and north of its centre.

Average day-time and night-time vertical potential temperature profiles observed by the RASS at the urban and the rural site (different data periods!) are shown in Fig. 1. At the urban site (Fig. 1a), the average vertical potential temperature profile shows a decrease between 40 and 60 m above ground, indicating an unstable layer to be attributed to the external heat sources and the building influence within the industrial complex. The unstable layer is stronger and a bit higher during daytime than during night. Above it, there is a well-mixed layer up to 120 m during daytime, followed by a steady increase in potential temperature with height; at night, this increase starts directly above the unstable layer. At the rural site (Fig. 1b) during daytime, an about 150 m deep well-mixed layer can be seen; above, potential temperature starts to increase slightly. At night, a strong stable layer develops near ground, and the gradient is reduced above about 100 m. The reduction in data availability with increasing height shows up in irregular fluctuations of the average potential temperature above 450 m above ground.

4   Discussion, Conclusions, and Outlook

The experience with field experiment planning and exercise gained in Linz can be transferred to other (future) field campaigns. It turned out that the selection of an urban site for sodar and RASS measurements is not trivial. Usually, a selection e. g. according to the recommendations of the COST Action 715 (Fisher et al., 2005; Piringer and Joffre, 2005) is seldom possible. In Linz, the industrial complex had been chosen because of lack of near-by residents who could be disturbed by the noise of the sodar/RASS. The impact of the buildings and external heat sources on the data of sodar/RASS and sonic, although anticipated by the Metek company, has been fully realised only in the course of the measurement period. As this was a pilot phase, the experience gained was used to plan and set up the main field phase of the project. It was decided to install and operate a sodar with RASS extension together with a sonic at the rural site upwind of the city and to mount an ultrasonic anemometer on top of a roof in the downtown area to obtain a representative urban wind and stability information. The sodar/RASS and the sonic will provide wind, temperature and stability information in the

undisturbed flow before it enters the city area; the downtown sonic will document the urban modifications of wind and stability.
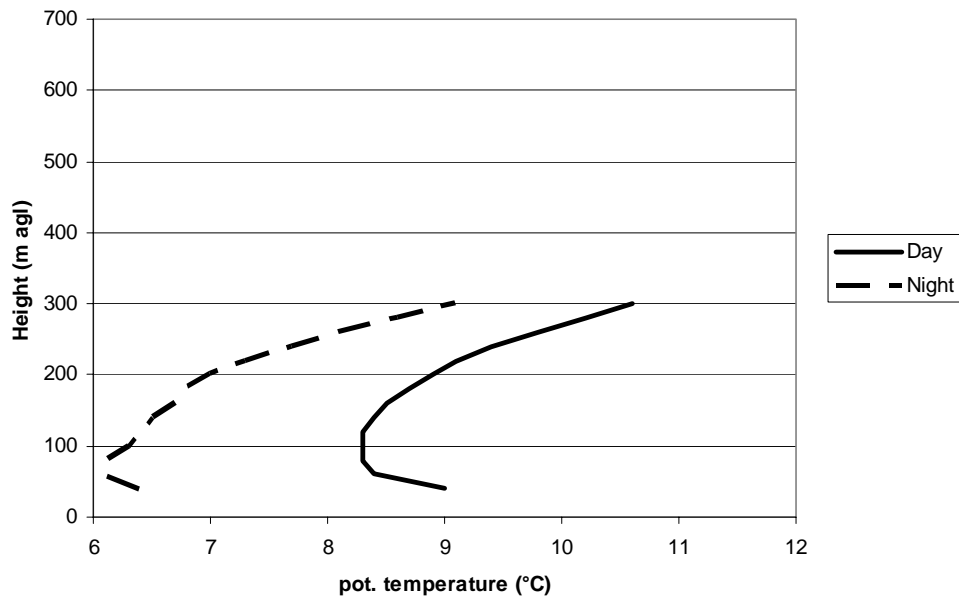
a) urban (2. 9. 2004 – 7. 4. 2005)
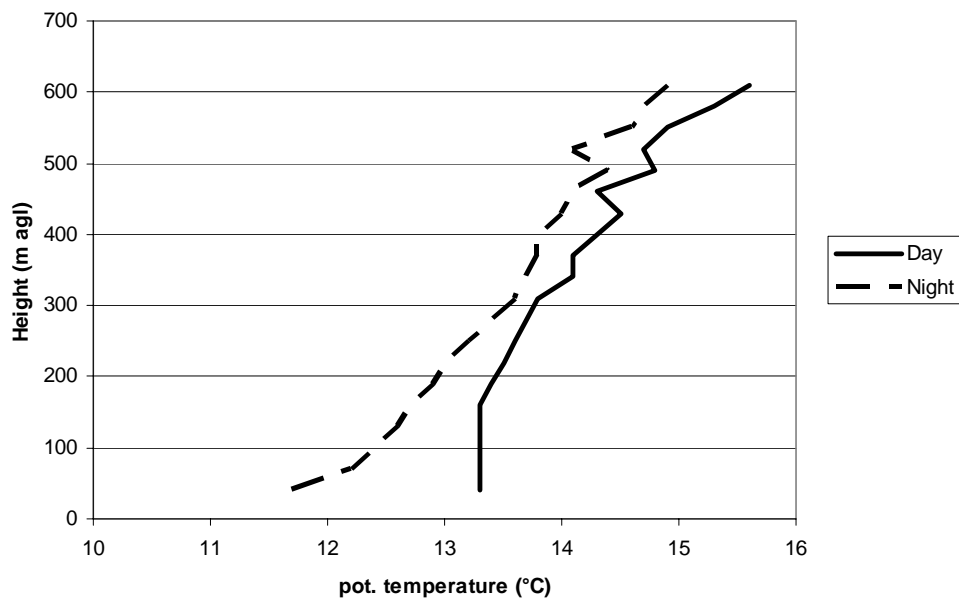
b) rural (8. 4. – 9. 5. 2005)

Figure 1. Average vertical profiles of potential temperature measured with RASS at the urban and rural site

Literature

Fisher, B., S. Joffre, J. Kukkonen, M. Piringer, M. Rotach, M. Schatzmann (Eds.), 2005: Meteorology applied to urban air pollution problems. Final Report of COST Action 715. ISBN 954-9526-30-5, 276 pp. Demetra Ltd. Publishers. Printed in Bulgaria.

Piringer, M., S. Joffre (Eds.), 2005: The urban surface energy budget and mixing height in European cities: data, models and challenges for urban meteorology and air quality.Final report of Working Group 2 of COST Action 715. ISBN 954-9526-29-1, 239 pp. Demetra Ltd. Publishers. Printed in Bulgaria.

Detection of urban air pollution by means of the ICAROS NET platform using satellite, SODAR, and ceilometer data

Schäfer[a] Klaus, Emeis[a], Stefan, Sarigiannis[b], Dimosthenis, Gotti[b], Alberto

[a]Forschungszentrum Karlsruhe, Institut für Meteorologie und Klimaforschung (IMK-IFU), Kreuzeckbahnstr. 19, 82467 Garmisch-Partenkirchen, Germany

e-mail: klaus.schaefer@imk.fzk.de

[b]European Commission - Joint Research Centre, European Chemicals Bureau, Institute for Health and Consumer Protection, Via E. Fermi, 1, 21020 Ispra (VA), Italy

Abstract

The networked interactive computational environment ICAROS NET was developed and demonstrated to determine the horizontal spatial distribution of PM concentrations within the mixing layer. The platform allows the integration and fusion of environmental information from satellite (Landsat, SPOT) and ground-based remote sensing observations, ground-based air quality measurements, and pollution transport models. While applying the platform to the region of Munich it was possible to integrate the PM10, PM2.5 and PM1 concentration determination using mixing layer height data from ceilometer and SODAR.

1   Introduction

For more than 20 years the air quality has been monitored by measurement networks in urban and sub-urban areas. But now, new tools are needed for the execution of the European Air Quality Framework Directive 96/62/EC and its daughter directives because 12-monthly air pollution maps with a spatial resolution of 200 m^2 are required. The satellite information can be developed as such a tool which provides aerosol optical depths (AOD) from satellite images (SPOT, Landsat) in an area of approx. 100 km x 100 km with spatial resolution of up to 10 m x 10 m (Sifakis et al., 1998; Sarigiannis et al, 2002). The AOD of the satellite images can be likewise interpreted by the particle concentration together with the mixing layer height (Schäfer et al., 2002). This task is solved by the ICAROS NET platform which was applied in the Munich region to determine information for the monitoring of particulate air pollution.

2   Instrumentation

In summer and winter 2003 during measurement campaigns (two weeks each) in and around Munich (3 measurement locations) air pollutants near the surface (including PM10, PM2.5 and PM1 by SEQ47/50 Leckel) and mixing layer heights by remote sensing (SODAR, RASS, ceilometer) were determined to evaluate the results of this type of satellite information. These data, ground-based monitoring network data and data retrieved from satellite images are fused in the ICAROS NET platform.

Image processing algorithms and respective software codes have been successively developed for application on different types of satellite data to allow the extraction of AOD values in the visible over urban areas (Sifakis et al, 1998). The method used by the codes consists in a radiometric comparison of multi-temporal satellite data sets of the same area acquired by the same sensor during different representative pollution conditions, allowing to locate, identify and assess the magnitude of the turbidity, which depends on the atmospheric loading of particles. Acquisition of two-image multi-temporal sets consisting of: (i) one image recorded under very clear atmospheric conditions and (ii) one image of the same geographical area recorded during different pollution levels and distinct meteorological conditions. The maps of AOD values derived from satellite data refer to the total atmospheric column. It is reasonable to assume, however, that the majority of the pollutants of interest for air quality assessment remain within an atmospheric layer that spans from the ground up to the mixing layer height. The relevance of the influence of the mixing layer height upon measured air quality data (e.g.

PM10, PM2.5, PM1, CO and NO_x concentrations) was found together with emission source strength during earlier studies (Schäfer et al., 2002) and was valid during these campaigns also. The information of mixing layer height is then used as the real optical path length of the determined AOD.

The mixing layer height data are taken from acoustic remote sensing by SODAR, which has an altitude range of up to 1,200 m altitude (Emeis et al., 2004). The SODAR site was about 30 km to the west of Munich. Temporal averages of mixing layer height over the whole day were taken. This was necessary because the PM10 / PM2.5 / PM1 data at that site, at the roof of a building in the city of Munich and at a site about 30 km to the east of Munich were taken over the whole day only. During summer the height range of the SODAR is not enough to detect the mixing layer height during the afternoon. During all time the ceilometer data from the site about 30 km to the east of Munich is used for mixing layer height determination too.

For the determination of particle concentrations from satellite images the necessary relationship between the AOD and the corresponding particle concentrations was investigated during the measurement campaigns. With this objective the AOD determined from the ground-based sun-photometer measurements at the three sites mentioned above were correlated with the corresponding particle concentrations measured at the same sites.

3   Results

Introducing the relative humidity parameter in the statistical model developed, improves its performance in PM10 prediction from AOD as evidenced by the R^2 index equal to 0.93. More specifically, the best relationships are

$$C_{PM10} = 122,067 \cdot b_{scat} + 0.70 \cdot RH \text{ during winter conditions and}$$

$$C_{PM10} = 54,771 \cdot b_{scat} + 5.69 \cdot RH \text{ during summer conditions}$$

where C_{PM10} are the PM10 daily average concentrations in $\mu g/m^3$, b_{scat} is the scattering coefficient calculated as the ratio between the AOD and the mixing layer height (expressed in meters) and RH is the measured daily average fractional relative humidity.

The Landsat image of April 16, 2000 was used as reference image while the image of April 1, 2003 represents the investigated image. Figure 1 shows the resulting PM10 concentration map at 30 meters of spatial resolution as calculated applying the relative humidity dependent data fusion algorithm.

4   Discussions, conclusions and outlook

In Figure 1 the location of the PM10 monitoring stations as well as the motorways and the border of Munich are clearly visible. In the city centre near station 8 (Lothstr.) and 9 (Stachus) high concentration values can be recognized. At the station 11 (Landsberger Chaussee), which is located at a very crowded city highway, and eastward high concentrations between 40 and 60 $\mu g/m^3$ appear. The high values near the river probably arise from the land use change of the vegetation near by. Otherwise there is a very satisfactory spatial agreement between some road outline and high PM10 values around it due to the high emissions from the vehicles. High concentrations are found also in some cases where the motorway crosses a city street. From the urban to the suburban areas the concentration decreases while the concentrations rise considerably especially in some areas in the north-east of the town. This can be due to the land use change and change in humidity of the soil. In the north of Munich some areas with higher values of PM10 are clearly visible. Their origin could be reasonably attributed to the intense emission from some large industrial plants located in that area. Zones without values in the city are sometimes areas of the railway.

Figure 1: Region of Munich with the spatial distribution of PM10 concentrations in µg/m³ on April 1, 2003 calculated with the reference image of April 16, 2000. The measurement sites of the Bavarian State Agency for Environmental Protection, rivers and motorways are indicated.

Finally, the comparison between the calculated values and the measured values shows a good agreement between the respective trends. After adding the background concentration measured at April 16, 2000, the calculated values of PM10 appear to be comparable and to fit well with the measured ones at the stations of the network within Munich at April 1, 2003.
The further application of the ICAROS NET platform requires a very careful selection of the reference image on the basis of the available network data.

Literature

1. **Sarigiannis, D.A., N. Soulakellis, K. Schäfer, M. Tombrou, N.I. Sifakis, D. Assimakopoulos, M. Lointier, A. Dantou, M. Saisana, 2002:** ICAROS: An Integrated Computational Environment for the Assimilation of Environmental Data and Models for Urban and Regional Air Quality. International Journal on Water, Air, and Soil Pollution: Focus 2, 641-654.
2. **Sifakis, N., N. Soulakellis, D. Paronis., 1998:** "Quantitative mapping of air pollution density using Earth observations: a new processing method and application to an urban area". International Journal of Remote Sensing 1**9**, 3289-3300.
3. **Schäfer, K., G. Fömmel, H. Hoffmann, S. Briz, W. Junkermann, S. Emeis, C. Jahn, S. Leipold, A. Sedlmaier, S. Dinev, G. Reishofer, L. Windholz, N. Soulakellis, N. Sifakis, D. Sarigiannis, 2002:** "Three-Dimensional Ground-Based Measurements of Urban Air Quality to Evaluate Satellite Derived Interpretations for Urban Air Pollution". International Journal on Water, Air, and Soil Pollution: Focus 2, 91-102.
4. **Emeis, S., C. Münkel, S. Vogt, W. Müller, K. Schäfer, 2004**: "Determination of mixing-layer height". Atmospheric Environment 38, 273-286.

Sodar-measured wind profiles in the Inn Valley as input for dispersion calculations

Petra Seibert (1), Wolfgang Spangl (2), Stefan Emeis (3), Klaus
Schäfer (3), Peter Suppan (3)
(1) Institute of Meteorology, University of Natural Sciences
and Applied Life Science Vienna (BOKU), 1190 Wien, Austria
petra.seibert@boku.ac.at
(2) Umweltbundesamt, 1090 Wien, Austria,
wolfgang.spangl@umweltbundesamt.at
(3) Forschungszentrum Karlsruhe Gmbh, Institut für Meteorologie
und Klimaforschung - Atmosphärische Umweltforschung (IMK-IFU)
Kreuzeckbahmstr. 19, 82467 Garmisch, Germany
stefan.emeis@imk.fzk.de

The INTERREG III B Alpine Space project ALPNAP (2005-2007) of the EU aims at demonstrating scientific methods for assessing air pollution and noise along major Alpine transport routes. In most Alpine valleys, routine wind measurements are available only from surface observations. In the Inn Valley near Innsbruck, several measurement campaigns have taken place which included sodar systems providing continuous vertical profiles of wind velocity and direction. The presentation will investigate how well surface wind measurements can be used to infer the wind in the lowest hundreds of metres in the Valley atmosphere, which is relevant for the transport of air pollutants. Data sets to be used include measurements by the Austrian Umweltbundesamt from July 1990 to March 1991 at Hall and by the IMK-IFU from October 2005 to February 2006 near Schwaz.

Inspection of sodar wind fields from the winter 2005/06 show that in clear cold nights several stable layers form in the lower 600 to 700 m above ground. The separate layers are alternatively dominated by the down-valley winds in the Inn valley and the down-slope winds from the nearest slope (Fig. 1). During afternoon hours the valley air often becomes well mixed and the layering disappears. Thus it can be expected that the surface wind measurements are representative only in well-mixed situations for the wind regime in the lower hundreds of metres in the Inn valley east of Innsbruck.
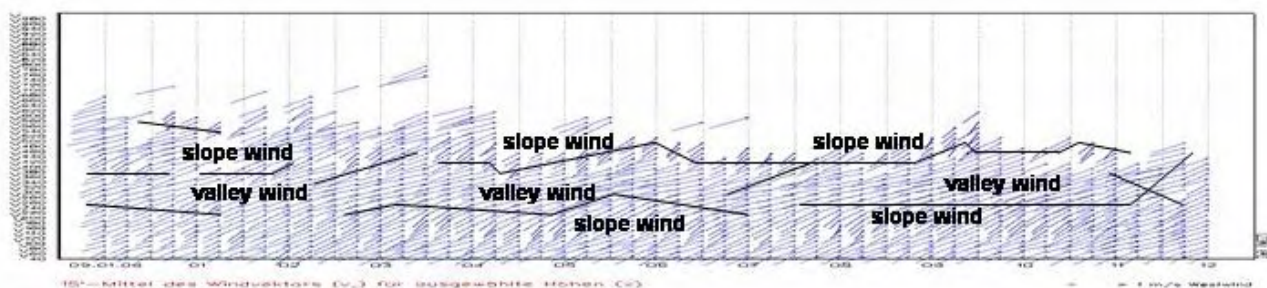
Figure 1. Horizontal wind vector, measured by the METEK DSDR3x7-Sodar of the IMK-IFU showing alternating layers with slope (more southwesterly) and valley (more westerly, parallel to the Inn valley) winds. Black lines indicate tops of stable surface layers and lifted inversions. Analysis of these lines was based on (secondary) maxima in the acoustic backscatter intensity recorded by the same sodar.

Sodar Diagnosis of Mesoscale Boundary Layer Convergence

John R. Taylor[1], David J. Low[1], Michael J. Reeder[2]

[1]School of Physical, Environmental and Mathematical Sciences (PEMS), UNSW@ADFA, Canberra, ACT
[2]Centre for Dynamical Meteorology and Oceanography, Monash University, Melbourne, Vic, Australia
j.taylor@adfa.edu.au

Abstract

Wind data from two sodars deployed approximately normal to the coast in tropical northern Australia reveal a regime of easterly to westerly and westerly to easterly wind transitions. Three techniques were used to estimate the convergence and uplift driven by these interacting wind systems: differencing the time series of horizontal winds; transformation of the time gradient of horizontal wind into a spatial gradient using a mean advection speed (a mesoscale version of Taylor's hypothesis for frozen flow); and direct measurements of the vertical velocities. A case study of these diagnostic calculations is presented.

1   Introduction

Organised convective cloud lines called North Australian Cloud Lines (NACL) are relatively common towards the end of the dry season in tropical northern Australia. NACL originate over the Cape York Peninsula (fig. 1) and propagate westwards over the Gulf of Capentaria (Goler *et al.*, 2006). The initiation of organised convection is usually linked with low-level convergence, either driven by external flows, such as sea breezes, or by outflows from the convective system itself (Moncrieff and Liu, 1999). We were interested in the mechanisms that initiate convection in the NACL case. Specifically, although the cloud systems occur (relatively) frequently they are much less common than the converging low level flows that are linked to their initiation. A question to test, then, is whether the *magnitude* of the low-level convergence is important to the convection, or if *any* convergence at all is sufficient to trigger convection. One approach to this problem is to make measurements of the low-level convergence. Here we report on some initial work using time series of wind profiles from two sodars to diagnose convergence. Section 2 describes the instrumentation and the deployment in northern Australia. Section 3 introduces and gives an example of the three approaches to the diagnosis of convergence that we are investigating.
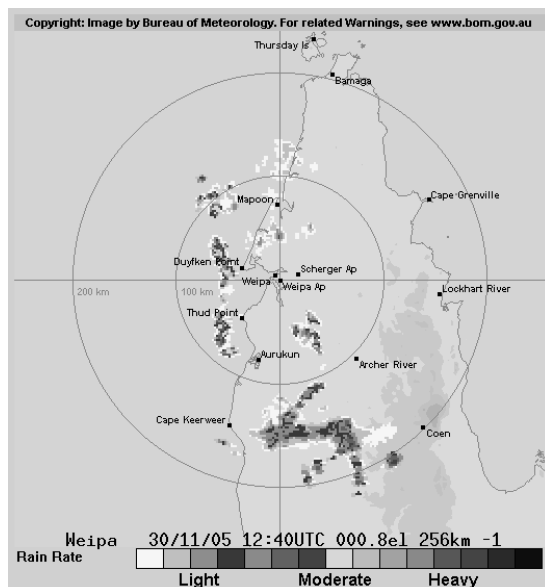
Figure 1. Radar Image from the Australian Bureau of Meteorology (www.bom.gov.au), showing precipitation echoes from a NACL in the Gulf of Carpentaria, 50km west of Cape York peninsula. One of the sodar locations, Weipa Aiport, is in the centre of the image (see text for details). Terrain elevation is shown by background shading in 150 m ranges.

2   Experiment and Instrumentation

From 18 November to 18 December 2005 two sodars were operated on Cape York Pensinsula in Northern Australia. One system was installed at Weipa Airport (12° 40.7′ S, 141° 55.5′ E), close to the west coast of the Peninsula, the other at Royal Australian Air Force base Scherger (12° 37.4′ S 142° 5.2′ E). The Scherger sodar was located approximately 18km east and 6 km north of the Weipa sodar (fig. 1). At the latitude of the experiment Cape York Peninsula is approximately 160 km wide, bounded on the east coast by the Coral Sea and on the west coast

by the Gulf of Carpentaria. The sodars were three-axis, single transducer, dish antenna type operating at 1.875 kHz. The instruments were developed and manufactured in-house in the School of PEMS. First sampled level was centred at 50 m and levels were spaced at 30 m intervals. For the full period of the experiment both raw Doppler spectra and radial winds from real time processing were logged on the sodar controller computer. The analysis presented here uses the real time wind data averaged into 10 minute blocks.

3   Results

Sea breeze circulations develop on both east and west coasts of the Cape but, primarily due to the prevailing south-easterly trade winds, the easterly flow dominates (Goler *et al.*, 2006). During the study period we typically observed the development of a westerly sea breeze at Weipa airport in the mid-afternoon. The west coast sea breeze front would arrive at Scherger one to one and a half hours later, where it would persist until it was displaced by the return of easterly flow (which often appeared simply as a wind change with little temperature contrast).

In the periods when different flow regimes exist at the two sodar sites there is low-level convergence in the boundary layer between the sites. Radar imagery of the sea breeze fronts show that they propagate approximately coast normal so that the convergence is dominated by the zonal gradient of zonal velocity ($\partial u/\partial x$). The uplift velocity w_z at a given height AGL, z, is then

$$w_z = \int_0^z \frac{\partial u}{\partial x} dz'.$$

Finite difference estimates for the velocity gradient can be found in two ways. The first is to difference the velocity time series from the two sodars at each height. Figure 2 gives a time-height cross section of the vertical velocities that result from this approach. Note that the diagnosed velocities are small because the uplift is averaged across the horizontal spacing between the sodars. The uplift associated with the sharp front of the west coast seabreeze was stronger than that associated with the more diffuse transition to easterly flow. A short period of strong convergence around 1930LT was due to a peak in wind speed at Weipa.

The second approach we used to estimating the convergence from the horizontal wind records is to transform the time derivative of the wind at each level to a space derivative

$$\frac{\partial u}{\partial x} = -\frac{1}{U}\frac{\partial u}{\partial t},$$

where U is a mean advection velocity. Here, we take U to be the speed of the structure moving past the sodar, or the sea breeze front speed, estimated from the arrival times of the front at the two sodar sites (the negative sign transforms into a front relative frame of reference). This approach requires westerly and easterly flow regimes to be analysed separately; however, it should give better horizontal resolution than the sodar differencing method. Time derivatives were computed using a central difference and thus have an effective time resolution of 20 minutes which corresponds to approximately 5 km spatial resolution for a typical frontal speed of 4 ms^{-1}. Compare this with the 18 km spacing of the stations in the *x*-direction. Figure 3 shows vertical velocities computed for the west coast sea breeze regime at the Weipa sodar site. Correspondence between the features in the two plots are good and the vertical velocities scale approximately as the ratio of the effective spatial averaging.

These two approaches can be compared with the directly measured average vertical velocities (fig. 4). The vertical velocities that occur with the passage of the west coast sea breeze, and with the 1930LT wind acceleration are clear. However, there was no clear upflow associated with the easterly transition. This is consistent with the much weaker average vertical

velocities from the differencing technique (fig. 2). Fig. 4 shows that the timescale of the westerly flow transition is similar to convective timescales. This complicates the interpretat
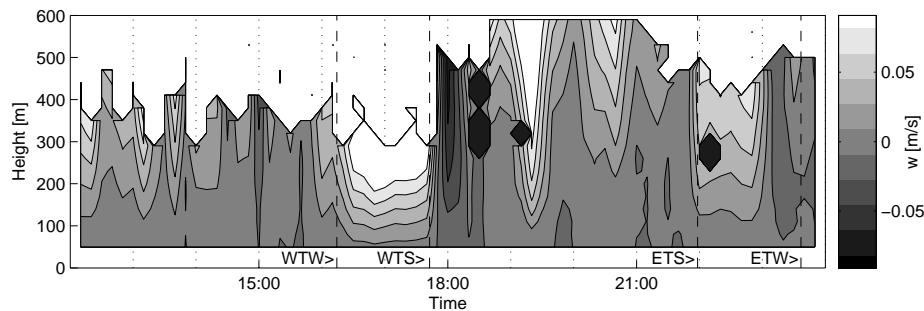
Figure 2. Time height cross section of vertical velocity estimated from differencing 10 minute averaged *u* profiles from the Weipa and Scherger sodars for 21st November 2005. Height is above local ground level. Times are local time (LT). UTC+10 hr. The times for the transitions to westerlies at Weipa and Scherger (WTW and WTS) and ε
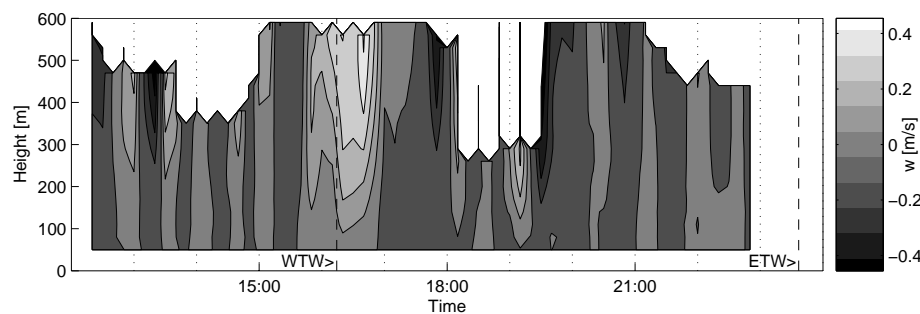
Figure 3. Time height cross section of vertical velocity estimated from time rate of change of 10 minute averaged *u* ι
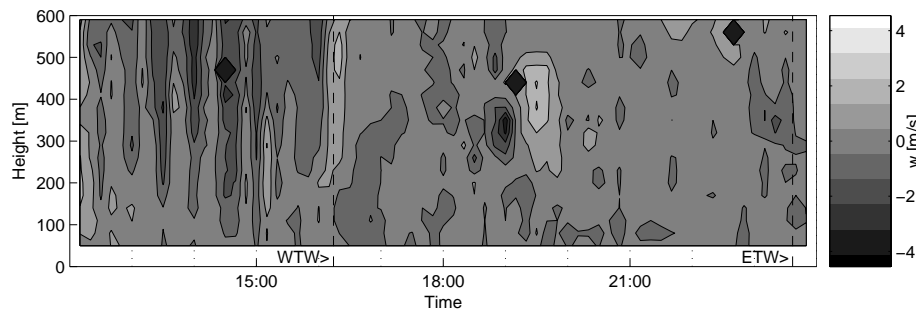
Figure 4. Time height cross section of 10 minute averaged vertical velocity from the Weipa sodar. Other details are as for fig. 2.

4   Outlook

Three techniques for estimating the vertical uplift associated with sea breeze transitions in Northern Australia have been presented. The next stage is to see whether the methods allow us to make a quantitative comparison of uplift across the different days of the study and to determine whether this comparison can give us an insight into the triggering of organised convection in this region.

Literature

Goler, R., Reeder, M. J., Smith, R. K., Richter, H., Arnup, S., Keenan, T., May, P., Hacker, J., 2005: Low-level convergence lines over Northeastern Australia. I. Northeasterly disturbances. In press, *Monthly Weather Review*.

Moncrieff, W. M. , Liu, C., 1999: Convection initiation by density currents: role of convergence, shear and dynamical organisation. *Monthly Weather Review*, 127, 2455-2464.

Analysis of coherent structures in the roughness-sublayer above tall canopies using a Doppler-SODAR

Mayer, Jens-C.[1,2], Thomas, Christoph[1+], Meixner, Franz X.[2], Foken, Thomas[1]

[1]Department of Micrometeorology, University of Bayreuth, Bayreuth, Germany;
[+] current affiliation: Department of Forest Science, Oregon State University, Corvallis, OR, USA;
[2]Biogeochemistry Department, Max-Planck-Institute for Chemistry, Mainz, Germany
email: jcmayer@mpch-mainz.mpg.de

Abstract

This study applies acoustic sounding to observe coherent structures in the roughness sublayer (RSL) above tall vegetated surfaces. The data analysis was done by wavelet transform of Doppler and non-Doppler variables. The flow in the RSL was found to be a superposition of dynamic Kelvin-Helmholtz instabilities and convective mixing. The degree of vertical coherency in the RSL increases with the flow evolving from neutral to near-convective conditions. An alternative conceptual approach for the definition of the RSL is proposed.

1   Introduction

The statistics of turbulent flow above tall vegetation differ from those in the surface layer above homogeneous surfaces and are largely controlled by coherent structures. In the proximity to tall canopies, coherent structures are an inherent part of the turbulent flow, which significantly contribute to atmospheric turbulent fluxes and originate from the dynamical instabilities of the inflected mean horizontal wind profile (e.g. Raupach et al., 1996). However, recent studies by Poggi et al. (2004) and Thomas et al. (2006) demonstrated that dynamical instabilities are not the only mode of organised motion near canopies and that effective spatial scales of coherent structures are a superposition of multiple processes. Until now, only tower based measurements were able to resolve the temporal scales of coherent structures, but they are limited in resolving the spatial scale. In this study, we analyse time series consisting of instantaneous soundings taken with an acoustic sounding system above tall vegetation. The advantage of using a SODAR system over conventional tower observations is the improved spatial scale of measurements with a high vertical resolution without sacrificing the necessary sampling resolution.

2   Instrumentation

The acoustic sounding system was a phased-array Doppler-SODAR (model DSDPA.90/64, Metek GmbH) in combination with a 1290-MHz RASS extension (Metek GmbH). The operating settings were optimized in respect to high resolution in time. By using an acoustic frequency of 2.0 kHz, and a vertical resolution of 10 m, a sampling frequency of 0.4 Hz was achieved, which is equivalent to a repetition rate of 2.5 s.

In concert with the SODAR measurements, vertical profiles of sonic anemometers and cup anemometers were used to observe the flow statistics in and shortly above the canopy at a nearby tower. Details about the experimental setup can be found in Thomas et al. (2006).

3   Results

The probability density function (PDF) of the detected characteristic time scales of coherent structures in the vertical wind and the acoustic backscatter intensity show a maximum density peak located between 20 and 30 s and continuously decreasing densities towards larger event durations with a minimum near 150 s. A second maximum becomes evident between 190 and 220 s event duration. The global maximum at approximately 25 s is in close agreement with

Collineau and Brunet (1993), Chen and Hu (2003) and Thomas and Foken (2005), who found similar characteristic time scales for coherent structures in the vertical wind.

The concept of the mixing-layer analogy (Raupach et al., 1996) was applied to the results of this study to address the question of the driving mechanism for the evolution of coherent structures close to the canopy-atmosphere interface. The canopy shear length scale $L_s = U_{hc}(du/dz)_{hc}^{-1}$ was evaluated from the tower measurements, where U_{hc} is the horizontal wind speed and $(du/dz)_{hc}$ is the gradient of the horizontal wind, both evaluated at canopy height (h_c). L_s was found to vary between 5 m and 10 m depending on stratification (Thomas and Foken, 2006). According to Raupach et al. (1996) coherent structures in active turbulence close to the canopy emerge from the dynamic Kelvin-Helmholtz instabilities created by the strong vertical shear. The streamwise spacing of coherent structures Λ is predicted to be a linear function of L_s with slope $m = \Lambda L_s$ ranging between 7 and 10. The observed values range from 8 to 15 and therefore confirm the dynamic origin of the coherent structures with time scales of approx. 25 s.

The second, local maximum located at approximately 210 s, is in close agreement with Petenko et al. (2004) for convective coherent structures. Increasing time scales with increasing height, resulting from a merging of small coherent convective elements (Williams and Hacker, 1993; Petenko and Bezverkhnii, 1999), has only been observed for coherent structures in the acoustic backscatter intensity.
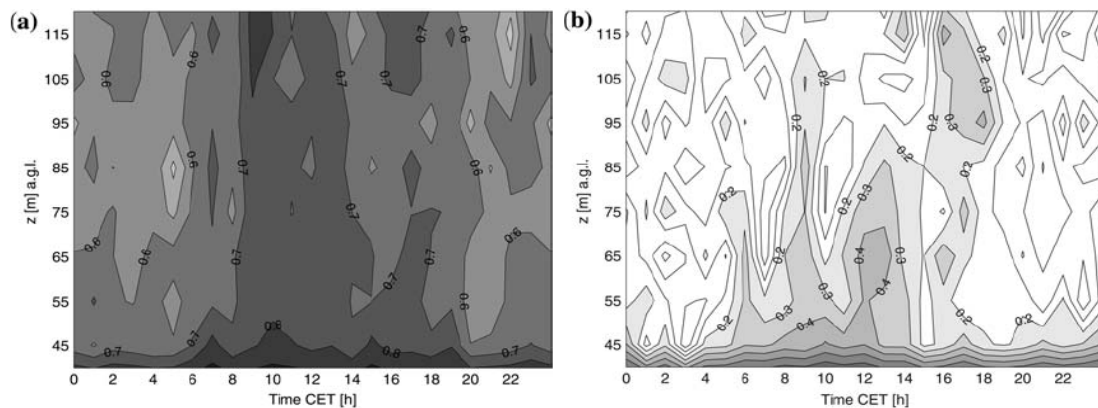
Figure 1. (a) Time-height cross-section of the ensemble averages of the correlation coefficient R_s for event durations $10 \leq D \leq 60$. (b) The same as in (a) but with event durations $60 \leq D \leq 240$.

As coherent structures are assumed to be a single entity which is correlated throughout the RSL (Gao et al., 1989), they are expected to be represented by the same peaks in spectra computed from different height levels. By computing the correlation coefficient R_s between the wavelet variance spectrum at a reference level and a comparison level, a measure of vertical coherency can be obtained (Thomas et al., 2006). The mean diurnal course of R_s, calculated over 15 selected days, is characterised by low ($R_s \leq 0.3$) values during night and high ($R_s \geq 0.5$) values around noon. As Kelvin-Helmholtz instabilities are assumed to be not affected by atmospheric stability, the observed diurnal course of R_s must be the result of the joint effect of dynamic instabilities and thermally induced eddies. The wavelet spectra were split into separate parts for dynamically induced coherent structures ($10 \leq D \leq 60$) and for thermal eddies ($60 \leq D \leq 240$) and R_s subsequently computed for each part separately. R_s is found to be generally high for the smaller time scales with low variability (Figure 1a). For the larger time scales, R_s is found to increase with the flow evolving to more unstable conditions (Figure 1b). The low diurnal variability of R_s for the smaller time scales indicates the omnipresence of coherent structures emerging from Kelvin-Helmholtz instabilities in the considered layer. In contrast, the strong diurnal cycle of R_s for larger time scales can be linked to thermal eddies with event durations exceeding 60 s.

The RSL is a concept to separate a layer in which flow is largely determined by the roughness elements of the surface from a layer above in which the surface roughness ceases to affect the flow. The vertical extend of the RSL is generally estimated as $3h_c$. Poggi et al. (2004) proposed a conceptual model for the canopy sublayer, consisting of a region with superimposed characteristics of boundary-layer flow, a mixing layer and von-Kármán streets. These characteristics resemble the results for the layer of increased vertical coherency, derived from the spatial SODAR data. Hence we can derive an alternate approach for the definition of the RSL as the flow region of increased vertical coherency resulting from both dynamic Kelvin-Helmholtz instabilities and convective processes. The vertical extent of the RSL thus can be estimated to be rather $5h_c$ than $3h_c$. From the observation of increased vertical coherency, it also follows that the height of the RSL can not be assumed as constant.

4   Conclusions

From the results of the wavelet analysis, the following conclusions can be drawn:
- The acoustic sounding system was successfully used for the observation of coherent structures above tall vegetation.
- The characteristic time scales of the flow in the RSL revealed that both Kelvin-Helmholtz instabilities and attached thermal eddies affect the effective mixing length in this region. Both processes can be separated in the frequency domain as their time scales differ significantly.
- Spectral correlation between neighbouring observation levels revealed an increasing vertical coherency as atmospheric stability approaches near-convective conditions. This increase could be related to the evolution of large attached eddies rather than to the presence of coherent structures emerging from Kelvin-Helmholtz instabilities, which were observed to show almost no variation with atmospheric stability.
- The proposed alternative definition of the RSL allows us to define its vertical extend to a maximum of $5h_c$. Hence, the influence of dynamic instabilities on characteristics of low-frequency turbulent flow reaches higher than is commonly assumed.

Literature

Chen, J., F. Hu, 2003: Coherent Structures Detected in Atmospheric Boundary-layer Turbulence using Wavelet transforms at Huaihe River Basin, China. Boundary-Layer Meteorology, 107, 429-444.

Collineau, S., Y. Brunet, 1993: Detection of turbulent coherent motions in a forest canopy. Part II: Time-scales and conditional averages. Boundary-Layer Meteorology, 66, 49-73.

Gao, W., R. H. Shaw, K. T. Paw U, 1989: Observation of Organized Structures in Turbulent Flow within and above a Forest Canopy. Boundary-Layer Meteorology, 47, 349-377.

Petenko, I., V. Bezverkhnii, 1999: Temporal Scales of Convective Coherent Structures Derived from Sodar Data. Meteorology and Atmospheric Physics, 71, 105-116.

Petenko, I., S. Argentini, A. Bolignano, G. Mastrantonio, A. Viola, 2004: Time and Horizontal Scales of Convective Plumes at Mid-latitudes. 12th International Symposium on acoustic remote Sensing, Cambridge, UK, British Antarctic Survey.

Poggi, D., A. Porporato, L. Ridolfi, J. D. Albertson, G. G. Katul, 2004: The Effect of Vegetation Density on Canopy Sub-Layer Turbulence. Boundary-Layer Meteorology, 111, 565-587.

Raupach, M. R., J. J. Finnigan, Y. Brunet, 1996: Coherent eddies and turbulence in vegetation canopies: the mixing-layer analogy. Boundary-Layer Meteorology, 78, 351-382.

Thomas, C., T. Foken, 2005: Detection of long-term coherent exchange over spruce forest using wavelet analysis. Theoretical and Applied Climatology, 80, 91-104.

Thomas, C., T. Foken, 2006: Organised motion in a tall spruce canopy: temporal scales, structure spacing and terrain effects. Boundary-Layer Meteorology, in print.

Thomas, C., J.-C. Mayer, F. Meixner, T. Foken, 2006: Analysis of Low-Frequency Turbulence Above Tall Vegetation Using a Doppler Sodar. Boundary-Layer Meteorology, DOI 10.1007/s10546-005-9038-0.

Williams, A., J. Hacker, 1993: Interactions between Coherent Eddies in the Lower Convective Boundary Layer. Boundary-Layer Meteorology, 64, 55-74.

Thermal Stratification and Weather Phenomena on Sodar Records

Lokoshchenko, Mikhail A.

Department of Meteorology and Climatology, Geography Faculty, Lomonosov Moscow State University. 119992, Lengory, Moscow, Russia. Phone: +7-495-9394284; E-mail: loko@geogr.msu.su

Abstract.

The results of analysis of low troposphere's thermal stratification in Moscow by the long-term sodar sounding have been presented for the period of one and half decades. Climatologic features of diurnal and annual courses of probabilities of various stratification types have been discussed. The sodar data on the thermal stratification all around the world have been summarized. The influence of meteorological parameters on the stratification has been investigated. Some examples of weather phenomena on sodar records have been presented.

1   Introduction and instrumentation.

Sodar records of echo-signal in 'time-height' co-ordinates represent specific and original kind of scientific information about the atmospheric structure which allows to investigate in details dynamics of small-scale thermal turbulence and stratification of the low troposphere. Vertical sodar «ECHO-1» of GDR production operates at Moscow University since 1988. Its operating frequency is 1666.6 Hz, vertical range of sounding – from 25 to 800 m, pulse duration – 75 ms, vertical resolution – 12.5 m (Kallistratova et al., 1986). These observations were started by common efforts of Moscow University and Institute of Atmospheric Physics (Lokoshchenko and Pekour, 1992, etc.).

As one knows (Krasnenko, 2001 and others) a type of the thermal stratification, i.e. a sign of vertical gradient of T or of the potential temperature θ can be successfully derived as a rule by the echo-signal structures on a sodar record. The reason of that is close connection between stratification type and the intensity of thermal turbulence and vertical motions, clearly detected by a sodar. For instance, thermal convection is simply distinguished at sodar records by appearance of typical vertically oriented structures, so-called 'plumes' as a result of passing of convective eddies above an observation site. Otherwice, clear horizontal layers of intensive echo-signal on a record as a result of dynamic turbulence indicate an existence of surface inversion under wind shear with a height. The determination of thermal stratification types was the eldest usage of non-Doppler sodars. For any separate hour this determination can be sometimes erroneous, but the long-term data are trustworthy because errors of different sign seem to be compensated in average. There are two principal limitations at this way. Firstly, it is difficult to automatize the procedure of coding which is made mostly manually and, hence, takes a lot of time. Secondly, any total international scheme of coding didn't be accepted that complicates precise comparison of this kind of climatology at various places – at least in details. However, this direction of the sodar data usage exists now among others and long-term sodar data on thermal stratifcation types have been accumulated all over the world – in India (Singal and Kumar, 1998 and others), in the United Kingdom (Spanton and Williams, 1988), in Poland (Walczewski and Feleksi-Bielak, 1988), in the USSR and Russia (Lokoshchenko, 2002 and 2006 b), in Greece (Asimakopoulos et al., 1994), in Ukraine (Maksymova et al., 2002), etc. Now the total amount of such coded data in Moscow (Russia) is nearly of 34.000 hours and involves all the period of sounding since 1988 till 2001 and, partially – till 2003. Hardly any longer row of sodar data, exceeding one decade and indicating values close to climatic, exists anywhere, except New-Delhi (India) and Krakow (Poland). The purpose of this paper is to present the most precise estimations of probabilities of various stratification types in Moscow, to compare them with similar ones at another places and to present at first their estimations under values of meteorological parameters.

2   Sodar data on the thermal stratification in Moscow.

The daily course of probabilities of the main stratification types has been presented for Moscow in average for year (Fig.1). The margins between surface inversions, slightly stable stratification and thermal convection are close to isothermal and dry-adiabatic vertical gradients of T at the ground air layer. Hence, a sum of these three types consists of 100 % everywhere. The daily course of surface inversions is quasi-sinusoidal. However, the amplitude of that is more in summer and in spring and less – in winter and in fall. As a result, the monthly values of surface inversions probability are nearly the same all over the year (from 35 to 40 %). The annual probability of surface inversions and of elevated ones in layer up to 800 m consists of 37 % and 18 % correspondingly in average. The annual probability of the thermal convection is 17 %; of indifferent or slightly stable stratification – nearly of 46 %.
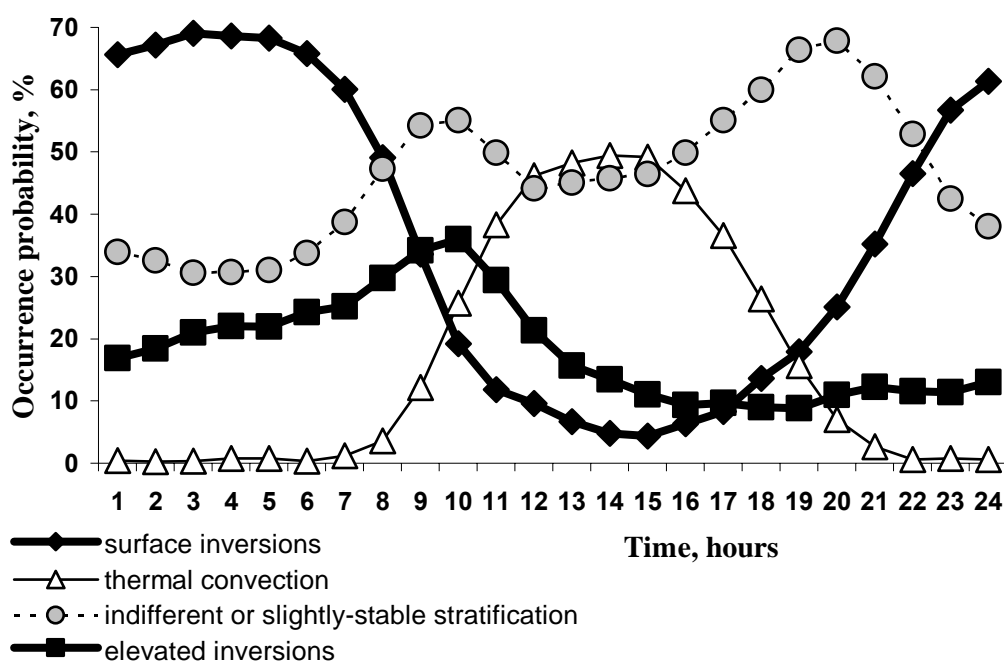
Fig.1. Occurrence probabilities of the thermal stratification types in Moscow by the sodar data all over the year, 1988-2003, in %.

Table 1 demonstrates the same statistics for various seasons. It has been discussed in details before (Lokoshchenko, 2006 b). Here let us note only that clear asymmetry exists between transitional seasons. The statistics in spring is close to one in summer, whereas the statistics in autumn, vice versa, is close to one in winter. The elevated inversions and slightly stable stratification have been detected more often in cold period of year.

Table 1. Occurrence probabilities of the thermal stratification types in Moscow at various seasons, 1988-2003, in %.

	Winter	Spring	Summer	Autumn
Surface inversions	**38.5**	**36.0**	**37.8**	**34.2**
Thermal convection	**3.0**	**24.3**	**30.0**	**10.1**
Indifferent or slightly-stable stratification	**58.5**	**39.7**	**32.2**	**55.7**
Elevated inversions	**21.4**	**15.2**	**16.9**	**19.9**

3   Geographical particularities of the thermal stratification by the sodar data.

At Table 2 similar statistics is summarized for various places of long-term sodar observations at different geographical regions. As it was mentioned above a comparison of the sodar data is not trivial task because of different schemes of coding. However, probabilities of the thermal convection and of elevated inversions can be compared successfully, because both types can be simply recognized on sodar records everywhere. Besides, the vertical range of sodars which were used is quite similar (as a rule, from 700 to 1000 m) that allows to compare the probability of elevated inversions. One can see that annual probability of the thermal convection consists of from 30 to 40 % in tropics and in subtropics. Nearly the same value has been received in mid-latitudes in summer (Odessa, Tomsk, Moscow), whereas the annual probability there is less than 20 %. It should be noted that the most of sites of sodar observations at Table 2 represent big cities when this parameter can be slightly overestimated due to local influence of the urban "heat island".

Table 2. Sodar data about thermal stratification of ABL.

Geographical region of long-term sodar observations about thermal stratification.	Probability of thermal convection	Probability of elevated inversions
New Delhi, India, 5 years (Singal et al., 1985)	32	16
Assam hills, India in winter (Singal and Kumar, 1998)	39	51
Tirupati, India (Narayana Rao et al., 1990)	30	14
Beijing, People's Rep. of China (Lu Naiping et al., 1990)	30	31
Athens, Greece (Asimakopoulos et al., 1994)	42	33
Krakow, Poland (Walczewsky et al., unpublished)	13 (22*)	17 (23*)
Odessa, Ukraine in July (Maksymova et al., 2002)	40	56
Tomsk, USSR in July (Krasnenko & Fursov, 1992)	39	18
Moscow, USSR-Russia (Lokoshchenko, 2006 b)	17 (31*)	18 (16*)

In July.

The probability of elevated inversions strongly depends on relief and other local factors and, as a consequence, demonstrates more differences. The most values of it seem to be expected at sea coast due to frequent inversions at breeze margins (e.g., in Odessa) or in mountains, especially in valleys. For instance, in Ptolemey valley in Greece elevated inversions were detected by sodar at half of all the time during one year (Asimakopoulos et al., 1994). Unfortunately, the data in London (Spanton & Williams, 1988) demonstrate unrealistic values. The only reason of it is erroneous coding, and these data were not included into Table 2.

4   Influence of meteorological parameters on the thermal stratification.

It is important, among others, to recognize what are the probabilities of stratification types in conditions of extreme values of the main meteorological parameters, i.e. under extremely hot or cold, wet or dry, windy or calm weather, etc. Hardly any similar statistics have been received before anywhere. For this purpose the combined database of the sodar data and results of the ground meteorological measurements of air temperature T, wind velocity V and relative humidity f has been created at Meteorological observatory of Moscow University

(Lokoshchenko, 2006 b). It should be noted that both the acoustic remote sensing, and measurements of T, V and f take place at the same site there. For comparison with the hourly sodar data the meteorological measurements being measured one time per each three hours were linearly interpolated for each hour. The result of calculations has been presented at the Table 3. Only the first column (T > 25 ˚C) represent average values for non-full daily course (except nocturnal hours). All the rest ones demonstrate values which were calculated proportionally for any hour at daily course and, hence, are comparative with each others. However, it should be noted that since 02 till 04 a.m. there were no cases under condition of V > 3 m/s and values for these hours were interpolated between ones for 01 and 05 a.m. Vice versa, the data under condition of V = 0 m/s in the afternoon exist but they seem to be not statistically sufficient. All the rest partial samples are sufficient (several decades of cases).

Table 3. Occurrence probabilities of the thermal stratification types in Moscow under various weather conditions, 1988-2003, in %.

	Hot weather* (T > 25 ˚C)	Cold weather (T < −15 ˚C)	Calm in summer (V = 0 m/s)	Windy weather in summer (V > 3 m/s)	Wet weather in summer (f > 90%)
Surface inversions	13	68	39	16	40
Thermal convection	51	5	25	28	4
Indifferent or slightly-stable stratification	36	27	36	56	56
Elevated inversions	14	32	17	9	23

Daily course of stratification types under the condition of 25 ˚C is not full, available data – from 8 to 22 hours.

One can see that the thermal convection occurs more often under hot weather in the comparison with average values in summer for period of from 8 a.m. to 10 p.m. Under very cold weather the probability of both surface inversions, and elevated ones is extremely high. Wind speed creates differences mainly in probability of surface inversions at night, whereas relative humidity – in probability of the thermal convection at daily hours.

5   Weather phenomena and synoptic events on sodar records.

Some examples of sodar records obtained in Moscow have been presented in Fig.2. The elevated inversion at frontal surface is presented in Fig.2 a). The passing of warm front took place at 23.30 of Moscow local time (marked by a sign). It is confirmed by baric tendency (quick falling of air pressure was stopped just at this time), wind turning, dynamic of T (which grew at night), etc. As it is seen an incline of elevated inversion at the record coincides with classic profile of warm front. An example of cold front passing at sodar record and dynamics of the ground air pollution has been discussed in (Lokoshchenko & Elansky, 2006).

An example of sodar record during solar eclipse in Fig.2 b) demonstrates decay of convection just before its beginning at 02 p.m. During eclipse which was noted by deep fall at global radiation course the stratification became firstly indifferent (no echo) and, then, even slightly stable in spite of summer day. Another example of sodar record under solar eclipse was received by Singal et al. in India which demonstrates convection weakening as well.
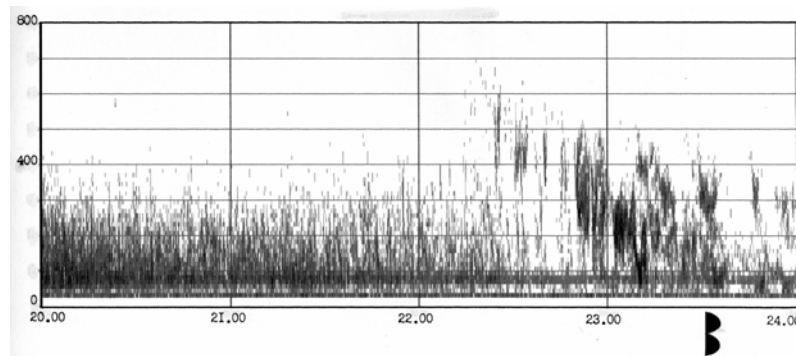
a) Frontal elevated inversion at the warm atmospheric front on Nov. 18[th,] 2004.
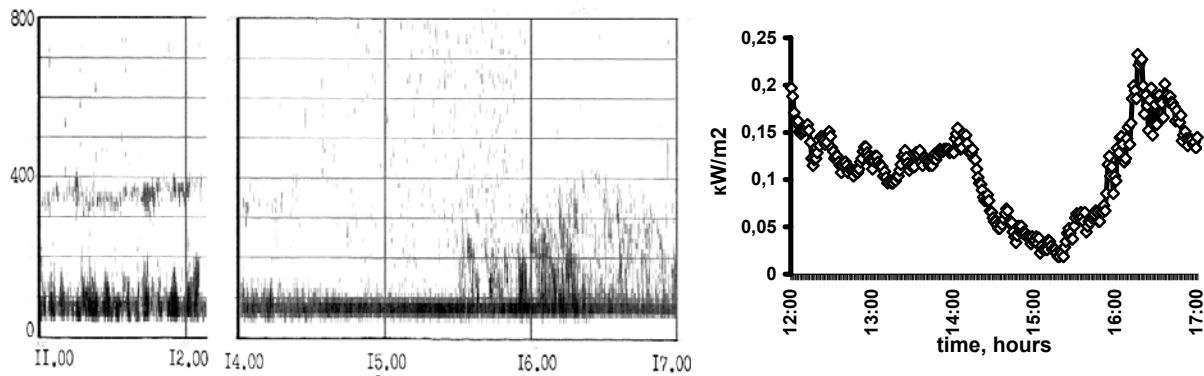
b) Solar eclipse on Aug. 11th, 1999. Sodar record (left) and global solar radiation (right).
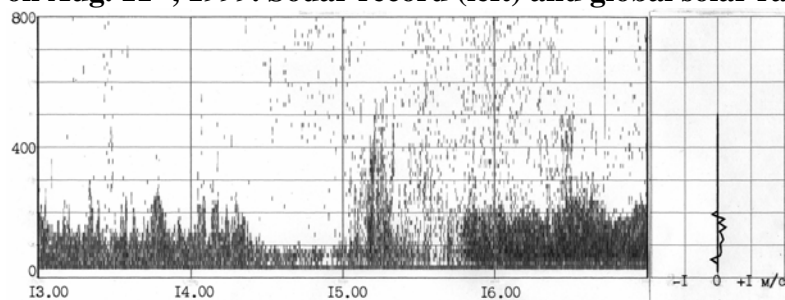
c) Thunderstorm and squall on July 24th, 2001. Record (left) and profile of W (right)
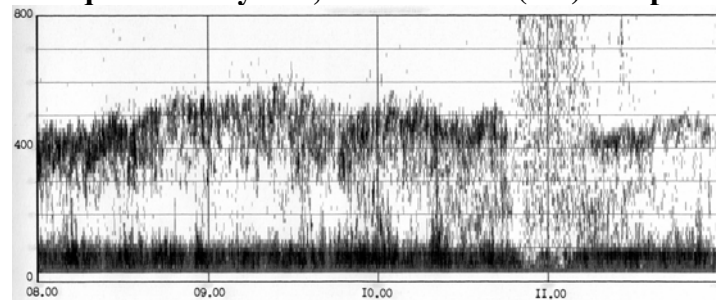
d) Temporal ruining of elevated inversion by strong shower on June 23rd, 2004.
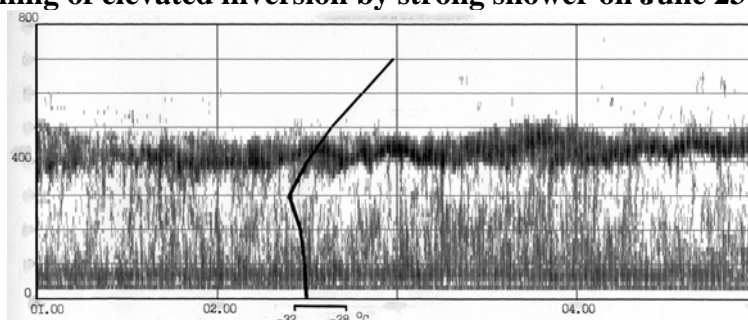
e) Inversion in time of strong frost on Jan.18th, 2006 (T = –30 ˙C).
Fig.2. Examples of sodar records, obtained at Moscow University (Moscow, Russia).

The sodar record during thunderstorm and ruining squall in Moscow (Fig.2 c) is analyzed in details in (Lokoshchenko 2006 a). Quick splash of echo-signal at 03.10 p.m. is quite typical for thunderstorm. In spite of strong vertical movements at zone of Cb clouds the averaged vertical component W for four hours is close to zero as it is seen at its profile. It is interesting to note the surface inversion after 03.50 p.m. This phenomenon during summer day is very rare and probable reason of it was evaporation of water after intense frontal showers.

Vanishing of elevated inversion in Fig.2 d) due to falling of intense shower during half an hour (from 10.45 to 11.15 a.m.) was followed by its appearing again. Evidently, air-mass shower, which was marked at the record by typical dot echo, took place at local area and then an air volume with the same inversion layer was replaced by wind from any side where weather remains dry.

The day of January 18th, 2006 was extremely cold in Moscow during a lot of recent years, the average daily T consists of −28 ˚C! However, the sodar record (Fig.2 e) demonstrates only the elevated inversion, but not the surface one. As it is seen, the radiosonde profile of T marked by black line confirms this conclusion. Probable cause of surface inversion's absence is cold advection from Siberia at this day and, besides, intense heating of big city.

Acknowledgements

References

Asimakopoulos D.N., Helmis C.G., and Deligiorgi D.G., 1994: Climatological evaluation of sodar recordings over complex terrain. Intern. Journal of Remote Sensing, 15, No.2, pp.383-392.

Kallistratova M.A., Lehmann H.-R., Neisser J. et al., 1986: Erste ergebnisse von messungen mit einem Vertical-SODAR. Z. Meteorolog., 36, № 4, pp.229-237.
Krasnenko N.P., 2001: Acoustic Sounding of the Atmospheric Boundary Layer (in Russian), 280 p. Tomsk, Russia, Institute of Optical Monitoring.
Krasnenko N.P. and Fursov M.G., 1992: The remote acoustic monitoring of meteorological parameters in the atmospheric boundary layer. Atmospheric and Oceanic Optics, Tomsk, 5, No.6, pp.412-414.
Lokoshchenko M.A., and Pekour M.S., 1992: Use of sound scattering for studying of temperature stratification of the atmospheric boundary layer. Atmospheric Oceanic Optics, Tomsk, 5, No.3, 205-207.
Lokoshchenko M.A., 2002: Long-term sodar observations in Moscow and a new approach of the potential mixing determination by radiosonde data, Journal of Atmospheric and Oceanic Technology, 19, 1151-1162.
Lokoshchenko M.A., 2006 a): Dynamics of thermal turbulence in low atmosphere in Moscow by the sodar data. Russian Meteorology and Hydrology, No.2.
Lokoshchenko M.A., 2006 b): The Thermal Stratification of Low Atmosphere in Moscow. Russian Meteorology and Hydrology (in print).
Lokoshchenko M.A. and Elansky N.F., 2006: Dynamics of Surface-Air Pollution during the Passage of a Cold Front. Izvestiya, Atmospheric and Oceanic Physics, 42, No.2, pp.148-155.
Lu Naiping et al., 1990: The detection of boundary layer structure with sodar in Western mountain area of Beijing. In: Proc. 5th ISARS, New Delhi, India, pp.345-356.
Maksymova N.G., Ulyanov Yu.N. and Shifrin Ya.S., 2002: Five-year sodar observations of PBL over land-sea boundary. In: Proc. 11th ISARS, Rome, Italy, pp.387-391.

Narayana Rao D. et al., 1990: Atmospheric boundary layer studies over Tirupati using sodar. In: Proc. 5th ISARS, New Delhi, India, pp.401-406.
Singal S.P. et al., 1985: Stability studies with the help of acoustic sounding. Atmospheric Environment, 19, No.2, pp.221-228.

Singal S.P. and Kumar S., 1998: Sodar studies of air pollution associated meteorological parameters in the hills of Assam, India. In: Proc. 9th ISARS, Vienna, Austria, pp.302-306.

Spanton A.M. and Williams M.L., 1988: A Comparison of the structure of the ABL in Central London and a rural/suburban site using acoustic sounder. Atmos. Environment, 22, No.2, pp.211-223.
Walczewski J., and Feleksi-Bielak M., 1988: Diurnal variation of characteristic sodar echoes and the diurnal change of atmospheric stability. Atmos. Environment, 22, No.9, 1793-1800.

Temperature and Inversion Strength Behaviour at Dome C, Antarctica, during the 2004-2006 Field Experiment

S. Argentini (*), I. Pietroni (*,°), G. Dargaud (*,^), A. Viola (*),
A. Conidi (*), G. Mastrantonio (*), A. Pellegrini (^), I. Petenko (*,+)

(*) ISAC-CNR Via del Fosso del Cavaliere, 100, 00133 Roma, Italy
(^) PNRA SCrl., C.R. Casaccia,Via Anguillarese 30100060 S. Maria di Galeria, Roma, Italy
(°) Università di Siena, Via del Laterino, 8 53100 Siena, Italy
(+) IAPh RAS, Pyzhevskiy, 3, 109017 Moscow , Russia
s.argentini@isac.cnr.it

Abstract

An atmospheric field experiment was held at the Franco-Italian station of Concordia (Antarctic plateau) during 2004-2005. With the exception of the summer period, a long-lived stable PBL was observed all the time. The lowest surface layer temperatures were observed in April and mid-August. Warming events occurred during the winter with temperatures reaching the summer values. The ground-based inversion strength in the first 100 m oscillated between 5 °C and 35 °C, the strength of the inversion increasing with decreasing temperature (5 °C at -35 °C, 35 °C at -70 °C). The inversion depth ranged between 100 m and 300 m. A weak convective boundary layer was observed during the summer in the warmest hours of the day.

1 Introduction

A large atmospheric field experiment STABLEDC (Study of the STABLE boundary layer at Dome C) was held at the Franco-Italian station of Concordia located on the Antarctic plateau at Dome C during 2004-2005. The RMO (Routine Meteorological Observation) programme was started during the same period. This was the first overwintering at Concordia. The aim of the field experiment was to study the processes occurring in the long-lived stable, and the weak convective, atmospheric boundary layers, observed during winter and summer respectively, and to collect the parameters relevant for the atmospheric models.

2 Site and Instrumentation

Dome C (75° 06' S, 123° 23' E) lies at 3306 m asl on the East Antarctic plateau, approximately 1000 km from the nearest coast. Surface slopes in the vicinity of the station are very small. Dome C is located on the top of a large dome, with no discernible slope, therefore it is not subject to the typical katabatic winds observed in Antarctica [*King and Turner*, 1997]. The annual mean wind speed is 3.4 m s^{-1} with extreme values up to 16 m s^{-1}. Monthly mean temperatures were –39 °C in summer and –61 °C in winter. Most of the time, strong surface inversions occur at Dome C, creating a large cold air source feeding the katabatic winds observed in some zones of confluence along the East Antarctic coast. In situ and ground based remote sensing sensors were used to monitor the meteorological parameters. Standard surface and upper-air (radiosounding) measurements were also part of the observations. The instrumentation as well as the measurements are given in Table 1.

3 Results

Figure 1 shows the temperature behaviour during the year. Strong warming events are periodically observed in winter corresponding to air temperature values typical of the summer. Figures 2 shows the behaviour of the shortwave and longwave radiation during the year.

Table 1

Radiometer mod.**CNR-1** (Kipp & Zonen) with two pyranometers (**CM3**) up and down two pyrgeometers (**CG3**) up and down	**Radiative budget: -** Incoming and outgoing shortwave and longwave radiation. -Net Radiation -Albedo
Conventional **HFP01** heat flux plates 0, 5, 15, 30, 50 cm	**Sub-surface energy fluxes Snow temperature profiles:** -Snow heat fluxes
A sonic anemo-thermometer mod. **USA - 1** (Metek) and a fast response LICOR **lyman-alpha-hygrometer** (only summer)	**Energy budget:** **-**Turbulent Fluxes (Heat, Latent, Momentum)
13-m Tower : thermometers, hygrometers and wind probes at 1.25, 2.5, 5, 10 and 13 m	**Surface layer profiles of mean variables**
A triaxial **Doppler mini-sodar** Range 12 - 400 m , Resolution 13 m	**PBL :** -Thermal structure of the ABL, Boundary layer depth, wind speed
Micro-lidar 532 nm wavelenght , Range 300 m	**PBL : -**Aerosols content; - Aerosol phase (liquid water or ice cristal), - Particles size
Passive Microwave radiometer by Kipp & Zonen. Range 0-500 m	**PBL :** - Temperature, Development and break down of atmospheric inversions
Radiosoundings	**Atmosphere:** - Temperature; - Pressure; -Wind speed
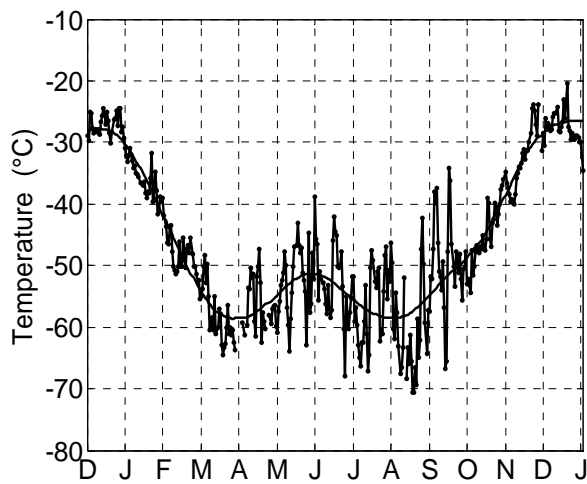
Figure 1. Temperature behaviour during the year.
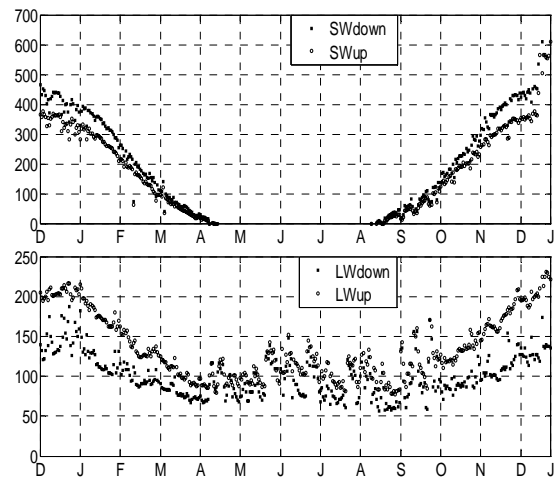
Figure 2. Shortwave and Longwave radiation up and down.
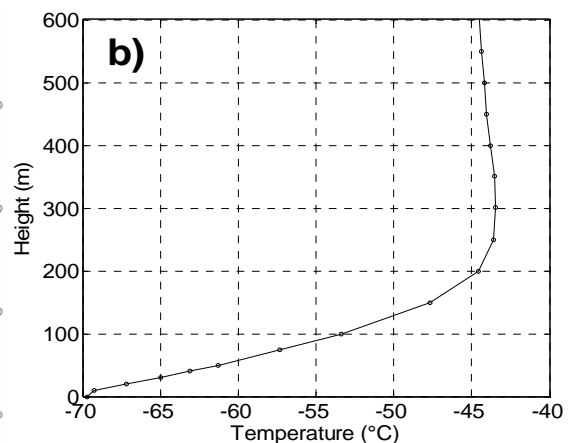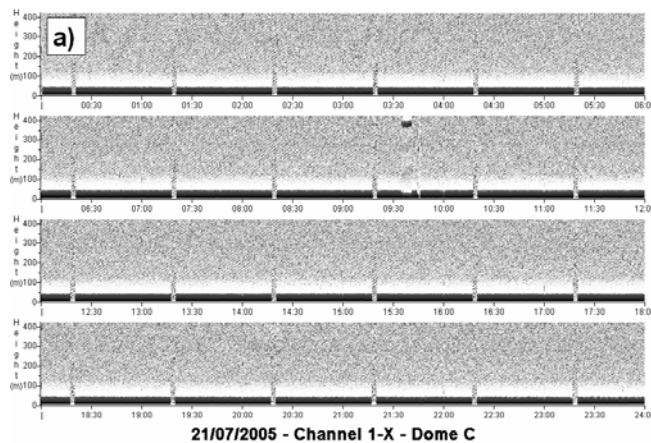
Figure 3. (a) Thermal structure of the atmosphere during winter as seen by a sodar for day 21 July 2005, (b) temperature profile by MTP5 for the same day at 1400 ST.

Figure 3a shows the thermal structure of the atmosphere for day 21 July 2005. No echoes are evident although a strong ground based inversion occurs below 150 m (figure 3b). Figure 4a and 4b give respectively the thermal structure of the atmosphere and the temperature profile for 7 January, 2005. The temperature profile refers to 1400 ST. A convective boundary layer occurs as shown by sodar and MTP5.
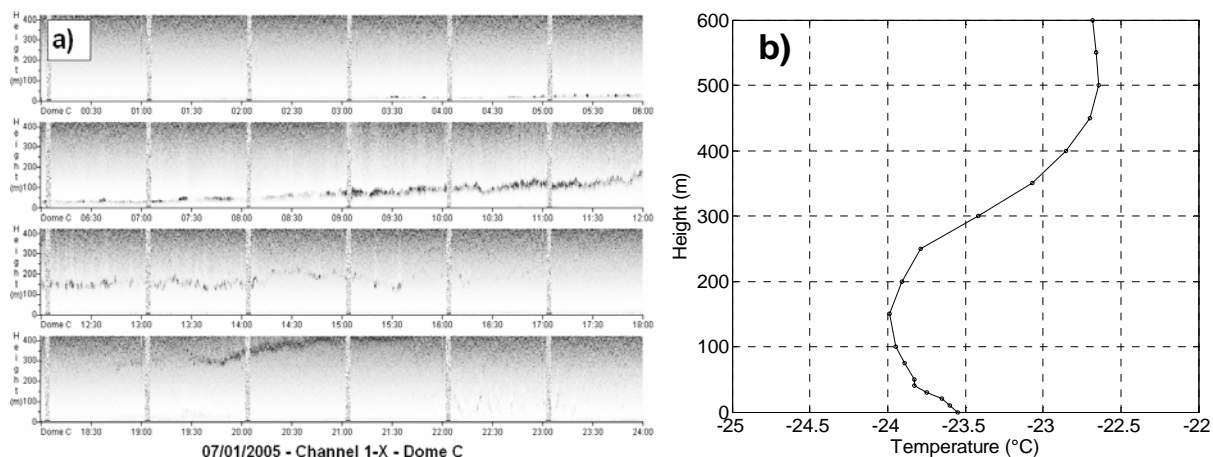
Figure 4. (a) Thermal structure of the atmosphere during summer as seen by sodar for day 7 January 2005, (b) temperature profile by MTP5 for the same day at 1400 ST.
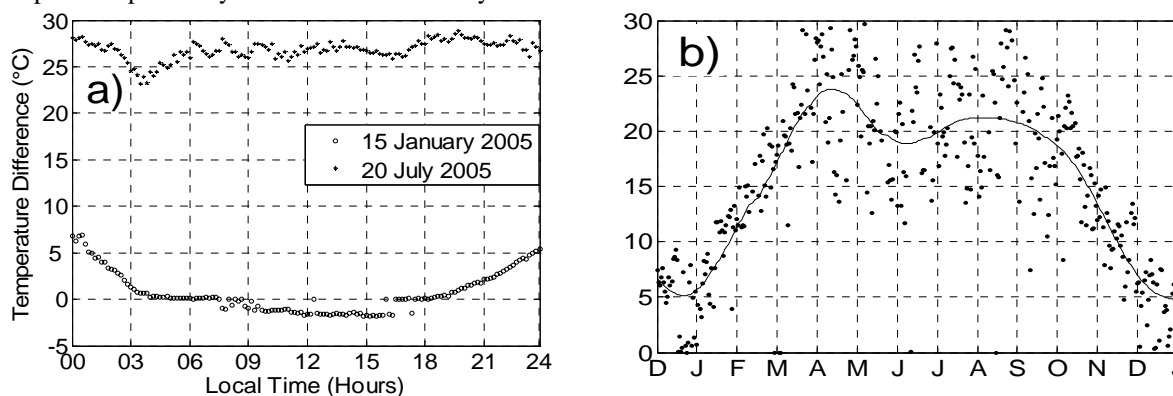
Figure 5. (a) Diurnal behaviour of temperature difference for 15 January 2005 and 21 July 2005, (b) Temperature difference during the year at 0200 LT.

Figure 5a shows the behaviour of the temperature difference between the ground and the beginning of the first inversion layer (generally around 150m -200 m) for a summer day (15 January 2005) and a winter day (21 July 2005). In winter the inversion strength varies between 24°-27° with small diurnal fluctuations. In summer instead a diurnal cycle is well evidenced with an inversion during the night and a weak convection during the day. Figure 5b shows the behaviour of the inversion strength during the year at 0200 LT. A larger temperature inversion is observed during spring and autumn. During the winter the temperature inversion strength decreases due to the warming events.

4 Summary

A large PBL experiment was held at Concordia station. This paper presents only a few preliminary results related to the intensity of the temperature inversion.

Acknowledgements

Literature

King, J.C., and J. Turner (1997), *Antarctic Meteorology and Climatology*, 409 pp., Cambridge University Press, Cambridge.

Use of SODAR/RASS data for analysing an anomalous dioxin concentration episode recorded in Milan urban area

A.Alberici[1], F.Curci[2], M.Favaron[1], D.Fraternali[1]

[1] Servizi Territorio

[2] AMSA

Abstract

This paper presents an experience about using a SODAR/RASS station to help analyzing the structure of the planetary boundary layer, aimed at understanding the possible causes of the high concentration of dioxins recorded during a passive samplers campaign held in the NW of Milan. The availability of RASS data sampled nearby the campaign area, at AMSA advanced meteorological station of Pero, allowed to detect a strong capping inversion, accompanied by extremely slow wind, which helps explaining the anomalous concentration..

1   Introduction

Because of its geographical structure, the area of Pianura Padana is characterized by a high incidence of stagnating conditions, caused by the concomitant occurrence of slow wind and a stable stratification of the first tens of meters of atmosphere.

These conditions have long been recognized as the main reason of the high atmospheric pollution measured in the area, but until recently there was scant instrumental coverage to assess quantitatively the phenomenon, as radio soundings are too largely spaced in time and vertical resolution, and given that station surfaces can not really measure beyond the height at which the anemometer is placed.

The situation has changed since the recent installation of SODAR and SODAR/RASS measurement nodes, one of which, located NW of Milan, was used for this work. These measurement nodes are beginning to collect and provide first-hand information about the actual stagnation phenomenon.

2   The trace pollutants monitoring campaign at the Milan-Silla 2 waste incinerator

Around the Silla 2 plant a one year monitoring activity has been carried out during winter 2004-05 in order to detect trace air pollutants (heavy metals, PAH, dioxins).
An anomalous high concentration of dioxins has been detected in the period 5-15 Dec 2004. This event has been thoroughly investigated in order to identify the possible source. In this context the authors analyzed the local micrometeorological conditions during the event.

3   Instrumentation

The instrument used is a Metek PCS-2000-64 SODAR with RASS extension, located within a wastewater treatment facility at Milan Pero. This instrument is part of an advanced meteorological station, equipped also with an ultrasonic anemometer, and part of the surveillance system of AMSA incinerator of Milan "Silla 2", with Servizi Territorio operating the management, maintenance and data processing.

The SODAR/RASS, shown in the figure, together with a small view of surrounding area, operates in continuous mode with a scan height from 60 to 500 m above ground, with a 20 minutes averaging time.

The relatively "low" maximum measurement height has been selected in order to ensure the averaged data are statistically meaningful with respect to the station's mission, that is, monitoring the AMSA Silla 2 incinerator plant.

3   Results
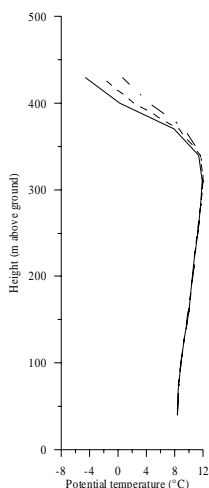
In the period investigated, from 05 to 15-Dec-2004, the statistical incidence of strong inversions was higher than usual, given the latitude and place.

The most common situation is depicted in the figure on left, where the whole thickness of the planetary boundary layer is presented. Because of the maximum height selected does not exceed 500m, there are various cases in which the inversion can not be seen completely.

In the time period indicated, wind speed was in the order of 1 m/s until 200m, as it can be seen in the figure on the right with reference to time 0630 of 06 Dec 2004.
Potential temperature gradient assumed in the period positive values ranging from 2 to 5 deg (very strong inversion).
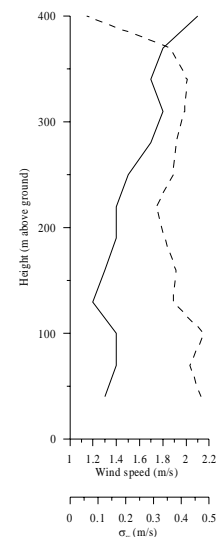
4   Discussion, Conclusions, and Outlook

In the period investigated, the wind direction is subject to intense variability, and this prevents executing a culpability analysis. However, the temperature gradient is large enough to explain the accumulation of pollutants within the PBL, with low wind speed which in turn prevent their advective removal. Thanks to the SODAR/RASS system these conclusions are supported by a quantitative evidence. This strong inversion, occurring at heights in most cases lower than its plume height, tend to exclude the Silla 2 incinerator as the source of dioxins; a possible future development is to collect additional micrometeorological data, helping specifically to identify possible source areas. For the future, we are considering to base further chemical campaigns following these anomalous meteorological conditions.

Blended Turbulence in Atmospheric Boundary Layers

Barth, Stephan*, Peinke, Joachim*, Böttcher, Frank**
*ForWind - Center for Wind Energy Research, University of Oldenburg, Germany
**Physics Department, University of Auckland, New Zealand
stephan.barth@forwind.de

Abstract

We introduce a model that interprets atmospheric increment statistics as a large scale mixture of different subsets of turbulence with statistics known from laboratory experiments. When mixing is weak the same statistics as for homogenous turbulence is recovered while for strong mixing robust intermittency is obtained.

1   Introduction

In this paper we focus on the scale dependent statistics of increments $u_\tau = U(t + \tau) - U(t)$ of atmospheric velocities $U(t)$, measured at different on- and offshore locations and compare them to statistics of homogenous, isotropic and stationary turbulence as realized in laboratory experiments. For homogenous, isotropic and stationary turbulence the statistical moments of velocity increments, the so-called structure functions have been intensively studied cf. [Frisch]. Their functional dependence on the scale τ is described by a variety of multifractal models. Besides the analysis of structure functions, probability density functions (PDFs) of the increments are often considered.

The atmospheric PDFs we examine here differ from those of common turbulent laboratory flows where - with decreasing scale τ - a change of shape of the PDFs is observed (e.g. [Castaing]). For large scales the "laboratory" distributions are Gaussian while for small scales they are found to be intermittent. The atmospheric PDFs however change their shape only for the smallest scales and then stay intermittent and non-Gaussian for a broad range of scales. Although the decay of the tails indicates that distributions should approach Gaussian ones (as for isotropic turbulence) they show a rather robust exponential-like decay.

The challenge is to describe and to explain the measured fat-tailed distributions and the corresponding non-convergence to Gaussian statistics. Large increment values in the tails directly correspond to an increased probability (risk) to observe very large events (gusts).

2   Superposition Model

We found that the observed intermittent form of PDFs for all examined scales is the result of mixing statistics belonging to different flow situations, which are characterized by different mean wind velocities. When the analysis by means of increment statistics is conditioned on periods with constant mean velocities results are very similar to those of isotropic turbulence. This can be seen in analogy to the *Castaing distribution* that interprets intermittent PDFs $p(u_\tau)$ as a superposition of Gaussian ones $p(u_\tau|\sigma)$ with standard deviation σ. The standard deviation itself is distributed according to a log-normal distribution. The *Castaing distribution* thus reads

$$p(u_\tau \mid \overline{u}) = \int_0^\infty d\sigma \frac{1}{\sigma\sqrt{2\pi}} \exp\left[\frac{u_\tau^2}{2\sigma^2}\right] \frac{1}{\sigma\lambda\sqrt{2\pi}} \exp\left[\frac{\ln^2(\sigma/\sigma_0)}{2\lambda^2}\right]$$

Two parameters enter this formula, namely σ_0 and λ^2. The first is the median of the log-normal distribution, the second its variance. The latter determines the form (shape) of the resulting distribution $p(u_\tau)$ and is therefore called *form parameter*.

We propose a model that describes the robust intermittent atmospheric PDFs as a superposition of isotropic turbulent subsets that are denoted with $p(u_\tau | \bar{u})$ and given by the equation above. Knowing the distribution of the mean velocity $h(\bar{u})$ the PDFs become $p(u_\tau) = \int_0^\infty d\bar{u} \cdot h(\bar{u}) \cdot p(u_\tau | \bar{u})$. We assume $h(\bar{u})$ to be a Weibull distribution:

$$h(\bar{u}) = \frac{k}{A}\left(\frac{\bar{u}}{A}\right)^{k-1} \exp\left[-\left(\frac{\bar{u}}{A}\right)^k\right],$$

which is well established in meteorology [Burton]. Combining the Weibull distribution and the Castaing formula the following expression for atmospheric PDFs is obtained:

$$p(u_\tau) = \frac{k}{2\pi A^k} \int_0^\infty d\bar{u} \int_0^\infty d\sigma \bar{u}^{k-1} \exp\left[-\left(\frac{\bar{u}}{a}\right)^k\right] \frac{1}{\lambda \sigma^2} \exp\left[-\frac{u_\tau^2}{2\sigma^2}\right] \exp\left[-\frac{\ln^2(\sigma/\sigma_0)}{2\lambda^2}\right].$$

Parameters A and k play a similar role as σ_0 and λ^2 in the *Castaing distribution*. With this approach intermittent atmospheric PDFs can be approximated for any location as long as the mean velocity distribution is known.
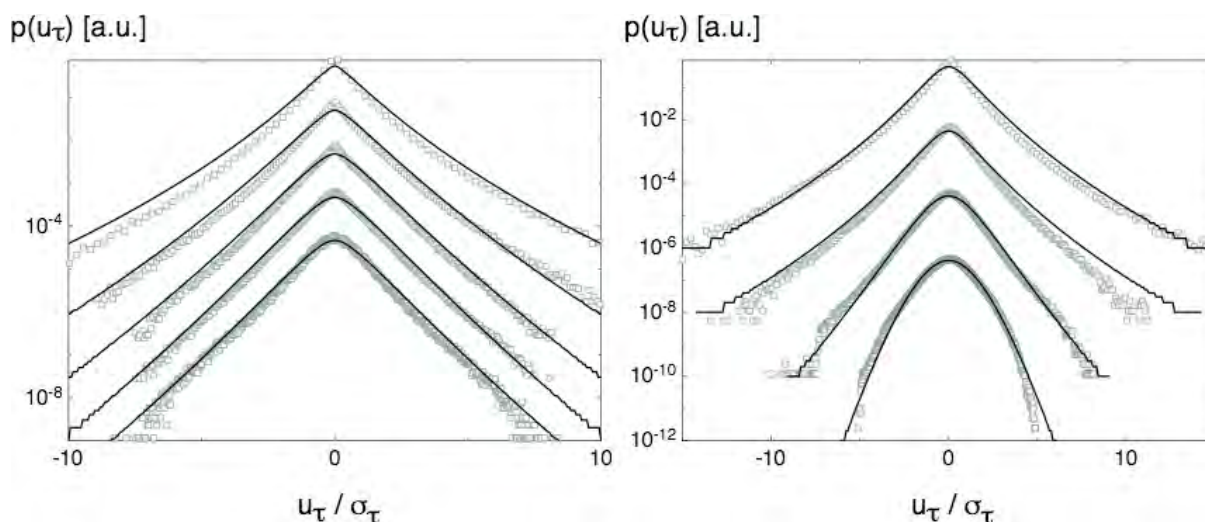
Figure 1. Atmospheric PDFs: Symbols represent normalized PDFs of the atmospheric data sets. Straight lines correspond to a fit of distributions according our model. All graphs are vertically shifted against each other for clarity of presentation. **Left**: sonic anemometer, non-stationary wind condition: From top to bottom τ takes the values: 0.5s, 2.5s, 25s, 250s and 4000s. **Right**: hotwire anemometer, stationary wind condition: From top to bottom τ takes the values: 2ms, 20ms, 200ms and 2000ms.

3   Conclusions and Outlook

Atmospheric velocity increments and their occurrence statistics are related to loads on wind turbines. For constructing wind turbines a model that reproduces the right increment distributions for every location should therefore be used. While our approach is a good candidate to achieve such a robust model for temporal velocity increments, it has to be checked on spatial velocity increments $u_{\vec{r}} = U(\vec{x} + \vec{r}) - U(\vec{x})$, where $\vec{r}$ is a separation vector. Such datasets could be obtained with remote sensing technologies like LIDAR.

Literature

Frisch, U., 1995: Turbulence. The Legacy of A. N. Kolmogorov, Cambridge University Press

Castaing, B., Gagne, Y., Hopfinger, E.J., 1990: Velocity Probability Density Functions of High Reynolds Number Turbulence. Physica D, **46**, 177-200

Burton, T., Sharpe, D., Jenkins, N., Bossanvi, E., 2001: Wind Energy Handbook, John Wiley & SonsISARS 13ISARS 13

Comparison of tethersonde and RASS vertical temperature profiles during a morning inversion break-up

Baumann-Stanzer, Kathrin and Piringer, Martin
Central Institute for Meteorology and Geodynamics, k.baumann-stanzer@zamg.ac.at

Abstract

During a winter episode with low winds, a SODAR with RASS extension and a tethered balloon have been operated simultaneously for several hours on February 10, 2005 at Linz, Austria at an industrial site to compare the in situ measured virtual temperature profiles to those of the remote sensing instrument.

1   Introduction

The daytime dilution of a temperature inversion and the rise of an elevated inversion layer are documented by the soundings of a SODAR with RASS extension and by a tethersonde balloon system operated near-by. The virtual temperature profiles from the two different systems are compared. Additionally, ultrasonic anemometer data from a 10 m mast next to the SODAR are available.

2   Instrumentation

Whereas the tethersonde system (Vaisala DigiCORA) measures instantaneous values every few seconds from which vertical profiles of about 1 m resolution are retrieved, the 482 MHz RASS extension of the SODAR delivers time- and height – averages every 10 minutes mean in height increments of 20 m. The RASS uses collocated radio wave and acoustic sources such that radio waves are scattered off the acoustic wavefronts. The propagation velocity of the acoustic wave fronts is related to the virtual temperature of the air.

Figure 1. SODAR DSDPA.90-64 with RASS extension (Metek) at an industrial site in Linz on a flat roof 5 m above ground.

The temperature sensor of the tethersonde (capacitive wire) has a reproducibility in sounding of 0.2°C (according to Vaisala). Humidity is measured with a thin film capacitor with 3 % accuracy. According to Metek, the resolution of the virtual temperature data of the RASS is 0.3°C. From the sound velocity of the ultrasonic anemometer (USA-1, Metek) an "acoustic" temperature is derived.

3   Results

Between 12 and 13 MEZ, a good agreement is found between the temperature profiles of the two systems, especially above 100 m above ground. Within the lowest 100 m, the RASS renders up to 0.5°C warmer temperatures than the tethersonde which was launched at a grass site nearby (80 m horizontal distance). The bias ranges between 0.1 and 0.5. After 13 MEZ, the RASS temperatures within the lowest 200 m increase more rapidly than in the tethersonde soundings. Between 13:30 and 14:30 MEZ, the RASS temperatures are on average 0.6°C higher than the tethersonde measurements. A good agreement is still found between the measurements of the two systems at the height of the elevated inversion layer between 270 and 320 m. The standard deviation of the temperature differences is between 0.3 and 0.4. The sonic temperature values are generally in better agreement with the tethersonde sounding.
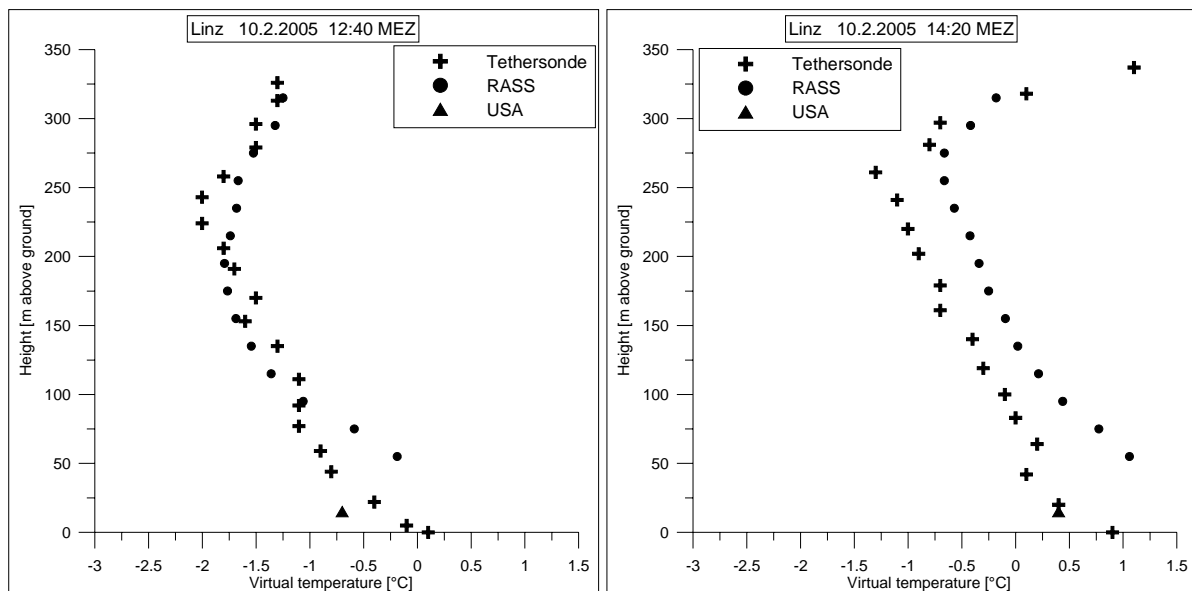
Figure 2. Comparisons of selected virtual temperature profiles from tethersonde (crosses) and from RASS (circles) and (acoustic) temperature from ultrasonic anemometer (triangle).

4   Discussion, Conclusions, and Outlook

A positive bias between RASS and tethersonde is found to increase during day-time. As the RASS is situated on top of a flat roof and next to high stacks, while the tethersonde is operated at a grass area near-by, these differences may be explained by the different heat-fluxes of these surfaces. This is contradicted by the fact that the temperature measurements from the ultrasonic anemometer on top of the roof are in good agreement with the tethersonde data. Further comparisons at a non-industrial, flat site are planned. The temperature differences found during this campaign are small compared to the accuracy of the instruments and are similar to results of other comparison studies. Goersdorf and Lehmann (2000) found less than 0.3 K bias between RASS and radiosonde and a standard deviation of temperature differences between 0.4 and 0.7 K.

Literature

Goersdorf, U., V. Lehmann, 2000: Enhanced Accuracy of RASS-Measured Temperatures Due to an Improved Range Correction. Journal of Atmospheric and Oceanic Technology 17, 406-416.

Acoustic Investigations of the Atmospheric Boundary Layer Structure, Dynamics and Turbulence

Bukhlova Galina, Krasnenko Nikolay, Stafeev Pavel
Institute of Monitoring of Climatic and Ecological Systems
of the Siberian Branch of the Russian Academy of Sciences
10/3, Akademicheskii Pr., Tomsk 634055, Russia
E-mail: galvik76@mail.ru, krasnenko@imces.ru, spg@iao.ru

Abstract

The results of investigations carried out in different seasons are presented. Measurements were performed with an ultrasonic meteorological complex and sodar. In addition to the standard meteorological parameters, we measured such turbulence parameters, as the turbulent kinetic energy, momentum and heat fluxes, wind and temperature scales including the Monin–Obukhov length, etc., and also their statistical characteristics. Classes of atmospheric stability were determined in the course of measurements. The results obtained are compared with the data of conventional measurements at the meteorological station. The behavior of the measured parameters is studied depending on the general atmospheric state.

1   Introduction

Acoustic methods based on effects of strong interaction of a sound wave with the atmosphere contribute significantly to investigations of the structure and dynamics of the atmospheric boundary layer. They are subdivided into remote methods implemented with the use of acoustic radars and local methods with the use of ultrasonic means. Associated methods and means expand the capabilities of such investigations.

2   Instrumentation

The several models of monostatic acoustic radars were created including the MAL-1, MAL-2, Zvuk-1, Zvuk-2, Zvuk-3 sodars and the mS-1 minisodar. These sodars were intended for investigations of the temperature stratification of the atmosphere (Zvuk-1) and of the temperature stratification and the wind velocity vector (all the others). These sodars were subsequently used for case and integrated, invoking some other measuring means, experimental studies of the atmospheric boundary layer.

Also were created the several ultrasonic meteorological complexes: onboard system, portable system, and various modifications of stationary automated meteorological complexes (AMC) for *in situ* measurements of the meteorological parameters (pressure, humidity, three wind velocity components, and temperature) and turbulent characteristics of the atmosphere. These systems have successfully passed the State tests, certification, and can be used to measure the friction velocity, turbulent heat flux, Monin–Obukhov length, structure constants of the temperature (C_T^2) and wind velocity fields (C_v^2), and many other characteristics with reconstruction of vertical profiles of meteorological characteristics in the atmospheric surface layer.

3   Results

We accumulated a large volume of data on the temperature stratification of the urban atmospheric boundary layer [1-5], for which the presence of temperature inversions was typical. The Zvuk-3 monostatic sodar was used to study the atmosphere of the Tomsk city. The structural constant of the temperature fluctuations and the mixing layer height were measured.

The outer scale of atmospheric turbulence was first measured together with the structural characteristic of the temperature fluctuations. The outer scale of turbulence plays an important role in the theory of atmospheric turbulence, because it determines the upper boundary of the inertial subrange in the spectra of temperature and wind velocity fluctuations [3].

Sodars can also be used in systems of monitoring of air basins when solving the problem of air pollution in industrial centers, because they yield information on the meteorological state of the atmospheric boundary layer and its dynamics.

Integrated studies of the structure and dynamics of the atmospheric boundary layer were use of standard meteorological means, a sodar, and an ultrasonic meteorological station capable of measuring a set of meteorological and turbulent atmospheric characteristics for two years. The synoptic situation was also monitored. Classes of atmospheric stability and heights of the mixing layer were determined. It was demonstrated that under conditions of urban building (in the city environs), the spatial variability of meteorological fields in the surface atmospheric layer was observed. This conclusion was also confirmed by the data of conventional meteorological sensors. The sodar and the ultrasonic meteorological station allowed us to record fine spatiotemporal structure of meteorological fields in the atmospheric boundary layer and its variability, supplementing standard meteorological measurements. At the same time, for example, classes of atmospheric stability determined from facsimile records of the sodar and from the Monin–Obukhov length scale correlated only slightly. This fact requires additional tests.

4   Conclusions

In the present report, the results of investigations into the structure, dynamics and turbulence of the atmospheric boundary layer are given. They illustrate the capabilities of remote sounding means and integrated approach to the study of the atmospheric boundary layer.

Literature

Krasnenko N., 2001: Acoustic sounding of the atmospheric boundary layer. Tomsk. 2001. 278 P. (in Russian).

Zuev V., Yu. Balin, B. Belan, N. Krasnenko, **1998:** Research of the optical, radiative, and meteorological characteristics of the boundary layer based on remote sensing data obtained during the 1996 intensive observing period in Tomsk / Proc. Seventh Atmospheric Radiation Measurement (ARM) Science Team Meeting, San Antonio, Texas, January 1998, p. 373-377.

Krasnenko N., L. Shamanaeva, **1998:** Sodar measurement of the structural characteristics of temperature fluctuations and the outer scale of turbulence / Meteorologische Zeitschrift, N.E. 7, December, p. 392-397.

Krasnenko N., P. Stafeev, 1999: Study of the variability of meteorological state of the lower atmosphere / Proc. SPIE, V. 3983, p. 505-514.

Buhlova G., N. Krasnenko, P. Stafeev, 2002: Monitoring of the turbulence in the near-ground layer of the atmosphere / Proc. SPIE, V. 4678, p. 431-438.

Applications of a Ground-based Microwave Radiometer in Aviation Weather Forecasting

P.W. Chan, K.C. Wu and C.M. Shun
Hong Kong Observatory, Hong Kong, China, email: pwchan@hko.gov.hk

Abstract

This paper discusses the aviation weather applications of a ground-based microwave radiometer as demonstrated in a field experiment in Hong Kong in early 2006. The radiometer is found to measure the boundary layer temperatures reasonably accurately by comparing with radiosonde measurements. Its data are analyzed with the other weather observations at the Hong Kong International Airport (HKIA), such as a Doppler SODAR, to demonstrate its application values in the stable boundary layer.

1 Introduction

The continuous availability of thermodynamic profiles in the boundary layer would be useful for aviation weather forecasting. In a previous study (Chan and Tam 2005), the application of a microwave radiometer in the nowcasting of severe convective weather was considered. The present paper would focus on the use of the radiometer in the stably stratified boundary layer, such as the monitoring of dense fog and terrain-induced airflow disturbances.

2 Instrument and field experiment

The radiometer (RPG-HATPRO) was used in the field experiment in Hong Kong from 10 January to 14 March 2006. In the first 36 days, the instrument was tested in the downtown area at about 1 km to the south of the radiosonde station for comparison. It was then moved to Siu Ho Wan wind profiler station (see Figure 3 for location), situated at about 5 km east of HKIA, to study the applications to aviation weather forecasting. It employed 7 oxygen channels and 7 water vapour channels to measure boundary layer temperature, tropospheric temperature and humidity, liquid water as well as integrated water vapour. This paper only considers the boundary layer temperature profiles, which were obtained by scanning at 6 elevation angles and available every 17 minutes.
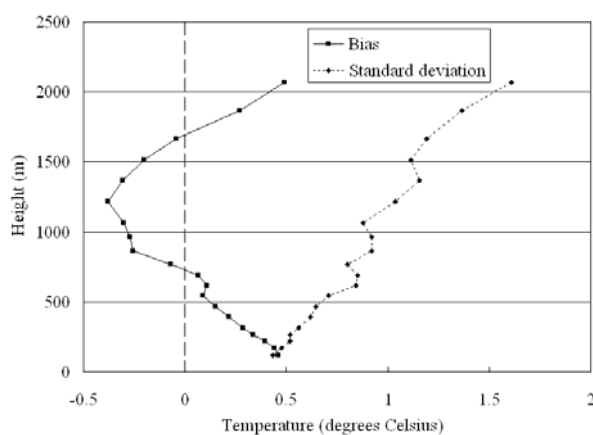
Figure 1. Comparison results for boundary layer temperatures between radiometer and radiosonde.
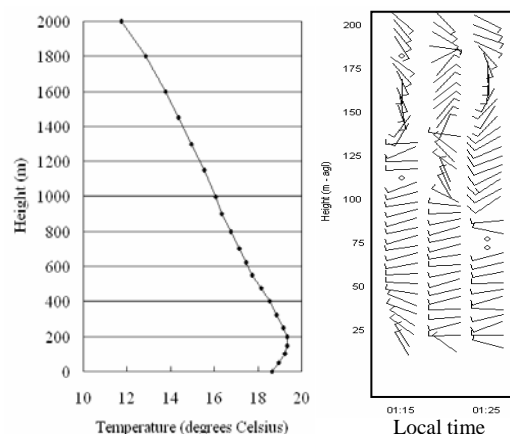
Figure 2. Boundary layer temperature profile from radiometer at 01:22 a.m., 7 March, and SODAR wind data.

3 Comparison with radiosonde measurement

Comparison results with radiosonde data during the downtown test are given in Figure 1. In this period, the bias and the standard deviation between the ground temperatures at the

radiosonde station and the radiometer site was 0.3 and 0.5^{o}C respectively. The bias of the radiometer was within 0.5^{o}C in magnitude, comparable with that of the ground temperature. Taking into account the standard deviation of ground temperature and making reference to the measurement accuracy of radiosonde (0.5^{o}C), the radiometer measurement was considered to be accurate (within 1°C from the radiosonde) up to about 1.2 km, consistent with the previous experience with the instrument.

4   Dense fog on 7 March 2006

Dense fog bringing a visibility as low as 100 m affected HKIA in the early morning on 7 March. Surface observations (not shown) suggested that the fog arise from the mixing of a cooler westerly airstream with a warmer easterly airstream, which were both near saturation. This was supported by the radiometer and the SODAR data at Siu Ho Wan. The radiometer indicated that there was a temperature inversion of about 0.7^{o}C below 200 m (Figure 2). As shown from the SODAR wind measurements (Figure 2), the cooler westerly reached an altitude of about 150 m and was capped by the warmer easterly aloft.

5   Windshear episode on 8 March 2006

Moderate east to southeasterly winds prevailed over Hong Kong on 8 March. In the morning, the radiometer showed a strong inversion (~3°C: Figure 3, left) and mountain waves were seen downstream of Lo Fu Tau from the LIDAR (not shown). Towards noon, the prevailing easterly flow abated slightly, the temperature inversion weakened and unstable layer near the ground extended upwards. This favours the occurrence of airflow disruption up to 250 m or so above ground to be capped by a stable layer aloft. In fact, from LIDAR velocity (Figure 3, right), airflow disruption was found in the jet emanating from the gap (height: ~150 m AMSL) south of Lo Fu Tau and affected the eastern portion of south runway. Windshear reports over that runway were only received in this period (between 11:26 and 11:42 a.m.). Later on, the prevailing easterly flow picked up again and the boundary layer became more stable.
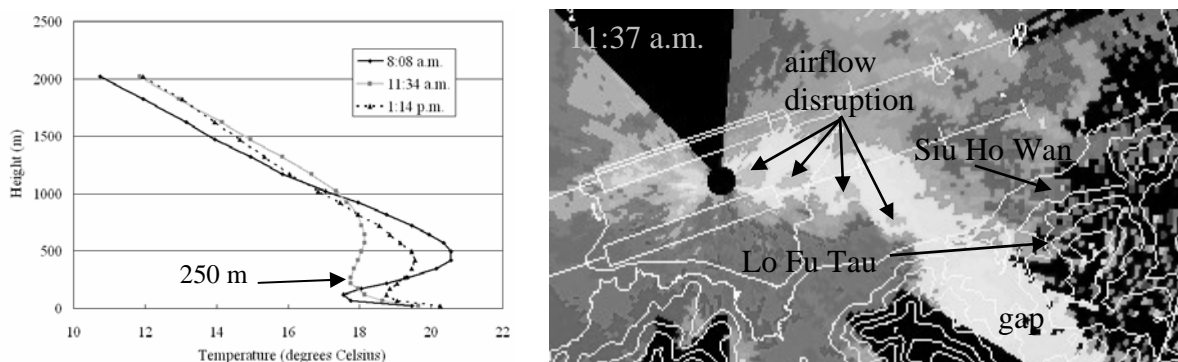
Figure 3. Selected boundary layer temperature profiles from the radiometer on 8 March 2006 (left) and LIDAR's 4.5-degree Plan Position Indicator (PPI) scan of radial velocity at 11:37 a.m. on that day (right).

6   Conclusions

The radiometer was found to provide useful boundary layer temperatures for aviation weather applications such as monitoring of fog and windshear.

Literature

Chan, P.W., and C.M. Tam, 2005: Performance and application of a multi-wavelength, ground-based microwave radiometer in rain nowcasting. *Ninth Symposium on Integrated Observing and Assimilation Systems for Atmosphere, Oceans, and Land Surface*, American Meteorological Society, San Diego, California, USA.

Diurnal and altitude variations of the turbulence kinetic energy derived from sodar data

Kramar, Valeri
Obukhov Institute of Atmospheric Physics Russian Academy of Sciences
vkramar@ifaran.ru

Abstract

Three-beam Doppler sodar and two sonic anemometers were used to collect atmospheric boundary layer (ABL) turbulence parameters during 30-days measurements at Zvenigorod Scientific Station in July 2005 (Zvenigorod-2005). Diurnal variations of the turbulence kinetic energy (TKE) allowed a contribution of different terms in the TKE budget equation to be estimated. The results for periods of strongly stable and strongly unstable states of the thermally stratified ABL are presented. Low level wind jets and the TKE budget discussed as well.

1   Introduction

Turbulence kinetic energy balance equation and the TKE value are widely used in a lot of turbulence models, approximations as well as for number of parametrisation of different ABL values. The Zvenigorod-2005 data were procecced using mathematical model of thermally stratified ABL. The model includes heat, momentum, TKE and dissipation of TKE transfer equations and the set of algebraic equations for second order turbulent moments and was designed close to widely used Rodi recommendations [Rodi, 1980].

2   Instrumentation

Breaf description of the Zvenigorod-2005 experiment and some profiles for stably stratified ABL one can find in [Kramar, 2006]. The data of the experiment were used to classify behavior of the ABL turbulence parameters and to select their trends repeated from day to day. The sodar profiles of wind velocity and variance of vertical velocity, and sonic data were used to calculate profiles of the TKE shear production term.

3   Results

Fig.1 shows an evolution of the TKE value, the TKE shear production term value, the TKE heat flux production term and the TKE dissipation rate (graphs from top to bottom) for July 10, 2005. The data measured by sonic anemometer situated at 56m altitude were complemented with horizontal wind profiles measured by the sodar. Low rate of TKE variability (look at the top of figures) permits to use the approximation of the local equilibrium of turbulence. Therefore TKE dissipation rate was calculated directly as a sum of generation terms. Nevertheless the difference of an order for the TKE values at the daytime and at the night time was registered.

With the help of the sonic anemometer data a set of empirical constants of the model was verified for each vertical profile. Then vertical distributions of unknown variables of the model were calculated using evolution of sodar vertical profiles of horizontal wind velocity and vertical velocity variance.

4   Discussion, Conclusions, and Outlook

The associated usage of the sodar measurement data, sonic anemometer measurement data and the mathematical model of thermally stratified turbulent ABL gives the possibility to

adjust values of the empirical constants of the model as well as to reconstruct vertical profiles of all unknown variables for the ABL for any time moment.
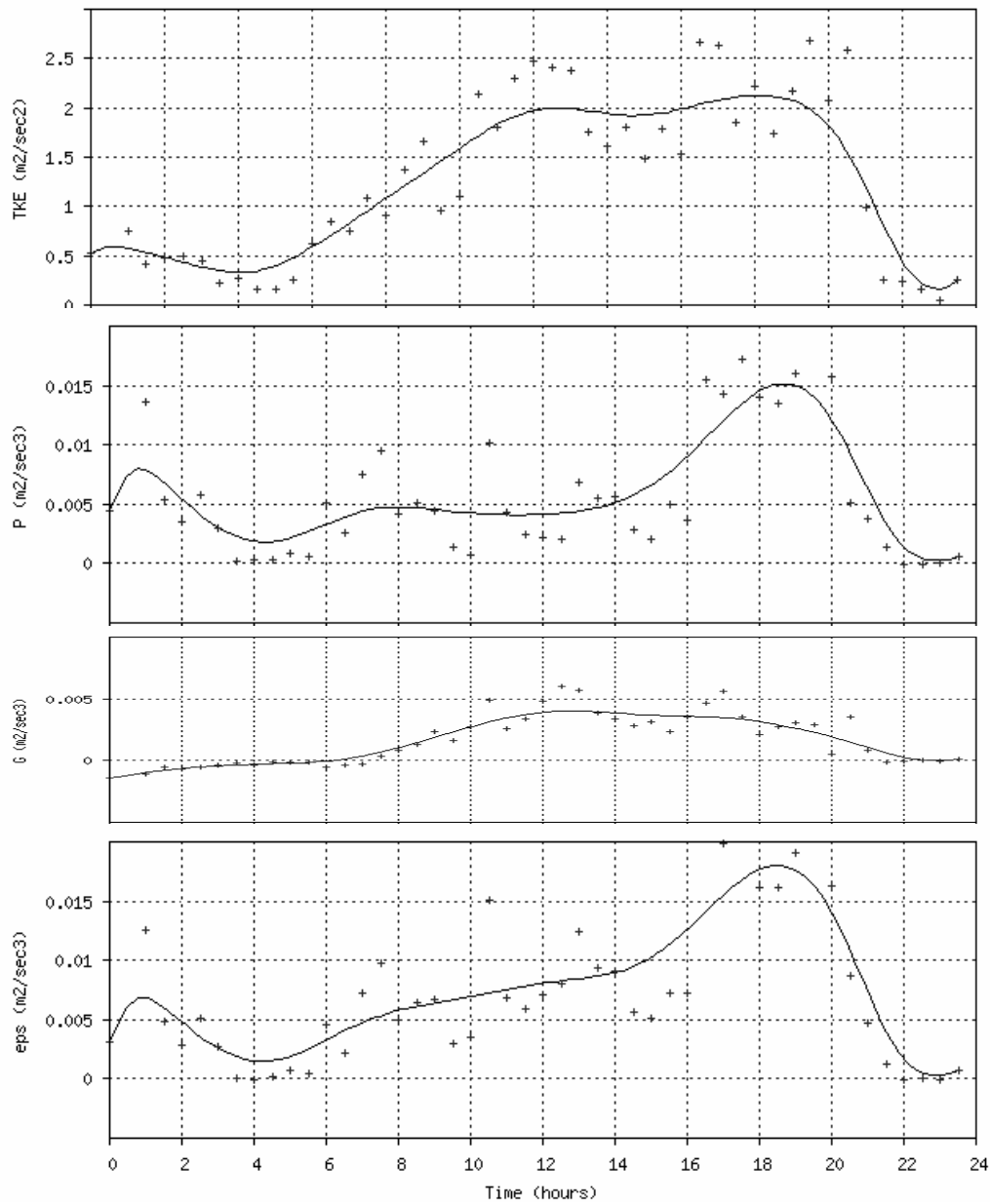
Figure 1. The evolution of the TKE balance components. Zvenigorod, July 10, 2005. Altitude 56m. Full lines are the Bezier smoothing of the data of measurements.

Literature

Rodi, W., 1980: Turbulence models for environmental problems. in Prediction Methods For Turbulent Flows (Kollman, W. Ed.). Hemisphere Publishing. Corporation, Washington, DC, pp. 259-350.

Kramar, V., 2006: A model for atmospheric boundary layer night cooling and its comparison with sodar data. Proc. 13-th Int. Symp. Acoust. Rem. Sens.— Garmisch, Germany: 2006.— pp. 180-182.

Sodar-derived surface heat flux and turbulent energy dissipation rate

Shamanaeva Lyudmila
Institute of Atmospheric Optics of the SB RAS, 1, Akademicheskii Ave., 634055 Tomsk, Russia
e-mail: sima@iao.ru

Abstract

The report presents quantitative estimates of the surface heat flux Q_0 and the turbulent energy dissipation rate ε derived from the data of acoustic sounding with the Zvuk-2 three-channel Doppler sodar capable of simultaneous measuring the backscattered signal power. An original closed data processing algorithm has been developed that allows the excess turbulent attenuation of sound on the propagation path to the sounding volume and back to the receiver to be taken into account in the sodar data interpretation.

1   Introduction

Based on the method suggested in (Shamanaeva 2000), the data of acoustic sounding with the Zvuk-2 three-channel Doppler sodar (Gladkikh *et al*. 1997) capable of measuring the backscattered signal power are interpreted. The closed iterative data processing algorithm (Shamanaeva 1999) which considers the excess turbulent attenuation of a sound pulse propagating from the transmitter to the sounded volume and back to the receiver was refined to additionally calculate the surface heat flux and turbulent energy dissipation rate.

2   Instrumentation and data processing algorithm

The Zvuk-2 sodar design and operation were described in detail in (Gladkikh *et al*. 1997). The sodar operated at a frequency of 1700 Hz, its pulse repetition period was 11.5 s, and its pulse length was 150 ms. A closed iterative algorithm (Shamanaeva 2000a) was used to derive simultaneous vertical profiles of the thermal, $C_T^2(z)$, and velocity structure parameters $C_V^2(z)$. The vertical profiles of the turbulent energy dissipation rate in the mixed layer were calculated from the sodar-derived vertical profiles $C_V^2(z)$ using the formula (Kaimal 1973)

$$\varepsilon(z) = \left[\frac{C_V^2(z)}{1.97} \right]^{3/2}. \tag{1}$$

The surface heat flux was calculated from the sodar-derived vertical profiles $C_T^2(z)$ using the formula (Wyngaard *et al*. 1980)

$$Q_0(z) = \left[0.75 C_T^2(z) \right]^{3/4} \kappa^{1/2} z \left(\frac{g}{T} \right)^{1/2}, \tag{2}$$

where κ is the Von Karman constant, g is the acceleration of gravity, and T is the mean atmospheric temperature.

3   Results and discussion

Figure 1 shows the vertical profiles of the turbulent energy dissipation rate calculated by Eq. (1) for sodar measurement sessions from 9 to 9:10 and from 10 to 10:10 a.m., LT on July 2, 1997. The turbulent energy dissipation rate increases with altitude. Three local maxima centered at 85, 240, and 420 m can be seen in the first vertical profile of ε. The maximum ε value reaches $0.0135 \text{ m}^2/\text{s}^3$. In the second profile, already 6 local maxima are clearly pronounced. The maximum ε value here reaches only $0.008 \text{ m}^2/\text{s}^3$.

The values of the heat flux calculated by Eq. (2) for these measurement sessions are shown in Fig. 2a and b, respectively. To calculate them, the sodar-derived profiles $C_T^2(z)$ were approximated by the $z^{-4/3}$ altitude dependence predicted theoretically, and Q_0 values were calculated for those altitude ranges for which the deviation of the experimentally measured thermal structure parameter from the theoretically predicted one did not exceed 30%. It can be seen that during both measurement sessions, $Q_0 = 0.045$–0.065 K·m·s^{-1}. This is in agreement with $Q_0 = 0.02$–0.1 K·m·s^{-1} obtained by (Asimokopoulos *et al.* 1996).
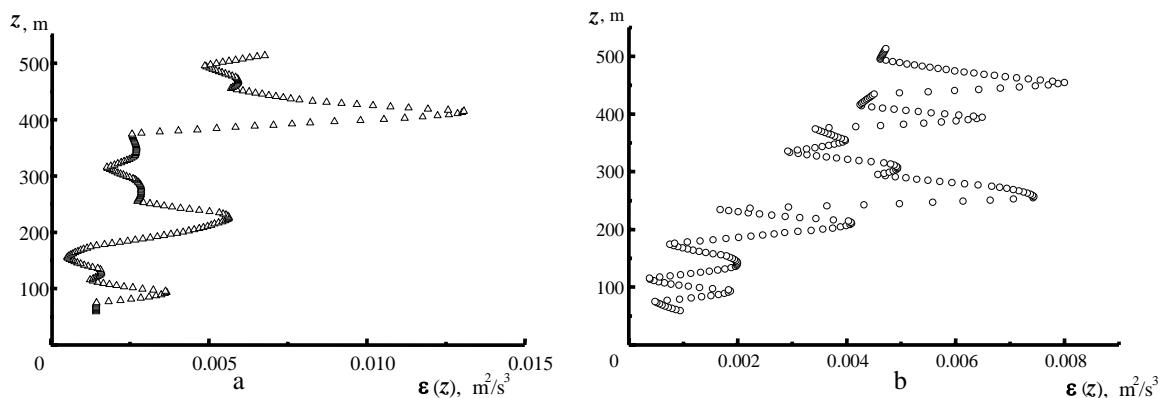
Figure 1.
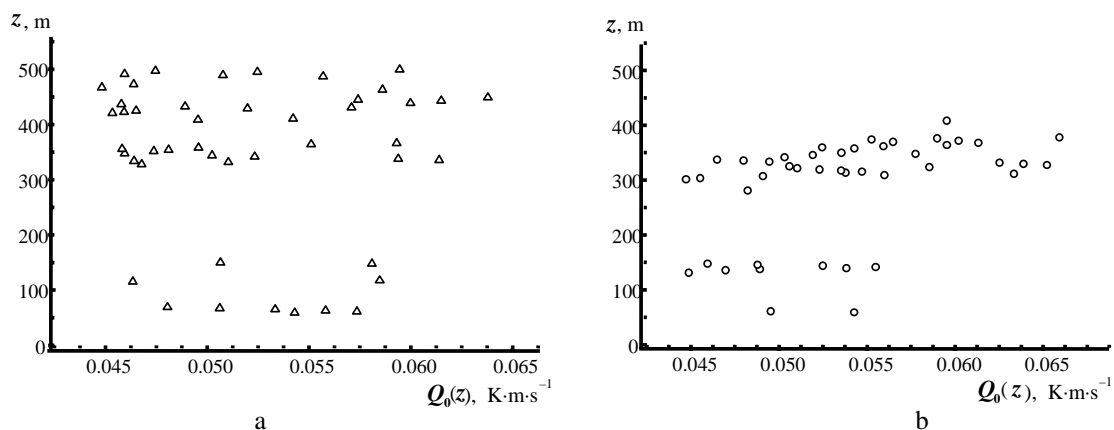
Figure 2.

Literature

Asimakopoulos, D. N., C. G. Helmis, J. A. Kalogiros, 1996: Quantitative estimation of CBL parameters using the vertical velocity and echo intensity measurements of an acoustic soulder. Proc. 8th ISARS, Moscow, G.85-G.96.

Gladkikh, V. A., N. P. Krasnenko, V. A. Fedorov, 1997: Zvuk-2 acoustic sodar. COST-76 Profiler Workshop, Engelberg, 174-177.

Kaimal J. C., 1973: Turbulent spectra, length scales and structure characteristics in the stable surface layer, Boundary-Layer Meteorology, Vol. 4, 289-309.

Shamanaeva, L. G., 1999: New method of acoustic sounding of the parameters of atmospheric turbulence. Proc. SPIE, Vol. 3983, 344-349.

Shamanaeva, L. G., 2000: Interpretation of the data of simultaneous sodar measurements of vertical profiles of C_T^2 and C_V^2 in the atmospheric boundary layer. Proc. SPIE, Vol. 4341, 316-322.

Shamanaeva, L.G., 2000a: Interpretation of the data of simultaneous sodar measurements of vertical profiles of C_T^2 and C_V^2 in the atmospheric boundary layer. Proc. 10th ISARS, Auckland, 334-337.

Wyngaard, J. C., M. A. LeMone, 1980: Behavior of the refractive index structure parameter in the entraining convective boundary layer. J. Atmos. Sci., Vol. 37, 1573-1585.

Sodar Spectra at Low Levels in the Stable Nocturnal Boundary Layer

John R. Taylor, Marija Jovanovich, David J. Low
School of Physical, Environmental and Mathematical Sciences (PEMS), UNSW@ADFA, Canberra, ACT, Australia, j.taylor@adfa.edu.au

Abstract

At mean horizontal wind speeds less than 1 ms^{-1}, we observed that the widths of Doppler spectra due to scattering in the stable nocturnal boundary layer fell below the spectral width "limit" set by the duration and shape of the transmit pulse. The fact that the widths fell below our expectations for non-turbulent broadening meant that it was not possible to extract turbulent contributions to spectral broadening for approximately 50% of the data from a high frequency sodar for the six range gates centred below 70 m AGL. Narrowing of Doppler peaks has also been observed at low turbulence levels in the mesosphere where it has been attributed to specular reflection of energy from horizontal layering in radio refractive index.

1   Introduction

To extract turbulence signals from the width of the Doppler spectra from profilers using either acoustic or electromagnetic radiation, an accurate representation of the non-turbulent component of the spectral broadening is required. For acoustic profilers the lower limit to the spectral broadening should be determined by the transmit pulse shape and duration. Other factors, such as the beamwidth, vertical shear in the horizontal wind, beam zenith angle, will add further broadening which can be represented by a function of the mean horizontal wind speed. Quintarelli (1993) found an expression for the non-turbulent beam width and plotted a large number of observations of spectral width against mean wind speed. A cloud of points with a clear lower limit was observed, trending towards the expected limit at zero horizontal wind. We followed this approach except that our lower limit was determined using the expression from Nastrom (1997), with plausible choice of parameters. Here we show observed spectral widths from the vertical beams on two sodars. We found the widths from one operating at a lower frequency (LF) of 1.875 kHz behaved as expected while at low levels and light winds the results from a high frequency (HF), 5 kHz, sodar fell below the theoretical curve as the horizontal wind speed fell to zero. This unexpected result severely limited the amount of turbulence data that could be extracted from the lower heights sampled by the HF sodar.

2   Instrumentation

The 1.875 and 5 kHz Doppler sodars were operated at our field site in the Majura Valley, northwest of Canberra airport (35° 17.2′ S, 149° 10.5′ E), during the autumn and winter of 2004. A Metek USA-1 ultrasonic anemometer was mounted on a 20 m tower at the field site. The sodars and anemometer were deployed along a SW to NE line, approximately 60 m apart. The two sodars are three-axis, single transducer, dish antenna type. For the 1.875 kHz system, first sampled level is 50 m and levels are spaced at 30 m intervals. Corresponding distances for the 5 kHz system are 20 m and 10 m respectively.

3   Results

Figure 1 compares the spectral widths from the two sodars and shows the curve for the non-turbulent broadening curves that we fitted. The low wind speed "tail" (widths falling below the non-turbulent broadening curve for U < 1 m s^{-1}) is prominent in the HF sodar plot but absent in the LF sodar plot. Breaking the HF widths into separate height levels (fig. 2) shows

that the tail points are predominantly from the lower range gates and this may explain why the width plot from the LF sodar, with its lowest range gate centred at 50 m, has no tail region.
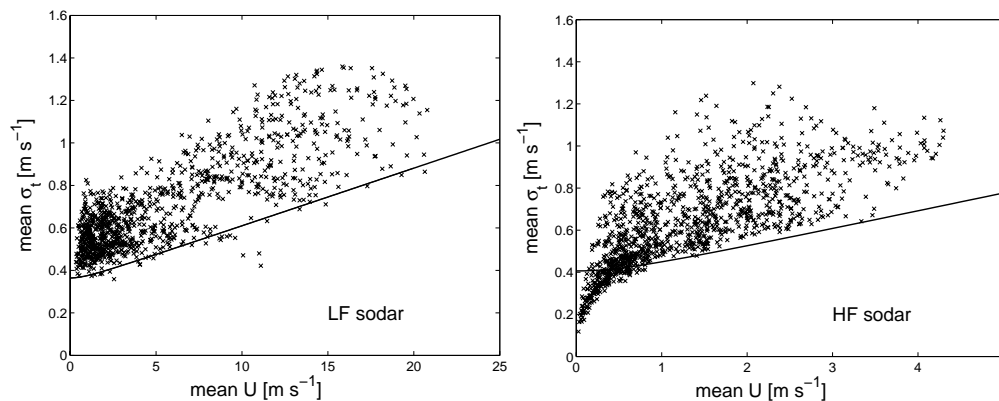
Figure 1. One hour average spectral width, σ_t as a function of mean wind speed, U. Data collected from 2400 LT April 24th to 2400 LT April 30th 2004. Left panel is for the LF sodar heights 50 to 200 m AGL (lowest 6 range gates), right panel for the HF sodar heights 20 to 110 m AGL (lowest 10 range gates). Note the different horizontal scales for the two plots: the strong winds seen in the LF plot occurred above the upper range gate displayed for the HF sodar.
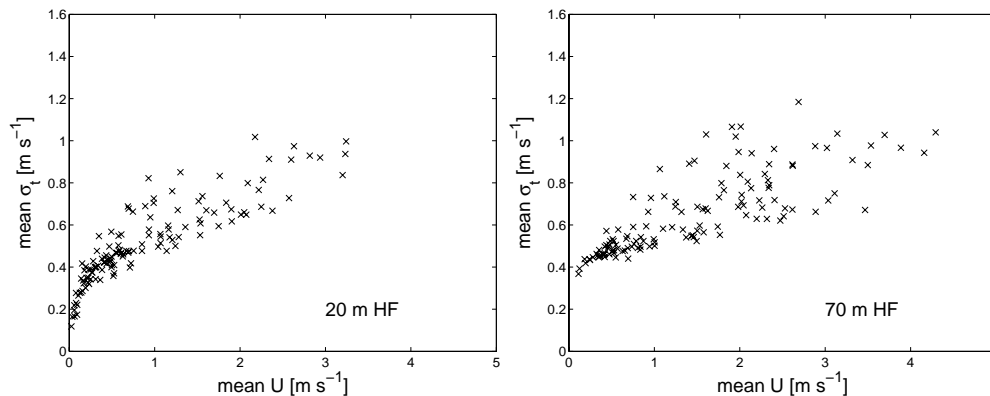
Figure 2. One hour average spectral width, σ_t as a function of mean wind speed, U. for the HF sodar. Data for the same period as fig. 1 but for two heights only. Left panel is for the lowest range gate (20 m) and right panel is for the range gate centred at 70 m.

4   Discussion, Conclusions, and Outlook

Spectral narrowing has been observed in signals from electromagnetic winds profilers (Hocking, 1985) where it is attributed to specular reflection from horizontal layers much thinner than the radar sampling interval. It is possible that layers with similar properties for acoustic radiation form in the lowest layers of the stable nocturnal boundary layer under light wind conditions. An alternative explanation for the tail region is an instrument or data processing problem and we are investigating this possibility.

Literature

Hocking, W. K., 1985: Measurement of Turbulent energy dissipation rate in the middle atmosphere by radar techniques: A review. *Radio Science*, 20, 1403-1422.

Nastrom, G. D., 1997: Doppler radar spectral broadening due to beamwidth and windshear. *Annales Geophysicae*, 15, 786-796.

Quintarelli, F., 1993: Acoustic sounder observations of atmospheric turbulence parameters in a convective boundary layer. *Journal of Applied Meteorology*, 32, 1433-1440.

Meteorological Aspects of Sodar Dot Coherent Echo Origin in PBL

Yuriy N. Ulyanov[1], Valery I. Vetrov[2] and Nina G. Maksimova[3]

[1] National Technical University "KhPI", Kharkiv, Ukraine (ulyanov@kpi.kharkov.ua)

[2] Company Res.-and-Production Ass. "Lantan", Moscow, Russia (vetrov@lantan-npf.ru)

[3] Kharkov National University of Radio Electronics, Kharkov, Ukraine (shifrin@kture.kharkov.ua)

Abstract

The long-term statistics of meteorological conditions accompanying occurrence of sodar anomalous high level dot coherent echo-signals (DCE) witnesses the meteorological origin of DCEs. The most probable shape of the atmospheric structures connected with DCEs is a closed axial vortex energized from the average-speed low level jet stream (LLJ) nearby the top of the ground-based temperature inversion or of the elevated one.

1   Introduction

A dot type of anomalous high-level sodar echo-signals is known since the beginning of using sodar in practice. However the question of their nature remains open. Having analyzed a huge scope of sodar records with DCEs obtained during long-term observations, the authors established a bold link of the DCE occurrence with specific meteorological conditions (Maksimova et al, 1990, Ulyanov et al, 2004). When comparing our data with the results of radar dot coherent echo observations given in Chernikov's work 1963, we revealed the essential distinction in nature of the echo sources. Especially we would like to emphasize the inversion behavior of the time variation of sodar and radar dot coherent echoes. Recurring meteorological conditions along with the peculiarities of sodar records of the PBL vertical structure within the intervals with the DCE high density have enabled us to conclude and become firmly convinced in the meteorological vortical origin of DCEs.

2   Results and discussion

The statistics of weather conditions accompanying the occurrence of DCE have shown that the DCE high density is obtained mostly in spring and autumn. Examples of such season statistics are given in Fig. 1, where time intervals with DCEs (depicted with bold arrows in the bottom) concur with the frontal activity, the light ground-based wind, the weak nebulosity and high values of the temperature daily variation. Additionally precipitation close in time to the intervals of DCE concentration can be noted.
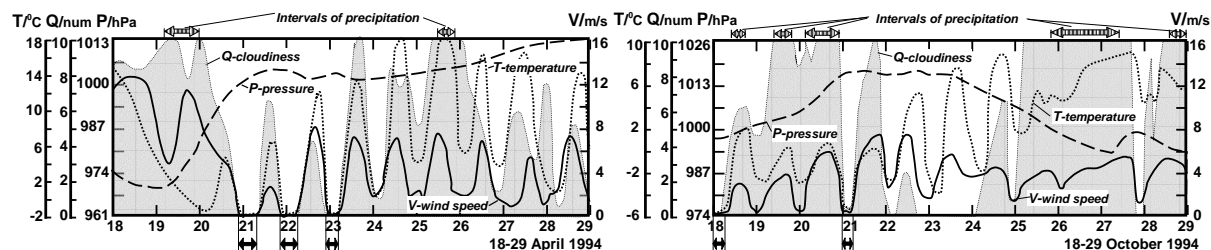
Figure 1. Atmospheric conditions of DCE existence in spring and in autumn.

The given in Fig.2 statistics of meteorological conditions, when DCEs are observed, shows that the most favourite conditions correspond to the high RH, the ground-based wind of 1..2 ms^{-1}, and the air temperature of about $+10^0$C. The list of meteorological conditions accompanying DCEs will be incomplete, if we do not mention such a phenomenon as low level jets (LLJ), internal waves and the connected with them local short-term steep temperature gradients (Ulyanov et al 1992, 1996): in accordance with the recent accurate experimental data

obtained by Balsley 2003, the gradients can reach 20 Km^{-1}. On our opinion, the power namely of the listed above phenomena is being consumed for the vorticity leading to formation of longliving stable dynamic structures shaped as spiral toroidal vortices stipulating effects of DCEs (Fig.3). Life time of such structures reaches a few minutes.
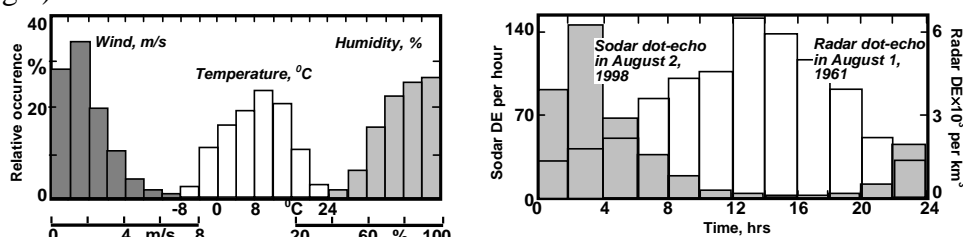
Figure 2. Hystograms for meteorological values and the daily variations of the DCE density.
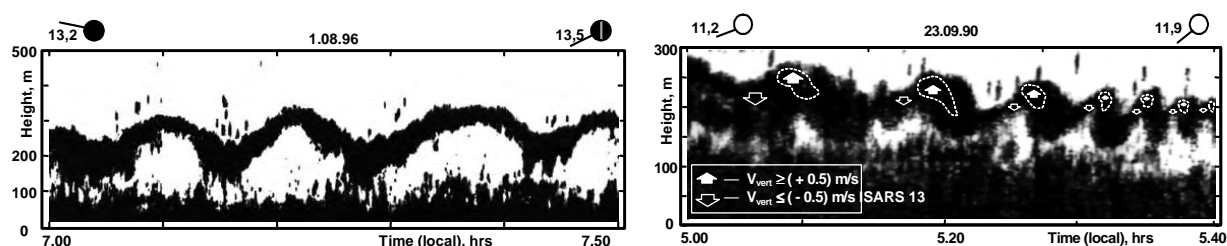
Figure 3. Examples of DCEs obtained under conditions of «diving» LLJ and wave activity.
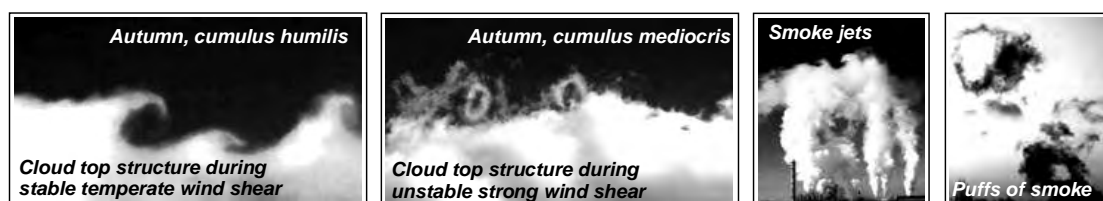
Figure 4. Examples of vortical structures on the cloud upper bound and in smoke jets.

In the PBL, similar vortical structures are optically observed nearby the cloud upper bound and in the smoke jets under the meteorological conditions similar to those when DCEs occur (Fig. 4).

3 Conclusions

The results of the analysis of meteorological conditions under which DCE of meteorological origin occur give strong case for that they appear on the account of vorticity effects at the top of ground inversion stipulated by the vertical wind shear due to the presence of LLJ and the wave activity. The new information about the significant magnitudes of local temperature gradients discovered in similar atmospheric conditions is the additional confirmation of this.

Literature

Maksimova N. G., Ulyanov Y. N.: Detection of bulk temperature and humidity air imperfections in low troposphere with joint sodar and RASS sounding. / Proc. XVI All Union Conf. on Radiowaves Propagation, Kharkov, USSR, 1990, part 2, p.309, in Russian.

Ulyanov Y. N., Vetrov V. I.: Discrete-coherent sodar echoes in the stable PBL and their nature according to long-term experimental findings / Proc. of the 12th ISARS, Cambridge, UK, 2004, p. 219-222.

Chernikov A. A. : Radar research of clear air reflections./ Proc. of TcAO, 1963, iss. 48, p. 56-97, in Russian.

Ulyanov Y. N., Vetrov V. I., Maksimova N. G. et al: Local imperfections in stable PBL according to sounding results at the seaside. / RAN IRTE, preprint 7(575), Moscow, 1992, 21 p., in Russian.

Vetrov V. I., Ulyanov Y. N. : A dot echo investigations with sodar and RASS techniques. / Proc. of the 8th ISARS, Moscow, Russia, 1996, p. 6.115-6.120.

Balsley B. B, Frehlich R. G., Jensen M. L. et al : Extreme gradients in the nocturnal boundary layer: structure, evolution, and potential causes. / Journal of the Atm. Sci. , 2003, vol. 60., p. 2496-2508.

Influence of Thermal Stratification and Synoptic Processes
on Surface Air Pollution in Moscow.

N.F.Elansky** and M.A.Lokoshchenko*

*Department of Meteorology and Climatology, Geography Faculty, Lomonosov Moscow State University.
119992, Lengory, Moscow, Russia
Phone: +7-495-939428 ; Fax: +7-495-9394284; E-mail: loko@geogr.msu.su
** Obukhov Institute of Atmospheric Physics of the Russian Academy of Sciences.
119017, 3, Pyzhevsky lane, Moscow, Russia.

The measurements of various air pollution concentrations (O_3, NO, NO_2, CO, SO_2, etc.) on the surface level were started at 2002 at Meteorological Observatory of Moscow University by common efforts of the Institute of Atmospheric Physics and Geography Faculty of Moscow University. The continuous monitoring of the thermal stratifictation of the Atmospheric Boundary Layer (ABL) is carried out there with the use of vertical sodar «ECHO-1». The influence of the thermal stratification of ABL as well as some weather phenomena and synoptical processes on dynamics of the air pollution levels have been studied.

The main climatological effect of the ABL thermal stratification, determined by the sodar data, is an asimmetry of diurnal course of NO and CO concentrations. In spring, in summer and in autumn the morning maximum of these pollutants is significantly more than the evening one. It is a result of additional accumulation of NO and CO in the surface air layer below elevated inversion in morning hours. Besides, the daily minimum of both species in summer is less than the nocturnal one. The cause of it is strong thermal convection at daily hours leading to intensive vertical transport of these pollutants.

Strong showers connected with atmospheric fronts usually lead to decrease of NO and CO surface concentrations and, vice versa, to increase of the surface ozone concentrations, especially at night. It is a result of specific vertical profiles of these pollutants. However, dynamics of the surface air pollutants during passing of atmospheric fronts is not so trivial. For instance, in winter when heating stations operate and smoky jets exist above site of observations, passing of turbulent zone of intensive vertical mixing just before cold front may leads to strong increase of the NO, NO_2 and CO surface concentrations.

The synopical processes have been analysed in details for conditions of one month (the March of 2002). The analysis was made with the use of synoptical charts and meteorological measurements in two aspects: baric field and type of predominant air mass. As a result of this work, the most concentrations of both NO and NO_2 have been found in conditions of weak-gradient baric field and the less ones – in conditions of cold thermal advection in rears of cyclones. Unlike them, the most concentrations of surface ozone have been detected in cyclone rears due to intensive vertical transport whereas the less ones at night have been measured in weak-gradient baric field (that is a centre of anticyclone, an axis of ridge, or a saddle). It is not a surprise because this synoptic situation is connected as a rule with clear sky and calm that leads to creation of strong surface inversions preventing the vertical mixing. As regards air mass types, the most ozone concentrations have been observed in conditions of Continental Polar and Arctic air masses, and the less ones – in conditions of warm Marine Polar air masses.

Sodar Data about Thermal Turbulence and Stability Parameters of the Atmospheric Boundary Layer above Moscow

M.A.Lokoshchenko*, V.G.Perepyolkin** and N.V.Semenova*

*Department of Meteorology and Climatology, Geography Faculty,
Lomonosov Moscow State University. 119992, Lengory, Moscow, Russia
Phone: +007-095-939428 ; Fax: +007-095-9394284; E-mail: loko@geogr.msu.su
** Russian Academy of Sciences Obukhov Institute of Atmospheric Physics.
119017, 3, Pyzhevsky lane, Moscow, Russia.

The results of long-term continuous acoustic remote sensing of the Atmospheric Boundary Layer (ABL) in Moscow up to the 800 m height have been presented. Vertical sodar «ECHO-1» of GDR production supplemented by Doppler measurements has been used. Two parameters – structural constant of temperature fluctuations C_T^2 and standard deviation of the vertical wind component $\sigma(W)$ – have been taken into account. The sodar data of C_T^2 have been calculated for period of 1999-2000 on a base of their experimental comparison with *in situ* measurements of this parameter made by high-sensitive thermal sensor at meteorological mast. The data of $\sigma(W)$ have been received for period of 2000-2005 by statistical calculation of Doppler sodar measurements of separate W values.

The values of C_T^2 vary as a rule since 10^{-2} till 10^{-5}, i.e. in limits nearly of four orders, depending on intensity of the thermal turbulence. In daily course the most values of C_T^2 have been detected usually at night or in morning. The most recordable C_T^2 values (more than 10^{-2}) can be observed inside layers of very strong nocturnal surface inversion and intense wind shear. Daily and evening values of C_T^2 are the least as a rule in daily course.

The $\sigma(W)$ data are received by statistical calculation of the «ECHO-1» Doppler measurements. They have been tested by the comparison with the $\sigma(W)$ data measured by sonic anemometer at high meteorological mast. The connection between both data of this stability parameter has been found as very close, correlation co-efficient consists of nearly 0.9. The average values of $\sigma(W)$ in Mocow city are in limits up to nearly of 1 m/s or even slightly more. The daily course of this parameter is clear in warm period when sharp daily maximum connected with strong thermal convection appears. In winter the daily course of $\sigma(W)$ is comparatively smoothed and values of this parameter are less (nearly of 0.5 m/s) that indicates stable stratification of ABL as predominant all around a day.

Climatological features of both parameters of ABL above Moscow are discussed.

Sodar Data about Wind Profiles above Berlin and Moscow

Lokoshchenko, Mikhail A.*, Kirtzel, Hans-Jürgen** and Belova, Eugeniya A.*
*Department of Meteorology and Climatology, Geography Faculty, Lomonosov Moscow State University.
119992, Lengory, Moscow, Russia. Phone: +7-495-9394284; E-mail: loko@geogr.msu.su
**METEK Meteorologische Messtechnik GmbH, Fritz-Straßmann-Str. 4, D-25337 Elmshorn, Germany.
Phone: +49(0)41214359-0; Fax: +49(0)41214359-20; E-mail: info@metek.de.

Abstract.

Vertical profiles of wind speed, wind direction and standard deviation of the wind vertical component have been compared in Moscow and in Berlin for period of one month in winter. The data of synchronous sounding at both sites by sodars of the same type MODOS (produced by METEK) have been used. Spatial features of wind field and atmospheric stability have been discussed.

1   Introduction.

The acoustic remote sensing allows to investigate in details spatial particularities of the wind field at the lower troposphere. With the increasing density of operational sodar sounding a European wide atlas on the wind climate observed by sodar seems to be a realistic prospect. The comparison of vertical profiles of the wind and of stability parameters, as well as comparison of wind roses and distributions of wind speed values above two capitals – Berlin and Moscow – is the task of our report and first step at this approach. The sodar data have been received at both places synchronously during one month – on December of 2004. Two identical Doppler sodars of type "MODOS" of "METEK" production (Germany) operate at both capitals that allows to compare results successfully.
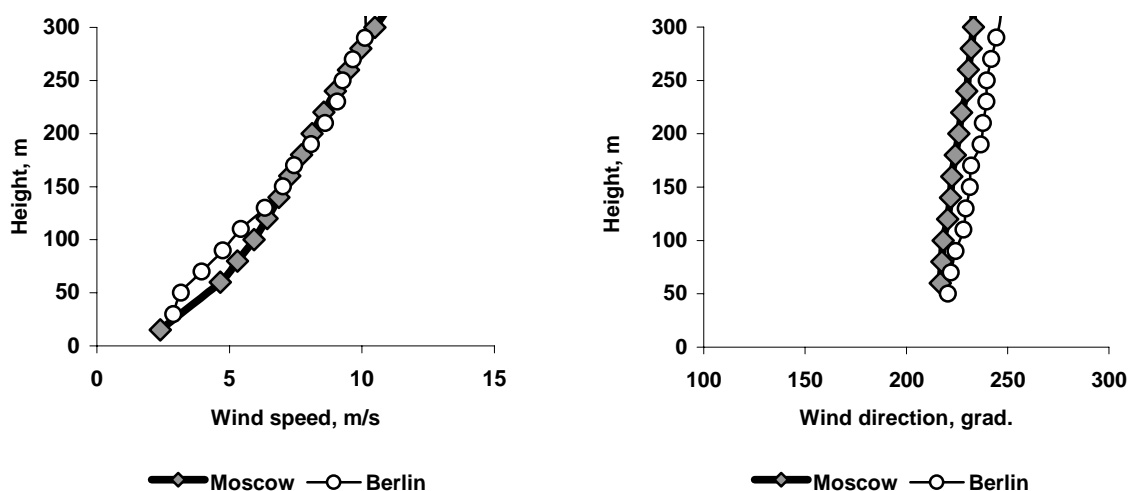
Fig1. Comparison of wind speed (left) and wind direction (right) in Moscow and in Berlin for period of December, 2004.

2   Results.

Both Berlin and Moscow are situated in moderate latitudes within a similar, nearly flat terrain relief. Nevertheless, in the surface air layer up to the 150 m level mean monthly wind speed in Berlin is less than in Moscow (the lowest point at profile for Moscow represents the vane data). Above 150 m any differs of wind speed between both sites go to nothing. As for wind direction both sites were under Southern and Western flows in average that is typical for mid latitudes in winter. However, mean direction in Berlin has been detected as South-Western with more Western component due to specific of synoptic processes.

Optical wind measurement techniques

Stefan Emeis

Institute for Meteorology and Climate Research – Atmospheric Environmental Research
Forschungszentrum Karlsruhe GmbH, Kreuzeckbahnstr. 19, 82467 Garmisch-Partenkirchen,
Germany, stefan.emeis@imk.fzk.de

Abstract

The use of wind energy requires precise wind measurements. The hitherto existing in situ-techniques with cup anemometers mounted on masts will meet mechanical and financial limits at future hub heights. Ground-based optical remote sensing methods that measure the vertical profile of wind speed up to some hundred metres height may be a way out from these problems.

1   Introduction

After diligent calibration considering correct turbulence intensities cups deliver precise wind data. However, due to the size of the anemometer, these measurements are representative for a quite small air volume only. The necessary masts for cup measurements are very costly and need permits from the respective authorities. Additionally, masts influence the measurements. Moreover, cups cannot measure the vertical wind component separately. It is expected that the magnitude of this wind component that can influence the wind measurements with some types of cup anemometers, increases with hub height. Further, it is not clear whether cup anemometers and wind turbines react equally to vertical wind components. Therefore, the separate measurement of the vertical wind component is desirable.

2   Optical wind measurements

Optical techniques to measure the wind for wind energy issues by Doppler shift analysis are still at their beginnings. Since recently one instrument is commercially vailable that performs the range determination by beam focussing (Harris et al. 2001). Naturally, experiences with this instrument are still very limited. Other wind lidars which base their range determination on signal delay do not offer a sufficient vertical resolution in the first one hundred metres above the instrument and must therefore perform slanted or conical scans (Banta et al. 2002). Also attempts to use Optical Coherence Tomography have been made (Bennett et al. 2004). For further details of wind measurements by optical remote sensing see Emeis (2006).

Optical techniques have clear advantages such as rather high data availability, low environmental impact, and low sensitivity to external disturbances. Moreover this technique offers new measurement geometries such as horizontal measurements of oncoming gusts ahead of the hub. On the other hand the price for purchasing the instruments is still quite high, the vertical resolution is only moderate, and for the determination of the three-dimensional wind vector a rather large volume averaging has to be made. The next years will show whether optical techniques will succeed in wind energy technology applications.

Literature

Banta, R.M., R.K. Newsom, J.K Lundquist, Y.L. Pichugina, R.L. Coulter, L. Mahrt, 2002: Nocturnal Low-Level Jet characteristics over Kansas during CASES-99. Bound.-Lay. Meteorol., **105**, 221-252.

Bennett, M., S.G. Bradley, S. von Hünerbein, J. Pease, 2004: Comparison of wind profiles measured with sodar and Doppler lidar. Proc. 12th ISARS, 11.-16. Juli 2004 Cambridge (UK), 141-144.

Emeis, S., 2006: Windmessung mit optischer Fernerkundung/Wind Measurement by Optical Remote Sensing. DEWI Magazin 28, 40-47.

Harris, M., G. Constant, C. Ward, 2001: Continuous-wave bistatic laser Doppler wind sensor. Appl. Opt., **40**, 1501-1506.

Coherent Laser Radar for Ground-Based Wind profiling

Michael Harris (mharris@qinetiq.com)
QinetiQ, Malvern Technology Centre
St Andrews Road, Malvern, Worcestershire WR14 3PS, U.K.

Abstract

Coherent laser radar (lidar) methods have been used for over thirty years for the remote measurement of wind speed. Recently, technological advances from the telecommunications industry have been exploited to develop more user-friendly systems (e.g. QinetiQ's ZephIR lidar), and these are beginning to demonstrate potential in a range of applications including meteorology research, wind energy and aviation.

1   Introduction

In order to reduce costs associated with the siting of tall masts, the wind energy industry requires methods for remotely obtaining accurate wind profiles; lidar offers an alternative to the more commonly used sodar, with some potential advantages. Lidar also has potential to contribute to a number of other wind energy applications, including turbine power curve measurement, assessment of turbine wakes, and real-time gust warning for individual turbines. In the mid-1990s, the QinetiQ lidar team investigated alternatives to their existing CO_2 lidar systems: new developments in optical fibre and related components from the telecommunications industry offered a promising approach to lidar construction. From the late 1990s the team successfully demonstrated continuous-wave (CW) and pulsed all-fibre lidar anemometers (at a wavelength 1.55μm) [1-3] and has remained at the forefront with the recent development of a production system (**ZephIR**) [4-7].

2   Instrumentation

QinetiQ began a programme to develop a commercial fibre-based lidar in 2001. Progress has built on previous fundamental work, and systems have been deployed successfully in several demanding applications that illustrate the flexibility and robustness of the solution. Initial deployment of the ZephIR lidar (March 2003) was on the nacelle of a large (2.3MW) wind turbine (figure 1), measuring the wind speed up to 200m in front of the blades. The lidar consisted of a rack unit containing laser source, detector and signal processing computer, situated in the base of the tower, connected via over 100m of electrical and optical fibre cable to the transceiver head mounted on the top of the nacelle. The lidar system was installed over an afternoon and was fully operational soon after, allowing advance warning of oncoming gusts and providing valuable experience in practical deployment issues. The system returned to Malvern having achieved several weeks of successful operation. It was then converted into a ground-based scanning unit for wind profiling (figure 2). The system was first trialled in December 2003, and has since been used in numerous campaigns in the UK, Europe, and other parts of the world.

The experience gained through these trials has built confidence in the robustness and reliability of the core ZephIR design. In late 2004, work started on a production instrument (figure 3), designed to perform autonomous wind profiling measurements at heights up to 150m, primarily for site surveys at proposed wind farm sites. Ten of these systems are currently deployed by customers around the world [7]. ZephIR is a lidar (more strictly *coherent laser radar*) based on a monostatic, continuous-wave design [8]. In general, lidar involves the emission of a coherent light beam, and detection of the weak return scattered from a distant target. The technique provides a means to measure the line-of-sight (axial) component of wind speed via detection of the Doppler shift for light backscattered from natural aerosols (particles of dust, pollen, droplets etc.) in the atmosphere. A basic underlying assumption that the scatterers accurately follow the flow is usually very reliable except in precipitation. The frequency shift is accurately measured by mixing the return signal with a

portion of the original beam (the local oscillator, or reference beam), and picking up the beats on a photodetector at the difference frequency. The Doppler frequency is then extracted via spectral analysis of the digitised detector output, achieved in ZephIR with a fast Fourier transform (FFT) block within a field-programmable gate array (FPGA).

Figure 1-3: Stages of evolution of the ZephIR lidar. Figure 1 shows the lidar head mounted on the nacelle of a Nordex N-90 wind turbine. Figure 2 shows prototype ground-based wind profiler at Risø wind energy test site, Høvsøre, Denmark. Figure 3 shows the ZephIR production model deployed in the field.

The local oscillator (LO) plays a crucial role in the operation of a coherent lidar. Firstly, it defines the region of space in which light must be scattered for detection of the beat signal; radiation from other sources (e.g. sunlight) is rejected, so that lidar systems are usually completely immune to the effect of background light. The LO also provides a stable reference frequency to allow very precise velocity determination; as a consequence such systems are inherently calibrated, provided there are no gross drifts in laser frequency. Finally, the LO amplifies the signal via the beating process to allow operation at a sensitivity that approaches the shot-noise (or quantum) limit. This very high sensitivity permits the operation of lidar systems in an unseeded atmosphere, relying only on detection of weak backscattering from natural aerosols. ZephIR performs approximately 50 such measurements of line-of-sight wind speed per second.

3   Results

The ZephIR lidar instrument has been configured to operate as a wind profiler, measuring wind speed and direction from a ground-based platform to altitudes up to 150m. This is achieved by offsetting the beam at an angle of 30 degrees to the vertical and scanning in azimuth at a rate of one revolution per second. As the beam rotates it intercepts the wind at different angles, thereby building up a map of wind speed around a disc of air. In a uniform air flow, a plot of Doppler velocity (V_{LOS}) versus scan angle takes the form of a rectified sine wave, with the peak Doppler values corresponding to upwind and downwind measurements:

$$V_{LOS} = \left| a \cos(\phi - b) + c \right|,$$

where ϕ is the scan azimuth angle. When V_{LOS} is displayed vs ϕ as a polar plot the output gives rise to a characteristic figure-of-eight pattern. A non-linear least-squares fit is performed of the model to the data from 3 revolutions of the scanner (roughly 150 points), from which the three best-fit parameters a, b and c are extracted. The wind data are then computed as follows:

Horizontal speed $(u) = a / \sin 30°$;   *Vertical speed* $(w) = c / \cos 30°$;   *Bearing* $= b$

An ambiguity of 180 degrees in bearing is normally easily resolved with reference to a simple ground-based reading. Typically, 10-minute averaged values of horizontal wind speed obtained by the lidar are compared with those from a mast mounted cup anemometer (figure 4). Rigorous verification is an important step towards wider deployment of lidar.

Lidar / Cup @ 100m, 21 august 2004
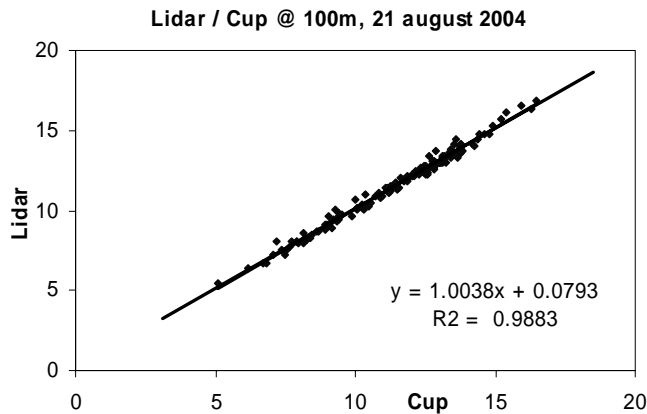
***Figure 4**: Regression plot of 10-minute averaged windspeed 100m above ground in m/s, measured by lidar and calibrated cup anemometer. The lidar was situated 120m from the base of the mast. The measurements were obtained over a 24hr period when there was little risk of shadowing of the cup (by the mast itself, or by adjacent turbines). The corresponding plots at other heights (40m, 60m, 80m) display similarly good agreement and correlation.*

We are aware of only two examples in which lidar systems have been mounted on the nacelle of a wind turbine. In the first experiment (to our knowledge) of this type [9] an early prototype of the QinetiQ ZephIR system was mounted on the nacelle of a Nordex N90 wind turbine at Postlow, 5km W of Anklam, N.E. Germany. In the other example, a ZephIR system was installed by Risø on a test turbine for wake analysis. The lidar was mounted on a rearward-looking pan-and-tilt scanner allowing measurement of wake windspeed deficit and wander [10].

4   Discussion, Conclusions and Outlook

The potential of lidar in the wind energy industry has been demonstrated for a range of applications, including wind farm site surveys, resource assessment, turbine power curve measurement, advance gust warning for turbine control, and turbine wake studies. From the many commercial and research deployments of ZephIR systems globally, it has been shown that lidar is highly capable of returning excellent performance (both quality of measurement and availability). ZephIR has rapidly become a powerful tool in aiding the understanding of wind behaviour within the wind energy industry and it is now proving its potential to deliver appropriate, reliable and accurate wind data, hence reducing the industry's most significant risk. Work is underway to examine ways to increase the measurement height for possible aviation-related applications.

References
[1] **M Harris**, "Bistatic laser Doppler wind sensor at 1.55μm", Proc. 10th CLRC, p.277 (1999)
[2] **C J Karlsson, F Olsson, D Letalick & M Harris**, "All-fiber multifunction CW coherent laser radar at 1.55μm", Applied Optics **39** 3716 (2000)
[3] **G N Pearson, P J Roberts, J R Eacock & M Harris**, "Analysis of the performance of a coherent pulsed fiber-lidar for aerosol backscatter applications", Applied Optics **41** 6442-6450 (2002)
[4] **H Jørgensen et al**, "Site wind field determination using a CW Doppler lidar - comparison with cup anemometers at Risø", Proc. "The science of making torque from wind", Delft, p.261 (2004).
[5] **D A Smith et al**, "Wind lidar evaluation at the Danish wind test site in Høvsøre", Proc. EWEC, London, p.44 (2004)
[6] **I Antoniou et al**, "Comparison of wind speed and power curve measurements using a cup anemometer, a lidar and a sodar", Proc. EWEC, London, p.47 (2004)
[7] http://www.qinetiq.com/home/commercial/energy/ZephIR.html
[8] **C M Sonnenschein and F A Horrigan**, "Signal-to-noise relationships for coaxial systems that heterodyne backscatter from the atmosphere", Appl. Opt. **10** 1600-1604 (1971)
[9] **M Harris et al**, "Advance measurements of gusts by laser anemometry", in preparation (2005)
[10] **F Bingöl**, "Adapting a Doppler laser anemometer to wind energy", Masters thesis (2005), http://www.afm.dtu.dk/Publications/msc.html

An 8 month test campaign of the Qinetiq ZephIR system: Preliminary Results

Kindler, Detlef [1], Oldroyd, Andrew [2]*, MacAskill, Allan [3], Finch, Danny [4]
[1] WINDTEST Kaiser-Wilhelm-Koog GmbH, Germany, [2] Oldbaum Services , UK, [3] Talisman Energy
(UK) Ltd, [4] Scottish & Southern Energy, UK
Email:andy@oldbaumservices.co.uk
*corresponding author

Abstract

The Beatrice Windfarm Demonstrator Project is a major part of the EU sponsored DOWNVInD programme that will install two REPOWER 5M Turbines in the Moray Firth Scotland, adjacent to the Beatrice Alpha oil platform, owned and operated by Talisman Energy. As part of the project, a programme has been designed and instigated over the last 8 months to thoroughly examine the performance and capabilities of the QinetiQ ZephIR LiDAR system as well as to establish its suitability for being the primary wind data acquisition instrument on the Beatrice project. This paper represents a first look at the results of this programme.

1   Introduction

This study looks at the performance of one of the first production LiDAR systems manufactured by QinetiQ, and as such it is the first detailed look at the performance of the system. The test programme was designed and implemented as part of the DOWNVInD programme to install two REpower 5M turbines in 40m of water in the Moray Firth Scotland. As part of the meteorology component, a QinetiQ ZephIR system has been chosen as the primary wind resource data acquisition instrument. The test programme is an 8-month programme split into two stages comprising of a 3-month onshore deployment and a 5-month offshore deployment. This paper presents a first look at the onshore phase test results as well as a preliminary look at the offshore test.

2   The Onshore Test Site

The test programme was split into two phases, comprising of both an onshore and offshore component. The onshore test campaign was undertaken at the REpower 5M test site Brunsbüttel, Germany. Comparison results are presented as compared to a 120m meteorological mast, for the top height and for two lower heights, i.e. 90 m and 60 m.
In general the 5M site was a difficult location for the performance of a comparison campaign considering the flow complexity on site. This was mainly because of significant buildings in the surrounding area, specifically wind turbines, topography issues were also present in the main wind direction sector for data to be analysed from. The LiDAR was located 70m from the mast so that the mast does not at any point intersect with the scan volume of the LiDAR. Cup anemometers attached to the met mast at 60m, 90m, and 120m height were used for wind speed correlations. At heights of 60 and 90m a narrowed data sector needed to be taken, due to the shadowing effect of the mast structure towards the cups mounted aside the mast on a boom.

3   The Offshore Test Site

The offshore component was undertaken on the German Research Platform FINO-1 (see figure 1, left) located in the German Bight area of the North Sea about 50 km off the coast. Comparison results are presented as compared to an 83m meteorological mast on the 20m platform, for the top height (103m) and for two lower heights, i.e. 81m and 61m. The ZephIR itself was placed on top of a container located on the Western most edge of the platform (figure 1, right) at a height of 25m above mean sea level, in a distance to the met mast of about 10m. Given the laser cone's opening angle of plus/minus 30° from vertical, means that an intersection of the laser cone by the met mast at about 20m height above the LiDAR was always present, i.e. for any of the scan heights.

Figure 1: Left - view on the platform during helicopter approach from the North-East, right - ZephIR as mounted on the Western edge of the FINO-1 platform on the roof of the generator container.

4 ZephIR specifications and settings

The ZephIR is equipped with a 1535 nm laser. Focused on the adjusted height and slanted 30° to the vertical it probes the wind speed on a circle obtaining 50 single points a second. After 3 seconds of operation on that height the laser is re-focused on the next user defined height.

Raw data suitable for post processing is stored for a period of 5 days. 3-second data suitable for building into 1-minute, 5-minute, or standard wind industry 10-minute intervals are stored for a maximum of 30 days. For most of the onshore campaign the cloud correction was disabled during operation. Hence, it had to be applied to the raw data in the post processing. The comparison between corrected and uncorrected data allowed a judgement of its effect in terms of data improvement. At the end of the onshore and during the whole offshore period the cloud correction was activated since it has proven its capabilities, successfully. The device was installed at ground level onshore and at 25m above mean sea level offshore. For both the onshore and offshore test the system was initially run at a single scan height corresponding with the top most sensor available, and then operated in a more normal profile mode with heights chosen to correspond with the available reference instruments.

5 Results

Figures 2 shows correlation plots for both the onshore and offshore test at the 90m onshore and 103m offshore. The correlation values are based on a regression line constrained through origin.
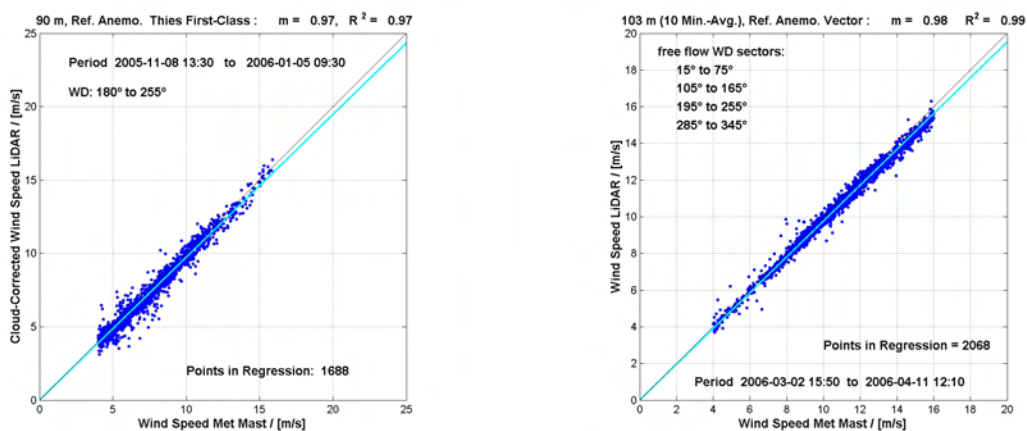
figure 2: Sample plots of correlation between a cup anemometer attached to a met mast and the LiDAR, left for the onshore @ 90m level and right for the offshore @ 103m level.

	Onshore			Offshore		
	120m	90m	60m	103m	81m	61m
N – single scan	3034	/	/	2068	/	/
R^2 – single scan	0.95	/	/	0.99	/	/
m- single scan	0.94	/	/	0.98	/	/
N – profile mode	2532	1688	1577	1849	2356	2657
R^2 – profile mode	0.96	0.97	0.99	0.99	0.99	1.00
m- profile mode	0.95	0.97	0.95	0.98	0.98	0.99

Table 1: Summary of correlation results for both the onshore and offshore phases between cup and LiDAR. N: number of 10 minute averages in regression, R^2: correlation coefficient, m: slope of regression line.

6   Discussion

The performance of the QinetiQ ZephIR system has been highly encouraging. Despite the onshore test phase taking place at a location that has few uncluttered sectors in terms of airflow, the system managed to achieve respectable correlation values with respect to the in-situ 120m mast. Of particular note is the effect of using the cloud correction algorithm. As mentioned previously the system stores raw spectra data for a period of 5 days before being written over. In practical terms, if the user wanted to continually post-process the data for cloud correction or other reasons, a visit to the system every 5 days to exchange data cards would therefore be necessary. In the case of remote location deployment, or standalone operation offshore, this would incur a high cost in terms of man-hours when looking after the system. Therefore the system as configured on FINO-1 can run for 30 days without intervention, but it is possible to connect to the system and download 3-second data, allowing the system to run autonomously. The improvement in correlation shown by the post processing analysis onshore, has led to the system being operated with the algorithm switched on. Initial results also show a very good level of correlation between the LiDAR and the reference system on FINO-1 for this case, and in fact an improvement in correlation levels has been seen. It is interesting to note that the result show a better level of correlation offshore. Although the scan volume intersects the reference mast on FINO-1, the quality of the correlation results points to a cleaner incident (less disturbed) flow approaching the platform from the valid sector. However, one possible reason for the improvement in results is the close proximity of the averaged centre of each scanned height to the reference instrument.

One of the main selling points with respect to Remote Sensing is the stated flexibility and manoeuvrability of the systems. In this case, on both installation sites, the system was easily setup and running within a few hours of arrival at site. In saying this, it should be noted that care has to be taken to assess the best position to install a system prior to deployment.

8   Conclusion

The Lidar system has been subject to an 8-month test campaign comprising of both a 3-month onshore and a 5-month offshore component. The system was tested in terms of correlation with standard cup anemometer sensors with care taken to ensure the results were not duly affected by flow disturbances due to shadowing or the systems being located in or out of a wake. The results returned from this study have shown that the QinetiQ system is very capable of returning good quality results in both an offshore and onshore environment. The level of the results returned show that the system under test should now be thought of as a powerful tool to aid in the understanding of flow conditions on sites being investigated.

Once the 5-month campaign has been completed, the system will be installed on Beatrice Alpha in the Moray Firth where it will operate as the primary wind data acquisition system for the DOWNVInD programme.

Calibration of SODARs for wind energy applications

von Hünerbein[1], S, Antoniou[2], I, Bradley[3], S G, Jørgensen[2], H E, Kindler[4], D
[1]University of Salford, UK, s.vonhunerbein@salford.ac.uk
[2]Riso National Laboratories, DK,
[3]University of Auckland, NZ,
[4]Windtest Kaiser-Willhelms-Koog GmbH, D,

Abstract

Traditionally SODAR wind profilers have been assumed to be largely self-calibrated, with measurement errors mostly random. However, increasing demand for accuracy in applications such as wind energy demand robust calibration and intercomparison procedures. Comparisons of three commercial SODARs show that performance can be optimised when care is taken with siting, parameter settings during the measurements and data filtering. Instrument design changes can give additional improvements. Recommendations for generic calibration procedures are presented. An outlook on a new standalone calibration method is given.

1   Introduction

As part of a larger EU project on use of SODARs for wind energy, the Profiler Intercomparison Experiment (PIE) developed and tested calibration procedures and formulated guidelines for manufacturers to optimise SODAR wind results. The primary goal was to compare SODAR measurements with a cup measurement on an inexpensive low mast (40 m) and extrapolate the calibration to the remaining range gates of the SODAR.
Three commercial SODARs from different manufacturers were operated at non-overlapping frequency bands about 70 m from a 118m meteorological mast at the Risø - Høvsøre Meteorological Station, DK from March to June 2004. The mast was instrumented with cup anemometers at six levels, 6 sonic anemometers and 2 vanes giving a detailed wind profile (Bradley et al., 2005, Antoniou et al., 2004 and Kindler et al., 2004). Data quality was assured by real time filtering and post processing of the SODAR data sets. Filtering of cup anemometer data excluded sectors affected by the mast construction and low wind speed data.

2   Sources of inaccuracy

While comparisons between meteorological masts and SODARs have a long history, a systematic tracking of error sources seems not to have been attempted.
The sources of error in SODAR data can broadly be classified into three categories: (1) Geometrical errors due to inaccurate height estimation tilt angle and scattering angle; (2) Bias in wind estimation due to problems with calibration, incomplete data, volume separation and averaging; and (3) Low signal-to-noise ratio (SNR) created by background noise or driven by atmospheric stability (Kindler et al. 2004). These errors may be combined to provide an error budget for SODAR measurements of wind speed (Table 1).
The first 3 errors are due to poor setting up of the SODAR and can usually be avoided. Rain data can be filtered out using a sensitive rain gauge. Beam spread, drift, separation and averaging (Antoniou et al., 2003) are fixed through SODAR design. A narrow beam SODAR with a moderate tilt angle will generally have small beam and beam separation error. Beam drift error is inescapable, but generally also negligible over common wind ranges. Some of the errors are larger for beams having a greater tilt angle, but the peak detection resolution is improved if the Doppler spectrum is more spread, which occurs for larger tilt angles.
All except for the peak position error can be systematic (rain and fixed echo errors vary with conditions, but when present can lead to persistent errors which are non-random).

Table 1. Error sources and estimates for SODAR derived wind speed

Source	Parameter	Slope error $\frac{\hat{u}}{u} - 1$	Parameter range	Error range
Temperature	ΔT [K]	$+\dfrac{\Delta T}{2T}$	± 20 K	± 3 %
Out of level	$\Delta\varphi$ [radian]	$-\dfrac{1}{2}(\Delta\varphi)^2$	$\pm 15°$ (± 0.3 rad)	-3.5 % to 0 %
Fixed echoes	Δx [m]		0 to 500 m	0 to -100%
Rain	R [mm/h]		0 to 50 mm/h	20 - 30 m s^{-1}
Beam spread	σ_φ [radian] φ [radian]	$+2\dfrac{\sigma_\varphi^2}{\sin^2\varphi}$	4°-8° (0.07-0.14 rad) 15°-24° (0.26-0.42 rad)	+6 % to +25 %
Beam drift	u/c	$\pm\sqrt{2}\,\dfrac{u}{c}$	0 to ± 0.06	0 % to ± 8.5 %
Beam separation	$\rho(\Delta x)$	$-(1-\rho)$	0.8? to 1	-20 % to 0 %
Vector averaging	z_0 [m] z [m]	$\dfrac{1}{2\left(\ln\dfrac{z}{z_0}\right)^2}$	0.01 to 2 m 10 to 1000 m	0 to 10 ?
Peak position	$\sigma_{\Delta f}$ [Hz] φ [radian] f_T [Hz]	$\pm\dfrac{c}{\sqrt{2}\sin\varphi}\dfrac{\sigma_{\Delta f}}{f_T}$	± 0.5 Hz 15°-24° (0.26-0.42 rad) 1000 to 6000 Hz	0 to 10

3   Results of regressions

One important question is how representative comparisons between a SODAR and a cup are, given that one is a spatially averaging and one an in-situ device. Figure 1 compares the RMS residual error of the Aerovironment-cup regression at 60m to that of the cups at 60 m and 80m for wind speeds between 0 and 20 m/s. Systematic differences between SODAR-cup and cup-cup comparisons are not evident.
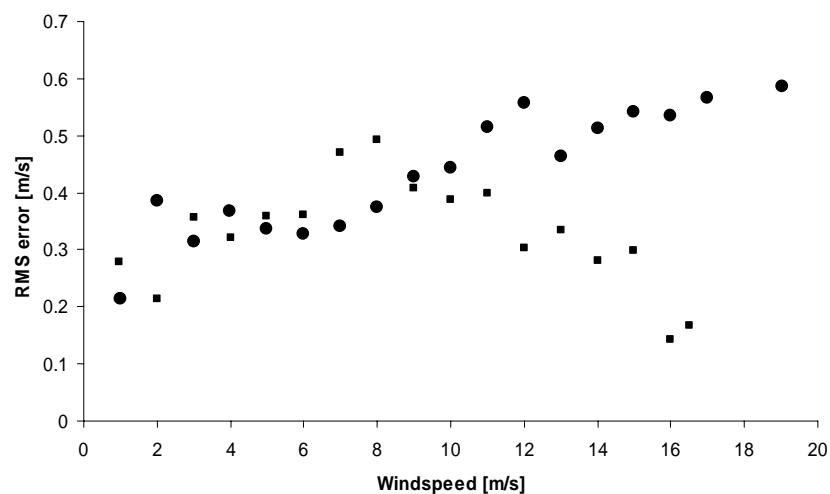

Figure 1. RMS residual error (i. e. uncertainty in least-squares fitted windspeed) vs windspeed. Circles: Aerovironment 4000 vs cups at 60 m; squares: cups at 80 m vs cups at 60 m.

Whereas a systematic bias between the SODAR and Cup measurements can easily be removed by the calibration method, care needs to be taken to avoid systematic changes in the regression slope with height to optimise the extrapolation procedure (Figure 2).
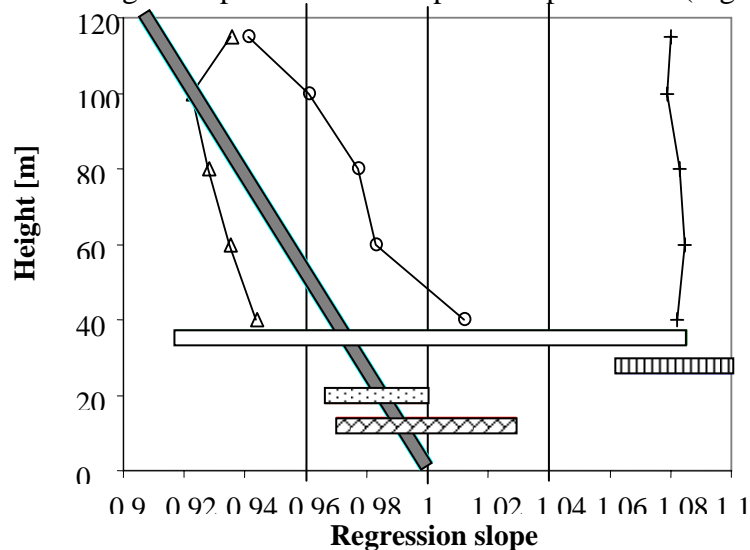
Figure 2. Variation in regression slope with height ($+$= Aerovironment, $\triangle$= Metek, $\bigcirc$ = Scintec) and regions of applicability of various errors, compared with calibrations. Temperature (diagonal filling); out of level (dotted filling); beam spread (vertical filling); beam drift (white filling); beam separation (grey filling).

Temperature, out of level, beam spread and beam drift errors introduce a constant slope error, whereas slope introduced by the beam separation decreases with height.

4   Conclusions, and Outlook

The PIE experiment has shown that SODAR performance can be improved by comparison with a meteorological mast. There is further scope for enhancement through the implementation of design changes for SODARs such as fixed echo detection algorithms and rain detection algorithms. In addition, the need for stand-alone calibration techniques which are independent of costly mast installations has become apparent. The European Framework 6 UpWind programme aims to develop such a standalone method utilising methods similar to those proposed by Baxter (1994). The aim is to use an acoustic transmitter/receiver device recording the emitted SODAR pulse or pulse sequence, simulating a wind-profile giving a pseudo-atmospheric response and feeding this response back into the SODAR in real time.

Literature

Antoniou, I., H. E. Jørgensen, F. Ormel, S. G. Bradley, S. von Hünerbein, S. Emeis, G. Warmbier, 2003: On the Theory of SODAR Measurement Techniques (final reporting on WP1, EU WISE project NNE5-2001-297). Ioannis Antoniou (ed.), Hans E. Jørgensen (ed.), Risø National Laboratory, Roskilde, Denmark.
Antoniou, I., H. E. Jørgensen, S. von Hünerbein, S. G. Bradley, D. Kindler, 2004: Inter-comparison of commercially available SODARs for wind energy applications. Proc. 12th International Symposium on Acoustic Remote Sensing and Associated Techniques of the Atmosphere and Oceans, 12 - 16 July 2004, Cambridge, UK.
Baxter, R. A., 1994: Development of a universal acoustic pulse transponding system for performance auditing of SODARs. Proc. 7th International Symposium on Acoustic Remote Sensing and Associated Techniques of the Atmosphere and Oceans, 3 – 7 October 1994, Boulder, US
Bradley, S. G., I. Antoniou, S. von Hünerbein, D. Kindler, H. Jørgensen, M. de Noord, 2005: SODAR calibration for wind energy applications, final reporting on WP3, EU WISE project NNE5-2001-297, Salford
Kindler, D., I. Antoniou, H. E. Jørgensen, S. von Hünerbein, S. G. Bradley, , 2004: Operational Characteristics of SODARs - External Meteorological Influences. Proc. 12th International Symposium on Acoustic Remote Sensing and Associated Techniques of the Atmosphere and Oceans, 12 - 16 July 2004, Cambridge, UK.

Wind energy related measurements with a commercial SODAR system

Günter Warmbier *), Frank Albers**), Klaus Hanswillemenke**)

*) GWU-Umwelttechnik GmbH, gunter.warmbier@gwu-group.de
**)WINDTEST Grevenbroich GmbH, f.albers@windtest-nrw.de or k.hanswillemenke@windtest-nrw.de

Abstract

Measurements of a commercial miniSODAR system are compared to sonic and cup anemometers to verify the usability of SODAR measurements for wind and turbulence measurements. Correlation with cup and ultrasonic anemometers are presented together turbulence intensity classification and a power curve for a wind turbine.

1   Introduction

Wind energy turbines tend to grow in power and size. To fully characterize the latest Megawatt turbines with hub heights and rotor diameters of more than 100 m wind measurements exceeding the maximum height of standard wind masts are required. A commercially attractive alternative to masts are remote sensing techniques like SODAR (Sound Detection and Ranging). SODARs have been used for meteorological applications for some decades but only in the past few years instruments with the required accuracy for wind energy applications have become available. Here some results of measurements with a commercial SODAR for wind energy applications are presented.

2   Instrumentation

The measurements presented here were performed with a miniSoDAR Model 4000 of ASC (Atmospheric Systems Corporation, formerly a division of AeroVironment) and compared to cup and ultrasonic anemometers.

3   Results

In addition to the results below a power curve measured with a SODAR and a cup anemometer is shown as well as a comparison of turbulence intensity measurements with cup anemometers, ultrasonic anemometers and SODARs in the poster.

The most widely used type of anemometers are cups so one of the most asked questions is how well SODARs compare to these instruments. As an example a measurement a few kilometres away from the western coastline of the Atlantic Ocean in France are presented. Due to the fact that the calibration of a cup anemometer usually comprises a positive offset the regression has been forced through the origin thus affecting the slope of the regression line.
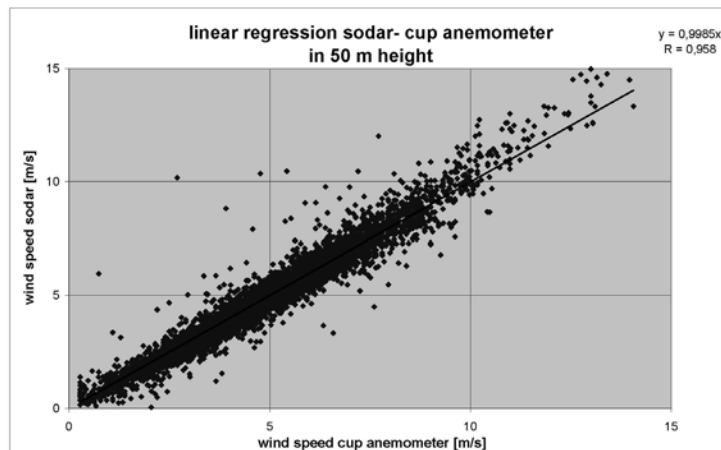
Figure 1. Correlation between wind measurements at 50 m height of a SODAR and a calibrated cup anemometer based on 10 minutes averages. A slope close to 1 and a correlation coefficient of 0.958 show the direct comparability of both measurements.

In a field experiment at the WINDTEST in-land test site for wind turbines a calibration between 2 ultrasonic anemometers has been performed. Afterwards one of the masts has been replaced by the SODAR. The two sites are separated by about 400 m.
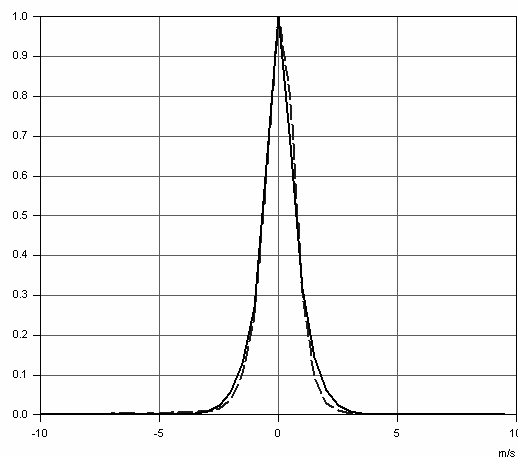

Figure 2. Frequency distribution of the differences between two ultrasonic anemometers (solid line) and between an ultrasonic anemometer and a SODAR (dashed line) at 50 m height and a distance of about 400 m.

4   Conclusion

SODARs can replace wind masts if operated properly and offer a cost-effective solution for wind measurements especially at higher altitudes.

Operational Windprofiler, Sodar and RASS Data and its Impact on NWP Model Forecasts

D.A.M. Engelbart [1], V. Lehmann[1], U. Görsdorf[1], J. Konopka[2], and Ch. Schraff[3]

[1] German Met. Service, Richard Aßmann Observat., Lindenberg, GERMANY
[2] DFS Deutsche Flugsicherung GmbH, Langen
[3] German Met. Service, Data Assimilation Dept., Offenbach

Abstract

Modern ground-based remote-sensing systems like WPR/RASS or Sodar/RASS may contribute to improvements in regional forecasts of NWP systems, when data qualities are sufficiently known and monitored thoroughly. An example of a positive impact on NWPs, where mostly boundary-layer WPR systems have been arranged in an operational network, is given by the CWINDE network of EUMETNET. For more than two years now, this network programme contributes to data assimilation of various European forecast systems by providing wind profiles in high time resolution.

Beside comparisons between NWP-generated wind profiles and "pure" measurements, the proposed presentation will first summarize some results from experience with data assimilation of wind profiles from the network. It will furthermore reveal potential deficits of Sodar measurements as a result from NWP monitoring statistics made by Météo France and, using a different model (LME), also made by the Richard Aßmann Observatory of the German Meteorological Service (DWD), at Lindenberg, Germany.

Although RASS temperature measurements from the whole boundary layer and above are available at least in some small subnet over Germany, this type of data has not been used in operational data assimilation schemes yet. In this context, the presentation will demonstrate the impact of RASS temperatures from a single operational WPR/RASS system on NWP, by showing a data assimilation case study from December 2005. In this case study, the data assimilation cycle ran strongly erroneous by the use of RASS data, resulting in significant forecast errors, e.g.with respect to precipitation compared to control forecasts without those RASS data. The presentation will therefore impressively outline that if any, only high-precision observational data will be able to contribute positively to NWP. Too bad data quality however, may not only have neutral, but strongly-negative impacts, especially in the boundary layer.

PRESENTATION:	**Oral** presentation preferred
CONFERENCE TOPIC:	"**Comparison** of remote-sensing information with results of boundary-layer **models**"

Comparison of modelled and sodar measured turbulence data in the proximity of a coastal area.

[1]*Gariazzo, Claudio, [1]Papaleo, Vincenzo, [1]Pelliccioni, Armando
[1]ISPESL – Dipartimento Insediamenti Produttivi e Interazione con l'Ambiente,
Via Fontana Candida, 1 00040 Monteporzio Catone (RM) Italy *(claudio.gariazzo@ispesl.it)

Abstract

The ability of the SPRAY particle dispersion model in estimating the actual variance of wind components has been studied by comparing the modelled σ_w data with those measured by a sonic anemometer and a SODAR system in proximity of an italian coastal area. Results exhibit a general underestimation of predicted σ_w data respect to the measured one. The level of agreement is found to be dependent on the atmospheric stability and on the land use of the model cell, as well as on its representativeness respect to the land/sea wind direction.

1   Introduction

The goodness of concentration results obtained from Particle Dispersion models (PD) are known to be dependent on the accuracy of the determination of fluctuation of wind components. In order to investigate the ability of PD model SPRAY (Gariazzo et al., 2004) in estimating these variances, measured σ_w data were compared with the calculated ones.

2   Turbulence measurements and modeling

Two field campaigns were conducted in winter and summer seasons. Surface turbulence parameters were collected by means of sonic anemometers located in the harbor of Taranto, a city located south of Italy. A SODAR system was used to collect turbulence vertical profiles up to 400 m agl at a vertical resolution of 20 m.

The turbulent fluctuation of wind components are calculated by SPRAY using parameterization codes (Hanna, 1982) based on scaling variables derived on the basis of the MO similarity theory and surface energy budget evaluation (Van Ulden and Holtslag, 1985). Inside the PBL, σ_w profiles are determined as follow, on the basis of the stability conditions:

Stable conditions	*Neutral conditions*	*Unstable conditions*	
$\sigma_w(z) = 1.3u_*(1- z/h)$ (1)	$\sigma_w(z) = 1.3u_* e^{(-2fz/u_*)}$ (2)	$\sigma_w(z) = 0.763(z/h)^{0.175}$ for $z \leq 0.4h$	
		$\sigma_w(z) = 0.722w_*(1 - z/h)^{0.207}$ for $0.4h<z\leq 0.96h$ (3)	
		$\sigma_w(z) = 0.37w_*$ for $0.96h<z \leq h$	

A total of 33 days were selected to simulate turbulence (σ_w). Model and observed σ_w data were first selected for season, then they have been studied under different atmospheric stability conditions. Since measurements were conducted in a quay of the port, wind turbulence has also been studied under both sea and land wind conditions. Furthermore, to study its dependence on the surface energy budget and roughness, two different grid cells, located respectively in the port and 1 km away from it over the sea, were selected.

3   Results and discussions

Table 1 shows statistical index (R^2) and parameters obtained applying a least-squares linear correlation between modelled and observed σ_w data at port station (labelled as *port*) under different seasons and atmospheric stability conditions. When data are selected only for season (all data) poor agreement is found regardless of season and height (R^2 from 0.19 to 0.33). Under stable conditions R^2 reaches a maximum value of 0.57 at 10 m height on summer season, showing a better capability to describe the observed σ_w behaviour. However, the

linear angular coefficients (referred as m) between modelled and measured σ_w, show a model underestimation of the actual σ_w (from 0.42 to 0.19) increasing with height. The bias value is close to the ideal value of 0. On winter season the highest value of R^2 is 0.4 calculated at 40 m. The underestimation is even stronger with an average value of about 0.2.

Under summer neutral conditions the model results are far to reproduce the observed values (R^2=0.16-0.28). Conversely on winter season better values of R^2 are calculated (R^2=0.42-0.58), but model underestimation of the measured σ_w is detected (m = 0.51-0.24 from 10 to 120m). This seasonal discrepancy can be justified by the different wind conditions detected in the two seasons under neutral conditions. While winter data are mainly involved with strong land wind conditions, the summer one are related with strong winds blowing from the sea.

According to both winter and summer R^2 values (R^2 from 0.16 to 0.27) calculated under unstable conditions, the model shows poor reproduction of the observed σ_w data. Based on its w_* dependence (see eq. 3), in the port cell the model predicts at daytime the typical convective behaviour linked with the solar radiation and surface energy budget. Conversely, the observed data, due to the particular location of the measurement site (a quay in front of the sea), do not show the presence of a well developed thermal convection, while the mechanical turbulence, produced by breeze winds, dominates in the measured data.

The best results of the R^2 are obtained under land wind conditions in both winter and summer seasons (0.68-0.57 and 0.58-0.4 on summer and winter respectively). About 70% of these wind conditions are linked with stable conditions, where, based on eq. (1), a u_* dependence is selected. The m coefficient results shown on table 1 under land wind conditions, also exhibit a strong underestimation (about 50%) of the observed σ_w data regardless of season or height.

Under sea wind conditions the model again shows a poor reproduction (R^2 up to 0.26) of the σ_w. It should be noticed that these wind conditions are linked with 77% and 51% of unstable conditions respectively in summer and winter seasons. So, based on the equation (3), the model uses a w* dependence to predict the σ_w data, which is not revealed in the observed data. As in these conditions the observed wind at the port station can be considered more related to the wind observed over the sea, the modelled σ_w at 1 km from the coastline was extracted and compared with that measured at the port station. Results shown on table 1 (labelled *sea*) exhibit a net improvement of R^2 (0.32-0.44 on summer and about 0.5 on winter) respect to values calculated at port cell (referred as *port*). This progress is more evident in the sodar data (from 40 to 120 m) than in the surface one (10m). Again even in this sea cell an underestimation of the observed turbulence is detected (m values from 0.22 up to 0.42). The above results seem to indicate that when σ_w is estimated by means of u_*, better predictions are obtained, although with a strong underestimation. Improvements on σ_w estimations can be obtained by using the measured value of u_*. Results are shown on table 1 (referred as *port(u_* obs)*). It can be noticed the net improvement of the overall correlation coefficients R^2, addressing to a better quality of reproduction of the actual turbulence.

4 Conclusions

A comparison study between observed and modelled σ_w data has been carried out. Results show SPRAY, in a model cell close to sea, is able to estimate σ_w data under stable and neutral stability conditions, while it fails when unstable one are considered. Strong underestimation of the observed σ_w are detected. Land use of the model cells is found to be an important parameter when the observed turbulence is compared with the modelled one. In a cell with port as land use, and located in proximity of the coastline, SPRAY is unable to appreciate the differences on turbulence between land and sea winds, caused by the surface roughness. A net improvement on σ_w estimations are also found when the measured friction velocity is used instead of the estimated one, addressing to a possible progress in the turbulence code.

Literature

Gariazzo, C., Pelliccioni, A., Bogliolo, M. P., Scalisi, G., 2004: Evaluation of a Lagrangian Particle Model (SPRAY) to assess environmental impact of an industrial facility in complex terrain. Water, Air and Soil Pollution 155: 137-158.

Hanna, S. R., 1982: Applications in Air Pollution Modeling. In. Atmospheric Turbulence and Air Pollution Modelling, F.T.M. Nieuwstadt and H. Van Dop, Reidel, Dordrecht, Chapter 7.

Van Ulden, A. P., Holtslag, A. A. M., 1985: Estimation of atmospheric boundary layer parameters for diffusion application. Journal of Climate and Applied Meteorology, 24, pp. 1196-1207.

Table 1. Statistical indexes of least-square linear correlation between modelled and measured σ_w data under different seasons and meteorological conditions.

Cell station	HEIGHT (m)											
	10			40			80			120		
	R^2	m	Bias (m/s)	R^2	m	Bias (m/s)	R^2	m	Bias (m/s)	R^2	m	Bias (m/s)
All data												
summer												
port	0.33	0.39	0.08	0.27	0.42	0.12	0.19	0.35	0.14	0.22	0.37	0.1
winter												
port	0.26	0.3	0.07	0.32	0.35	0.07	0.3	0.33	0.07	0.24	0.3	0.06
Stable												
summer												
port	0.57	0.42	0.00	0.55	0.36	0.00	0.47	0.29	0.00	0.41	0.19	0.01
port(u· obs)	0.9	1.04	-0.03	0.68	0.73	0.00	0.55	0.58	-0.01	0.5	0.42	-0.01
winter												
port	0.2	0.2	0.07	0.4	0.28	0.03	0.35	0.21	0.03	0.28	0.15	0.04
port(u obs)*	0.9	1.06	-0.05	0.59	0.72	0.00	0.52	0.48	0.02	0.43	0.32	0.01
Neutral												
summer												
port	0.28	0.46	0.29	0.26	0.35	0.32	0.16	0.25	0.38	0.23	0.29	0.32
port(u· obs)	0.86	1.01	-0.02	0.28	0.44	0.26	0.13	0.28	0.37	0.18	0.31	0.32
winter												
port	0.58	0.51	0.23	0.56	0.4	0.24	0.52	0.32	0.27	0.42	0.24	0.3
port(u· obs)	0.87	0.89	0.01	0.73	0.67	0.04	0.61	0.51	0.1	0.43	0.35	0.18
Unstable												
summer												
port	0.16	0.12	0.21	0.24	0.32	0.33	0.2	0.24	0.35	0.21	0.23	0.34
winter												
port	0.24	0.12	0.17	0.26	0.17	0.28	0.25	0.17	0.31	0.27	0.18	0.31
Land-wind												
summer												
port	0.64	0.53	-0.02	0.68	0.57	0.00	0.66	0.54	-0.04	0.57	0.51	-0.04
winter												
port	0.52	0.46	-0.03	0.58	0.46	-0.01	0.5	0.41	0.00	0.4	0.35	0.01
Sea-wind												
summer												
port	0.25	0.35	0.16	0.26	0.54	0.21	0.08	0.31	0.29	0.1	0.29	0.28
sea	0.22	0.24	0.08	0.44	0.42	0.02	0.32	0.32	0.02	0.29	0.22	0.02
winter												
port	0.12	0.29	0.17	0.07	0.26	0.22	0.01	0.11	0.25	0.01	0.07	0.23
sea	0.11	0.2	0.12	0.5	0.4	0.02	0.51	0.3	0.01	0.51	0.25	0.01

Quality assessment of boundary-layer parameters predicted by REMO and observed by ground-based remote sensing

Hennemuth[1], Barbara, Weiss[2], Alexandra, Bösenberg[1], Jens, Jacob[1], Daniela,
Peters[3], Gerhard and Pfeiffer[1], Susanne

[1]Max-Planck-Institute for Meteorology, Hamburg,, [2]British Antarctic Survey, Cambridge CB30ET, GB,
[3]Meteorological Institute, University of Hamburg, Germany, hennemuth@dkrz.

Abstract

In this study a twelve weeks comparison of several water cycle parameters in the atmospheric boundary layer derived from the regional model REMO and from observations is presented. The predicted boundary layer appears to be too shallow and too moist. As one reason a wrong partitioning of the energy fluxes at the surface can be identified which is caused by a wrong representation of soil moisture during drying periods. Boundary layer clouds in the model therefore have a too low cloud base, and they are shallower than observed clouds.

1   Introduction

The atmospheric boundary layer relates surface and atmospheric processes and is the region of large vertical transport of heat and water. The moisture transport leads to the formation of boundary-layer clouds which have an essential impact on the energy balance of the earth's surface. Boundary-layer humidity field, soil moisture, surface evaporation, entrainment flux, and boundary-layer height are the important parameters interacting in the cloud formation process. This process must be simulated properly in models which are used not only as forecast but also as climate models.
The ability of the regional model REMO to simulate the boundary-layer processes is tested in a comparison of model predictions and observations of various parameters.

2   Regional model REMO and quality assessment experiment

The regional model REMO is a hydrostatic, three-dimensional atmospheric model developed at the Max-Planck-Institute for Meteorology in Hamburg (Jacob, 2001). REMO was run in forecast mode in order to simulate the atmospheric conditions as close to the real weather as possible. The horizontal resolution was $1/6°$ i.e. approximately 18 km. The model runs were initialized and driven at the boundaries with ECMWF analyses, the $1/6°$ run was nested within a $1/2°$ run. The model domain comprised central Europe. Nearly all relevant transport and phase change processes for water in the atmospheric boundary layer (ABL) are parameterised. REMO uses the physical package of the global circulation model ECHAM4 (DKRZ, 1994, Roeckner et al., 1996).

The quality assessment experiments were conducted in May / June 2003 (LITFASS-2003), May / June 2004 and August / September 2004 at the Meteorological Observatory Lindenberg (MOL) of the German Weather Service (DWD), 60 km southeast of Berlin. The instrumentation includes energy balance stations, a network of 14 rain gauge, ceilometer, microwave cloud radar, micro rain radar (Peters et al., 2005), Differential Absorption Lidar (DIAL), Doppler lidar (Bösenberg and Linné, 2002), and some additional instrumentation in the frame of the LITFASS-2003 experiment.
All observed quantities are transformed to an average REMO grid by vertical and time averaging.

3   Results of comparison

Statistical analysis of humidity is performed for all grid boxes with observations (Fig.1). Simulated and observed values are well correlated within the convective boundary layer below 1000 m.
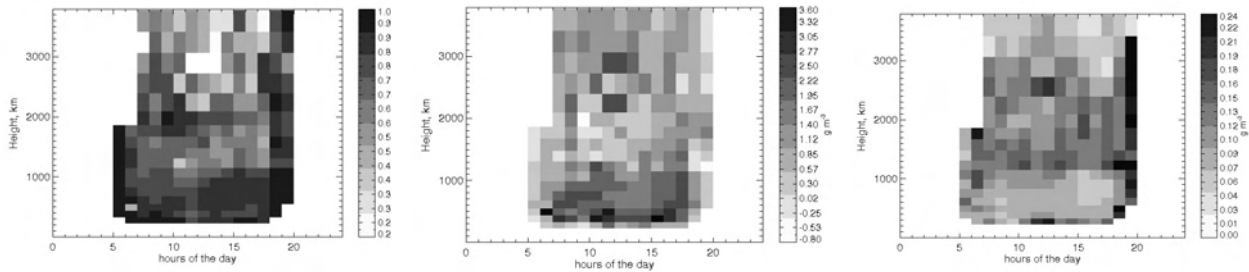

Figure 1.   Correlation coefficient (left), bias (middle) and rms-error (right) of REMO versus observed humidity.

While the humidity values below 1000 m are strongly biased by 1.5 to 3 g/m but exhibit a low rms-error the humidity values above the CBL agree much better on the average but show a large rms error. From this we conclude that in most cases the simulated boundary layer is too low and too moist.

One crucial parameter for the humidity field in the ABL is surface evaporation. During LITFASS-2003 REMO predictions can be compared with area averages from a network of micrometeorological stations (Fig.2). The simulated latent heat flux is much larger than the observed one, the sensible heat flux is lower, only on days with precipitation they agree.
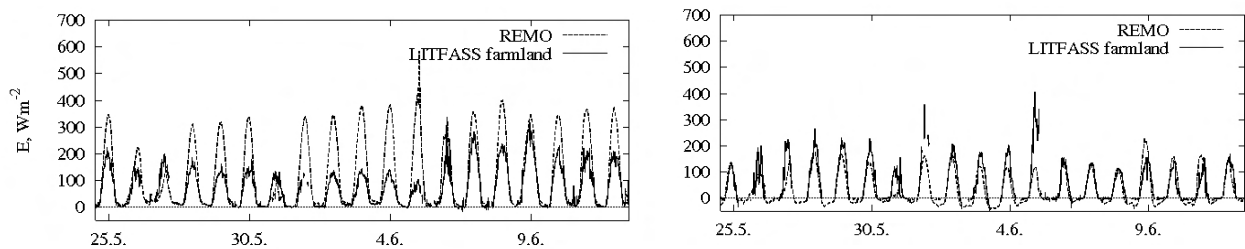
Figure 2.   Time series of latent heat flux (left) and sensible heat flux (right) from 1 to 12 June 2003.

Boundary layer processes are influenced by soil parameters, so soil moisture is also compared, however, only qualitatively (Fig.3). It is obvious that during dry periods the soil moisture decreases steadily in all depths and after rain events the upper layers are moistened. REMO also predicts decreasing soil wetness, but shows only little reaction to rain events.
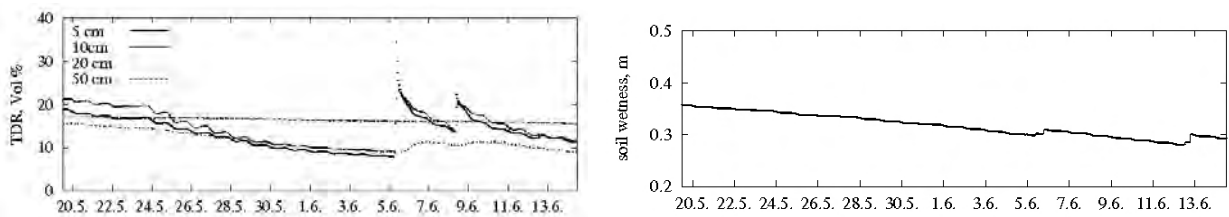
Figure 3.   Time series of observed (left) and simulated (right) soil moisture during LITFASS-2003.

A statistical analysis of observed and predicted clouds (Fig.4, right) shows that REMO under-estimates cloud cover particularly in lower levels. Observed ABL clouds extend over several grid levels whereas model ABL clouds are often restricted to one, two or three layers. More-over, simulated boundary layer cloud bases are lower than observed ones.
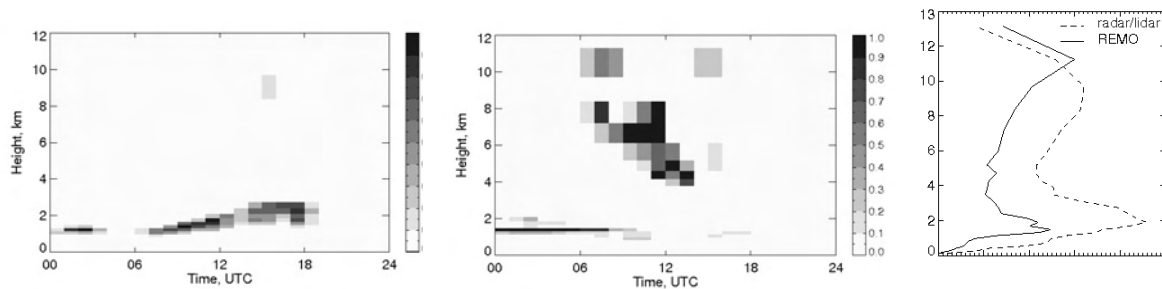
Figure 4. Time-height cross-section of cloud cover, left: observed, middle: simulated, and number of predicted and observed clouds (right).

4   Conclusions and Outlook

The comparisons show that the model boundary layer is too low and too moist. One reason for this is a too large evaporation and a mostly too low sensible heat flux. The wrong parti-tioning of available energy at the surface is probably caused by the unrealistic representation of soil moisture in the model. The simple bucket model of REMO is not capable to simulate the drying of the soil. Consistently, it is found that the model ABL clouds are lower than ob-served ABL clouds. The predicted and measured water vapour flux profiles (not shown here) have similar structure and confirm that the vertical transport of water vapour in the CBL is simulated in the right way. So the low cloud base is determined by the low top of the CBL. The comparisons also show that the vertical extent of simulated ABL clouds is smaller than for observed clouds. This may be a result of the parameterisation scheme, which may be not capable of extending the ABL clouds to more than a few levels. In fact, we observe a large variability of the top of boundary layer clouds.

Some of the shortcomings found in parameterisation schemes in REMO are currently cleared up. REMO will be upgraded with a new prognostic equation for ice water content. The REMO soil moisture scheme which was found to be insufficient for dry periods will be exten-ded to more layers. There are also considerations to improve the parameterisation scheme of turbulent and convective vertical transport in the ABL by regarding also non-local transport.

Literature

Bösenberg, J. and H. Linné, 2002: Laser remote sensing of the planetary boundary layer. Meteorol. Z. 11, 233 – 240.
DKRZ, 1994: The ECHAM3 atmospheric general circulation model. Techn. Report~6, Hamburg, Germany.
Jacob, D., 2001: A note to the simulation of the annual and inter-annual variability of the water budget over the Baltic Sea drainage basin. Meteorol. Atmos. Phys. 77, 61-73.
Peters, G., B. Fischer, H. Münster, M. Clemens and A. Wagner, 2005: Profiles of raindrop size distributions as retrieved by microrain radars. J. Appl. Meteorol. 41, 1930-1949.
Roeckner, E. and 9 co-authors, 1996: The atmospheric general circulation model ECHAM-4: Model descrip-tion and simulation of present day climate. Report 218, Max-Planck-Inst. f. Meteorologie, Hamburg, Germany.

A model for atmospheric boundary layer night cooling and its comparison with sodar data

Kramar, Valeri
Obukhov Institute of Atmospheric Physics Russian Academy of Sciences
vkramar@ifaran.ru

Abstract

To calculate vertical profiles of turbulence characteristics a model of the thermal behavior of atmospheric boundary layer (ABL) parameters is developed. The one-dimensional non-stationary system of hydrodynamic and turbulence equations was used for this aim. Sodar and sonic-anemometer data acquired at the Zvenigorod-2005 field experiment were used for the model verification. Vertical profiles of heat flux were calculated from the above model and the mixing layer depth was estimated.

1   Introduction

To solve a lot of problems of the ABL theory one needs to use complex non stationary mathematical models that can describe the ABL processes in details. The models are based on differential equations of momentum and heat transfer and include multiparametric model of turbulence. Such models are hard to resolve, besides they contain sets of empiric constants which values should be verified separately.

It is proposed to use remote acoustic sensing data including the measured profiles directly in the equations of the ABL model, as well as for verification of values of the sets of empiric constants.

An example of the approach permitting to simplify the solution is described below. Restrictions and quality of the proposal one can estimate independently.

2   Instrumentation

July 10, 2005 was selected to demonstrate the approach as one in the sequence of typical days that were observed in the Zvenigorod-2005 field experiment. The experiment was carried out July 2005 at the Zvenigorod Scientific Station of the IAPh RAN. Three-component Doppler sodar LATAN-3 designed and manufactured in the IAPh was used in the experiment with two sonic anemometers USA-1 [Peters, 1998] (sonic) mounted at two levels of the 60m meteorological mast. Well horizontal uniformity of the tested ground should be underlined specially. Other features of the experiment its equipment and method details one can find in [Kouznetsov, 2006].

3   Theoretical background

To describe the thermally stratified non stationary turbulent ABL behaviour the well known and widely applied mathematical model was selected. Besides, differential transfer equations mentioned above the model contained a set of algebraic equations as second order turbulent moments closure. Detailed description of such kind of models one can find, for example, in the Rodi's large review [Rodi, 1980]. The system of equations of the model was transformed to unidimensional non stationary form due to mentioned above horizontal uniformity of the tested ground.

Consecutive simplifications are as follows. The evolution of vertical profiles of the wind velocity was measured by the sodar directly. The presence of such data permits to find momentum flux directly from the equation of motion. If X-axes is directed collinear with

wind direction then the equation can be written (it should be underlined that observed wind direction variations were small during selected period) in ordinary form:

$$dV/dt = -d/dz \ (<uw>)$$

where V is wind velocity, t – time, z – vertical coordinate, <uw> - turbulent shear stress.
As the left side of the equation is known then shear stress profile can be found with the integration procedure along the vertical coordinate z. The constant of the integration can be found from the sonic data. So, from the sodar measurements we get profiles of three unknown values with their evolution in time: wind velocity, turbulent shear stress and vertical component of the turbulence kinetic energy - $<w^2>$. Any between value can be found with the help of time interpolation technique. When values of these three variables are found any three equations can be excided from the set of equations of the model. In current analysis momentum and heat transfer equations as well as the equation for the dissipation of the turbulence kinetic energy are dropped from the general model. After that the ordinary hypothesis of local balance of turbulence generation and dissipation rates is applied to the model. Then we get the result – non linear system of algebraic equations with no time derivatives which is more simple to resolve than the initial one. As the system remains to be closed, the values of all unknown variables can be found as a result of the system solution procedure.

4   Results

Evolution of vertical profiles of wind velocity measured by the sodar and time dependencies of heat fluxes and temperatures for two levels of meteorological mast measured by sonics are shown in Fig.1. The following features are important for verification of the proposed model: good uniformity of cooling of the ABL with linear decreasing of the temperature and complex vertical structure of the ABL illustrated by the sharp-cut low level jet profile.
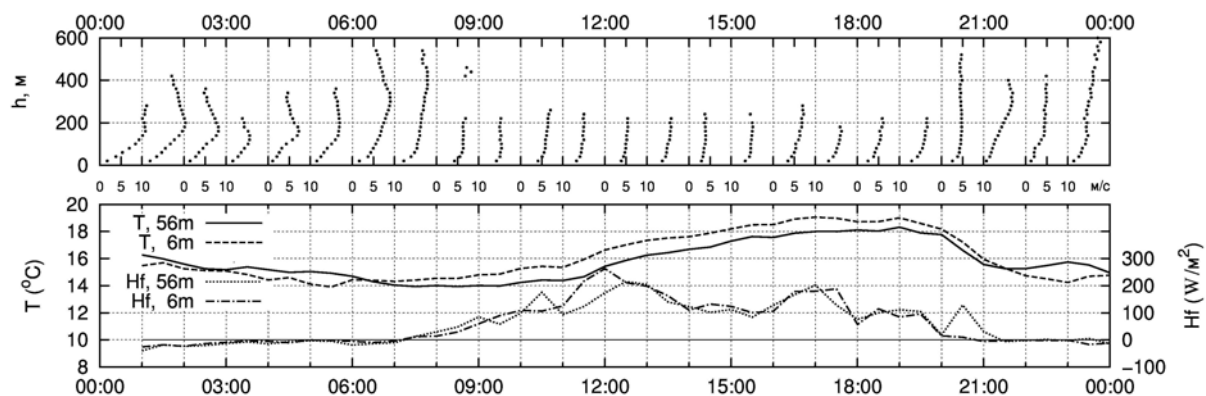
Figure 1. Evolution of vertical wind velocity profiles measured by the sodar (top) and temperature and heat flux measured by the sonic (bottom) during 10 July, 2005

Fig.2 shows the profiles in the middle of ABL cooling period. They are: measured by the sodar vertical profile of wind velocity; calculated from the equations of simplified model profile of heat flux; turbulent shear stress calculated from the motion equation where wind profiles are used; eddy viscosity coefficient calculated using ordinary Boussinesque approximation in which in its turn measured wind profile and calculated shear stress profile are used.
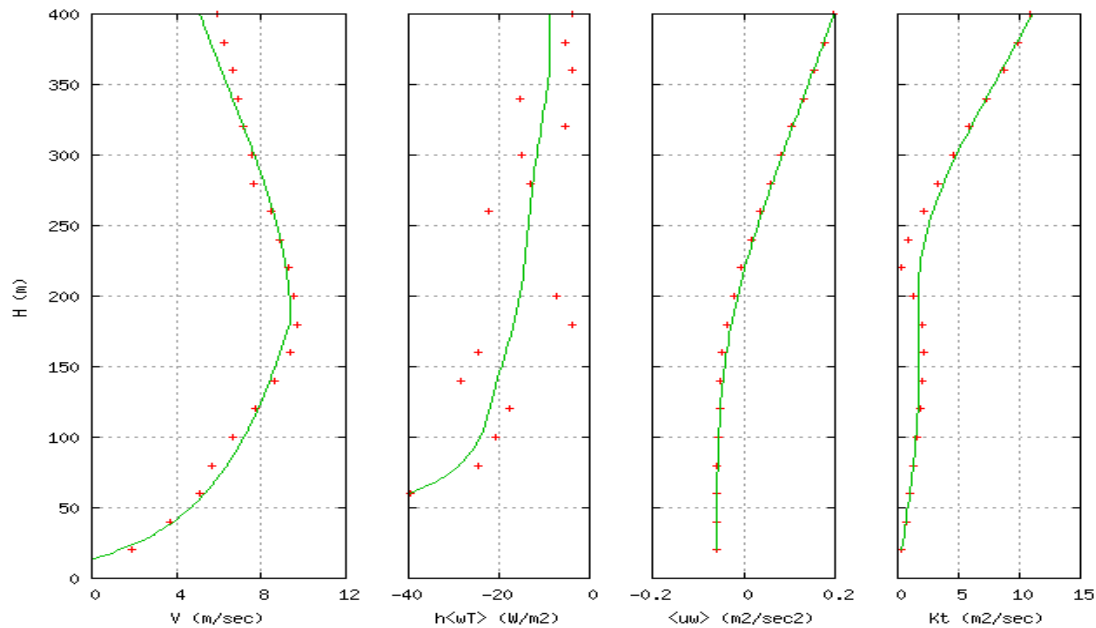
Figure 2. 10 July, 2005, 02:00 LMT. Examples of calculated profiles for period of cooling ABL. Left to right: measured by sodar wind velocity profile, calculated from the simplified model heat flux profile, calculated from the motion equation turbulent shear stress profile, calculated eddy viscosity coefficient profile.

5   Discussion, Conclusions, and Outlook

Despite the fact that the initial model was appreciably simplified the important features of calculated profiles can be apparently seen. In particulare, negative to positive conversion of calculated turbulent shear stress value near wind velocity maximum; small and relatively constant values of turbulent shear stress and eddy viscosity coefficient inside the low part of ABL from its bottom to the wind velocity maximum. Inside the inversion layer turbulence is strongly suppressed and the model shows the feature. On the contrary linear increase of the turbulent shear stress and eddy viscosity coefficient on the upper part of the ABL means near neutral stratification increase of turbulence and low value of the heat flux. The level where the ABL turbulent characteristics behavior converts is close to black bound on sodar echogram (approx. 200m).

Good predictability of mentioned features for ABL of complex structure and for strongly stably stratified ABL allows to use the proposed model in more simple cases without any hesitation.

Literature

Peters, G., B. Fischer, H.-J. Kirtzel, 1998: One-year operational measurements with a sonic anemometer-thermometer and a Doppler sodar. Journal of Atmospheric and Oceanic Technology, Vol. 15, pp. 18–28.

Rodi, W., 1980: Turbulence models for environmental problems. {in Prediction Methods For Turbulent Flows. (Kollman, W. Ed.)} Hemisphere Publishing. Corporation, Washington, DC, pp. 259-350.

Kouznetsov, R., 2006: The new PC-based sodar LATAN-3. Proc. 13-th Int. Symp. Acoust. Rem. Sens.— Garmisch, Germany, pp. ***.

Modelling and measuring the atmospheric excess attenuation over flat terrain

Ziemann, Astrid, Balogh, Kati, Arnold, Klaus
University of Leipzig, Institute for Meteorology, ziemann@uni-leipzig.de

Abstract

The model SMART (Sound propagation model of the atmosphere using ray-tracing) calculates the modified sound propagation due to sound-ray refraction in a stratified and moving atmosphere. For validation of the simulated data a measuring campaign was carried out over flat terrain in autumn 2004. The comparison of the modelled with measured data during clear night conditions with strong temperature inversion shows a satisfactory agreement, which leads to the conclusion that the main effects on outdoor sound propagation are reliably described by the model SMART.

1   Introduction

The influence of the atmospheric structure on the sound propagation is utilised by different acoustic measuring techniques, e.g. SODAR (scattering) and acoustic tomography (transmission of sound, temperature and wind-dependent sound velocity). One of the most important effects on the sound propagation is the refraction of sound rays due to the vertical temperature and wind vector profile. The subsequent deviation of sound paths from straight lines leads to sound parameters, whose changed values should be estimated regarding the accuracy of acoustic remote sensing data and the applicability of low-end models of sound propagation (e.g. guidelines) without the special atmospheric influence. Thus, a geometrical sound propagation model is presented in this study to include on one side the state of the atmosphere into the forecast of sound immission and to minimize on the other side the computing time of such a physical model.

2   Sound propagation simulation

The model SMART (see e.g., Ziemann, 2003) calculates the modified sound propagation conditions due to sound-ray refraction for an area according to the given thermal stratification of the atmosphere and the vertical profile of wind vector. Thereby, a special refraction law was implemented, that is valid for a two-dimensional, stratified moving medium. Outgoing from the ray tracing the model SMART calculates the attenuation level. The change of the sound intensity level (attenuation level) at the height of sound immission is only dependent on geometrical quantities, e.g. on the relation between the cross sections of a sound tube in a reference distance and in another distance from the sound source. Furthermore, the frequency-dependent effects of sound absorption in air and sound-ray reflection at the ground surface were integrated. The difference between the attenuation level for an actual atmospheric structure and for an atmosphere without temperature and wind gradients leads to the meteorological excess attenuation as a measure for the influence of atmospheric refraction on the sound immission.

3   Sound propagation measurement

To validate the simulated data a measuring campaign was carried out over flat terrain (grassland) in autumn 2004 at the research station of the Institute of Tropospheric Research Leipzig, where two different measurement systems were used. Firstly, the method of acoustic tomography provided relative amplitudes of artificially generated sound signals propagating on distances between some ten to hundred meters to calculate the excess attenuation. Secondly, there was a commercial system for monitoring sound pressure levels (and attenuation levels) directly. The correlation between the measurement and modelled data was compared for

sound propagation in downwind and upwind direction during night time, because a significant influence of atmospheric refraction on the sound propagation was expected due to a strong temperature inversion (Balogh et al., 2006).

4   Results

During the measurement period the sound propagation was influenced by a nearly always positive gradient of effective sound speed $\Delta c_{eff}/\Delta z$. Under these conditions the sound rays were mainly downward refracted followed by multiple reflections at the ground surface. Therefore the meteorological excess attenuation generated by the coupled influence of atmosphere and ground surface was always negative in downwind direction and mostly negative in upwind direction (see Fig. 1). From this it follows an increased sound immission in comparison to an undisturbed sound propagation situation without atmospheric refraction.
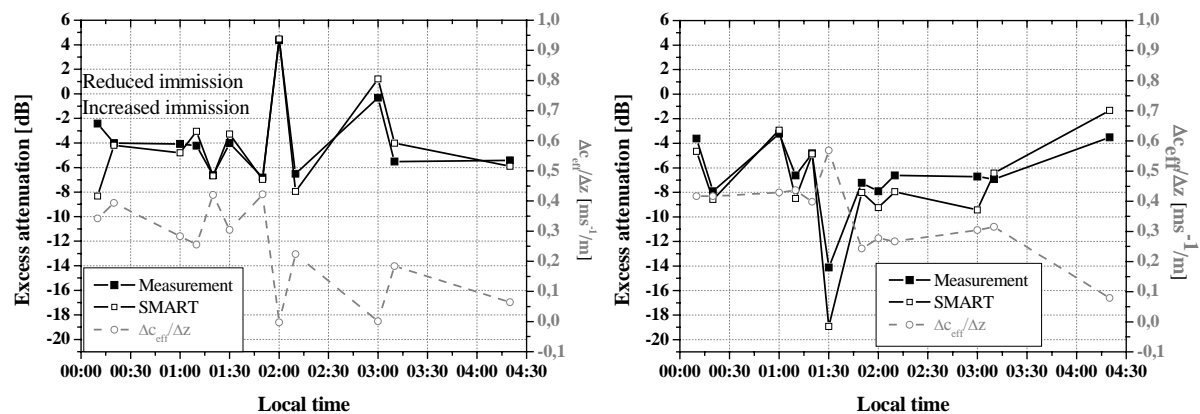
Figure 1. Comparison of measured (only commercial measurement system) and modelled meteorological excess attenuation influenced by refraction in the atmosphere and reflection at the ground surface for a sound propagation distance of 75 meters in upwind (left) and in downwind (right) direction on the 8th October 2004 at the test site near Leipzig (grassland).

5   Conclusions and Outlook

Measured and modeled data show, that under conditions of a strong temperature inversion an increase of sound level of about 10 dB is often possible also over short sound propagation paths. This result is contrary to low-end models like the VDI-Guideline in Germany which estimates that the coupled influence of the atmosphere and ground surface leads always to a reduced sound immission. Furthermore, the comparison between SMART and measurements demonstrates a satisfactory agreement. So it can be concluded that the main effect on outdoor sound propagation is reliably described by the model. Nevertheless the data are slightly better correlated in the upwind than in the downwind direction. This result is caused by the circumstance, that not all influences on sound propagation are included in the model SMART. The interference of direct and at the ground surface reflected waves, which especially occur in the downwind direction, is among such not considered effects in the ray model. Additionally, the model SMART should be further developed to include other influences of atmospheric phenomenons, like turbulence, on the sound propagation and sound level forecast.

Literature

Balogh, K., A. Ziemann, D. Daniel, 2006: Influence of atmospheric refraction on sound propagation over a flat ground surface, Acustica, accepted.

Ziemann, A., 2003: Auswirkungen unterschiedlicher Schallausbreitungsmodelle auf die Lärmprognose, Wiss. Mitt. Inst. für Meteorol. Univ. Leipzig, 30, 61-72.

List of authors